Models of Jupiter's Polar Aurora

By

Nataly Özak Muñoz

Submitted to the Department of Physics and Astronomy and the
Faculty of the Graduate School of the University of Kansas
in partial fulfillment of the requirements for the degree of

Doctor of Philosophy

Committee members

Prof. Thomas E. Cravens, Chair

Prof. Barbara J. Anthony-Twarog

Prof. Steven A. Hawley

Asst. Prof. Gregory Rudnick

Prof. Carey K. Johnson

Date defended: May 9, 2012

The Dissertation Committee for Nataly Özak Muñoz certifies
that this is the approved version of the following dissertation:

Models of Jupiter's Polar Aurora

Committee:

Prof. Thomas E. Cravens, Chair

Prof. Barbara J. Anthony-Twarog

Prof. Steven A. Hawley

Asst. Prof. Gregory Rudnick

Prof. Carey K. Johnson

Date approved: May 9, 2012

Abstract

Auroral emissions from Jupiter have been observed across the photon spectrum including ultraviolet and x-ray wavelengths. UV observations suggest an input flux power of $10^{13} - 10^{14}$ W for the aurora in each hemisphere. X-ray emissions with a total power of about 1 GW were observed by the Einstein Observatory, the Roentgen satellite, Chandra x-ray Observatory (CXO), and XMM-Newton. Previous theoretical studies have shown that precipitating energetic sulfur and oxygen ions can produce the observed x-rays. This study focuses on the ion precipitation of the polar region and its effects in the ionosphere. We present the results of a hybrid Monte Carlo model for sulfur and oxygen ion precipitation at high latitudes, look at differences with the continuous slowdown model, and compare the results to synthetic spectra fitted to observations. We concentrate on the effects of altitude on the observed spectrum and find that the opacity of the atmosphere to the outgoing x-ray photons is important for incident ion energies greater than about 1.2 MeV per nucleon for both sulfur and oxygen. Quenching of longer-lived excited states of the oxygen ions is also found to be important. Opacity considerably diminishes the outgoing x-ray intensity calculated, particularly when the viewing geometry is not favorable. We estimate an emission efficiency for the x-ray aurora of $\varepsilon \approx 7 \times 10^{-5}$. Secondary electrons from the ion precipitation as well as photoelectrons and auroral electrons also affect the polar cap atmosphere. We calculated the secondary electron production due to the oxygen ion precipitation for the first time.

We analyze the secondary electron fluxes due to the ion aurora and estimate their effects on the ionosphere and field aligned electrical currents. We find that the secondary electrons affect the ionosphere similarly to auroral electrons responsible for the diffuse UV aurora and are therefore important for the magnetospheric dynamics and our better understanding of the ionosphere-magnetosphere coupling.

Acknowledgements

I would like to acknowledge and thank my advisor T. E. Cravens for his guidance during my graduate studies. I would like to thank D. R. Schultz for calculating the cross sections that made our models possible. I would also like to thank Tizby Hunt-Ward for all her help with my work. I would also like to acknowledge and thank my family and my husband for all the help and support they provided that allowed me to complete this work.

Contents

List of Figures

List of Tables

Chapter 1

Introduction - Overview

In the present work we are interested in the auroral emissions at the polar cap of Jupiter and the main mechanism responsible for these emissions. In particular we are interested in the x-ray aurora mechanism at Jupiter and its effect on the Jovian ionosphere. The main tasks of this work can be summarized as follows:

- Develop a Monte Carlo simulation to model energetic oxygen and sulfur ions that precipitate in Jupiter's polar cap.
- Simulate x-ray emissions due to k-shell transitions in the excited ions as they precipitate in the atmosphere of Jupiter.
- Explore the effects of atmospheric absorption and quenching in the x-ray spectrum.
- Calculate the secondary electron production from the ion aurora.
- Adapt existing two-stream numerical codes to the conditions in Jupiter. This means collecting the appropriate electron cross sections for an atmosphere composed of H_2, H, He and CH_4.

- Use the adapted two-stream numerical code (Jupiter version) to calculate upward and downward electron fluxes along a magnetic field line in the ionosphere.

- Evaluate the effects of the secondary electrons in the ionosphere, estimate airglow emissions due to the electrons and estimate the currents carried by ions and electrons.

- Develop a photochemical code for Jupiter that uses ion production rates calculated by the two-stream code and Monte Carlo model in order to calculate the ionospheric densities where ion precipitation occurs.

This is a very complex subject that involves many aspects of physics. To have a better understanding of the material and background, we first have an overview in the present chapter to cover the subjects of magnetospheres, ionospheres, aurorae, and mangetosphere-ionosphere coupling. Chapters 2 and 3 deal with the cross sections for electron-neutral and ion-neutral collisions for all processes needed in our simulations. Chapter 4 explains the ion precipitation modeled with the Monte Carlo simulation, as well as opacity effects that exist that may affect the observed spectrum. In Chapter 5 we model electron transport in the ionosphere with a two-stream numerical model, which we adapted for Jupiter. We compare our results to previous models in order to verify our code. In Chapter 6 we explain the calculation of the energy distribution of secondary electrons and their transport in the ionosphere. We calculate electron fluxes and currents, ion production rates and airglow emissions due to the electron-neutral collisions. Lastly, Chapter 7 concludes our work and summarizes our findings.

1.1 Magnetospheres

Every planet in the solar system that has an intrinsic magnetic field, forces the solar wind to be deflected around the planet like an obstacle, forming a cavity with low density plasma. This cavity or region is known as the magnetosphere, as introduced in 1959 by T. Gold [25] after the Earth's magnetosphere was observed by Van Allen and others in 1958. In his paper, Gold defined the magnetosphere as "the region above the ionosphere in which the magnetic field of the earth has a dominant control over the motions of gas and fast charged particles". Today, this term has a much broader definition, used to define the region around an object, where its intrinsic magnetic field dominates the dynamics of the charged particles in the local medium.

In the solar system magnetospheres have been detected on Mercury, Earth, Jupiter, Saturn, Uranus, Neptune and Jupiter's moon Ganymede. There are three factors that are key to the formation and maintenance of the magnetosphere: First, the intrinsic magnetic field of the planet must be strong enough to actually slow down the solar wind, or other external medium, and deviate it around the planet or object. Second, an internal or external source of plasma must populate the magnetosphere, and third, it needs a source of energy to power it [1,26,27]. Depending on the planet, different mechanisms may act to achieve these factors. Figure 1.1 shows the structure of the Earth's magnetosphere as an example. On Earth, the solar wind plasma acts as an external source that populates and powers the magnetosphere. On Jupiter the mechanism is different than on Earth. It's moon Io is an internal source of plasma and the rapid planetary rotation is the energy source of the magnetosphere [28–30]. Saturn's magnetosphere, on the other hand, appears to be driven strongly by the solar wind, but with different conditions than those seen on Earth [31, 32]. The rapid planetary rotation and some internal plasma sources (the moon Enceladus, for example) also appear to contribute to the physics of

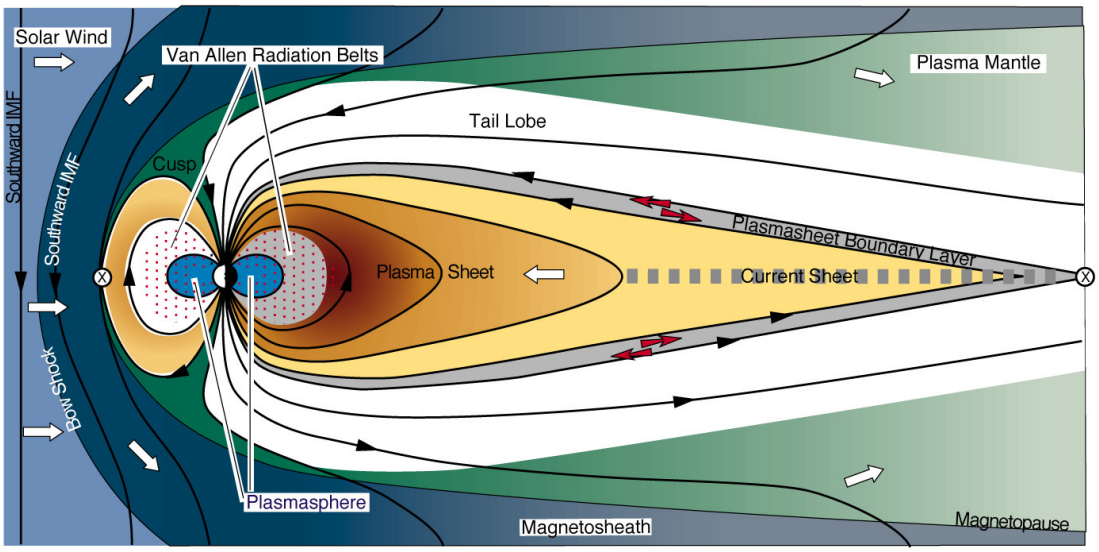

Figure 1.1: Structure of the Earth's magnetosphere

Saturn's magnetosphere, but to a smaller extent than in Jupiter. One could say that Saturn is an intermediate case between Jupiter's and Earth's magnetospheres.

There may also be cases in which the magnetic field of the object is too small to have an effect on the external medium but where similar structures to those found in magnetospheres are observed. Such situations are called magnetosphere-like systems and have been observed at Venus, Mars, Jupiter's moon Io, and Saturn's moon Titan [27].

With the discovery of Earth's magnetosphere began a search for the existence of magnetospheres in other planets. In 1955 radio emission from Jupiter attributed to electron cyclotron radiation was observed (see references within [33]), revealing the existence of a Jovian magnetic field and making it officially the first magnetosphere discovered, even though the term had not been proposed yet. Unfortunately, it was not possible to demonstrate the existence of a planetary magnetic field for Saturn by

early remote observations as done with Jupiter. It was not until the Pioneer 11 flybys in 1979, Voyager 1 in 1980 and Voyager 2 in 1981 that the existence of a magnetosphere at Saturn was observed. After the discovery of Jupiter's and Saturn's magnetospheres it was expected for Neptune and Uranus to also have magnetospheres. In 1982 the IUE (International Ultraviolet Explorer) observed UV emissions from Uranus and observed Neptune [34], finding it to have an excess of internal energy, which suggested the existence of an internal energy source. These speculations were later confirmed also by a Voyager 2 fly-by on January 24, 1986, for Uranus and August 25, 1989, for Neptune (see [33] and references therein).

Table 1.1 summarizes important parameters on Earth, Jupiter, and Saturn as known today. This table allows us to better grasp the differences in magnitude from the Earth's parameters compared to the giant planets. Jupiter's magnetosphere is the biggest object of the solar system. As the parameters on the table show, the magnitude of the processes happening inside of it are very energetic compared to our own planet. Understanding the underlying processes in the Jovian magnetosphere has long been a topic of research because the way this magnetosphere is powered and populated is different than on Earth. However, the distance to the planet limits our capability of taking measurements and making observations. The same is true for Saturn, but with latest Cassini observations a better understanding of the physics behind this magnetosphere has evolved [35]. In August 2011 NASA launched the JUNO mission. One of its tasks is measuring the polar magnetosphere and particle fluxes present. We hope that with the arrival of the Juno spacecraft to Jupiter sometime in the summer of 2016 some of our unanswered questions regarding the magnetosphere will be addressed.

Table 1.1: Comparative Magnetospheres (Adapted from [24])

PROPERTY	EARTH	JUPITER	SATURN
Distance from Sun (AU)	1	5.2	9.5
Orbital Period (yrs)	1	11.9	29.6
Radius (km)	6,371	71,492	60,268
Inclination (°)	23.5	3.1	26.7
Main Atmospheric Species	N_2, O_2, O	H_2, H, He	H_2, H, He
Magnetic field (T)	3.1×10^{-5}	4.28×10^{-4}	2.2×10^{-5}
Magnetic Moment $(M_E)^*$	1	20,000	600
Dipole tilt wrt rotation axis	+11.3 °	-9.6 °	0.0 °
Magnetosphere size	6 – 12 R_E	50 – 100 R_J	16 – 22 R_S
Energy Source(s)	Solar Wind	Rotation	Solar Wind + Rotation
Magnetospheric Plasma source	Ionosphere, Solar Wind	Io, Galilean Satellites	Satellites, Rings, Ionosphere
Auroral Input (relative to Earth)†	1	10^3 – 10^4	10 – 100

* $M_E = 7.9\times10^{15}\,Tm^3$

† Auroral power input at Earth = $10^{10}\,W$

1.2 Ionosphere

The ionosphere is a region in the most upper atmosphere of a planet. It is created by the ionization of atoms and molecules forming a partially ionized plasma region. This ionization occurs mostly due to photoionization from solar extreme ultra violet (EUV) and soft x-ray radiation or due to energetic particle impact ionization. The latter dominates at higher latitudes. The characteristics of the ionosphere will depend upon the neutral composition and temperature in the upper atmosphere as well as the ion-neutral chemistry present in the planet. For example in the terrestrial atmosphere, the major constituents are N_2, O_2 and O, while in the Jovian atmosphere the predominant species is H_2 with also some He and H present to a lesser extent. Ionospheres have been observed in every planet in the solar system and have been studied either by in-situ measurements or by radio occultation techniques. Mercury is an exception, in that it does not have a true ionosphere but a so-called ion exosphere, since this planet does not have a gravitationally bound atmosphere. Comets and some planetary satellites like Titan and Io have also been found to have ionospheres.

Ionospheres show density variations with local time and latitude, showing its dependance on the UV radiation input. As ions are produced in the ionosphere (wether by photoionization of by energetic paricle ionization) they may also undergo chemical reactions with neutrals or recombine with electrons. These processes will be further developed in section 5.4. These collisions can affect cooling and heating rates and are important for the temperature estimates in the upper atmosphere. Apart from these collisions, the ions may also be affected by diffusion and transport effects that may be strongly influenced by the planet's intrinsic magnetic field. For example, at high latitudes the ions and electrons may follow magnetic field lines that extend deep into space and maybe even escape from the ionosphere all together, especially when the field line

along which they are being transported is an open field line. At mid-latitudes the magnetic field lines are closed and the plasma along the field lines just co-rotates with the planet. However, if the ion or electron is energetic enough it may enter the conjugate hemisphere and have a collision in the conjugate ionosphere.

1.3 Auroral Emissions

Aurorae are defined as any electromagnetic radiation at high planetary latitudes generated through the excitation of atmospheric neutrals by energetic charged particles (ions and/or electrons) as they precipitate into the upper atmosphere [1, 33]. Auroral processes are observed in every planet or satellite with/within a magnetosphere combined with a collisionaly thick atmosphere. There are two ways in which an energetic charged particle can precipitate into the upper atmosphere giving rise to two different auroral components. The first one is referred to as diffuse aurora. The term diffuse in this case means that this particular type of aurora has no observable internal structure. It is generated by trapped particles in the magnetosphere that are scattered by waves into the loss cone and form broad regions of low intensity emissions. The second kind is the discrete aurora, which is formed by charged particles that have been accelerated by the Birkeland (magnetic field aligned) currents and form brighter and more localized auroral arcs [35, 36]. For discrete aurora at Earth, reconnections in the magnetotail and it is related to substorms.

Auroral emissions are a very useful tool in the understanding of the magnetospheres and ionospheres of the outer planets and the way these two regions are linked electrodynamically (what is called ionosphere-magnetosphere or MI coupling). Auroral emissions can be observed in different wavelengths: visible, UV, IR, x-ray, and radio. The study of the aurora by modeling it and observing it at different wavelengths allows the

understanding of the underlaying mechanisms that generate it and it becomes a tool to explore the composition, structure, energy transport, temperature, and plasma properties of the upper atmosphere and magnetosphere of the planets. Since it is not always feasible to send probes to make in-situ measurements, observation of auroral emissions is a good way to probe the magnetospheres and ionospheres of these distant objects. Whenever possible, simultaneous remote observations have been scheduled with measurements from in-situ probes, to further understand the correlations between certain plasma parameters and the emissions observed [37, 38]. In the following subsections a review of the aurorae of Earth, Jupiter and Saturn will be given, focused mostly on the UV and x-ray emissions, which are of most interest to the present study.

1.3.1 Earth's Aurora

Auroral emission at Earth is generated by magnetospheric high energy charged particles, particularly electrons, that precipitate along magnetic field lines into the upper atmosphere. These charged particles are accelerated in the magnetotail region by field aligned potentials in the topside of the ionosphere. The auroral activity on Earth is highly related to the solar activity and specifically to solar wind conditions arriving at Earth [39]. For an auroral storm to occur, the interplanetary magnetic field (IMF) must be pointing southward allowing reconnection with the Earth's magnetic field lines to occur at the magnetopause boundary. This means that the Earth's magnetic field lines are topologically connected to the sun's magnetic field lines and the solar wind plasma is then able to precipitate into the earth's ionosphere through these open magnetic field lines. Large geomagnetic storms are generally caused by coronal mass ejections (CMEs) on the Sun directed toward Earth at high speeds. The terrestrial aurora (Figure 1.2) is normally an oval shaped pattern centered at each magnetic pole and fixed

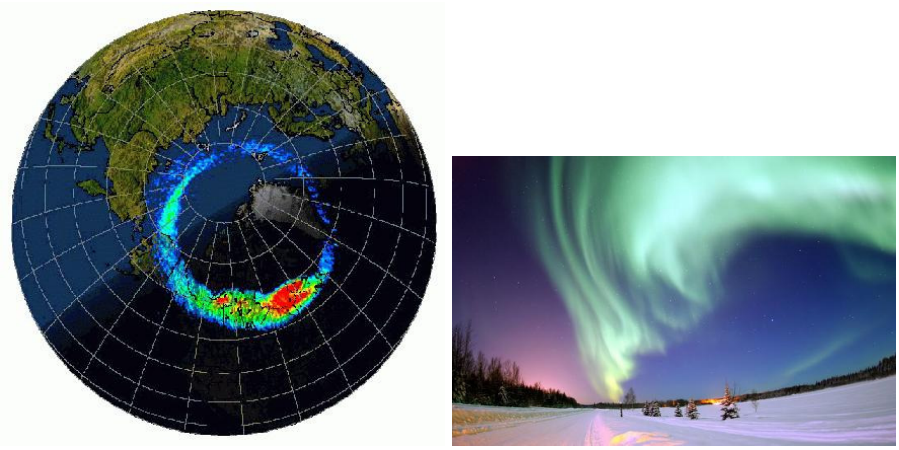

Figure 1.2: Model of the auroral oval (left) and aurora emission as seen from Earth (right)

on local time (Earth rotates under the aurora). The intensity and diameter of the auroral oval will vary upon solar wind conditions [1, 26, Ch. 8].

1.3.2 Jovian Aurora

As shown by Table 1.1, Jupiter's magnetospheric parameters are a lot stronger than those at Earth or Saturn, or any other planetary body in the solar system; consequently it also exhibits the strongest and brightest aurora. However, these strong auroral emissions had not been detected until a Voyager 1 flyby in 1979 [33], which first observed the Jovian aurora in UV with the Voyager UV Spectrometer (UVS). The first x-ray auroral emission from Jupiter was observed by the Einstein X-ray Observatory and was reported by [40]. The observed UV aurora is mainly due to Werner and Lyman bands with emitted wavelengths ranging between 900 – 1600 Å and x-ray emission is observed in the 20 – 40 Å range.

The Jovian aurora is composed of three auroral emission regions that are physically separated from each other. Each of these regions vary independently in space and time,

suggesting that the driving processes in each may be different. The first region is the auroral oval, visible in UV (see Figure 1.3). This oval is continuously present and is seen in both northern and southern hemispheres at about 15° magnetic co-latitude. The auroral ovals are narrow (100 – 500 km width) and bright ($\sim$ 100, kR – 1 MR, where R = 1 Rayleigh = 10^{10} photons per m^2 per column per second) ([1] and references therein). Based on observations, the total input power in this auroral region is about 10^{13} – 10^{14} W. This amounts to an auroral to solar radiation ratio of 20 – 50 times more than on Earth [33].

It was originally believed that the auroral oval of Jupiter was magnetically connected to the Io plasma torus. However, Hubble Space Telescope imaging studies showed that the auroral oval maps to $\sim$ 30 R_J. Mapping emissions seen in the magnetosphere requires the knowledge of the magnetic field line path by a reliable model. Throughout the years several models have been developed [1], but the most commonly used in recent years is the VIP magnetic model developed by [41]. The fact that the magnetic footprints of Io ($\sim$ 6 R_J), Europa ($\sim$ 9 R_J) and Ganymede ($\sim$ 15 R_J) are located equatorward of the oval, gives it a minimum mapping distance of $\sim$ 20 R_J [1, 30]. These observations suggested that the main auroral oval is connected to the magnetosphere-ionosphere current system associated with the maintenance of corotation in outwardly diffusing plasma. Consequently energetic electrons, accelerated by upward Birkeland currents, are proposed as the main precipitating species into the oval.

The second region in the Jovian aurora consists of the satellite magnetic footprints. Io, Europa and Ganymede have visible footprints equatorward of the oval, with Io's footprint being the brightest and showing a tail (see Figure 1.3 b). Callisto's magnetic footprint has never been observed, since it overlaps with the main auroral oval, which is brighter and hides any emissions from the moon's footprint.

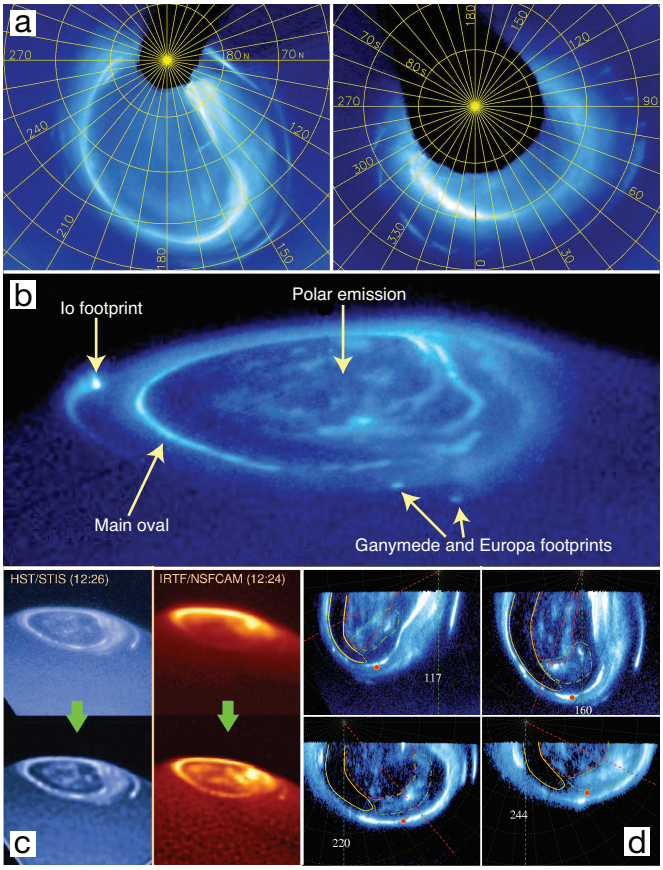

Figure 1.3: Auoral images. a) Mean of all HST STIS images from Dec 2000 – January 2001. Image on the left shows the northern polar region and the image on the right shows the southern region. b) HST STIS UV image of the northern aurora. c) Comparison of UV (left) and H_3^+ IR (right) images of Jupiter's aurora. Lower panels show the images after processing. d) Polar projections of Jupiter's aurora from STIS UV images. [1]

The third region is the polar emission region. After Earth's x-ray auroral emissions were detected, the presence of x-ray emission from the polar regions of Jupiter was expected by analogy. The emissions in this region are highly variable and map to the outer magnetosphere. On Earth, polar region emissions are associated to open field lines. On Jupiter polar cap emissions might be associated to both open and closed field lines. The polar emissions are seen in UV, IR, and x-ray. There is a bright polar region and a dark polar region, which form a "yin-yan"-like structure (see Figure 1.3 d.). Polar emissions are important, since they provide a projection of the dynamics and energetics in the distant magnetosphere, but they are not quite as well understood as the main auroral oval emissions. They are mostly observed in x-rays and some UV, suggesting that the same particle population could be the source of both emission types. Because the Jovian x-ray aurora is the main topic of this study in the following subsection a more in-depth treatment will be given.

1.3.3 Jovian X-ray Aurora

As mentioned earlier, the first observations of this x-ray auroral emissions were done by the Einstein X-ray Observatory in 1979 and 1981 [40]. By analogy with Earth, the source of the Jovian x-ray aurora was expected to be electron bremsstrahlung. The observations done by ROSAT [42] did not have enough spectral resolution to differentiate between a continuous spectrum (characteristic of bremsstrahlung) and a line spectrum. However, several observations models [42–44] discarded bremsstrahlung as the mechanism for this emission, since the expected flux was by up to three times smaller when compared to the observations. Instead, the hypothesis that the x-rays were caused by a K-shell emission mechanism caused by heavy ions (most probably oxygen and sulfur)

precipitating into the upper atmosphere of Jupiter, as proposed by [40], was adopted as the generating mechanism (see Figure 1.4) for the x-ray emission from high latitudes.

The proposed heavy ion precipitation model was further developed to more accurately model the observed data and to investigate the acceleration and collision mechanisms needed to produce the x-rays [19, 45–52]. In particular, [46] explained that electron removal collisions (i.e. stripping collisions) produce high charge state ions (O^{8+}, O^{7+}, S^{11+}, S^{13+}, etc), which collide with the atmospheric H_2 in charge transfer collisions that leave the ions in an excited state. Consequently an x-ray photon will be emitted as the ion decays to the ground state. The estimated incident ion energy needed to reproduce the observed x-ray emissions, as calculated by current models, is about 1 – 2 MeV/u for oxygen and about 1 MeV/u for sulfur [19, 52].

Recently, observations done by the Chandra X-ray Observatory advanced carbonate compensation depth imaging spectrometer (CXO–ACIS–S) [53, 54] and by XMM–Newton [2,55,56] indeed showed a spectrum dominated by line emission, corroborating the adopted K-shell emission mechanism (Figure 1.4), instead of a continuum spectrum. Interestingly, recent XMM–Newton observations [57] showed a harder x-ray spectrum ($E \geq 1$ keV) associated with the main auroral oval, but with only a few percent of the total x-ray power emitted, which might be attributed to electron bremsstrahlung emission.

Energetic sulfur and oxygen ions were measured by the Voyager spacecraft in the middle magnetosphere (10 – 20 R_J) [58] and the Jovian emissions were initially linked to this ion population. However, the main auroral oval as observed in the UV is located equatorward from the polar emissions is found to map to distances between 20 – 30 R_J [1]. This suggests that the polar cap precipitating particles had to originate from an even further radial region. Recently, [53] reported that the northern auroral x-rays

mapped to a hot spot in the middle magnetosphere at distances > 30 R_J as seen by CXO observations in December 2000 and confirmed by [54].

The outer magnetospheric region where the hot spot is located did not have the necessary flux of MeV per nucleon particles needed to produce the observed emissions as required by the x-ray auroral models. Ref. [49] argued that the observed x-ray emissions could be explained by either highly stripped solar wind heavy ions that precipitate into the atmosphere, since they don't need to be very energetic as they are already highly stripped, or most likely by outer magnetospheric oxygen and sulfur ions, present in low charged states that are accelerated by field aligned potentials before precipitating into the atmosphere. The associated Birkeland current (i.e. field aligned) was estimated to be 1000 MA for the solar wind case and 10 MA for the magnetospheric case.

[59] also explored the origin of these ions and why ion precipitation would originate near the magnetopause. They proposed a pulsed reconnection mechanism operating at the dayside magnetopause, similar to the flux transfer events observed at Earth's magnetosphere. This pulsed reconnection also could explain the periodic (roughly 40–minute period) x-ray emissions that are sometimes observed [53].

Newer spectral observations by CXO–ACIS–S in 2003 clearly showed line emission from highly charged states of oxygen and possibly sulfur [54]. Lower energy emission features were also observed in the spectrum, but the spectral resolution was insufficient to tell the difference between sulfur lines (0.31 – 0.35 keV) and carbon lines (0.35 – 0.37 keV) (Please refer to spectrum shown in Figure 1.4). The distinction between these lines is important for determining the origin of the heavy ions. If the lower energy emissions are sulfur lines, the ions are most likely of magnetospheric origin. However, if the emissions are carbon lines, it could suggest a contribution of the solar wind. Recently, ref. [52] calculated auroral emission spectra including carbon ions and compared their results to CXO observations, concluding that the carbon ion emission

is negligible. However, uncertainties in the model do not allow to completely discard the possibility of solar wind ions to be responsible for the x-ray emissions.

1.3.4 Saturn's Aurora

Until the Cassini mission observations of Saturn in 2004 it was believed that Saturn's magnetosphere, the aurora and their corresponding processes were intermediate between Earth's and Jupiter's [32]. These observations revealed that the morphology as well as the triggering mechanisms of the aurora are different than those of Jupiter and Earth. For example, HST observations give evidence to believe that Saturn's main auroral oval is associated with currents near the boundary between open and closed field lines and from Voyager measurements this region has been mapped to $6-7$ R_S [32,35]. The HST–Cassini campaign observations have shown that the oval is responsive to the solar wind [37], however, unlike the Earth, Saturn's aurora is affected not by the orientation of the IMF but by the solar wind dynamic pressure and the convection electric field $-\vec{u}\times\vec{B}$. It also appears that the magnetosphere response to the solar wind is driven by solar wind shocks [31,32,35,60].

The size of Saturn's magnetosphere and rapid planetary rotation suggest that some Jovian-like processes should occur. During quiet solar wind times, it has been observed that the features that form the oval aurora still corotate with the planet [61]. This could indicate that the magnetosphere can have more than one state depending on solar wind parameters and each state is manifested with different auroral features. However, the auroral oval tends to be at much higher latitudes at Saturn than at Jupiter and its morphology changes. Observations have shown a morphology evolution of the oval at Saturn that changes from a closed loop to an open loop, showing a spiral-like shape. The mechanism for this change is still unknown [32]. Another difference with

Jupiter is that there are no bright satellite footprints as is the case of Io, Europa and Ganymede. Only recently, an auroral footprint of the moon Enceladus was observed on Saturn caused by electrodynamic coupling between the two objects [62, 63] . This footprint was very hard to observe because it is much dimmer than the Io footprint in Jupiter and in instances the emission might be below the observable threshold .

The most interesting feature relevant to the present study is the fact that no x-ray aurora has been measured at Saturn, although one has been expected [24, 33, 64]. It is speculated that these x-ray emissions are there, but that the sensitivity of current observatories is not enough to detect them, since they are much dimmer than Jupiter's emissions. Late observations showed that Saturn's x-ray emission is concentrated in non-polar latitudes and has a large temporal variability correlated to the solar x-ray flux [64–66] . This suggests that these disk emissions are solar x-rays scattered of the atmosphere, just like it has been observed in Jupiter [17, 67] . While Jupiter has been observed to produce 1 GW x-ray luminosity in the polar region [54, 56], upper limits calculated for Saturn only reach 8 – 24 MW [68] making it hard to observe with current observational thresholds.

Ref. [69] investigate the possibility of x-ray emission at Saturn based on mechanisms analogous to Jupiter, namely, highly charged solar wind ions or a magnetospheric ion population which is accelerated before precipitating into the atmosphere. They find that magnetospheric ions that start inside the magnetosphere are not capable of producing a large enough x-ray flux in order to achieve the observational limits. However, solar wind heavy ions may be able to precipitate along open magnetic field lines near the cusp magnetopause and produce x-rays. These ions will have to be accelerated in order to produce an observable x-ray flux, even though they are already stripped. There are no current models for auroral x-ray emission at Saturn, only estimates on the possible emissions. This present study, although initially designed for Jovian modeling,

could be applied to Saturn in the future in order to estimate the x-ray emissions and explain why they are not observed yet.

1.4 Magnetosphere – Ionosphere (MI) Coupling

The study of aurorae in space objects is important because it provides a way to link the magnetospheric dynamics and how they affect the planet and its atmosphere. The aurora is a manifestation of the effects of the magnetosphere projected onto the atmosphere like a screen. It is also a diagnostic of the electrical currents that couple this ionosphere – magnetosphere system together. By observing the changes in the aurorae and understanding what causes them, magnetospheres can be modeled and the currents and other internal processes acting may be analyzed.

1.4.1 MI Coupling of the Main Auroral Oval at Jupiter

The vast study of the Jovian auroral oval emissions has led to a basic understanding of its origins by relating the energetic electron precipitation to field aligned currents. The middle magnetosphere of Jupiter has a massive source of plasma due to the presence of its volcanically active moon Io at 6 R_J. This iogenic plasma (mostly sulfur, oxygen and electrons) is confined to the equatorial region due to centrifugal forces and at the same time diffuses radially outward forming a plasma disk. As the plasma diffuses outward, its angular velocity (ω), which was initially close to corotation with Jupiter, decreases slowly to conserve angular momentum. When the angular velocity falls bellow the angular velocity of the planet (Ω_J), a differential velocity exists between the neutral particles in the upper atmosphere that rotate with the planet, and the charged particles in the ionosphere which rotate with the magnetospheric flux tubes. This leads to collisions between the plasma and neutrals in what is called the Pedersen-conducting layer of the

ionosphere [3]. The collisions produce a frictional torque on the flux tubes that tends to bring them back up to corotation, while an opposite torque will slow down the upper atmospheric particles.

The ionospheric torque is then related to the magnetospheric plasma in the equatorial region of the magnetosphere by the magnetic field, which is now distorted to a lagging configuration (see Figure 1.5. This figure also shows the associated current system to this magnetic field configuration based on Jovian models done by [28] and [70]). The Pedersen current (i.e. the current component perpendicular to the magnetic field) in the ionosphere will then balance the frictional torque with a $\vec{j} \times \vec{B}$ force directed in opposite direction to the rotation of the planet. At the same time, the outward radial current in the equatorial plane will also have a $\vec{j} \times \vec{B}$ in the same direction as the rotation. This force tends to accelerate the plasma to near corotation. The current circuit is then closed by field-aligned currents directed downward from the magnetosphere to the ionosphere and upward from the ionosphere to the magnetosphere [36]. As mentioned in section 1.3, the upward field aligned (i.e. Birkeland) current is the source of the auroral oval observed in Jupiter.

1.4.2 Polar cap magnetosphere–ionosphere coupling

The current system that leads to the Jovian polar aurora is, however, not very well understood. A model for this region is described by [59] and [4]. A view of the northern polar ionosphere with its corresponding current and flows is given in Figure 1.6 (right). This model, considered to be in a steady state, consists of three flow regions: The first region is the sub-corotating *Hill* region, which is at lower latitudes and has upward field aligned currents (main auroral oval currents described above). The second region surrounds the *Hill* region and is also driven by planetary rotation. Although it is faster,

it is still sub-corotating. The field lines connecting to this region stretch out into the dusk sector down-tail, eventually pinching off by reconnection and forming plasmoids that bring iogenic plasma down-tail (Vasyliunas cycle). The third region describes the flow associated to the solar wind interaction by reconnection of open magnetic field lines with northward-directed interplanetary magnetic field lines at the dayside magnetopause (Dungey cycle). The resulting open field lines will be carried over the poles, flow predominantly from dusk to dawn and will pinch off through reconnection at the tail. To complete the cycle the return flow will take place only at the dawn side region, since the Vasyliunas cycle plasma flow already occupies the midnight to dusk sector.

The MI coupling is a complicated system with lots of dynamics involved. However, it is still not clear if the polar ionosphere-magnetosphere coupling proposed by [3, 4] and [59] is correct, since the link between the polar emissions and the associated solar wind signatures has not been found yet. It is hoped that the modeling of the x-ray aurora on this project will provide some insight on this issue. The complicated current system shows how aurorae are important to the understanding of the physics of the MI coupling, as they are a manifestation and diagnostic of the field aligned currents that connect the two regions.

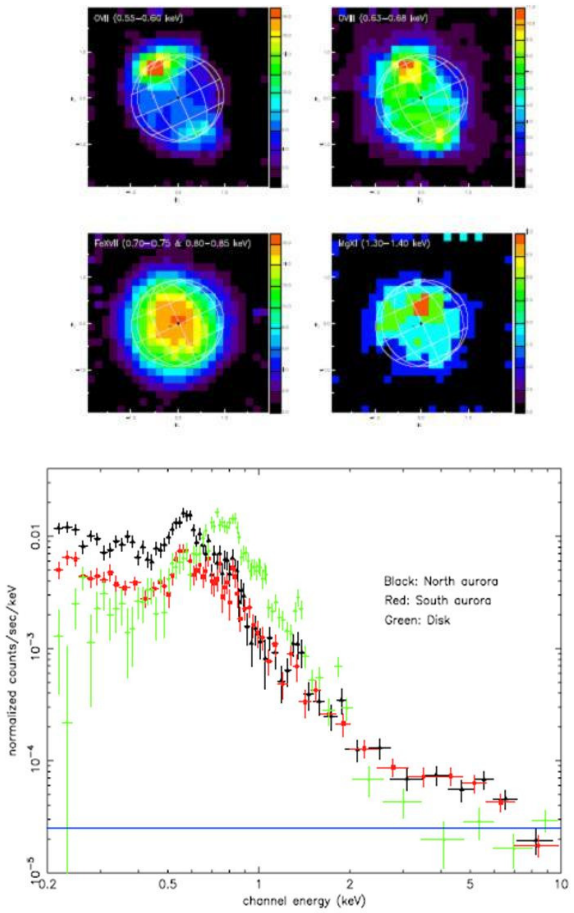

Figure 1.4: Top: Smoothed XMM–Newton EPIC images of Jupiter. From top left, clockwise: OVII, OVIII, MgXI, FeXVII. The color scale bar is in units of EPIC counts. Bottom: Combined EPIC spectra for the North (black) and South (red) aurorae and of the low latitude disk emission (green) [2]. The x-axis shows the photon energy and the y-axis shows the normalized counts/sec/keV.

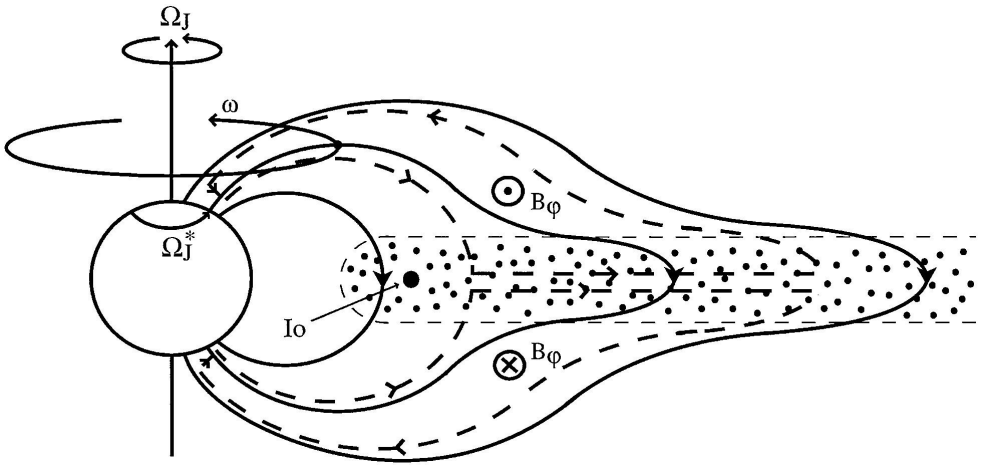

Figure 1.5: Cross section of the Jovian magnetosphere. Arrowed solid lines indicate magnetic field lines, which get distorted outward in the middle magnetosphere region by azimuthal currents in the plasma sheet. The plasma is shown in the dotted region. Three different velocities relevant to the processes are shown: Ω_J is the planetary angular velocity, ω is the angular velocity of the field lines, and Ω_J^* is the angular velocity of the Pedersen layer in the magnetosphere. The dashed lines show the current system responsible for the auroral oval. From [3].

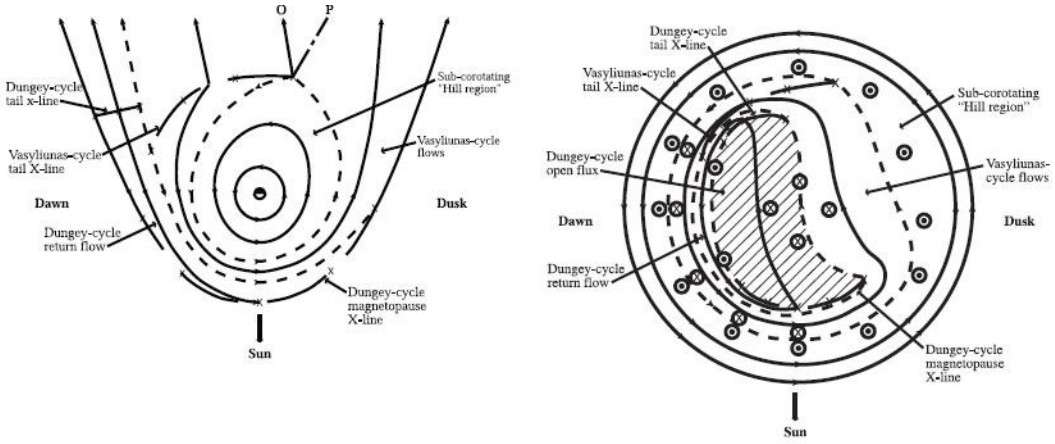

Figure 1.6: Sketches of the magnetospheric flows and currents. The left figure shows an equatorial cross section of the magnetosphere, showing the three different regions and their cycles. The figure on the right shows the north polar ionosphere and its current and flows. From [4].

Chapter 2

Collision Processes – Electron Impact Cross Sections

2.1 Introduction

Collisions play a key role, when modeling the dynamics and energetics of atmospheres, ionospheres and magnetospheres. Collisions between particles are responsible, for example, for ionization of atmospheric constituents, energy exchange between particle populations leading to their cooling or heating, observable emissions due to excitation of the impacted or impacting particle, etc. Collisions can be classified as elastic or inelastic, where the first type of collision will conserve kinetic energy and momentum of the particles involved, while the second type will not. An inelastic collision leads to excited or de-excited states. It is a fundamental process considered in auroral emissions and dayglow. In general, elastic collisions will be the dominant type of collision for low energies, while inelastic collisions become more important when the relative kinetic energy between the particles increases. There exist different types of collisions that can be organized according to their importance: elastic, rotational, vibrational, electronic excitation, and ionization [71].

The different collision processes are important for modeling because each process will affect the transport of plasma, the sources and losses in the plasma equations, as

well as momentum/energy calculations in a different way. For the present work many types of collisions must be taken into account because of the nature of the problem. For example, in Chapter 4 ion neutral collisions are the most important when modeling x-ray emission at the Jovian high latitudes. Chapters 5 and 6 deal with the modeling of electron transport. In these chapters electron collisions with neutral species, ions and other electrons are most important. Another important process that is considered when modeling ionospheres is the production of electrons and ions due to solar radiation, as it will also be mentioned in several sections. In the present chapter electron impact collisions cross sections as well as photoabsorption and photoionization cross sections are compiled for those atmospheric species relevant to Jupiter and the Saturnian inner magnetospheric environment. The following chapter contains all the pertinent cross sections for ion-neutral collisions that are used in the model.

The cross sections are extremely important for the development of the proposed model in this thesis, because they are used to calculate the transport, energy losses, absorption, and other important parameters. Some of the cross sections were found in the literature and are reviewed in the following sections. Other cross sections were calculated by most up to date codes available to our collaborators from the Oak Ridge National Laboratory and Northern Texas University. I would like to take the opportunity to thank them for their work, making this extensive cross section compilation possible for our work.

2.1.1 Cross Sections – Overview

Let's first review the concept of a cross section as explained by classical scattering theory. Consider an incident particle with energy E and impact parameter b, which then emerges at some scattering angle θ. At the lab, for example, measurements usually use

a beam of particles with a flux Γ that is scattered off target particles, usually a contained gas. A single fixed-target molecule acts as a center of force, which when repulsive will scatter away the particles from the molecule. If the incoming particles has a small impact parameter b, it will be scattered through a bigger angle θ. The differential cross section $d\sigma$ is an important value because it determines the angular distribution of the scattered particles and it is defined as the number of particles scattered per solid angle $d\Omega$ per unit time, divided by the incident intensity. One can write the differential cross section as:

$$\frac{d\sigma}{d\Omega} = \frac{b}{\sin(\theta)} \left| \frac{db}{d\theta} \right| \tag{2.1}$$

One can calculate the number of particles scattered into a solid angle $d\Omega$ per unit time as:

$$dN = \frac{d\sigma}{d\Omega} 2\pi \sin\theta d\theta \Gamma. \tag{2.2}$$

An important parameter that is often used in the present work is the total cross section σ or σ_{tot}. The total cross section gives the total number of particles scattered per unit time divided by the incident flux. That is, all the scattered particles at all possible angles. It is defined as:

$$\sigma_{tot} = \int \frac{b}{\sin(\theta)} \left| \frac{db}{d\theta} \right| d\Omega = \int \frac{d\sigma}{d\Omega} d\Omega \tag{2.3}$$

Another important cross section that is frequently used in particle scattering problems is the momentum transfer cross section, which is defined as the total momentum transferred to the target particle per unit time divided by the incident flux. The momentum transfer cross section can be calculated as:

$$\sigma_{MT} = \int \frac{d\sigma}{d\Omega} (1 - \cos\theta) d\Omega \tag{2.4}$$

Coulomb collisions, which are long-range interactions between charged particles, are very important in the ionosphere models. In order to calculate their cross section, one must first evaluate the differential cross section as given by equation 2.1. Let us relate the scattering angle θ with the impact parameter b by:

$$\tan\left(\frac{\theta}{2}\right) = \frac{1}{4\pi\varepsilon_0}\frac{q_{scat}q_{target}}{\mu_{st}g_{st}^2 b}; \tag{2.5}$$

where q_{scat} and q_{target} are the charges of the scattering particle and target respectively, μ_{st} is the reduced mass of the scattering and target particles and g_{st} is their relative velocity. With this relation, one can calculate $db/d\theta$ and plug in the answer to the right hand side of equation 2.1 and obtain:

$$\frac{d\sigma_{scat}}{d\Omega} = \frac{4\pi\varepsilon_0\mu_{st}g_{st}^2}{q_{scat}q_{target}}\frac{b^3}{2\sin\cos^2(\theta/2)}. \tag{2.6}$$

After some manipulation we obtain the Rutherford scattering cross section for Coulomb collisions:

$$\frac{d\sigma_{Rutherford}}{d\Omega} = \left(\frac{q_{scat}q_{target}}{4\pi\varepsilon_0\mu_{st}g_{st}^2}\right)^2\frac{1}{(1-\cos\theta)^2} \tag{2.7}$$

In many cases the cross sections can be calculated analytically. The compilation of cross sections given in the present and following chapters includes experimental electron impact cross sections fitted by analytical functions for electron impact cross sections and classical trajectory Monte Carlo simulations used to calculate the ion-neutral impact cross sections. Species of interest in Jupiter are sulfur and oxygen ions, electrons, molecular and atomic hydrogen, helium, and methane. Species of interest in the inner magnetosphere of Saturn and the Enceladus plume are electrons, water, carbon dioxide, and methane.

2.2 Electron Impact Cross Sections

Electron impact cross sections are important when modeling electron precipitation in Jupiter's atmosphere. The electron precipitation may be primary or secondary, for example, as a product of ion-neutral collisions. However, the cross sections and collisional processes involved in both cases are the same, as it is hard to differentiate between secondary electrons, photoelectrons, or primary electron precipitation. The electron cross section data that is used in the codes of our model required a large compilation of information. Cross sections are needed for the impact with each neutral species. For Jupiter the most important neutral species is molecular hydrogen. We have also compiled cross sections for electron impact with helium, atomic hydrogen and methane. The cross sections for electron impact with molecular hydrogen are based on a compilation by [10]. The cross sections used from this paper are recommended by the authors as the best values under their criteria at the time it was written. The authors included the reliability of experimental methods employed, agreement between individual measurements, and experimental uncertainties. For the data compilation given in the present chapter experimental data are preferred to theoretical data, as the data measurements are constantly being improved. The theoretical data found in the literature dates from 30 – 40 years ago, when the experimental techniques were just being developed.

In order to have the cross section information in a format compatible with the code, all the inelastic electron cross sections are represented by an analytical function that fits the recommended experimental data by [10]. The analytical function is adapted from [72] and [73], and is given by:

$$\sigma(E) = \frac{q_0 f_0 C_0}{W^2} \left(\frac{W}{E}\right)^{\Omega} \left[1 - \left(\frac{W}{E}\right)^{\beta}\right]^{\nu}. \tag{2.8}$$

This analytical function has been able accurately represent large amounts of data. In the equation, $q_0 = 4\pi a_0^2 R^2 = 6.514 \times 10^{-14}$ eV^2 cm^2, where a_0 is the Bohr radius and R is the Rydberg energy = 13.6 eV. f_0, C_0, Ω, β and ν are so called Generalized Oscillated Strength (GOS) parameters, which can be adjusted to fit the experimental data. For each different species and each different excitation state there are a different set of parameters used. When experimental data was available (for example the cross sectional data recommended by [10]) the parameters in the analytical cross section were adjusted to best fit the data. The parameters that best fit the cross sections for all the neutral species relevant to this work are given in the Appendix. We refer the reader to the Appendix for more useful information on the cross section calculation details.

For the ionization processes there is a different set of cross sections that is used in the code. To represent the differential ionization cross section $S(E,T)$ that best fits experimental data, [74] suggested the following form as a better approximation:

$$S(E,T) = A(E)\left[\frac{\Gamma^2}{(T-T_0(E))^2+\Gamma(E)^2}\right]^{\kappa} \tag{2.9}$$

where

$$A(E) = \sigma_0 \frac{K}{E}\ln\left(\frac{E}{J}\right) \tag{2.10}$$

$$\Gamma(E) = \Gamma_s \frac{E}{E+T_b} \tag{2.11}$$

$$T_0(E) = T_s - \frac{T_a}{E+T_b} \tag{2.12}$$

The form adopted had already been used in other aspects of physics in connection with damped harmonic oscillator. In nuclear physics the form of equation 2.9 with different κ values is recognized as the Breit–Wigner formula of resonance shapes. Here E is the primary electron energy, T is the secondary electron energy. The secondary electron is defined as the electron with the least energy leaving an ionization event. σ_0 is a unit

cross section taken as 10^{-16} cm^2 and $\kappa = 1$ for ionization cross sections. In the code there is a modification of equation 2.10 and it is used as:

$$A(E) = \sigma_0 \left(\frac{K}{E} + K_b \right) \ln \left(\frac{E}{J} + J_b + \frac{J_c}{E} \right). \tag{2.13}$$

The variables K, K_b, J, J_b, J_C, Γ_s, Γ_b, T_s, T_a, and T_b are adjustable parameters for different ionization states of each gas species.

In order to obtain the total ionization cross section one must use equation 2.9 with $\kappa = 1$ and integrate over a secondary energy range $T_m = 1/2(E - I)$. Here E is again the primary electron energy and I is the ionization threshold. Then, the total ionization cross section is given by:

$$\begin{aligned} \sigma_{ioniz}(E) &= \int_0^{T_m} S(E,T)dT \\ &= A(E)\Gamma(E) \left(\arctan \left[\frac{T_m - T_0}{\Gamma} \right] \right) \end{aligned} \tag{2.14}$$

2.2.1 Electron Impact Cross Sections For H_2

There is a vast collection of papers with cross section information regarding electron collisions with molecular hydrogen. For most of the cross sections I chose the references given by [10] as the recommended experimental values. Their paper is the most recent that I found to have such a compilation. The recommended papers have the experimental values considered to be most accurate, when the paper was written in 2008. I fitted the experimental values for the cross sections using the analytical functions given by equations 2.8 and 2.14 by adjusting the parameters.

There are 22 electronic state excitations that are considered in the H_2 cross sections, 6 singlet states and the rest are triplet states. Please refer to Tables A.1 and A.3for a list

of all the excitations considered and their corresponding thresholds. Table A.2 contains a summary of the sources of the cross section values and/or the GOS parameters used to fit the cross sections. In some cases only analytical functions were found as a source of information. These cases are labeled as "analytical expression" in the details column of the Appendix tables. Every state that had experimental values available was fitted with the analytical expression given by equation 2.8.

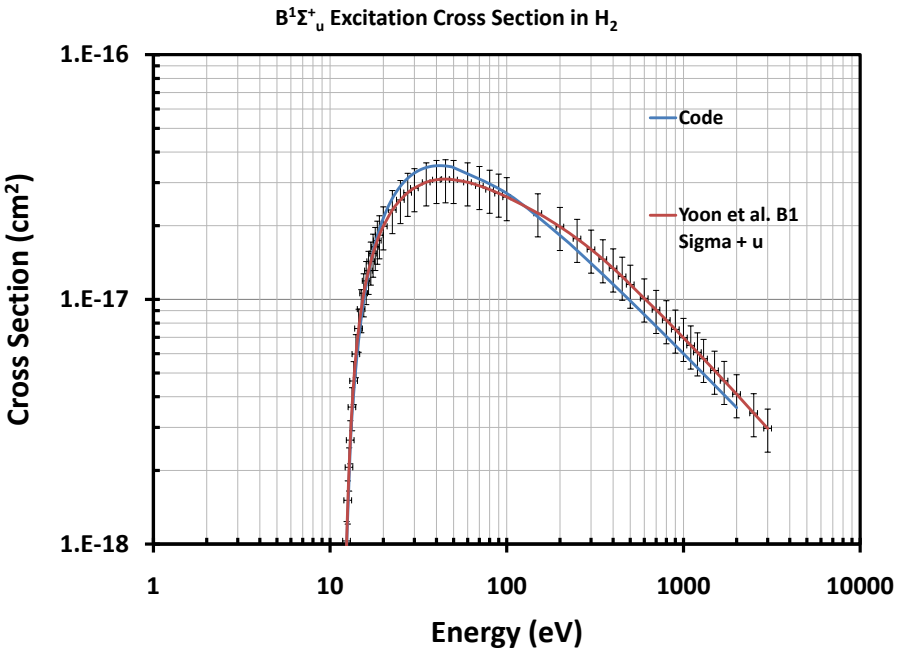

Figure 2.1: Cross sections for the excitation of the $B^1\Sigma_u^+$ electronic state (Lyman Bands) as a result of electron impact excitation on H_2. Vertical bars represent a 20% experimental error. Experimental data measured by [5] is illustrated by the red curve. The analytical fit obtained by our code is shown by the blue curve.

The most important excited singlet states are the $B(^1\Sigma_u^+)$ and the $C(^1\Pi_u)$ states, which give the Lyman and Werner excitation bands respectively. [5] measured the rec-

ommended experimental values, which were then fitted with the parameters given in the summary table A.2. Figures 2.1 and 2.2 show the experimental values with error bars corresponding to 20 %. The authors in [5] estimated the errors to the cross sections to be ± (15 – 25) % for electron energies between 20 – 500 eV, ± (7 – 15)% for higher energies and ± 30 % for energies below 20 eV. The analytical fit achieved by the code is also shown in the figure as a comparison.

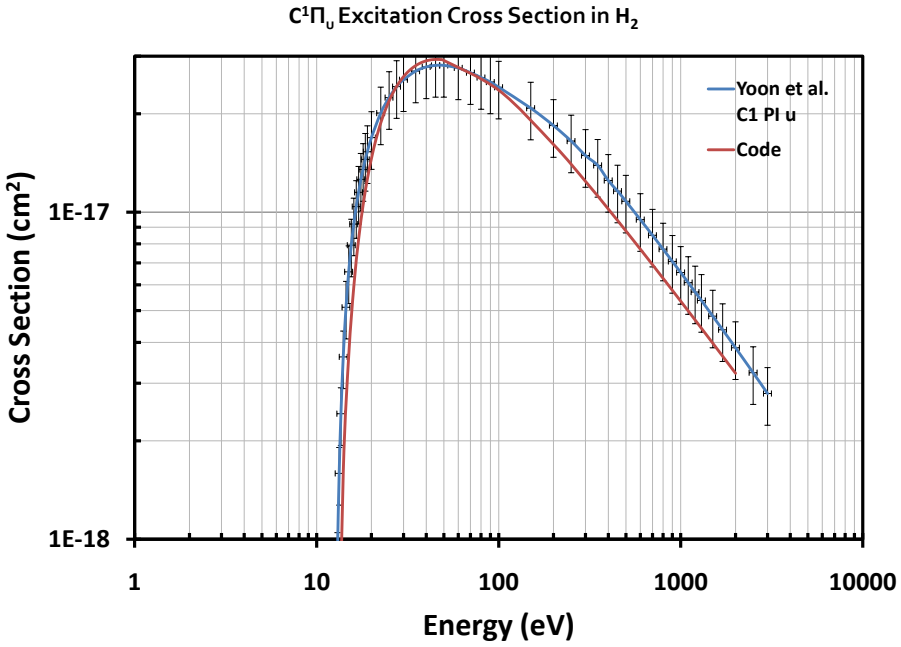

Figure 2.2: Cross sections for the excitation of the $C^1\Pi_u$ electronic state (Werner Bands) as a result of electron impact excitation on H_2. Vertical bars represent a 20% experimental error. Experimental data measured by [5] is given by the blue curve. The analytical fit obtained with the chosen parameters and calculated with our code is shown by the red curve.

The cross section for the $E, F^1\Sigma_g^+$ state recommended by [10] is taken from the experimental values achieved by [6]. The experimental uncertainty is ± 25 %, as given

by the authors. The analytical fit to the cross section calculated by the code is shown in Figure 2.3 as a comparison.

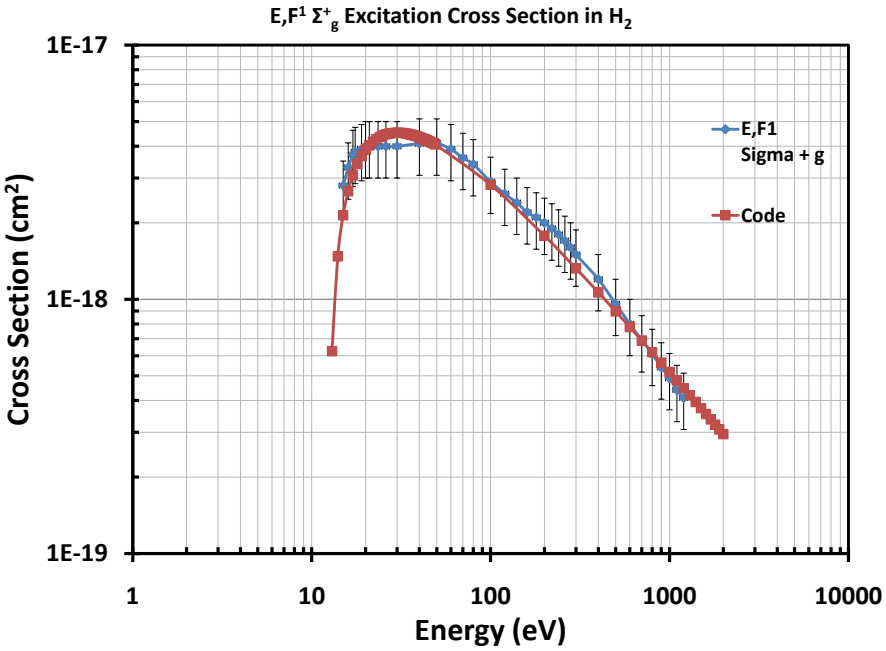

Figure 2.3: Cross sections for the excitation of the $E,F^1\Sigma_g^+$ electronic state as a result of electron impact excitation of H_2. Vertical bars represent a 25 % experimental error as measured by [6]. Their experimental data is shown by the blue curve and the analytical fit to the cross section calculated is given by the red curve.

The cross sections for the other singlet excitation states $B'(^1\Sigma_u^+)$, $D(^1\Pi_u)$, $D'(^1\Pi_u)$, and $B''(^1\Sigma_u^+)$ are not available in the *Yoon et al.* compilation. Their values are adapted from [7] Figure 4c. However, the cross sections for the $D'(^1\Pi_u)$ and $B''(^1\Sigma_u^+)$ states are extremely similar and they were combined as a single cross section labeled $D'(^1\Pi_u)B''(^1\Sigma_u^+)$ in the plots. The cross sections for these states can be seen in Figure 2.4.

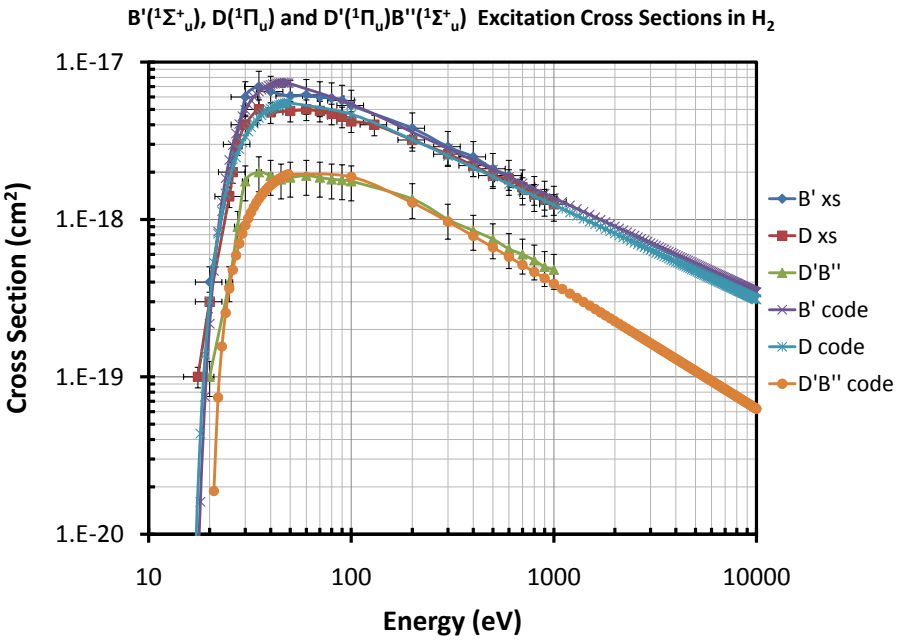

Figure 2.4: Cross sections for the excitation of the $B'(^1\Sigma_u^+)$, $D(^1\Pi_u)$, and the $D'(^1\Pi_u)B''(^1\Sigma_u^+)$ electronic states as a result of electron impact excitation of H_2. Vertical bars represent a 25 experimental error. These cross sections were adapted from [7] and fitted by adjusting the GOS parameters in our calculations.

Only four triplet excitation states have experimental cross section data recommended by [10]. These are the states $a(^3\Sigma_g^+)$, $b(^3\Sigma_u^+)$, $e(^3\Sigma_u^+)$, and $c(^3\Pi_u)$. Please refer to Figure 2.5 for these cross sections. All other triplet states used in our calculations are found by analytical fits with GOS parameters adapted from [73, 75]. Please refer to these papers for more details on the cross sections. A summary of all the excitation cross sections is shown in Figure 2.6.

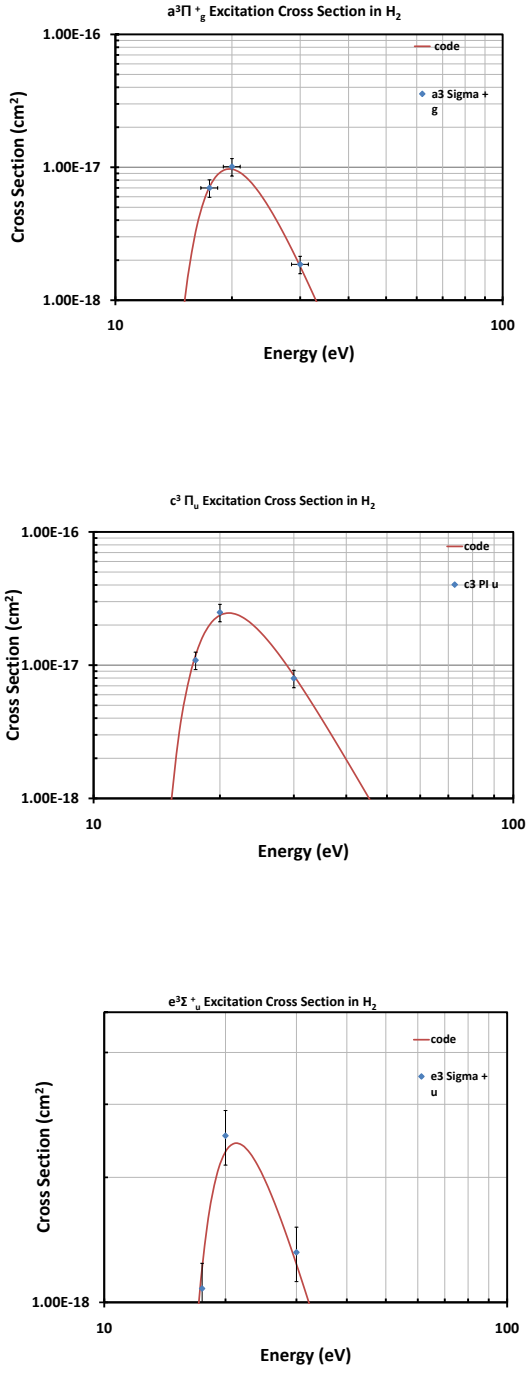

Figure 2.5: Cross sections for the excitation of the $a^3\Sigma_g^+$ (upper left), $c^3\Pi_u$ (upper right), and $e^3\Sigma_u^+$ (bottom) electronic states as a result of electron impact excitation of H_2 molecules. The experimental cross section values are from [8] and the error bars are taken to be 15 %.

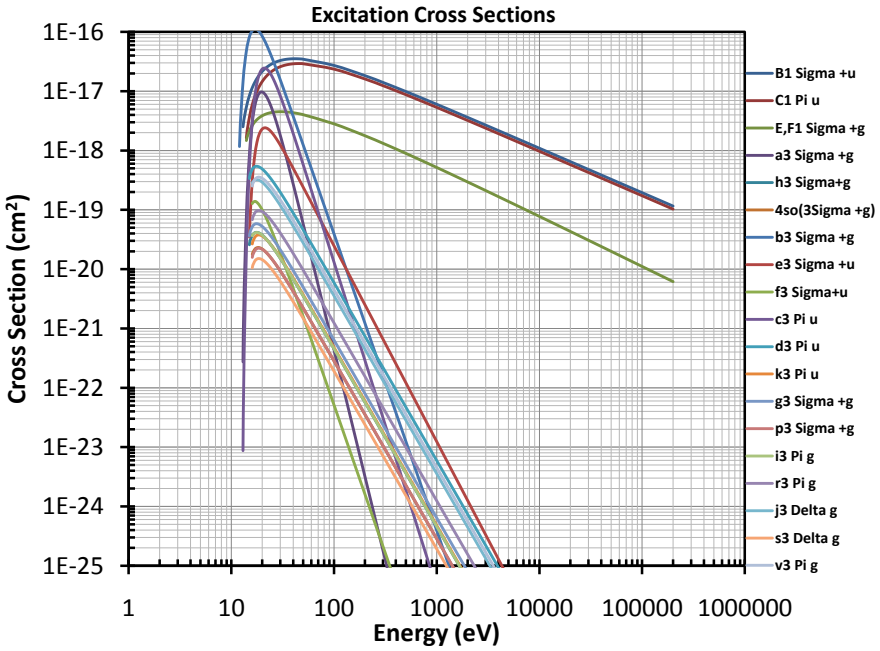

Figure 2.6: Summary of all excitation cross sections for different states. The cross sections shown are calculated using equation 2.8 and the parameters used for each are shown in the Appendix section, Table A.2. The information regarding the experimental data or analytical parameters used is also summarized in the Appendix section, Table 4.5

Since we are dealing with an electron impacting a molecule, the rotational and vibrational excitation cross sections are important in the calculations, especially for the heating and cooling effects of the collisions. [10] also recommends a set of rotational and vibrational excitation cross sections. In the code we consider two vibrational excitation cross sections; $v = 0 \rightarrow v = 1$ and $v = 0 \rightarrow v = 2$. We also consider four different rotational excitation processes: $J = 0 \rightarrow J = 2$, $J = 1 \rightarrow J = 3$, $J = 2 \rightarrow J = 4$, and $J = 3 \rightarrow J = 5$. Please refer to the Appendix Tables A.4 and A.3 for the details on the parameters and references on these cross sections. The vibrational and rotational cross sections are shown in Figure 2.7.

When an electron has a collision with a hydrogen molecule it may also dissociate the molecule, leaving it in an excited state that may lead to an emission. H Ly-α emission by dissociative excitation of H_2 is an important process that is taken into account in our code. This emission line is the most prominent emission line in the UV airglow and aurora in the outer planets, since their atmospheres are all dominated by H_2 or H. The reaction can be expressed as: $e + H_2 \rightarrow H(Ly\alpha) + H + e$. The cross sections for this process have been obtained from [9]. In their work they measure a fast and a slow component of the H Ly-α emission. The fast data is fitted using an analytical cross section having the modified form:

$$\Omega_{ij} = C_0(1-1/X)(X^{-2}) + \sum_{k=1}^{4} C_k(X-1)\exp(-kC_8X) + C_5 + C_6/X + C_7\ln(X) \quad (2.15)$$

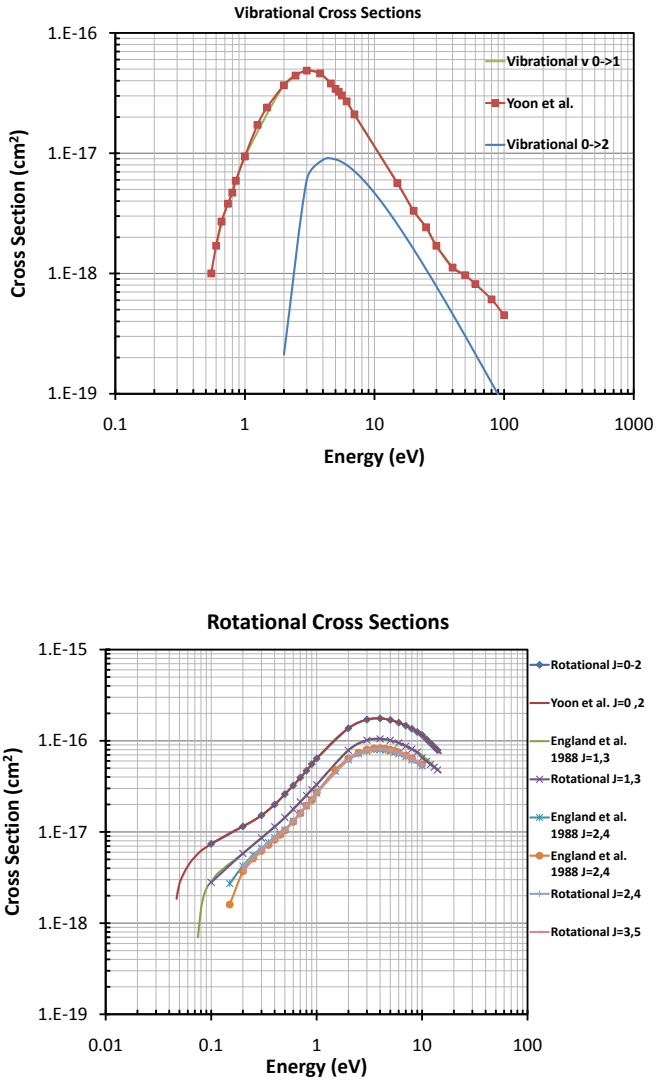

Figure 2.7: Vibrational and rotational excitation cross sections due to electron impact on H_2. Experimental data is shown if available. The other curves illustrate the calculated cross section by the code with the appropriate parameters as given in Table A.4 in the Appendix.

Here, $\Omega_{ij}(X)$ is the collision strength, X is the electron energy in threshold units, and C_k are constants given in Table A.5 in the Appendix. For more details, see [76]. To calculate the excitation cross section, the collision strength is used as follows:

$$\sigma_{ij} = \Sigma_{ij}(X)(E_{ij}X)^{-1}. \tag{2.16}$$

Here, σ_{ij} is the cross section in atomic units and E_{ij} is the transition energy in Rydberg units. The experimental data obtained by [9] showed that the fast component of the H Ly-α emission has a contribution from two different states, which they labeled Q_1 and Q_2. They also estimated an energy dependence for each state with 40% of the cross section arising from the Q_1 states and 60% of the cross section arising from the Q_2 state. Therefore, to calculate the cross section for the fast component, we use:

$$\sigma_{fast} = 0.4\sigma_{Q_1} + 0.6\sigma_{Q_2} \tag{2.17}$$

The cross section for the slow contribution was taken directly from the data shown in Figure 4 of [9]. The data points interpolated are given in the Appendix Table A.6. The total cross section for dissociative excitation of hydrogen molecules by electron impact is found by adding the fast and slow cross sections. The slow and fast components, as well as the total dissociative cross section leading to H Ly α emission are shown in Figure 2.8.

Another very important set of cross sections that is needed for the processes in the code is the electron impact ionization cross section for H_2. The analytical function used in the calculation of these cross sections is given by Equation 2.14 and the corresponding parameters to obtain the best fit are given in Table A.11. For a list of the ionization states please refer to Table A.10. For this cross section we use the recommended values measured by [77]. There are two possible outcomes to this process. The first is the

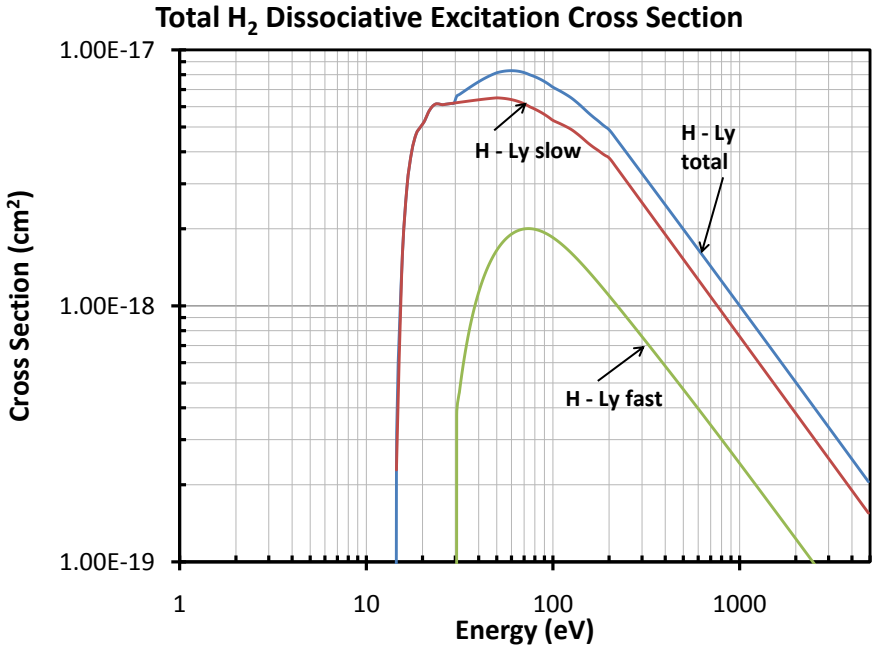

Figure 2.8: Cross section of the fast and slow components of the Ly-α emission. The total dissociative excitation cross section is calculated by adding up the cross sections for the two components. See text above for more details and the Appendix for the cross section values and coefficients used to fit the cross sections as measured by [9]

ionization of the H_2 molecule (H_2^+) and the second is the production of H^+ by dissociation and then ionization. Both processes are considered in the calculations and their corresponding cross sections can be found in Figure 2.9.

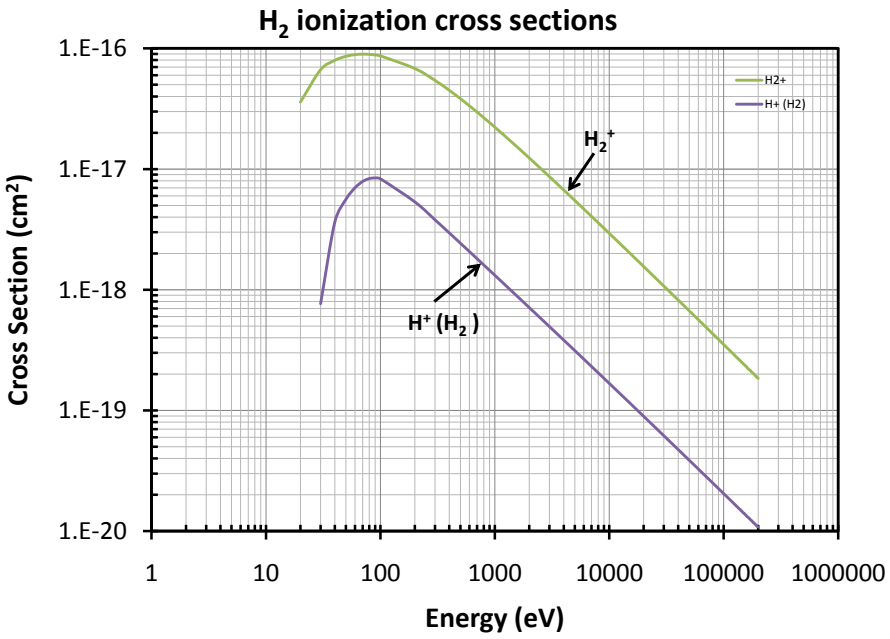

Figure 2.9: Total ionization cross sections for the production of H_2^+ and H^+. Based on recommended values by [10].

2.2.2 Electron Impact Cross Sections For He

The electron impact cross sections for He that give the excitation and ionization states are calculated in the code with the same analytical cross section expressions used for H_2. As a reminder, the analytical cross section formulations are given by Equations 2.8 and 2.14. The parameters for the data were obtained by [11] and are shown in the Appendix Table A.7. There are no vibrational or rotational excitation cross sections for He because being an atom and not a molecule those states do not exist. Figure 2.10 illustrates the cross sections for the electronic excited states of He considered in our models. Figure 2.11 shows the ionization cross sections for He.

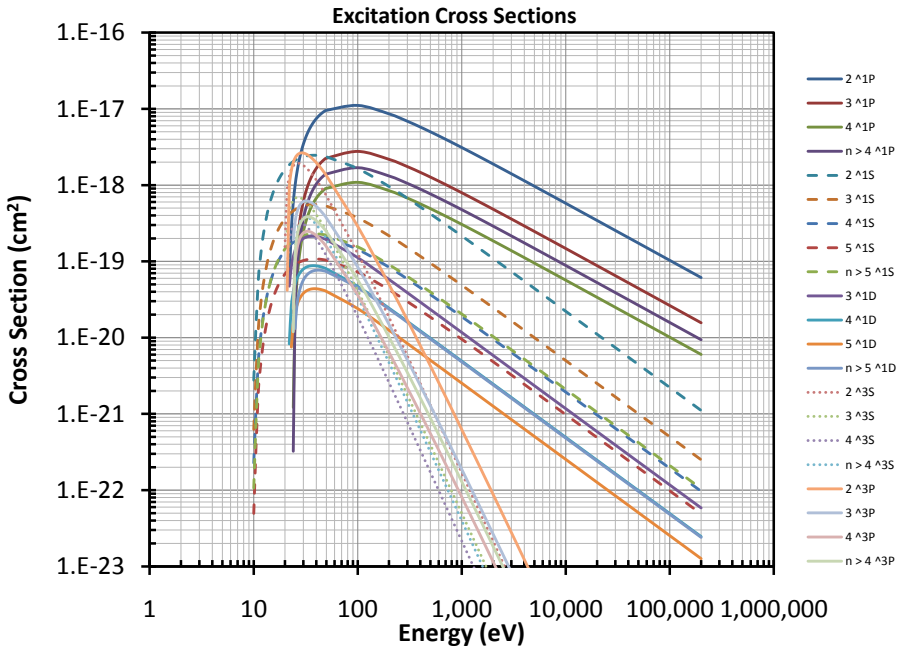

Figure 2.10: Cross sections for the electronic excitation states used in our model for He. The parameters for the analytical cross section fit are given by [11] and are also shown in Table A.7.

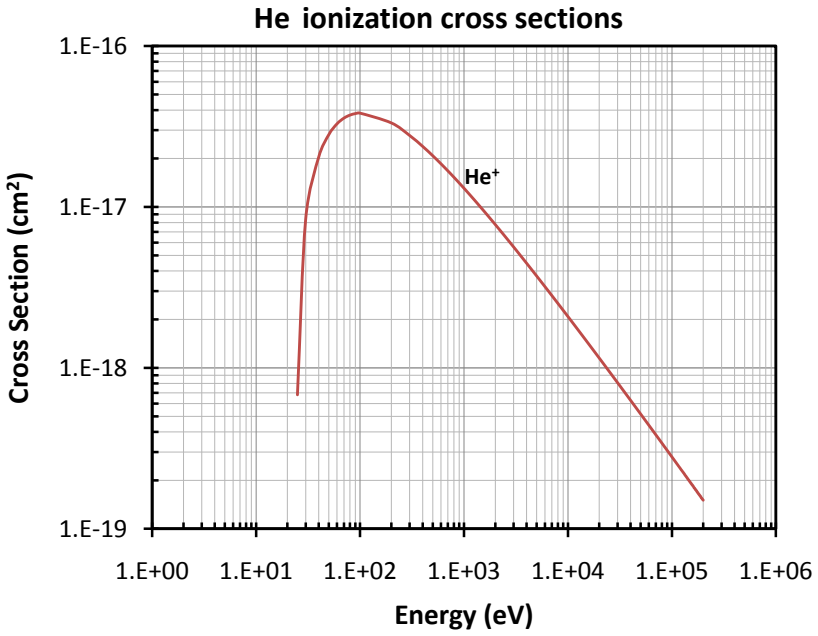

Figure 2.11: Total ionization Cross section for production of He^+ by electron impact collisions. The parameters to calculate analytical function given by Equation 2.14 are taken from [11] and are shown in Table A.11.

2.2.3 Electron Impact Cross Sections For H

The electronic excitation states of H that are considered for the calculations are given in the Appendix Table A.8. The cross sections are calculated by two sets of parameters. The first set is for incident electron energies below 3 keV and are taken from [12]. The cross section is calculated using Equation 2.8. The second set of parameters is for incident electron energies higher than 3 keV. To calculate the electronic excitation cross sections for these higher energies, we use a different analytical expression given by [13], equation 5 in their paper. This analytical expression uses the Bethe formula for the plane-wave Born approximation for fast, but not relativistic incident electrons. The extended expression has the form:

$$\sigma_{ext} = \frac{4\pi a_0^2 R}{T+B+E}\left[a\ln(T/R) + b + cR/T\right] f. \tag{2.18}$$

Here, a, b, and c are dimensionless constants, E is the excitation energy for each particular state, T is the incident electron energy, R is the Rydberg energy, f is a scaling factor and B = 13.5984 eV is the experimental ionization energy used in the scaling. The values used for each excitation state is shown in the Appendix Table A.8. There is a small jump at E = 3 keV due to the change in the analytic formula used for the cross sections. However, the jump can be considered small compared to the errors that the experimental measurement of cross sections have in general (about 20%).

The excitation cross sections for H for the different states used in our work are shown in Figure 2.12. The total ionization cross section was calculated using the analytic function given by Equation 2.14. The parameters were adjusted to fit the experimental data reported by [14]. The cross section is shown in Figure 2.13.

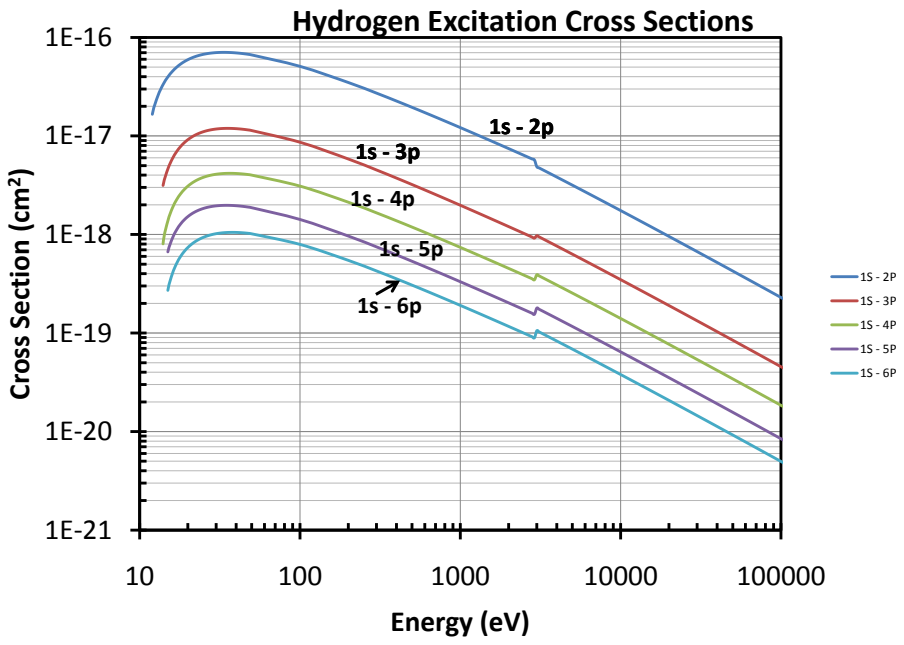

Figure 2.12: Electronic excitation cross sections for electron impact on hydrogen gas. The cross sections below 3 keV are calculated by adapting the cross sections given by [12]. Cross sections above 3 keV are calculated based on a different analytical expression for higher energies given by [13]. The change in the analytical function used to fit the data explains the observed "bump". See text for more details.

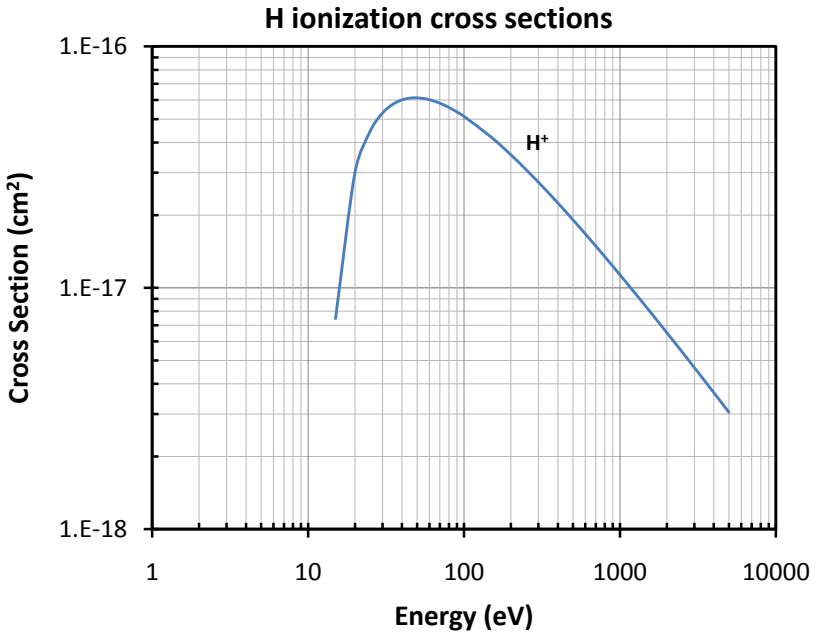

Figure 2.13: Total ionization cross section as a function of incident electron energy in eV. The parameters for this cross section were adjusted to fit the data given by [14] and are shown in Table A.11.

2.2.4 Electron Impact Cross Sections For CH_4

The cross sections for CH_4 used by the codes in this work have been carefully compiled by our group for previous works. Therefore, I will be brief on this section and refer the reader to [15] and [78] for more details on these cross sections. The excitation states considered (electronic, dissociative and vibrational) are given in the Appendix Table A.9 and the ionization parameters are given in the Appendix Table A.11. All cross sections are calculated by the analytic functions given by Equations 2.8 and 2.14. The cross sections are shown in Figures 2.14 and 2.15.

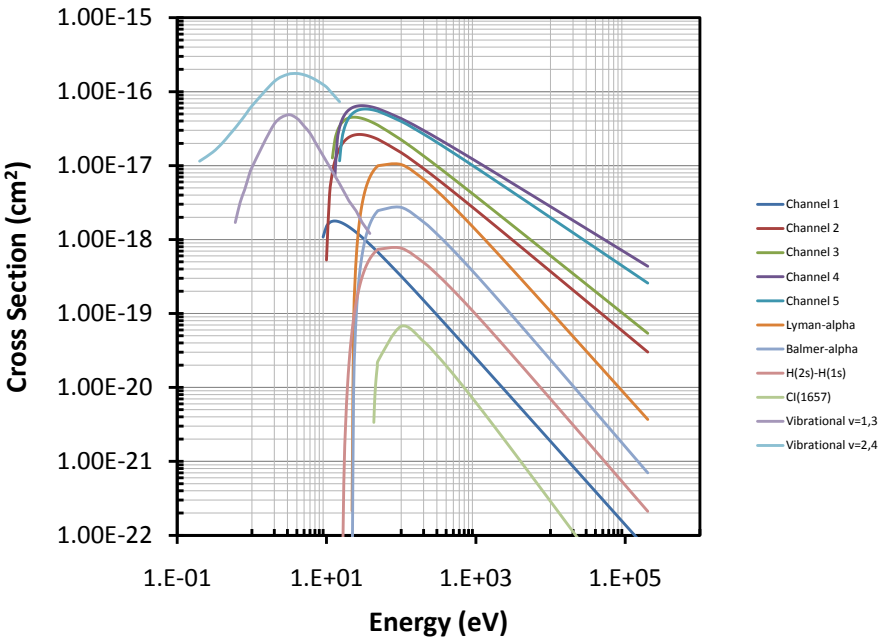

Figure 2.14: Excitation cross sections for CH_4 (electronic, dissociative and vibrational) as a function of incident electron energy in eV. For more details on these cross sections, please refer to [15]. All the parameters used can be seen in the Appendix table A.9.

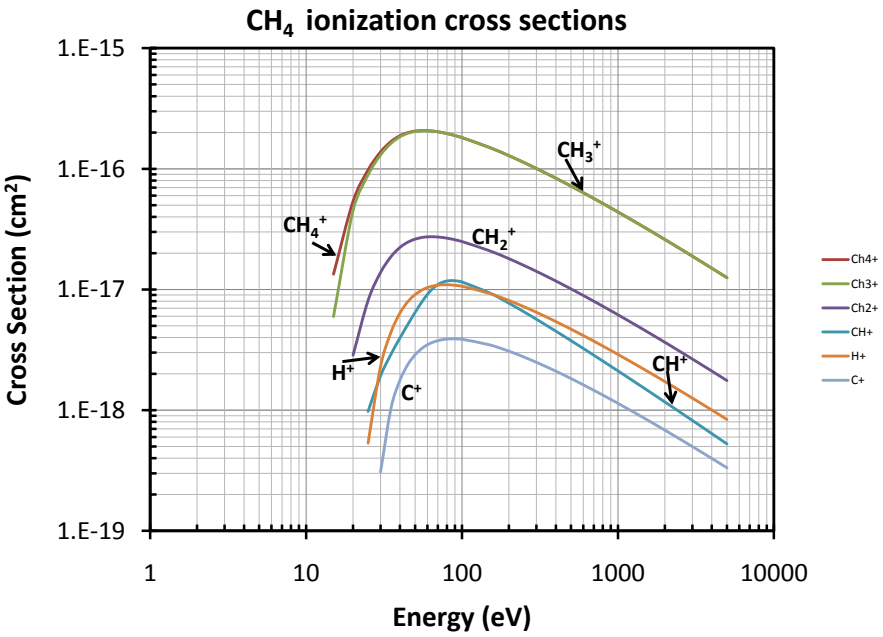

Figure 2.15: Ionization cross sections of CH_4 by electron impact. Refer to [15] for more detailed information. The parameters used for the ionization cross section analytical fits can be found in the Appendix table A.11.

2.3 Loss Function

In order to double check the cross sections and to obtain some more useful information about the interactions between the precipitating electrons and the atmospheric neutrals, we calculated the loss function for each species. The loss function gives the energy loss of each species after the collision. It is given by the following equation, taken from [7]:

$$L(E) = (2m_eE/M)\sigma_{mt}(E) + \frac{1}{n_M v_e}\frac{dE}{dt} + \Sigma_n \sigma_n(E)\Delta E_n + \Sigma_n \int_0^{(E-I_n)/2} (I_n+\varepsilon)\frac{d\sigma_n^i}{d\varepsilon}(E,\varepsilon)d\varepsilon \tag{2.19}$$

For our purpose, the loss function can be obtain by just adding the third and fourth terms of the equation. Therefore, using the following equation we obtain the loss function for each species as shown in Figure 2.16.

$$L(E) = \Sigma_n \sigma_n(E)\Delta E_n + \Sigma_n \int_0^{(E-I_n)/2} (I_n+\varepsilon)\frac{d\sigma_n^i}{d\varepsilon}(E,\varepsilon)d\varepsilon \tag{2.20}$$

In general, one can calculate the energy loss per unit path length x in a gas with density n by taking:

$$L(E) = -\frac{1}{n}\frac{dE}{dx} \tag{2.21}$$

The results for the energy loss function for the major species in the Jovian atmosphere can be found in Figure 2.16.

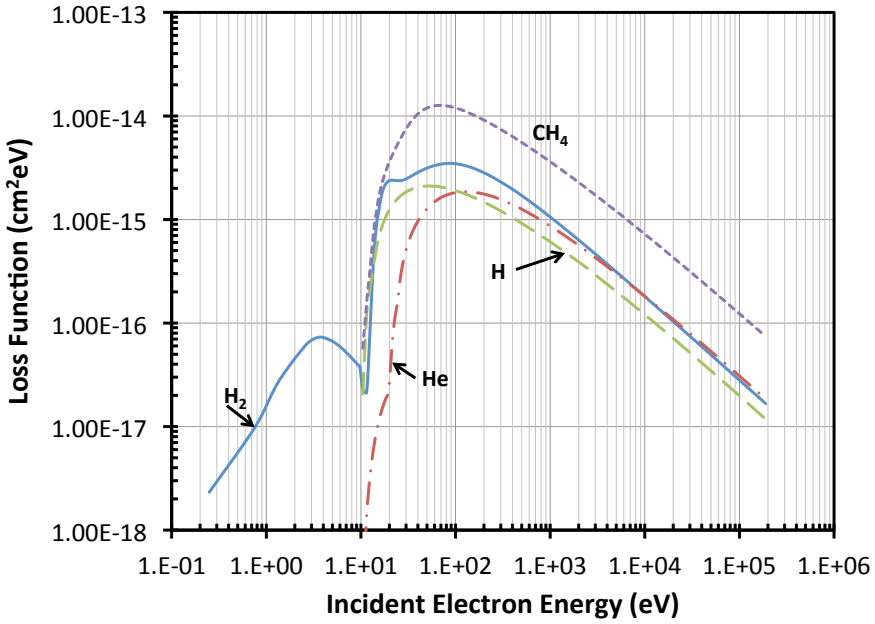

Figure 2.16: Energy loss functions for H_2, H, He, and CH_4 as a function of incident electron energy (eV).

2.4 Backscatter Cross Sections

For the two-stream code calculation, it is important to know the fraction of electrons that scatters back after a collision. In order to do this, one needs the elastic and inelastic backscatter cross sections and probabilities. We performed this calculation for the electron collisions with H_2 using the differential elastic scattering cross sections $\frac{d\sigma}{d\Omega}$ measured by [16]. *Shyn et al.* measured differential cross sections for energies ranging from 2 – 200 eV and for angles between 6 – 168 degrees. Their measured differential cross section as a function of angle is shown in Figure 2.17. We can obtain the total

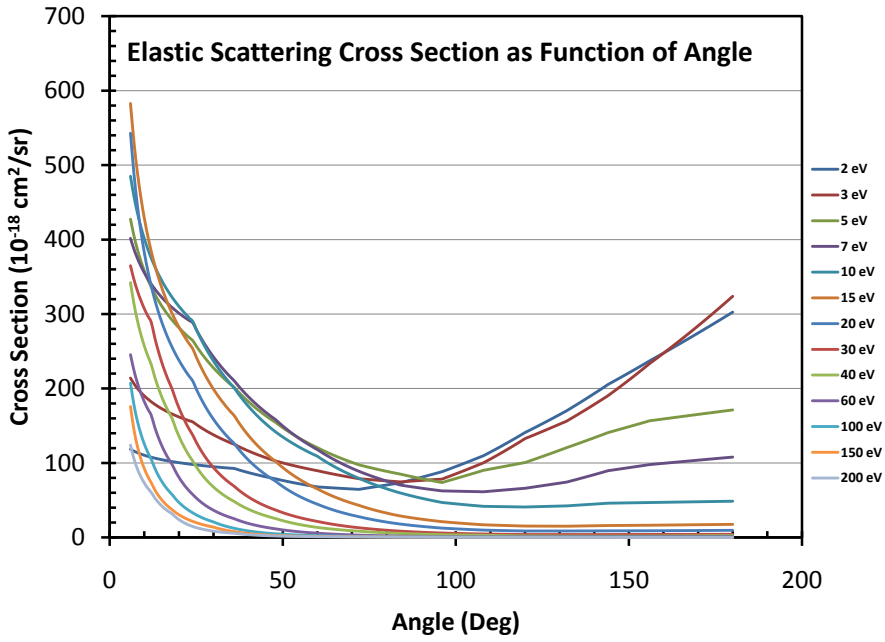

Figure 2.17: Differential cross section for elastic electron impact collisions on H_2 as a function of angle for different incident electron energies (eV). Data adapted from [16]

elastic cross section by integrating:

$$\sigma_{el} = \int_{\Omega} \frac{d\sigma}{d\Omega} d\Omega \tag{2.22}$$

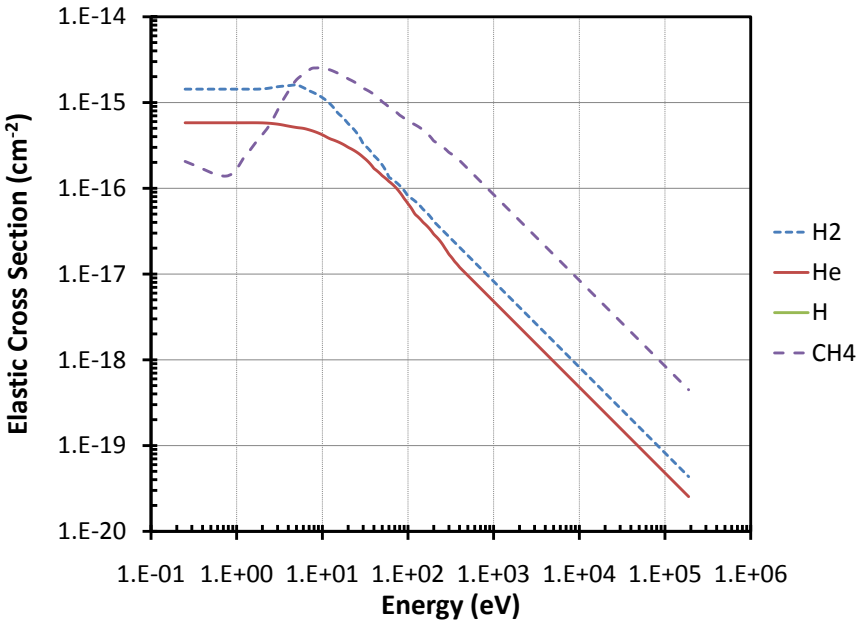

Figure 2.18: Total elastic cross section for electron impact on H_2, H, He, and CH_4 as a function of incident electron energy (eV). Calculated by using equation 2.22

The elastic backscatter probability is obtained by calculating the fraction of electrons that would scatter to angles greater than 90°and then dividing it by the total elastic cross section. The backscatter probability multiplied by the elastic cross section will give the backscatter cross section. There is no data available for the inelastic cross sections. Therefore, the elastic and inelastic backscatter probabilities are taken to be equal in our model until new cross sections become available. Please refer to Figures 2.18 and

2.19 for the backscatter probabilities and cross sections for the different neutral species. The values for the cross sections of H, He and CH_4 are taken from previous work done by our group (see for example [78]). The values for the backscatter probabilities of H and He are taken to be equal.

The differential cross sections also allow us to calculate the momentum transfer cross sections for electron impact collisions with molecular hydrogen. This can be done by integrating the following equation:

$$\sigma_{MT} = \int_{\Omega} \frac{d\sigma}{d\Omega}(1-\cos\theta)d\Omega. \tag{2.23}$$

The resultant momentum transfer cross section calculated for electron impact on H_2 can be seen in Figure 2.20.

2.5 Photoionization and Photoabsorption Cross Sections

Sunlight (photons) are the key component for the formation of a planetary ionosphere. Solar photons will interact with the atmosphere exciting the neutral species and producing ions and secondary electrons.These, in turn, will further interact with each other and other atmospheric constituents producing a unique atmospheric population. In particular, parts of the modeling of the Jovian aurora require photoabsorption, photoionization and photodissociation cross sections to calculate collisions of solar photons with the atmospheric neutrals present. All these processes involve an interaction between a photon and a neutral. Photoionization occurs when an incident photon has at least as much energy as the binding energy needed to ionize the neutral. The ejected electron will have a kinetic energy equal to the the photon energy minus the binding energy. If the photon has an energy lower than the binding energy it will be absorbed or scattered by

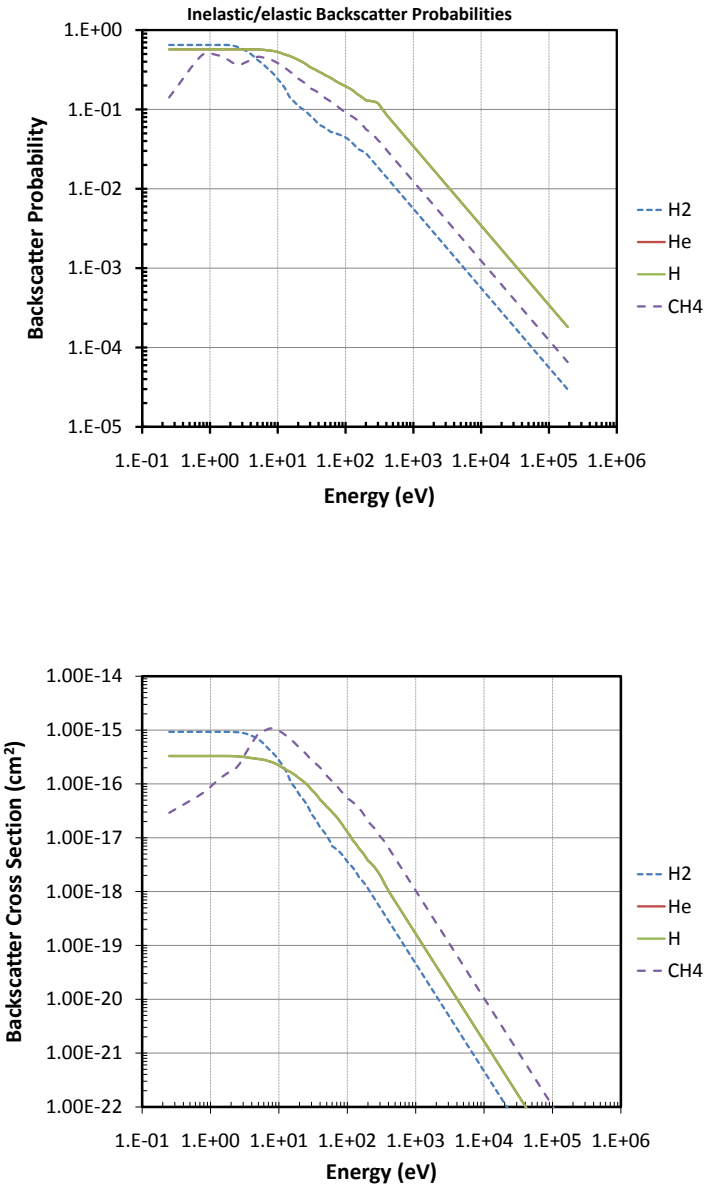

Figure 2.19: Backscatter probability (left) and cross section (right) for H_2, H, He, and CH_4 as a function of incident electron energy (eV). The probability is calculated by taking the fraction of particles that scatter with angles greater than 90° divided by the total elastic cross section. The cross section is calculated by multiplying the backscatter probability with the elastic cross section (see Figure 2.18).

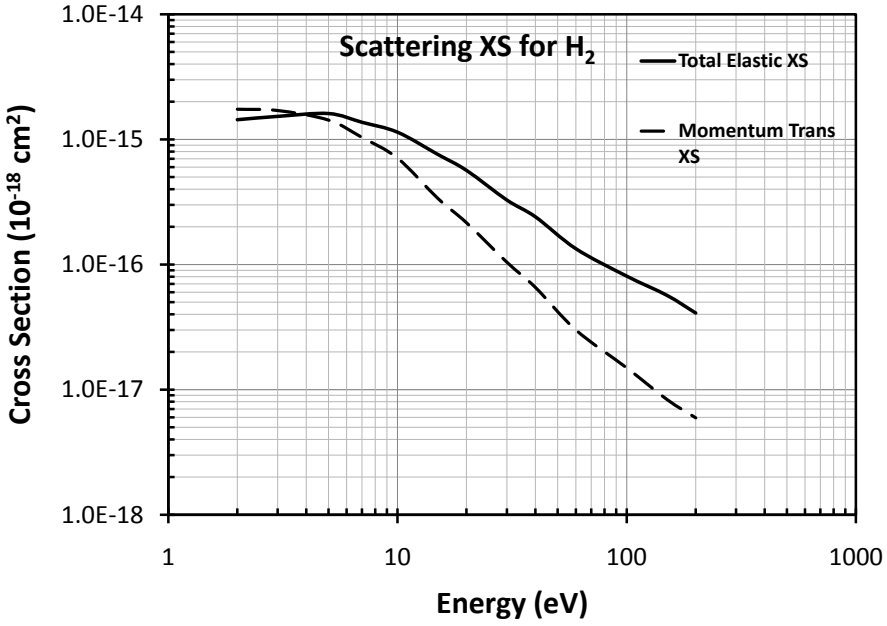

Figure 2.20: Momentum transfer cross section for H_2 as a function of incident electron energy (eV). The total elastic cross section is shown for comparison. Adapted from [16].

the neutral. When photoabsorption occurs, an electron in a lower energy level will be excited to a higher energy level by the absorption of the photon energy. The atoms will absorb only those photons with the right amount of energy, since the energy levels are quantized and an exact energy is required to jump between the levels, as explained by quantum mechanics. Photoabsorption may also lead to heating the atmospheric neutrals. Photodissociation of a molecule may occur when a photon is absorbed that has the right energy needed to dissociate a given molecule. The following equations sum-

marize the important processes considered in the model:

$$M + h\nu \rightarrow M^{+} + e \qquad \text{for } h\nu \text{ binding energy} \tag{2.24}$$

$$M^{+} + h\nu \rightarrow M^{++} + e \tag{2.25}$$

$$M_2 + h\nu \rightarrow M + M \qquad \text{dissociation} \tag{2.26}$$

$$M + h\nu \rightarrow M^{*} \qquad \text{excited state} \tag{2.27}$$

When modeling planetary ionospheres all three processes are important, since solar radiation will contribute to changes in the ionospheric composition by these photo-processes. For instance, when we model the x-ray emission from the energetic ion precipitation, we need the photo-absorption cross sections for the neutral species to calculate the opacity effects that the atmosphere has on the emitted radiation. The photoabsorption cross sections we used to calculate equation 4.13 are shown in Figure 2.21. We adopted the cross sections from [79].

Other parts of our model include absorption of solar radiation as well as the ionization and dissociation of the neutral species due to solar EUV and x-ray photons. To evaluate this, several cross sections have been compiled by [17] and will be used in our work. Some of the sources for this cross sections include [80–82]. Please refer to Figures 2.22 and 2.23 for the different cross sections that are used in our model.

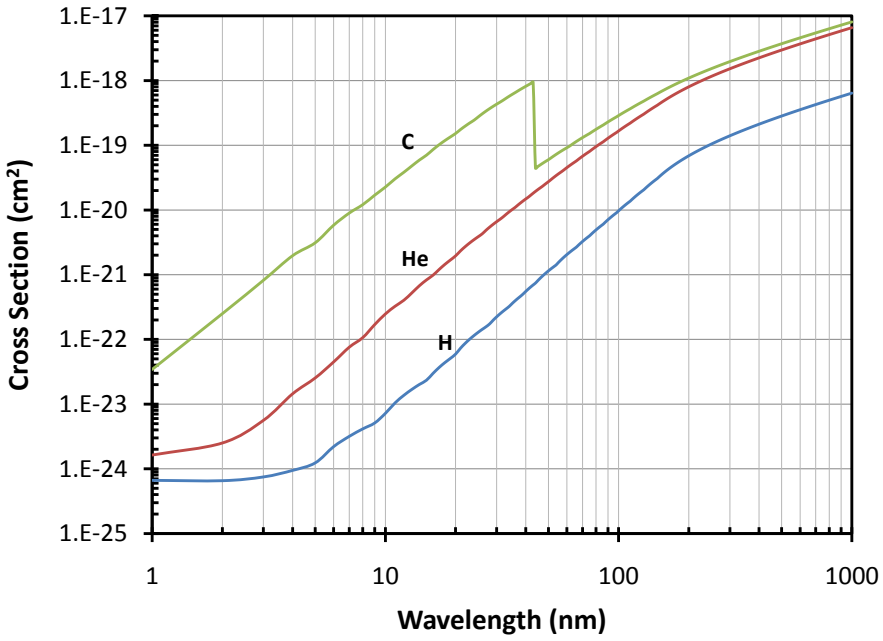

Figure 2.21: Photo-absorption cross sections for the neutral species H, He, and C as a function of photon wavelength in nm. These cross sections are used to estimate the opacity effect of the atmosphere on the emitted x-ray from the energetic ion precipitation in the Jovian polar region (See Chapter 4).

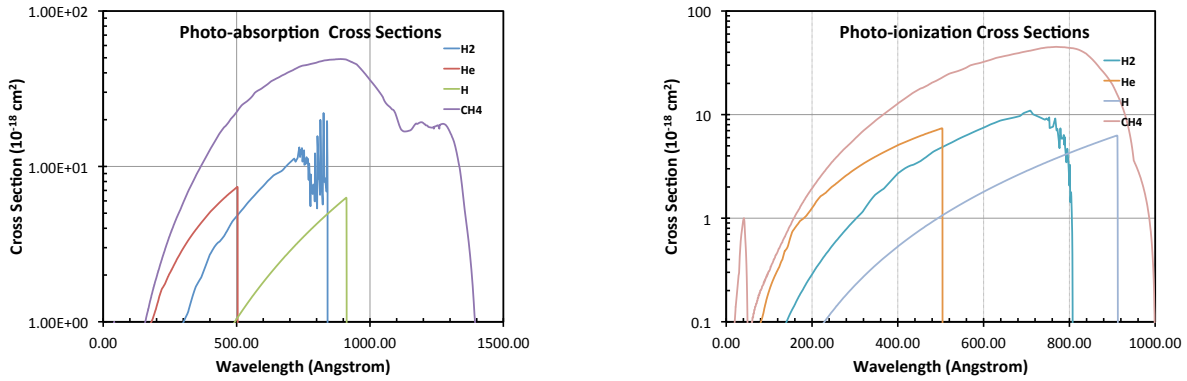

Figure 2.22: Photo-absorption and photo-ionization cross sections as a function of photon wavelength in Å. Cross sections adapted from [17].

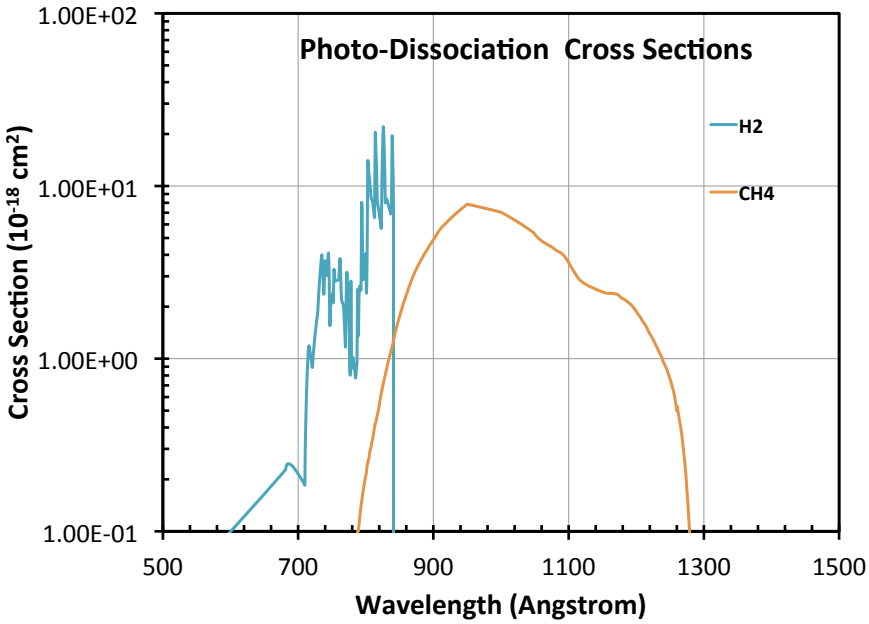

Figure 2.23: Photo-dissociation cross sections for H_2 and CH_4 as a function of photon wavelength in Å. Cross sections adapted from [17].

Chapter 3

Collision Processes – Ion Impact Cross Sections

3.1 Introduction

The ion cross section data that are used in our model for the Jovian atmosphere modeling are part of an even larger database that our collaborators at Oak Ridge National Laboratory and currently at Northern Texas University have been working on for several years. [1] The database contains cross section information for collisions between carbon, sulfur, and oxygen ions and hydrogen molecules. For each ion species one can find the cross section information for processes like charge transfer, which includes single charge transfer, transfer ionization, double-capture auto-ionization, $q, q-1$ transitions and double capture. Other cross section information is available for ionization and stripping processes. The following subsections will show the cross sections used to model energetic oxygen and sulfur ion precipitation at Jupiter. The calculation of the cross sections is not the emphasis of my work. Therefore, I will just briefly explain some of the methodology behind the cross section calculation done by our collaborators.

[1] This is still an ongoing research project as it takes several years to compile such large cross section information. The database can be found online at: `http://www-cfadc.phy.ornl.gov/astro_data/dave/`.

The relevant inelastic cross sections for all ionization stages of oxygen and sulfur colliding with molecular hydrogen over a very wide range of collision energies (10 – 1000 keV/u) have been calculated using the classical trajectory Monte Carlo (CTMC) method [83, 84]. This method assumes that all particles obey Newtonian physics during collisions. It calculates numerically the time evolution of a classical distribution $f(\vec{x}, \vec{p}, t)$ in phase space. The CTMC is preferable due to its tractability in treating this wide range of systems and collision energies. An *ab initio* treatment of many different partially stripped ions interacting with a molecular target would require the solution of the many-electron, molecular Schrödinger equation. Approximations for this exist for very high collision energies using perturbation theory, and at intermediate and low energies, methods based on expansion of the many-electron, multi-center wave function spanning both bound and continuum states of the projectile and target are the most appropriate. However, such *ab initio* treatments are not presently feasible for this large range of projectiles colliding with molecular hydrogen over several orders of magnitude of collision energy. Therefore, CTMC, which simulates the projectile-H_2 collision by sampling classical trajectories computed from a large ensemble of configurations chosen to mimic the correction quantum mechanical initial conditions, is rather used.

In the CTMC method the initial electronic orbits on the H_2 target are prepared as described by [85, 86]. The motion of the particles (projectile ions, hydrogen nuclei, and active electrons) is then determined by an iterative solution of Hamilton's equations of motion. At the end of each Monte Carlo trajectory, the relative binding energies of the electrons to the projectile and target are calculated to determine if a reaction has occurred. Here we focus attention on the range of inelastic channels relevant to modeling the precipitating ions' slowing down and charge evolution, namely, target ionization (either single ionization or double ionization), charge transfer (single electron capture by the projectile, charge transfer with simultaneous target ionization, double

capture, and double capture followed by autoionization), and projectile stripping (a single active electron on the projectile is considered coupled with the independent electron model [87]).

We note that for O^{q+} and S^{q+} (q = 0, 1, ..., 8 or q = 0, 1, ..., 16) + H_2, almost no relevant experimental data exists, especially for this huge range of ionization stages and collision energies. The limited data for oxygen allows some benchmark of the presently utilized data, as does comparison of CTMC results for other systems, but does not allow a consistent and useful adjustment of the database. That is, when considering the full range of ions, the several inelastic collision channels, and the large range of collision energies, it is not possible to make adjustments to one collision channel for a small number of ions over a small range of energies and maintain a self-consistent set of inelastic cross sections. Improvements in the database must await many more experimental measurements and *ab initio* calculations to allow a comprehensive and consistent set of improved, evaluated data to be produced. For additional information on cross section calculations see [7, 88–90].

3.2 Charge Transfer Collisions

Several processes are relevant to the energetic ion precipitation at Jupiter. Charge transfer collisions are an important process that must be taken into account in an ionospheric model. It is the controlling process due to a high rate coefficient [91]. For the case of oxygen, charge transfer collisions are dominant for energies below 100 keV/u. When such a collision occurs an ion and a neutral or an ion and a molecule exchange charge between them. During a charge transfer reaction one or more electrons may be transferred. In charge exchange reactions the participating particles tend to conserve their kinetic energy after the collision. Therefore, this process is a way to convert energetic

ions into energetic neutral particles. Such process occurs in the magnetospheres of Jupiter and Saturn and are the cause of mass loading.

In general a charge transfer reaction will have the outcome

$$X^+ + Y \rightarrow Y^+ + X. \tag{3.1}$$

In our case X represents the incoming oxygen or sulfur ion and Y the hydrogen molecule from Jupiter's atmosphere. There are several processes that can have the same outcome and we consider all of them in our calculations:

$$X^{q+} + H_2 \rightarrow \begin{cases} X^{(q-1)+} + H_2^+ \\ \text{Single Capture} \\ X^{(q-1)+} + 2H^+ + e \\ \text{Transfer Ionization} \\ X^{(q-2)+} + 2H^+ \rightarrow X^{(q-1)+} + 2H^+ + e \\ \text{Double-Capture Auto-Ionization} \end{cases} \tag{3.2}$$

The total charge transfer cross section is given by the sum of the individual cross sections:

$$\sigma_{q,q-1} = \sigma_{sc} + \sigma_{ti} + \sigma_{dcai} \tag{3.3}$$

The total charge transfer cross sections for oxygen and sulfur ions are shown in Figures 3.1 and 3.2.

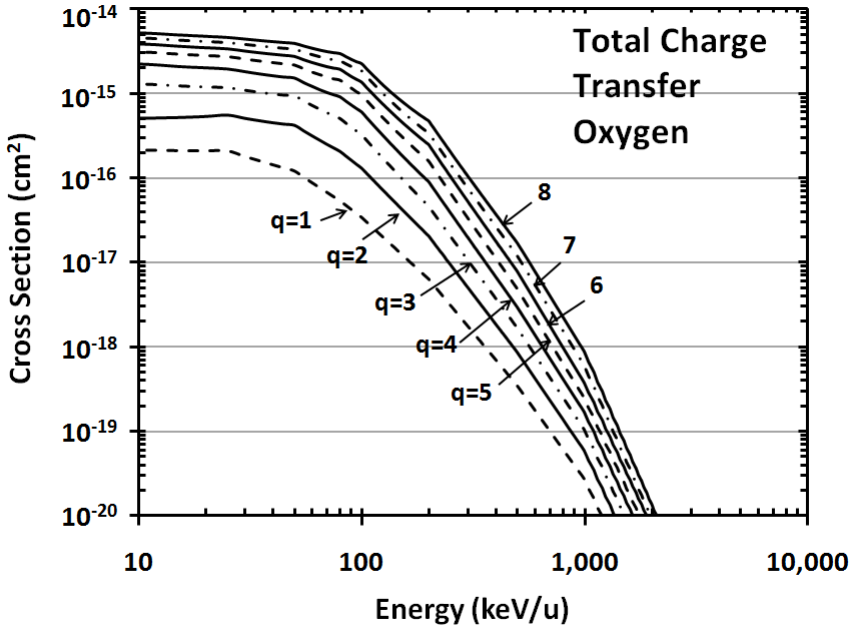

Figure 3.1: Total charge transfer cross section as a function of energy for collisions of O^{q+} and H_2, given by the sum of single charge transfer, transfer ionization and double-capture auto-ionization cross sections ($O^{q+} + H_2 \rightarrow O^{(q-1)+*} + H_2^+$). The curves correspond to a different oxygen charge state $q = 1 - -8$ [18, 19].

3.3 Electron Stripping Processes

In ionospheric studies the electron stripping process of an incident ion that collides with an atmospheric neutral is also an important process to consider. In general, this process can be described as:

$$X^{q+} + Y \rightarrow X^{(q+1)+} + Y(\Sigma) + e, \tag{3.4}$$

where $Y(\Sigma)$ denotes all electronic states including ionized states. As an example, the stripping process of oxygen ions will have the form:

$$O^{q+} + H_2 \rightarrow O^{(q+1)} + H_2^* + e. \tag{3.5}$$

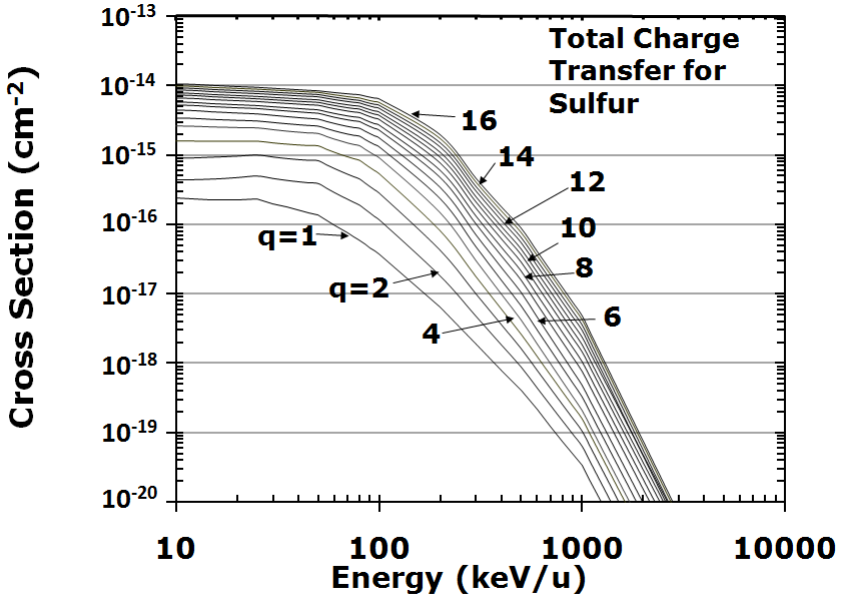

Figure 3.2: Total charge transfer cross section as a function of energy for collisions of S^{q+} and H_2, given by the sum of single charge transfer, transfer ionization and double-capture auto-ionization cross sections ($S^{q+} + H_2 \rightarrow S^{(q-1)+*} + H_2^+$). The curves correspond to a different sulfur charge state from $q = 1 - 16$ [18, 19].

The same stripping process occurs for the sulfur ions, replacing the oxygen ion for sulfur in the previous reaction. Each time there is a stripping collision the ion will lose an electron. Electron stripping is the process by which ions will reach highly charged states. The stripping cross section calculated by the CTMC method for sulfur and oxygen ion interacting with hydrogen molecules are shown in Figures 3.3 and 3.4.

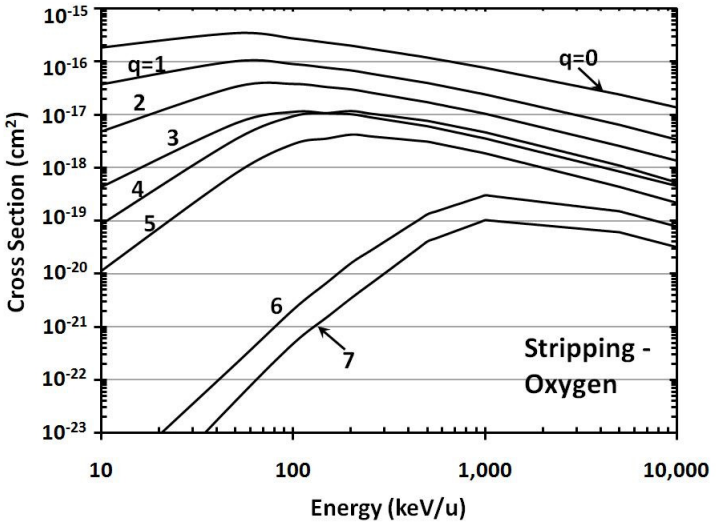

Figure 3.3: Electron stripping cross sections for oxygen as a function of ion energy for all charge states q of oxygen in molecular hydrogen $(O^{(q-1)+} + H_2 \rightarrow O^{q+} + H_2 + e)$ [18, 19].

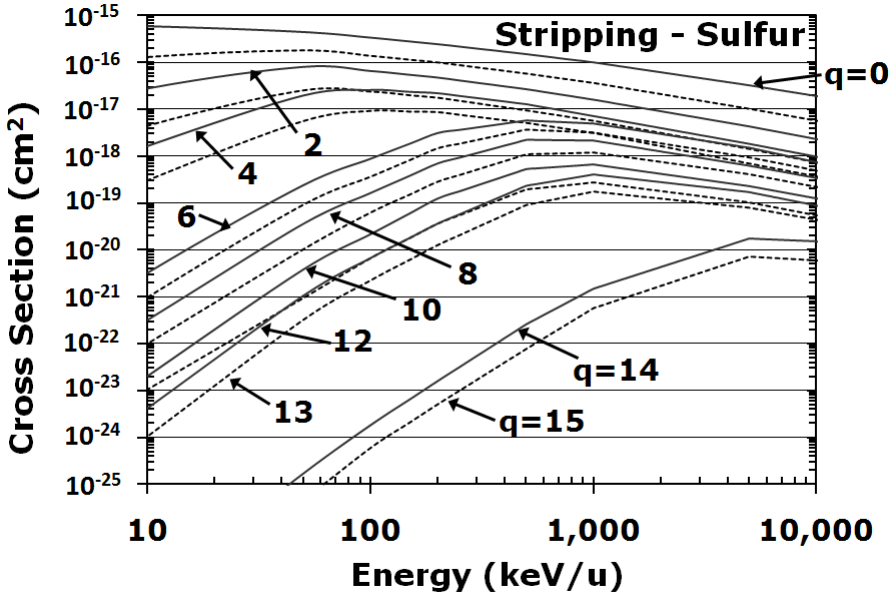

Figure 3.4: Electron stripping cross sections for sulfur as a function of ion energy for all charge states q of sulfur in molecular hydrogen [18, 19].

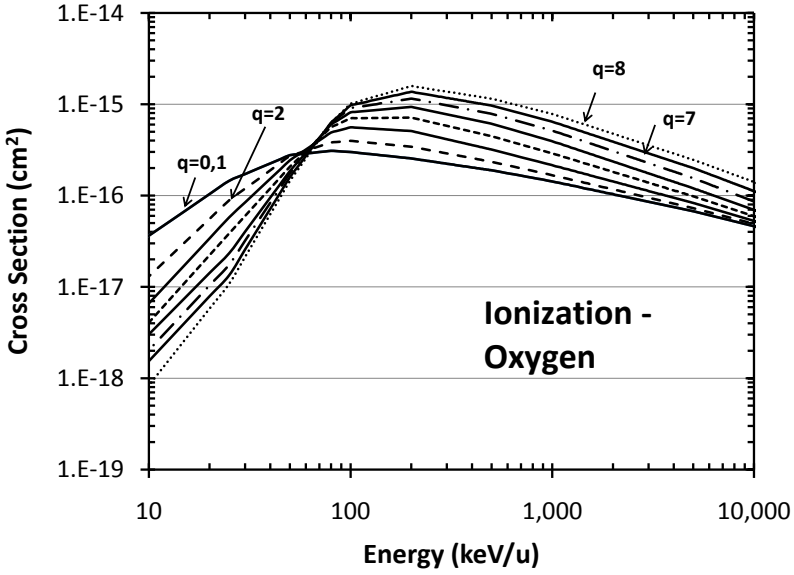

Figure 3.5: Ionization cross section for oxygen in molecular hydrogen as a function of energy. Each curve represents an oxygen charge state [18].

3.4 Ionization

Ionization of the neutrals is an extremely important process in ionospheric modeling. When the incident ions reach high enough energies, they will mostly ionize the neutral species in the atmosphere and lose energy in each ionization collision. One can describe an ionization process by

$$X^{q+} + H_2 \rightarrow X^{q+} + H_2^+ + e, \tag{3.6}$$

where X can be either oxygen or sulfur. The corresponding cross sections can be seen in Figures 3.5 and 3.6.

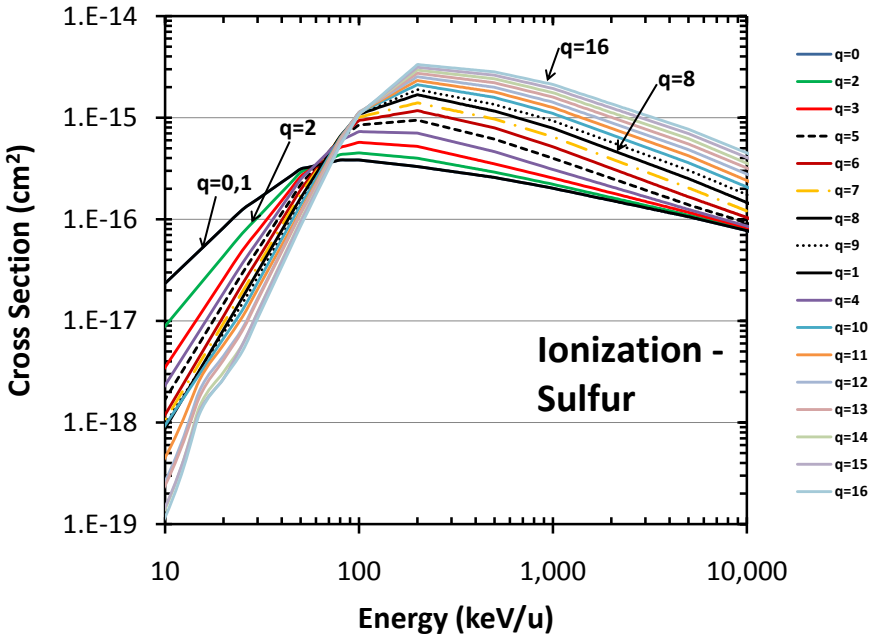

Figure 3.6: Ionization cross section for sulfur in molecular hydrogen as a function of energy. Each curve represents an oxygen charge state [18].

3.5 Secondary Electrons from Ion–Neutral Collisions

Ionization and stripping collisions between ions and atmospheric neutrals can lead to the production of secondary electrons as given by equations 3.4 and 3.6. This secondary electron population is important for the dynamics of the ionosphere, since they may also create currents or further ionize the neutrals or recombine with ions present in the atmosphere. In general, the secondary electrons are indistinguishable from primary or photoelectrons. It is important for us to determine the secondary electron distribution that is created as a product of the energetic ion precipitation in high latitudes of the Jovian upper atmosphere as they will also contribute in the ionospheric dynamics essential in the models. To calculate the probability of ejecting an electron with secondary energy E_s or at in a particular direction, the single or double differential cross section of the specific process is needed. The single differential cross section (sdxs) can be given as a function of ejected electron energy, $d\sigma/dE$, such that:

$$\int_0^\infty \frac{d\sigma}{dE} dE = \sigma_{tot}, \tag{3.7}$$

where σ_{tot} is the total cross section for the given process (ionization or stripping in our case) for a given primary ion energy. Similarly, the single differential cross section may be given as a function of the ejected angle to which the electron is scattered, such that:

$$\int \frac{d\sigma}{d\Omega} d\Omega = \sigma_{tot}. \tag{3.8}$$

A double differential cross section would simultaneously give both angular and energetic information of the ejected electron, however, it is extremely difficult to calculate

with the current models. It must still hold that:

$$\int \frac{d^2\sigma(E,\Omega)}{dEd\Omega} = \sigma_{tot} \tag{3.9}$$

Both single and double differential cross sections are extremely hard to measure and the available data in the literature is outdated and very limited (mostly for proton-neutral collisions). This makes it very difficult for us to determine the single differential cross section $d\sigma/dE$ that we would need for oxygen and sulfur, as they may be substantially different than those for proton collisions. The main reason being that the heavy ions have many electrons that will affect the interaction, which are not present in the proton-neutral collisions. With the available CTMC codes developed by our collaborators we were able to construct a very small data set of sdxs for ionization collisions (either target ionization or projectile ionization) for incoming oxygen ions for ion energies of 0.5, 1 and 2 MeV/u to sample the high energies and initial ion energies of 1, 10, 50 and 100 keV/u to sample the low energies. This exploratory work is by no means complete, but given the time constraints in the calculation of a single data sets it is the best we can do with the available models and literature. In the following subsections we presents our results for the single differential cross sections for ionization and stripping collisions of oxygen ions and neutral hydrogen. These cross sections will serve as a guide and approximation for models described in Chapter 6.

3.5.1 Single Differential Cross Sections for Ionization Collisions

As shown by equation 3.6, the collision between a fast ion and a neutral (in our case H_2) leads to the production of a secondary electron. For ionization collisions, in particular, the secondary electron is ejected from the neutral. Therefore, in our case, we have two cases that have to be considered: 1) single ionization, where only one electron is

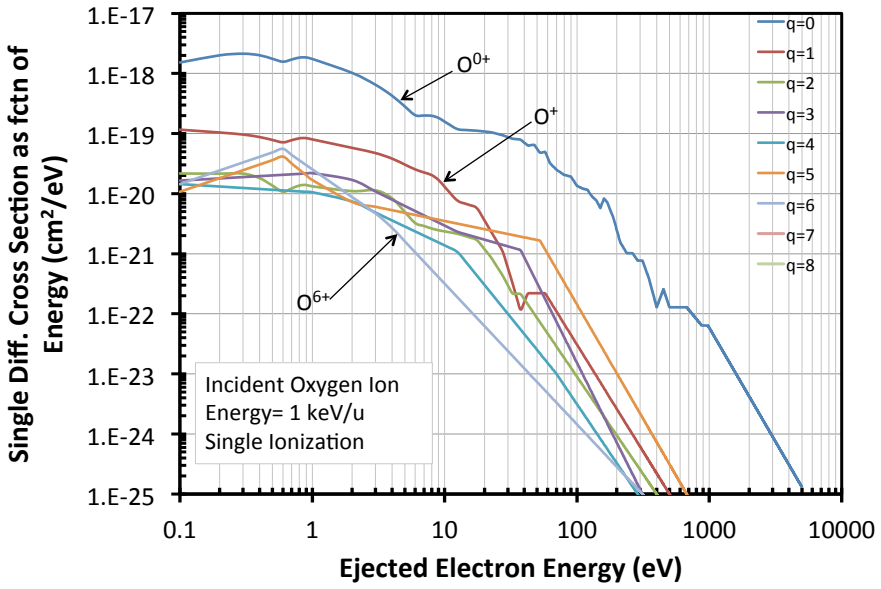

Figure 3.7: Single differential cross section as a function of ejected electron energy for a single ionization collision between an O^{q+} ion and H_2 as a function of ejected electron energy (eV). The ion has an incident energy of 1 keV/u. Due to the low ion energy, the statistics are very low. Each curve represents a different charge state from $q = 0-6$. For $q = 7,8$ there is no cross section shown because it is too low.

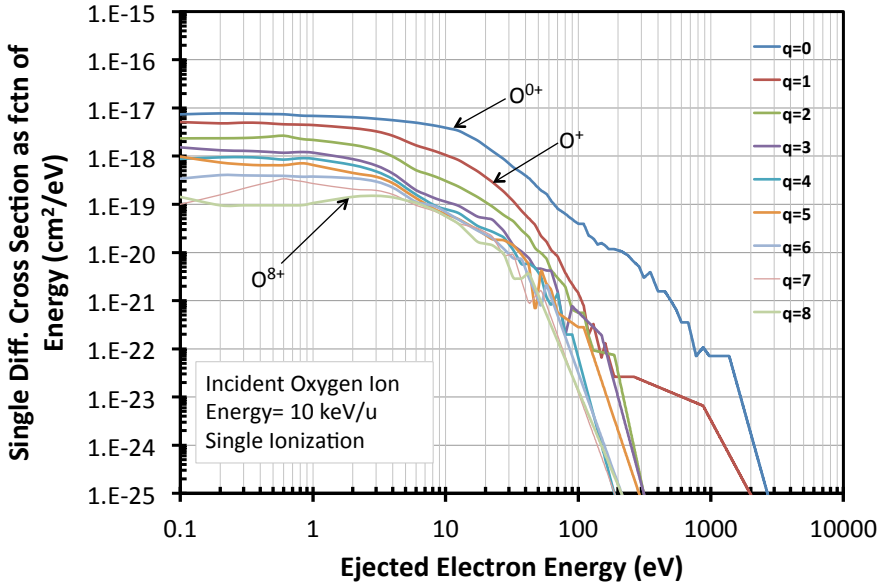

Figure 3.8: Single differential cross section as a function of ejected electron energy for a single ionization collision between an O^{q+} ion and H_2 as a function of ejected electron energy (eV). The ion has an incident energy of 10 keV/u. Each curve represents a different charge state from $q = 0 - 8$.

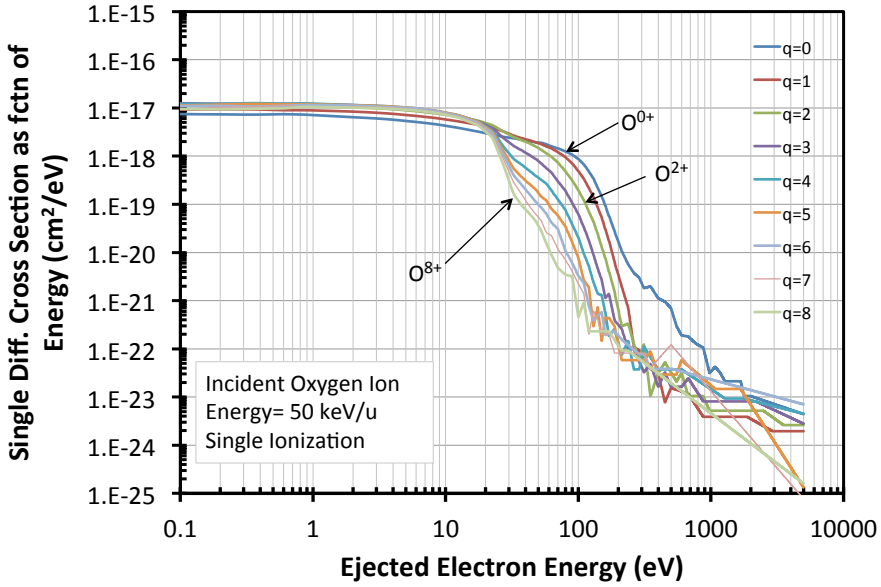

Figure 3.9: Single differential cross section as a function of ejected electron energy for a single ionization collision between an O^{q+} ion and H_2 as a function of ejected electron energy (eV). The ion has an incident energy of 50 keV/u. Each curve represents a different charge state from $q = 0 - 8$.

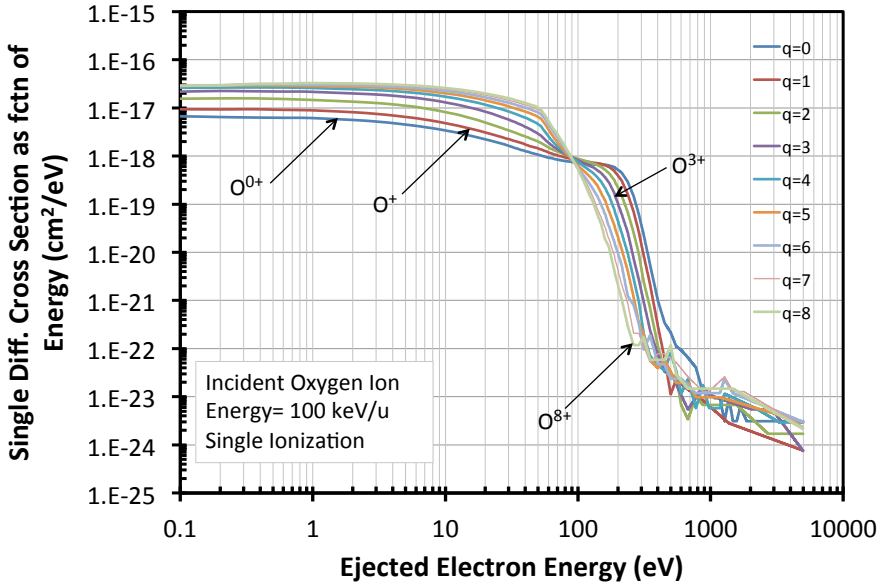

Figure 3.10: Single differential cross section as a function of ejected electron energy for a single ionization collision between an O^{q+} ion and H_2 as a function of ejected electron energy (eV). The ion has an incident energy of 100 keV/u. Each curve represents a different charge state from $q = 0 - 8$.

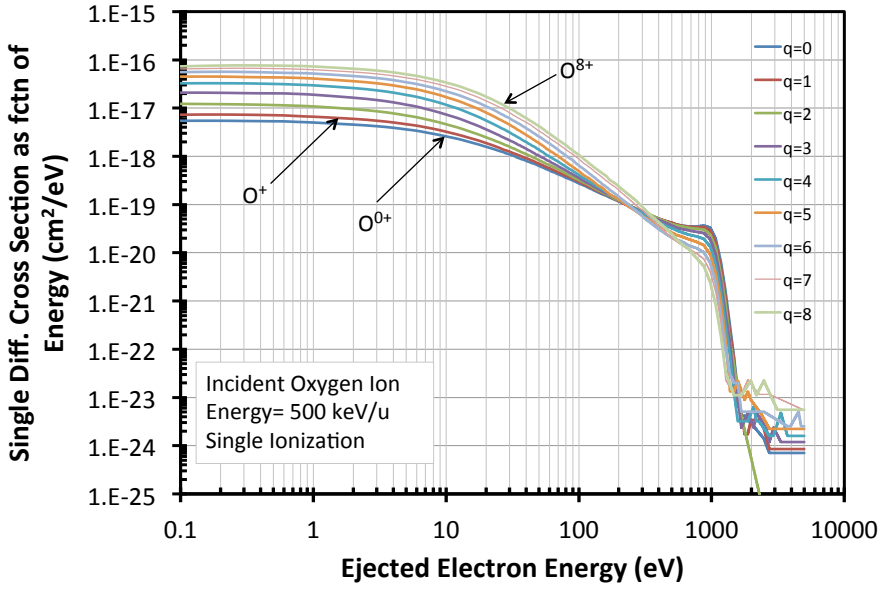

Figure 3.11: Single differential cross section as a function of ejected electron energy for a single ionization collision between an O^{q+} ion and H_2 as a function of ejected electron energy (eV). The ion has an incident energy of 500 keV/u. Each curve represents a different charge state from $q = 0 - 8$.

ejected and the product ion is H_2^+, or 2) double ionization, where the neutral molecule is dissociated and ionized and two electrons will be ejected. The double ionization process includes removal of the two electrons by direct ionization, by transfer ionization (one electron is captured by the projectile and the other one is ionized), double capture resulting in autoionization. We have calculated the single differential cross sections for both (single and double) types of collision. The sdxs for single ionization as a function of ejected electron energy for initial oxygen ion energies of 1, 10, 50, 100 and 500 keV/u, and 1.0, 2.0 MeV/u are shown in Figures 3.7 to 3.13. The "wiggles" in the curves at high energies are due to low statistics in in the Monte Carlo simulations used to obtain the cross section data. However, the behavior of the cross section is very clear and rather interesting. For example, for low energies the highly charged states have higher cross sections, but at secondary electron energies around 300 eV, this behavior inverts, i.e., the cross section fro the highly charged states become the lowest cross sections. Another important structure in the cross section behavior is the formation of a secondary peak at ejected electron energies around 1 keV. This second peak is the binary interaction. Ions with energies less than 10 keV/u have very low cross sections for the single and double ionization processes and therefore are not included in the data set. For low ion energies like 1 keV/u the cross sections are very low and it is hard to build up enough statistics. This explains the behavior that is seen in figure 3.7. We tried our best to make the shape of the curve as approximate as we could, however, some guesses had to be made to smooth out the curves. There is no cross section calculated for O^{7+} and O^{8+}.

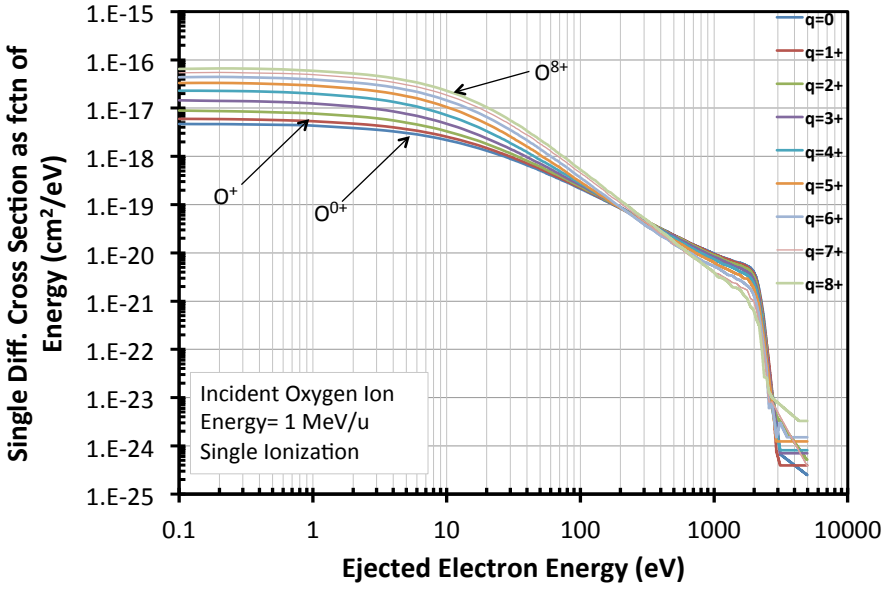

Figure 3.12: Single differential cross section as a function of ejected electron energy for a single ionization collision between an O^{q+} ion and H_2 as a function of ejected electron energy (eV). The ion has an incident energy of 1 MeV/u. Each curve represents a different charge state from $q = 0 - 8$.

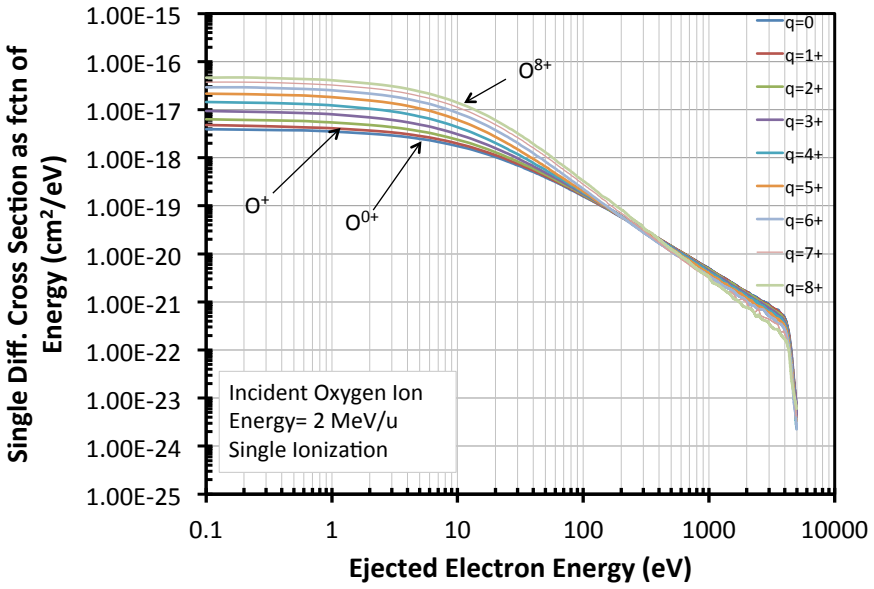

Figure 3.13: Single differential cross section as a function of ejected electron energy for a single ionization collision between an O^{q+} ion and H_2 as a function of ejected electron energy (eV). The ion has an incident energy of 2 MeV/u. Each curve represents a different charge state from $q = 0 - 8$.

The sdxs for the double ionization gives the cross section for the ejection of one electron after the collision in which two electrons are produced. It is not known at the time how the energy of the pair of electrons is distributed. After a double ionization collision each electron will have a different energy, i.e., the energy is not necessarily distributed equally between the two ejected electrons. However, it is not simple to calculate the energy of each electron at the same time. Until this data becomes available, for the purpose of our model, we will individually calculate the energy of each electron in a double ionization collision independently of the other electron energy with the sdxs for the double ionization as shown in Figures 3.14 to 3.20.

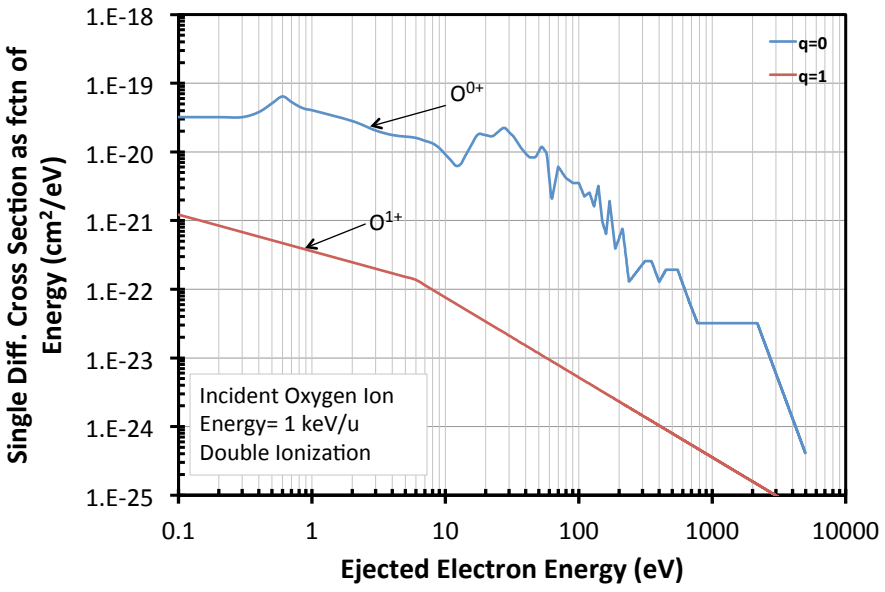

Figure 3.14: Single differential cross section as a function of ejected electron energy for a double ionization collision between an O^{q+} ion and H_2 as a function of ejected electron energy (eV). The ion has an incident energy of 1 keV/u. Each curve represents a different charge state from $q = 0 - 1$. Higher charge states are not shown as their cross section is too small.

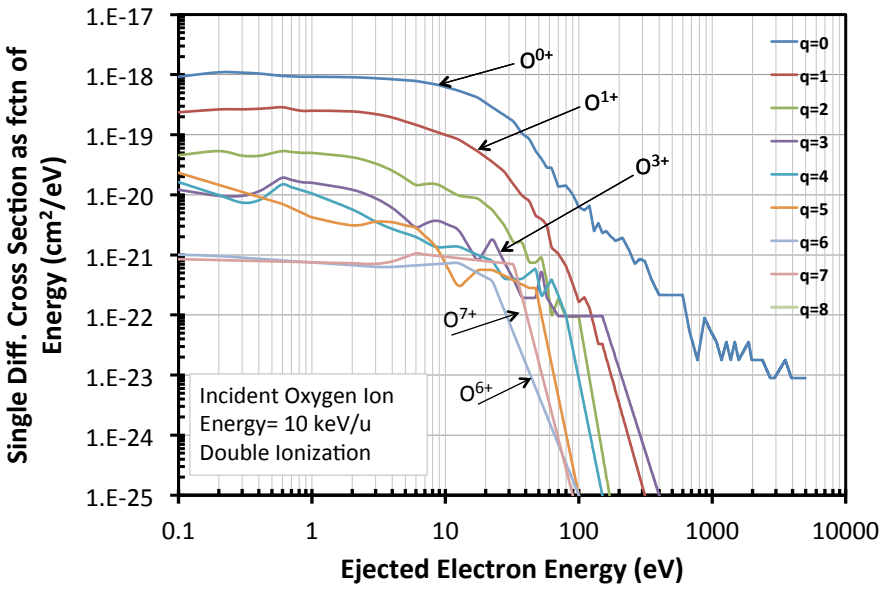

Figure 3.15: Single differential cross section as a function of ejected electron energy for a double ionization collision between an O^{q+} ion and H_2 as a function of ejected electron energy (eV). The ion has an incident energy of 10 keV/u. Each curve represents a different charge state from $q = 0 - 7$. The sdxs for O^{8+} is too low and therefore it is not shown.

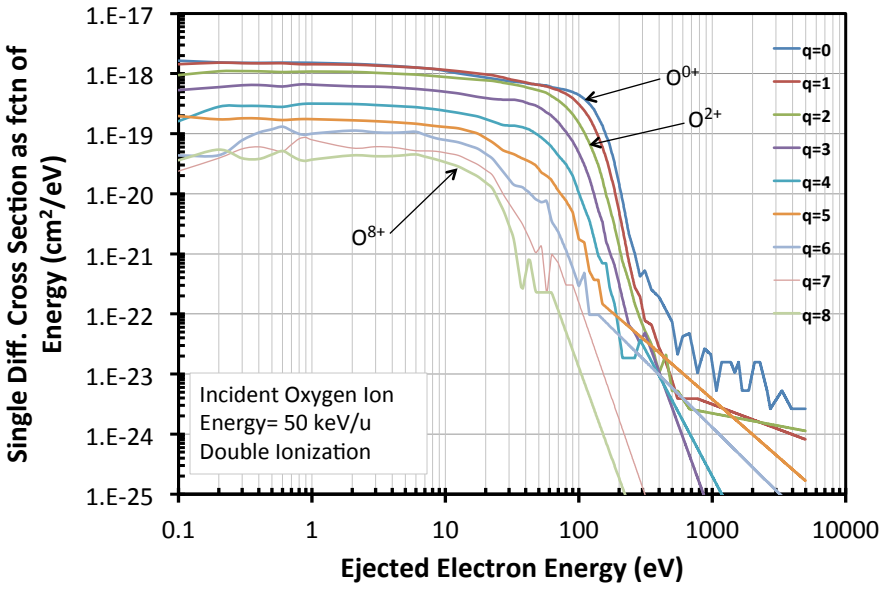

Figure 3.16: Single differential cross section as a function of ejected electron energy for a double ionization collision between an O^{q+} ion and H_2 as a function of ejected electron energy (eV). The ion has an incident energy of 50 keV/u. Each curve represents a different charge state from $q = 0 - 8$.

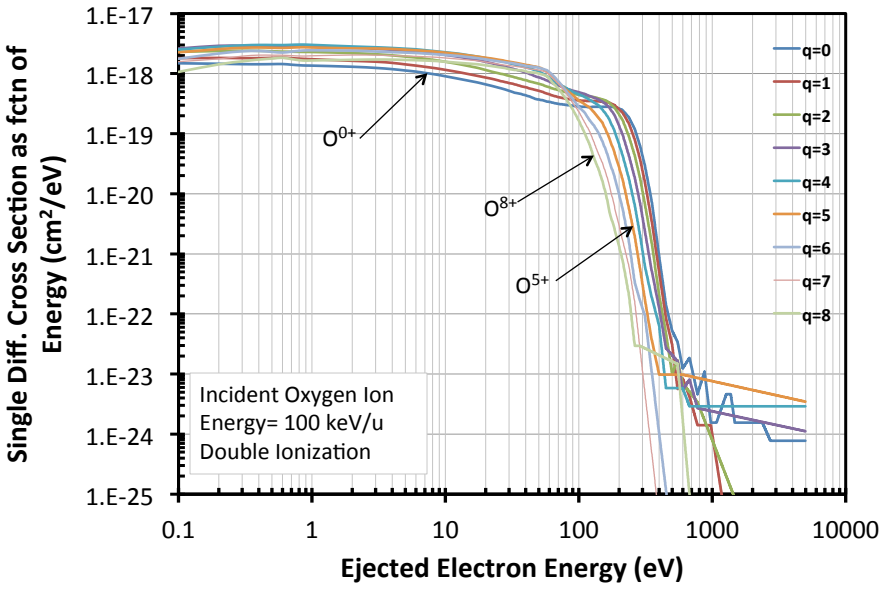

Figure 3.17: Single differential cross section as a function of ejected electron energy for a double ionization collision between an O^{q+} ion and H_2 as a function of ejected electron energy (eV). The ion has an incident energy of 100 keV/u. Each curve represents a different charge state from $q = 0 - 8$.

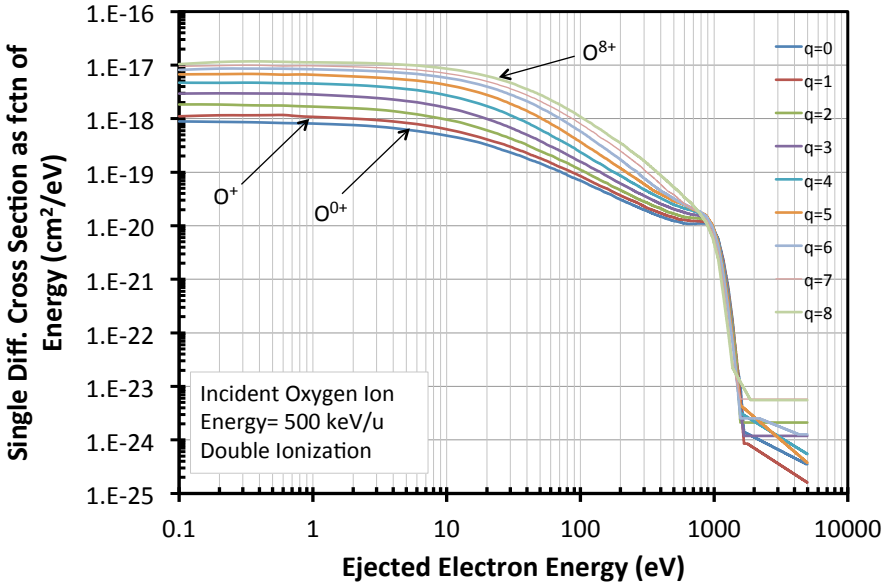

Figure 3.18: Single differential cross section as a function of ejected electron energy for a double ionization collision between an O^{q+} ion and H_2 as a function of ejected electron energy (eV). The ion has an incident energy of 500 keV/u. Each curve represents a different charge state from $q = 0 - 8$.

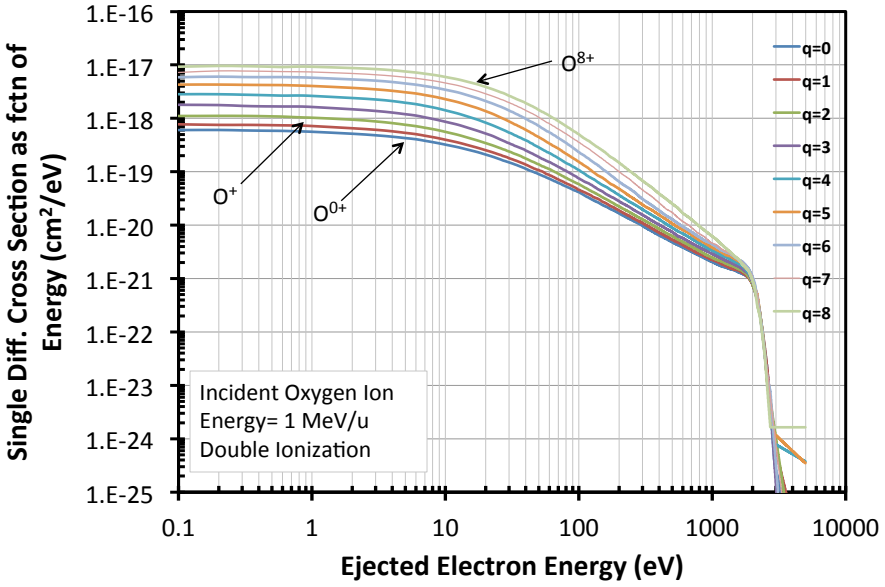

Figure 3.19: Single differential cross section as a function of ejected electron energy for a double ionization collision between an O^{q+} ion and H_2 as a function of ejected electron energy (eV). The ion has an incident energy of 1 MeV/u. Each curve represents a different charge state from $q = 0 - 8$.

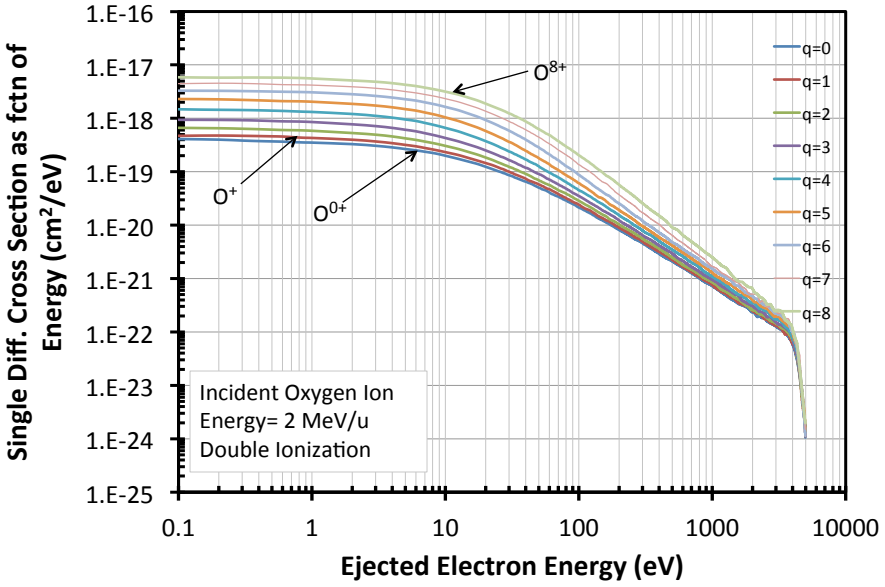

Figure 3.20: Single differential cross section as a function of ejected electron energy for a double ionization collision between an O^{q+} ion and H_2 as a function of ejected electron energy (eV). The ion has an incident energy of 2 MeV/u. Each curve represents a different charge state from $q = 0 - 8$.

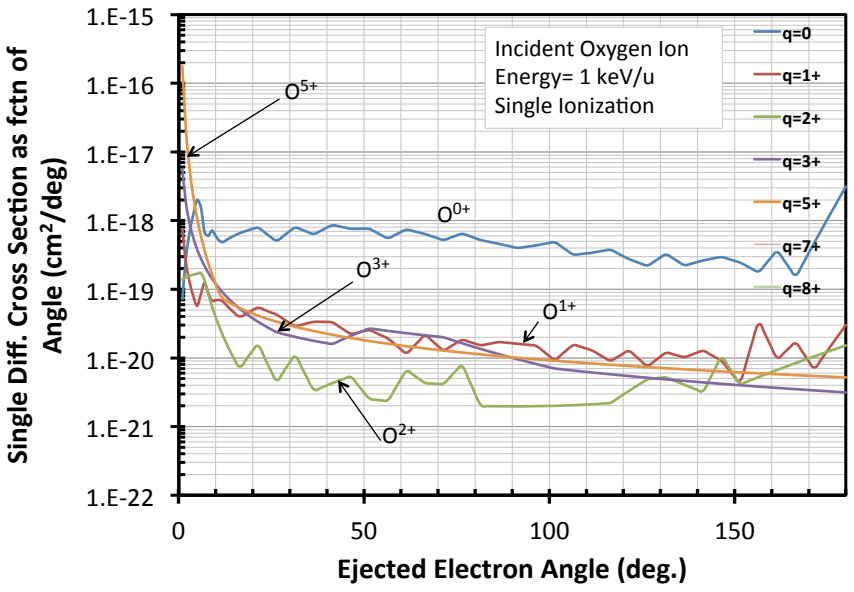

Figure 3.21: Single differential cross section as a function of ejected angle for a single ionization collision between an O^{q+} ion and H_2 as a function of ejected electron energy (eV). The ion has an incident energy of 1 keV/u. Each curve represents a different charge state from $q = 0 - 6$.

As mentioned above, the angle at which the ejected electrons are scattered is also important information that can be obtained with the single differential cross section as a function of angle. With this sdxs, for example, we can calculate the ratio of forward to backward scattering. We present the sdxs as a function of angle for single and double ionization in the following figures (Figures 3.21 to 3.34). As before, the sdxs were calculated for incoming ions with initial energies of 1, 10, 50, 100, 500 keV/u, 1 and 2 MeV/u.

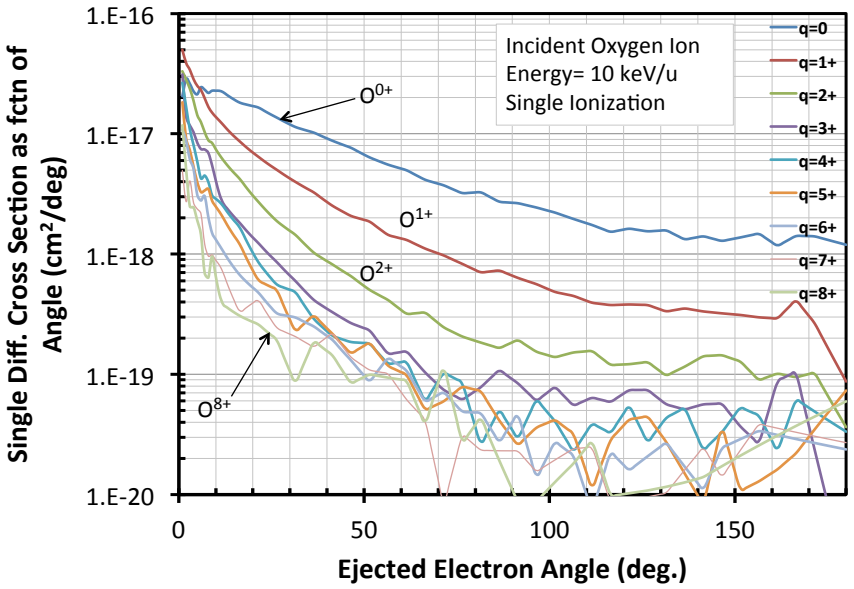

Figure 3.22: Single differential cross section as a function of ejected angle for a single ionization collision between an O^{q+} ion and H_2 as a function of ejected electron energy (eV). The ion has an incident energy of 10 keV/u. Each curve represents a different charge state from $q = 0 - 8$.

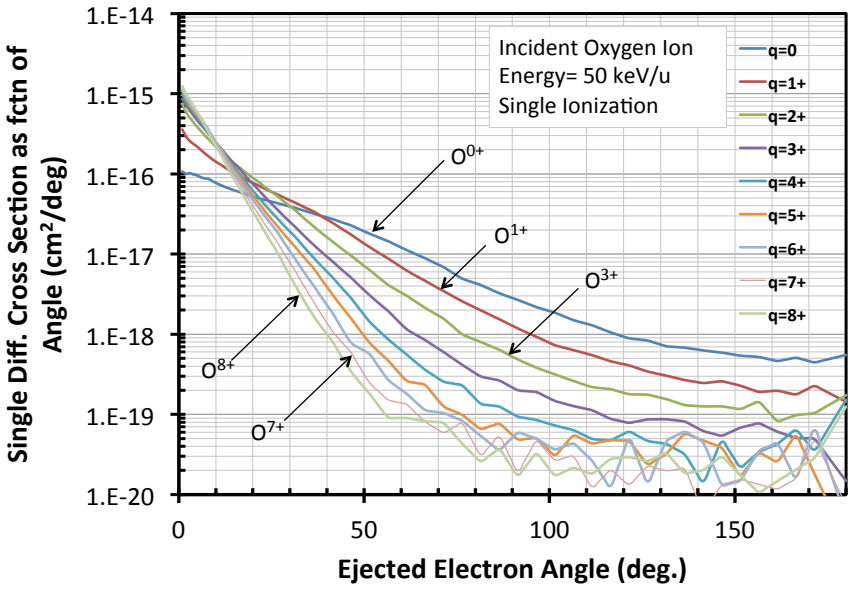

Figure 3.23: Single differential cross section as a function of ejected angle for a single ionization collision between an O^{q+} ion and H_2 as a function of ejected electron energy (eV). The ion has an incident energy of 50 keV/u. Each curve represents a different charge state from $q = 0 - 8$.

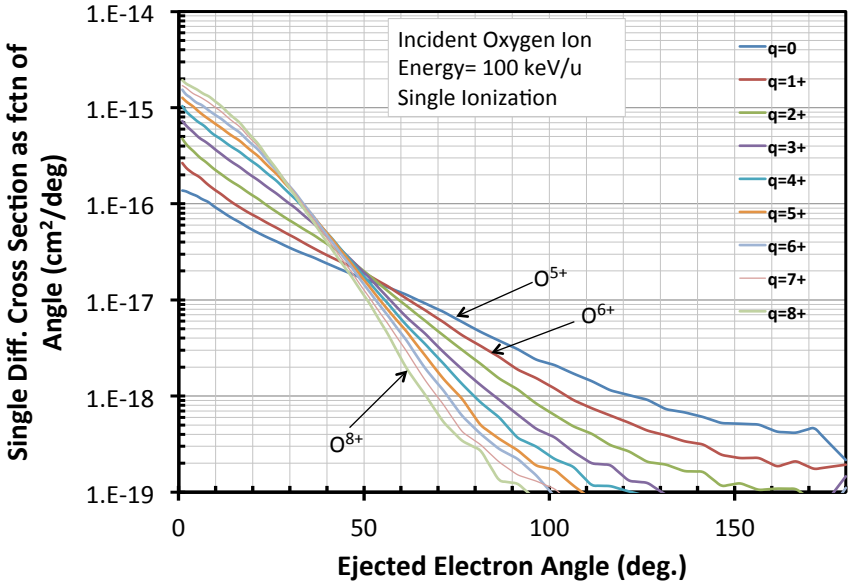

Figure 3.24: Single differential cross section as a function of ejected angle for a single ionization collision between an O^{q+} ion and H_2 as a function of ejected electron energy (eV). The ion has an incident energy of 100 keV/u. Each curve represents a different charge state from $q = 0 - 8$.

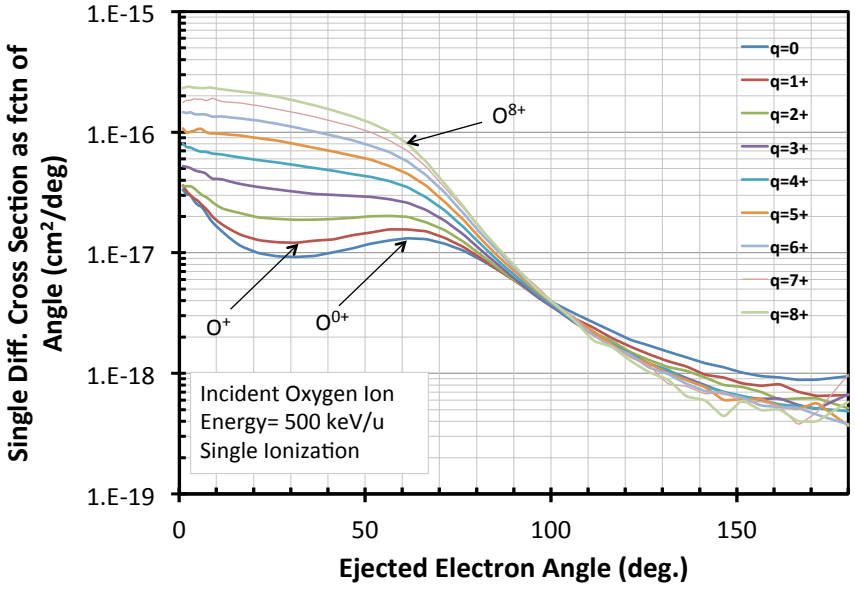

Figure 3.25: Single differential cross section as a function of ejected angle for a single ionization collision between an O^{q+} ion and H_2 as a function of ejected electron energy (eV). The ion has an incident energy of 500 keV/u. Each curve represents a different charge state from $q = 0 - 8$.

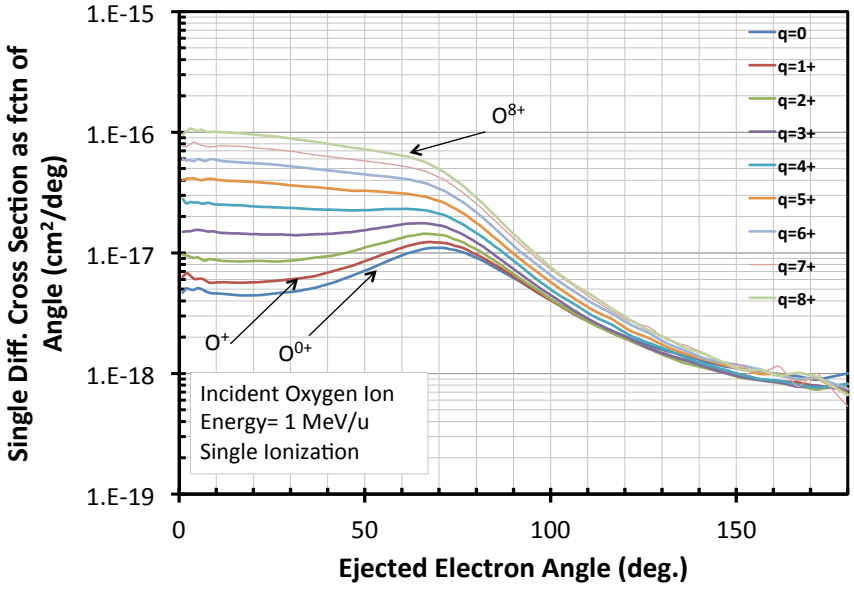

Figure 3.26: Single differential cross section as a function of ejected angle for a single ionization collision between an O^{q+} ion and H_2 as a function of ejected electron energy (eV). The ion has an incident energy of 1 MeV/u. Each curve represents a different charge state from $q = 0 - 8$.

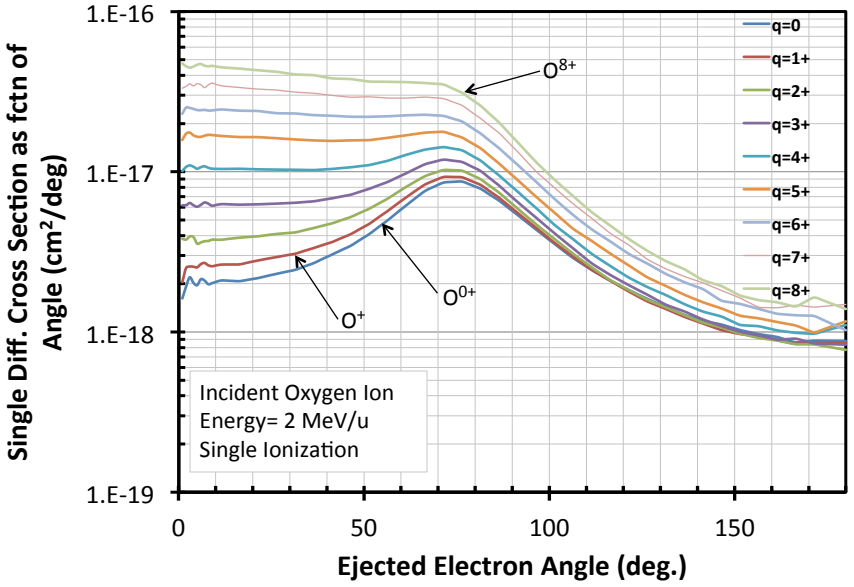

Figure 3.27: Single differential cross section as a function of ejected angle for a single ionization collision between an O^{q+} ion and H_2 as a function of ejected electron energy (eV). The ion has an incident energy of 2 MeV/u. Each curve represents a different charge state from $q = 0 - 8$.

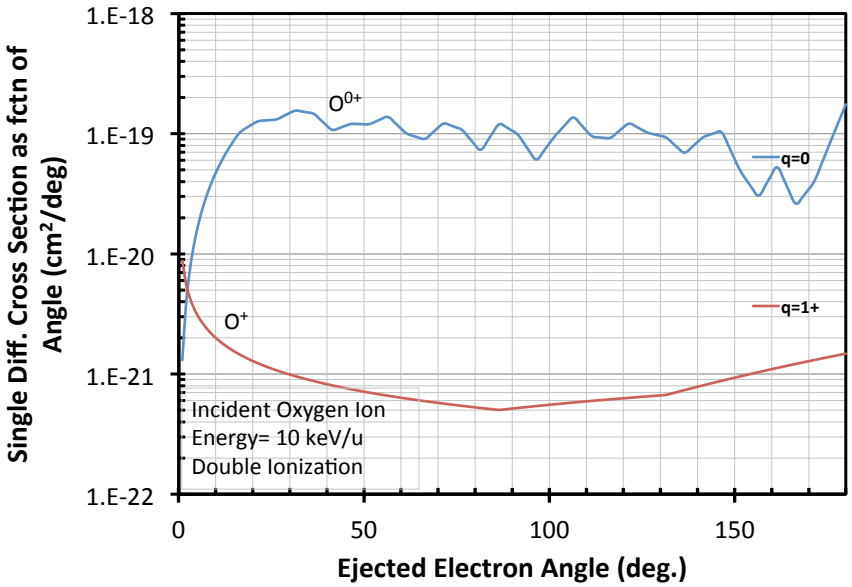

Figure 3.28: Single differential cross section as a function of ejected angle for a double ionization collision between an O^{q+} ion and H_2 as a function of ejected electron energy (eV). The ion has an incident energy of 1 keV/u. Each curve represents a different charge state from $q = 0 - 1$.

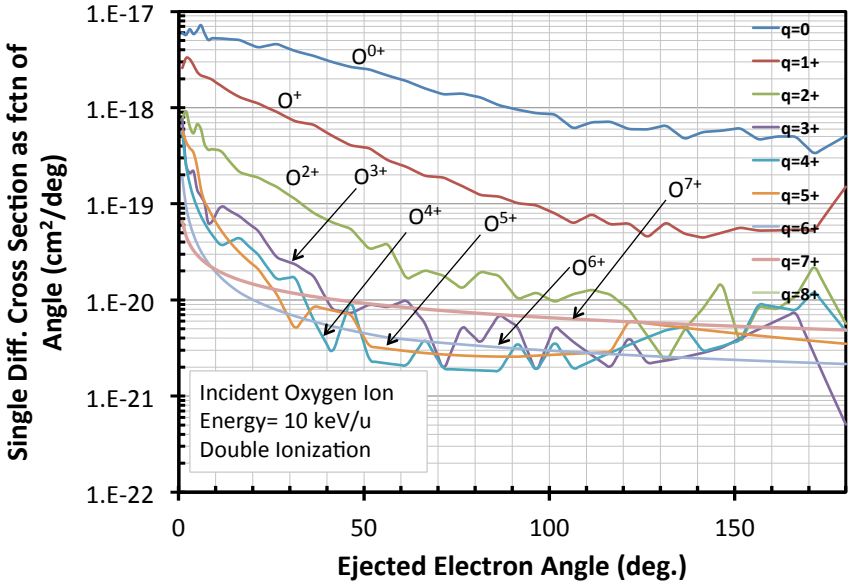

Figure 3.29: Single differential cross section as a function of ejected angle for a double ionization collision between an O^{q+} ion and H_2 as a function of ejected electron energy (eV). The ion has an incident energy of 10 keV/u. Each curve represents a different charge state from $q = 0 - 7$.

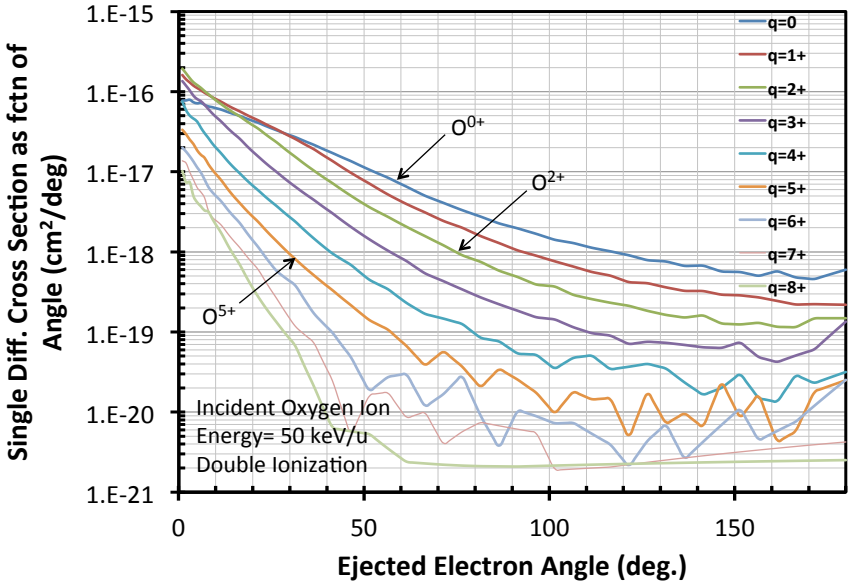

Figure 3.30: Single differential cross section as a function of ejected angle for a double ionization collision between an O^{q+} ion and H_2 as a function of ejected electron energy (eV). The ion has an incident energy of 50 keV/u. Each curve represents a different charge state from $q = 0 - 8$.

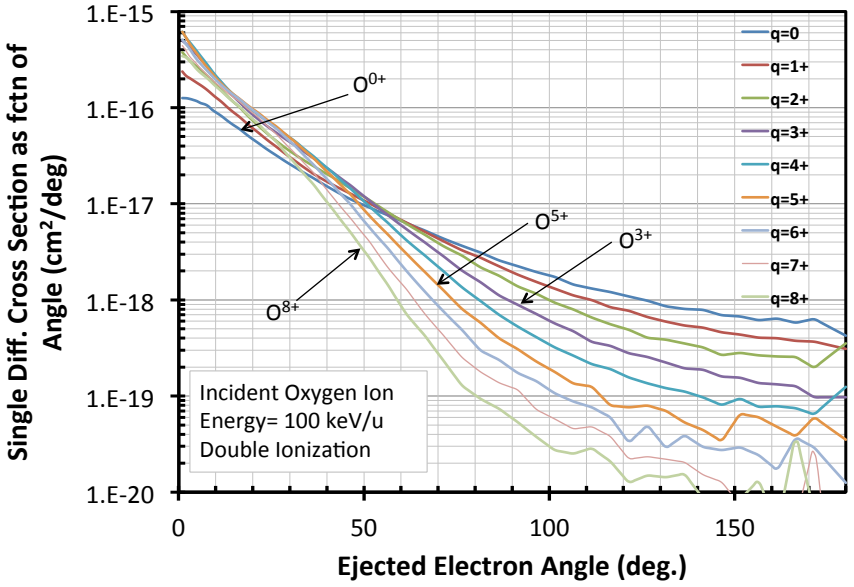

Figure 3.31: Single differential cross section as a function of ejected angle for a double ionization collision between an O^{q+} ion and H_2 as a function of ejected electron energy (eV). The ion has an incident energy of 100 keV/u. Each curve represents a different charge state from $q = 0 - 8$.

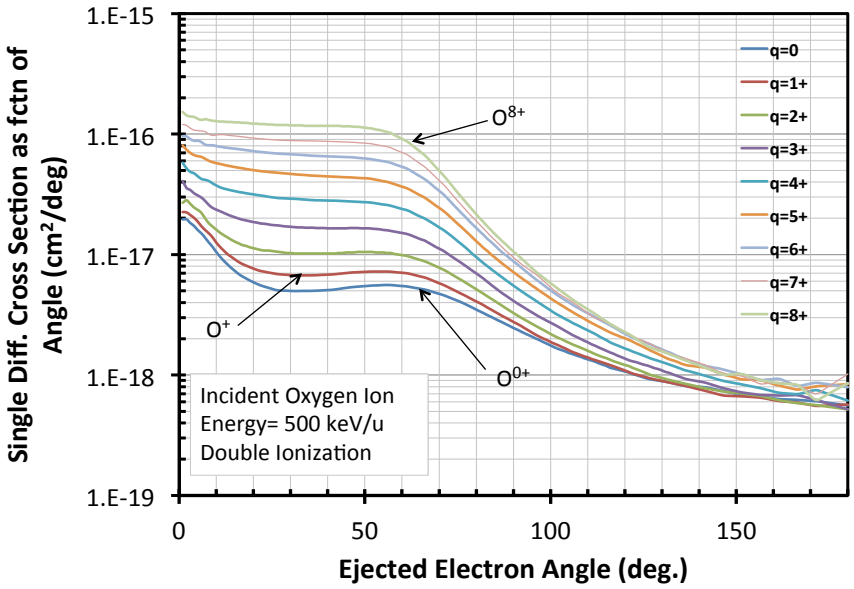

Figure 3.32: Single differential cross section as a function of ejected angle for a double ionization collision between an O^{q+} ion and H_2 as a function of ejected electron energy (eV). The ion has an incident energy of 500 keV/u. Each curve represents a different charge state from $q = 0 - 8$.

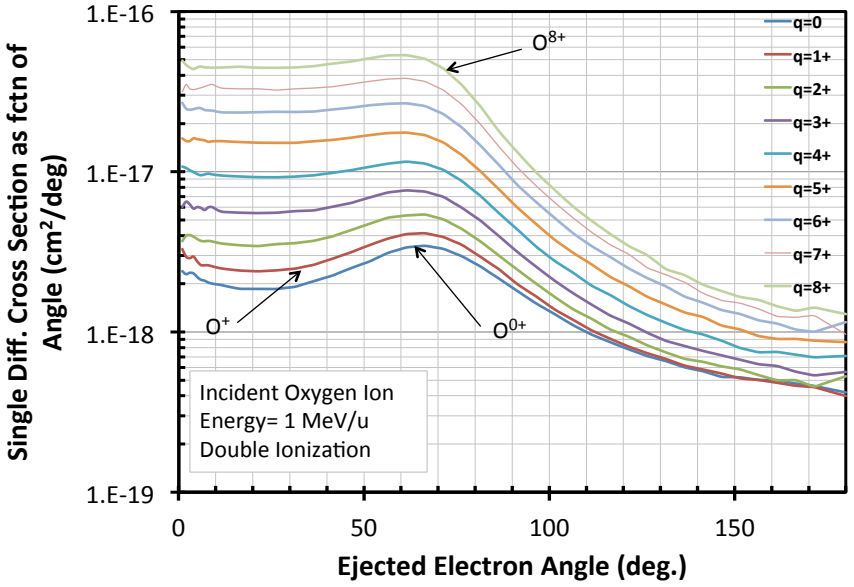

Figure 3.33: Single differential cross section as a function of ejected angle for a double ionization collision between an O^{q+} ion and H_2 as a function of ejected electron energy (eV). The ion has an incident energy of 1 MeV/u. Each curve represents a different charge state from $q = 0 - 8$.

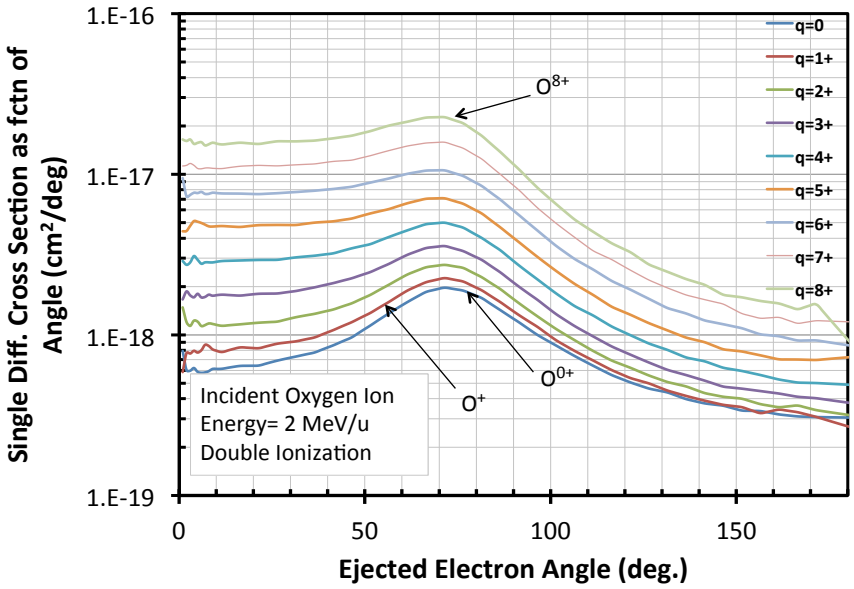

Figure 3.34: Single differential cross section as a function of ejected angle for a double ionization collision between an O^{q+} ion and H_2 as a function of ejected electron energy (eV). The ion has an incident energy of 2 MeV/u. Each curve represents a different charge state from $q = 0 - 8$.

We have calculated the ratio of forward scattering over backward scattering with these cross sections. To simplify this calculation, we have assumed that all the ejected electrons with an angle smaller than 90° are considered to go forward and those with a greater angle will scatter backward. We then integrate the cross section for all the forward angles (0° to 90°) for each charge state and for each initial ion energy, and divide by the total cross section, i.e., the integral over all angles 0° to 90°. This gives us the fraction of electrons that will scatter forward. However, this is only an approximation as the real scenario would use a double differential cross section, which would have the angular and energy dependance together. For example, an electron ejected in a collision occurring along a magnetic field line, may scatter forward and stay in the field line if its energy is low. If that same electron has high energy, it may cross field lines and cause a drift. Also, the ejected electron energy may affect the angle at which it is ejected, which is not considered in the sdxs. Because of the lack of data we will assume this to be a good approximation for our model at this time. Figures 3.35 and 3.36 show the percent of forward scattering electrons, i.e., ejected angles less than 90°, for each charge state and initial energy considered in both single and double ionization collisions.

In a single ionization collision, the figure shows that for ion energies of 50 keV/u and 100 keV/u almost 100% of the electrons will be scattered forward. For 1keV/u ions, the behavior is rather inconsistent, due to the low cross sections and statistics achieved with the CMTC calculation. However, it appears that for low charge states ($q \leq 3$) between 60% – 90% of the electrons will be scattered forward. For higher charge states almost 100% of the electrons will be scattered forward. For the higher energy ions (0.5 – 2 MeV/u) the curves follow a nice behavior, where the low charge states tend to have more backward scattering the the higher charge states. At the same time, higher ion energies appear to have a higher percentage of backward electrons at these low charge states then the lower energy ions. However, over 70% of the electrons will

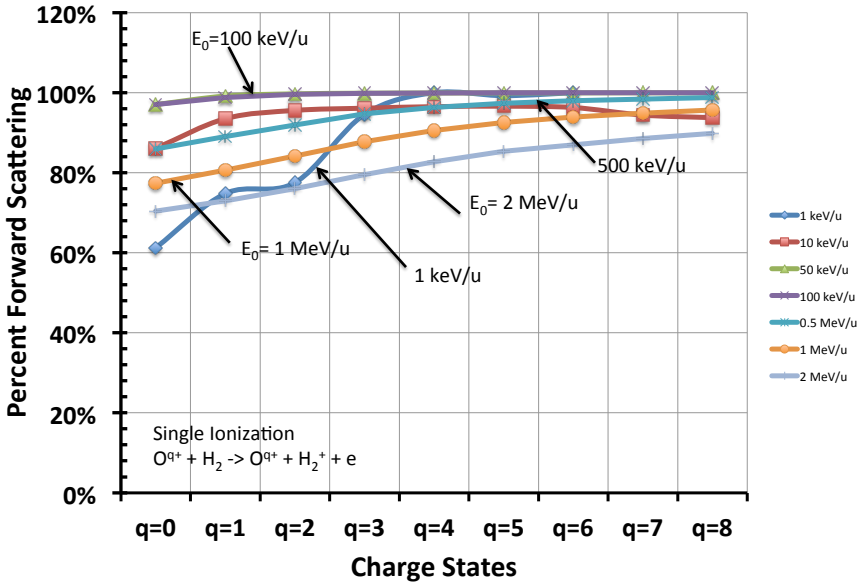

Figure 3.35: Percent of forward scattering for each charge state after a single ionization collision. By forward scattering we mean electron ejection angles less than 90°

still be scattered forward. The double ionization collisions exhibit the same behavior. The 10 keV/u ion has an irregular behavior due to the low sdxs calculated.

3.5.2 Transfer Ionization

As the ions penetrate the atmosphere they loose energy mainly by ionization collisions with the neutrals. As they slow down, charge transfer becomes the dominant process. For these lower energies other ionization channels become important besides single and double ionization. Transfer ionization is one of these channels and it is therefore included in ion precipitation model (see Chapters 4 and 6) our model for ion energies

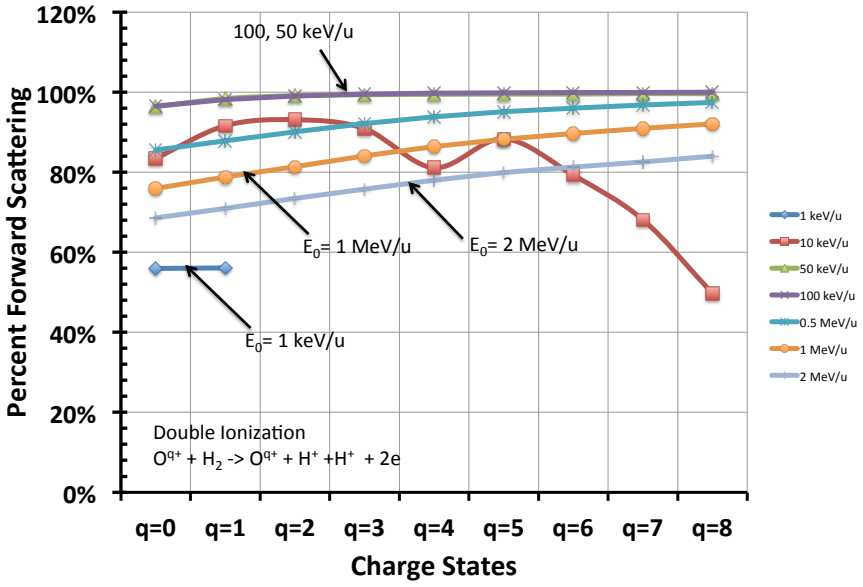

Figure 3.36: Percent of forward scattering for each charge state after a double ionization collision. By forward scattering we mean electron ejection angles less than 90°

below 100 keV/u and greater than 1 keV/u. Transfer ionization is actually a type of charge transfer, where the target (in our case H_2) dissociates and ionizes. One of the "ejected" electrons is captured or transferred to the projectile (oxygen in our case) and the other electron remains free. For example:

$$O^{q+} + H_2 \rightarrow O^{(q-1)} + 2H^+ + e \tag{3.10}$$

We have calculated the single differential cross sections (sdxs) as a function of energy and angle for such process by the same CTMC methodology as mentioned above. Figures 3.37 to 3.40 show the sdxs that will be used in the energetic ion precipitation model seen in later chapters. We have also calculated the sdxs as a function of angle for transfer ionization and the results are shown in Figures 3.41 to 3.44.

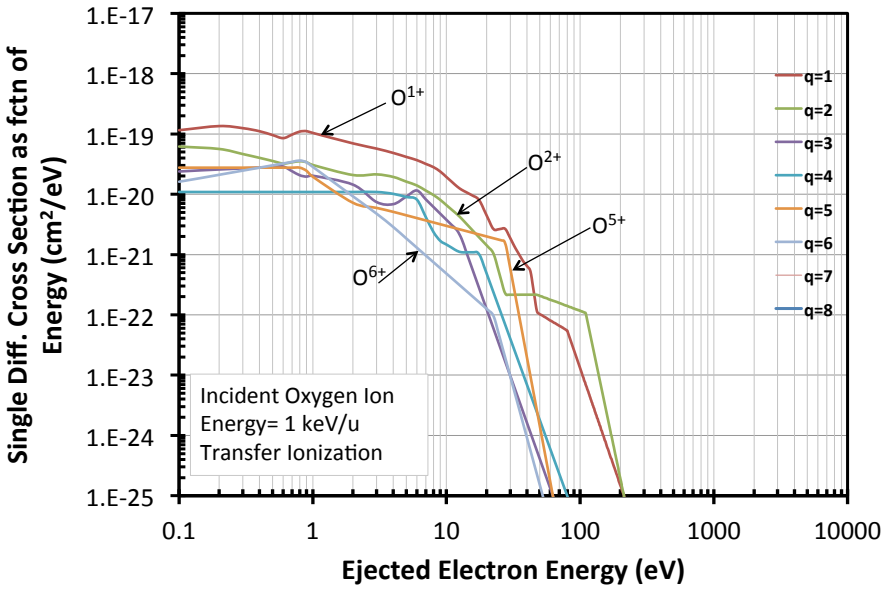

Figure 3.37: Single differential cross section as a function of ejected electron energy for a transfer ionization collision between an O^{q+} ion and H_2 as a function of ejected electron energy (eV). The ion has an incident energy of 1 keV/u. Each curve represents a different charge state from $q = 1 - 6$. Highest charge states have a very small sdxs and they are not shown.

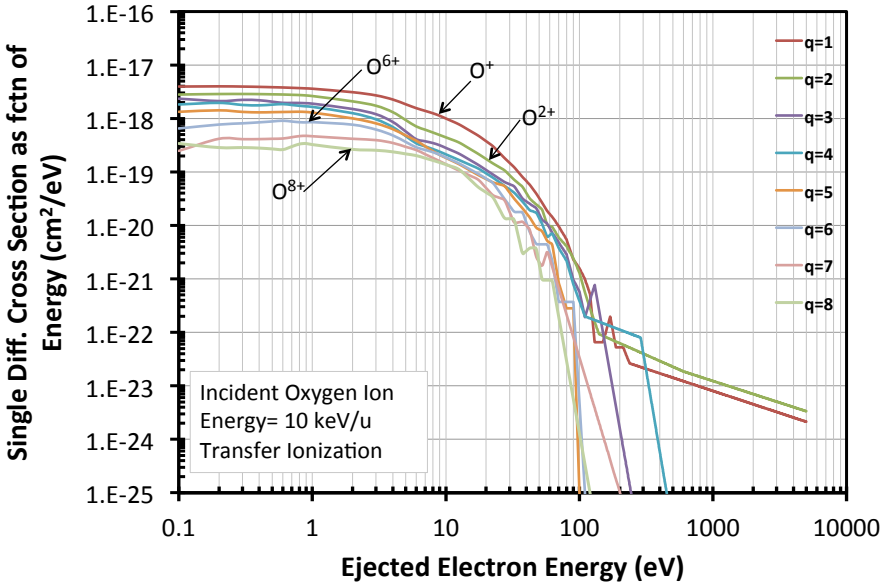

Figure 3.38: Single differential cross section as a function of ejected electron energy for a transfer ionization collision between an O^{q+} ion and H_2 as a function of ejected electron energy (eV). The ion has an incident energy of 10 keV/u. Each curve represents a different charge state from $q = 1 - 8$.

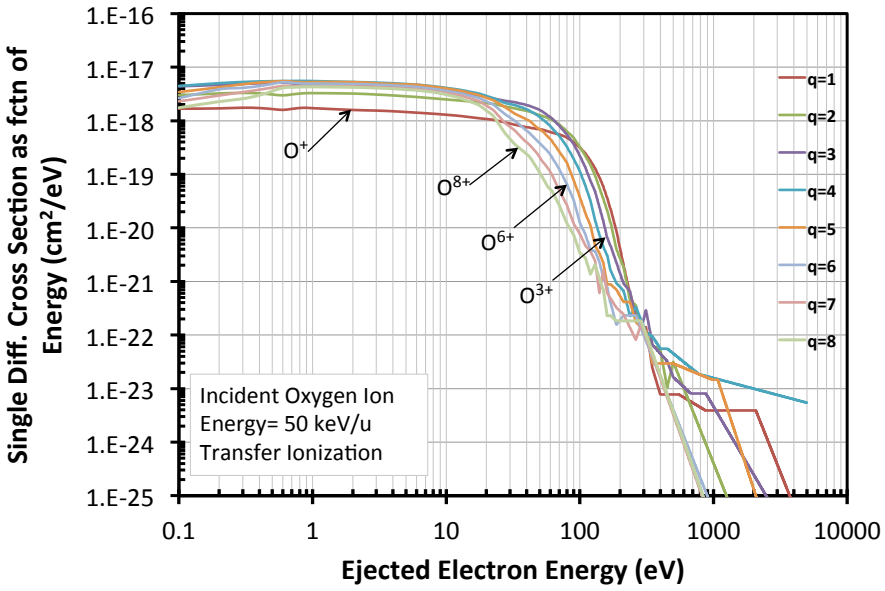

Figure 3.39: Single differential cross section as a function of ejected electron energy for a transfer ionization collision between an O^{q+} ion and H_2 as a function of ejected electron energy (eV). The ion has an incident energy of 50 keV/u. Each curve represents a different charge state from $q = 1 - 8$.

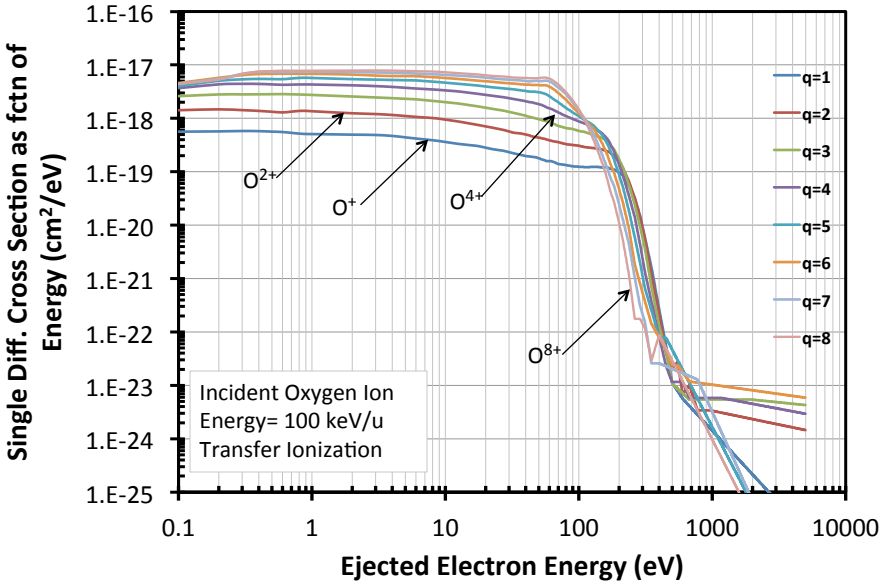

Figure 3.40: Single differential cross section as a function of ejected electron energy for a transfer ionization collision between an O^{q+} ion and H_2 as a function of ejected electron energy (eV). The ion has an incident energy of 100 keV/u. Each curve represents a different charge state from $q = 1 - 8$.

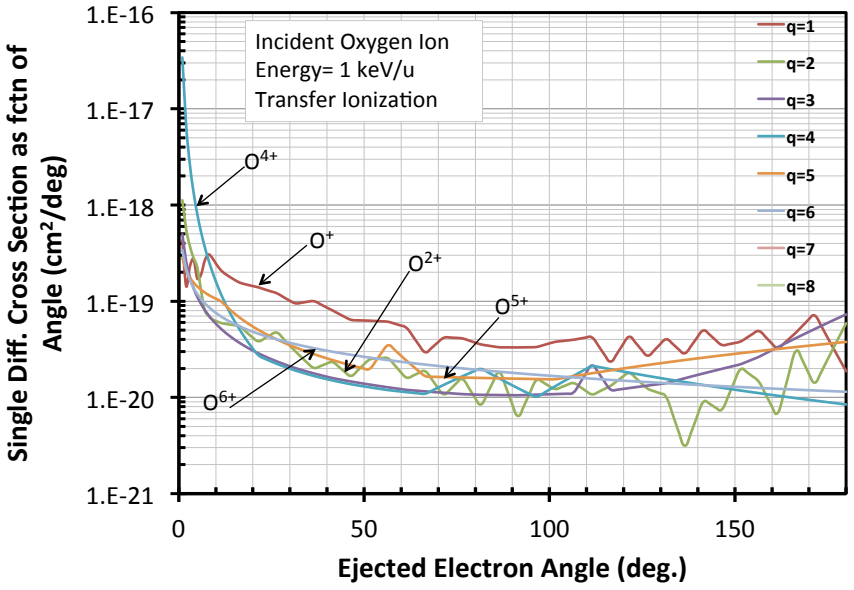

Figure 3.41: Single differential cross section as a function of ejected angle for a transfer ionization collision between an O^{q+} ion and H_2 as a function of ejected electron energy (eV). The ion has an incident energy of 1 keV/u. Each curve represents a different charge state from $q = 1 - 6$. Higher charge states have a very low sdxs and are not shown.

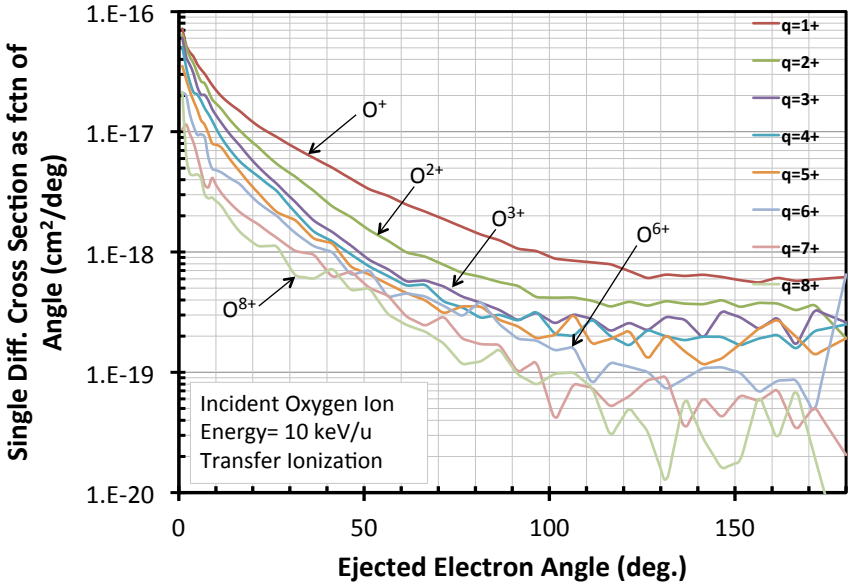

Figure 3.42: Single differential cross section as a function of ejected angle for a transfer ionization collision between an O^{q+} ion and H_2 as a function of ejected electron energy (eV). The ion has an incident energy of 10 keV/u. Each curve represents a different charge state from $q = 1 - 8$.

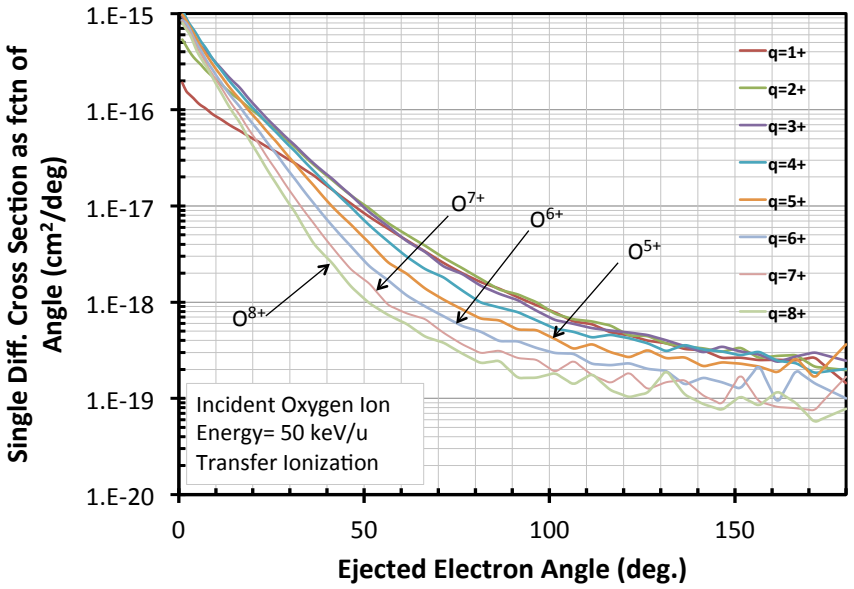

Figure 3.43: Single differential cross section as a function of ejected angle for a transfer ionization collision between an O^{q+} ion and H_2 as a function of ejected electron energy (eV). The ion has an incident energy of 50 keV/u. Each curve represents a different charge state from $q = 1 - 8$.

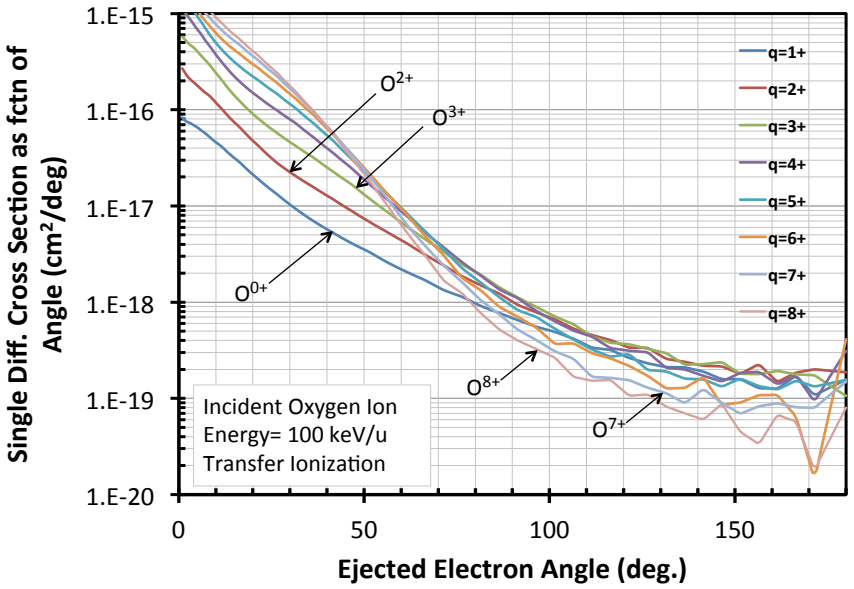

Figure 3.44: Single differential cross section as a function of ejected angle for a transfer ionization collision between an O^{q+} ion and H_2 as a function of ejected electron energy (eV). The ion has an incident energy of 100 keV/u. Each curve represents a different charge state from $q = 1 - 8$.

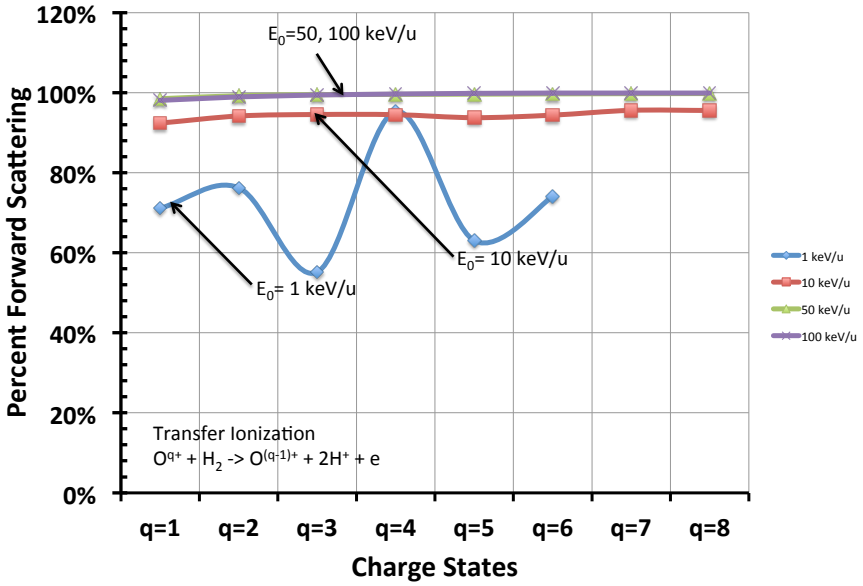

Figure 3.45: Percent of forward scattering for each charge state after a transfer ionization collision. By forward scattering we mean electron ejection angles less than 90°

As mentioned previously, an important piece for our model is to be able to determine the directionality of the ejected electron, i.e. whether it was ejected forward or backward. We have calculated this percentage for transfer ionization, as explained previously. Please see Figure 3.45 for the results. For ion energies of 100, 50 and 10 keV/u over 90% of the electrons are scattered forward in a transfer ionization collision for all charge states. However, for 1 keV/u it is hard to determine the behavior due to the small cross sections. However, on average for all charge states about 70% of the electrons will be scattered forward for this low energy.

3.5.3 Double Capture Auto–Ionization

Another important ionization channel that is included in our model for low ion energies (below 100 keV/u) is double capture auto-ionization or DCAI. This is also a charge transfer process. In such a collision, the projectile first captures two electrons from the target (H_2). Often the two electrons are in an excited state, so they can auto-ionize by having one electron drop to a lower energy level (usually the ground state) and the other electron ionizes conserving energy. For example:

$$O^{q+} + H_2 \rightarrow O^{(q-2)} + 2H^+ \rightarrow O^{(q-1)} + 2H^+ + e \tag{3.11}$$

The ionization (or to be more specific, auto-ionization) occurs on the projectile as it scatters away from the target. Therefore the electron that is ejected from such an interaction is boosted by the projectile velocity. We have calculated the single differential cross sections for such process by the same CTMC methodology used for the other cross sections. Figures 3.46 to 3.49 show the sdxs that will be used to determine the ejected electron energies given such process. Only charges $q = 2-8$ are considered in the model as calculating this cross section for a O^+ is too complicated with the current tools. The figures show a large peak where the energy of the electron has been boosted by the projectile.

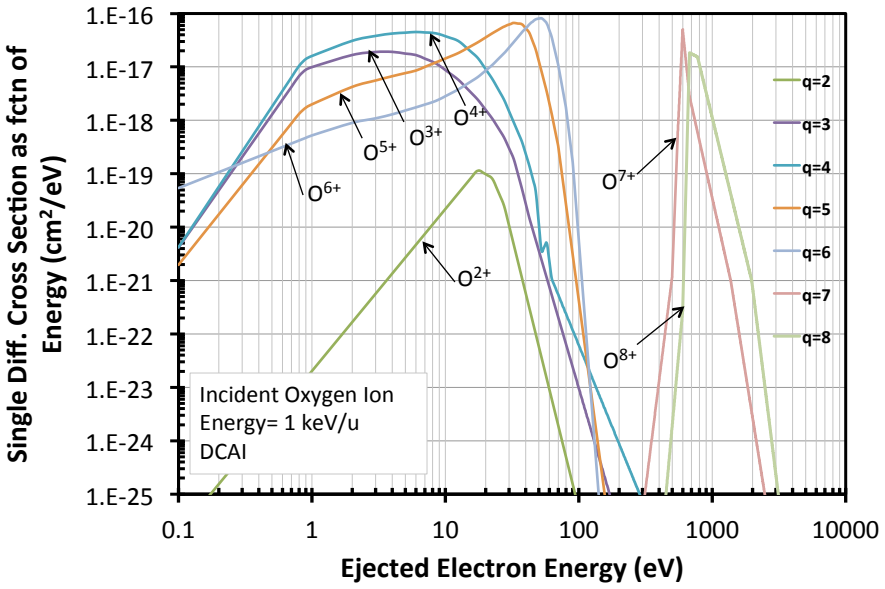

Figure 3.46: Single differential cross section as a function of ejected electron energy for a double capture auto-ionization (DCAI) collision between an O^{q+} ion and H_2 as a function of ejected electron energy (eV). The ion has an incident energy of 1 keV/u. Each curve represents a different charge state from $q = 2 - 8$.

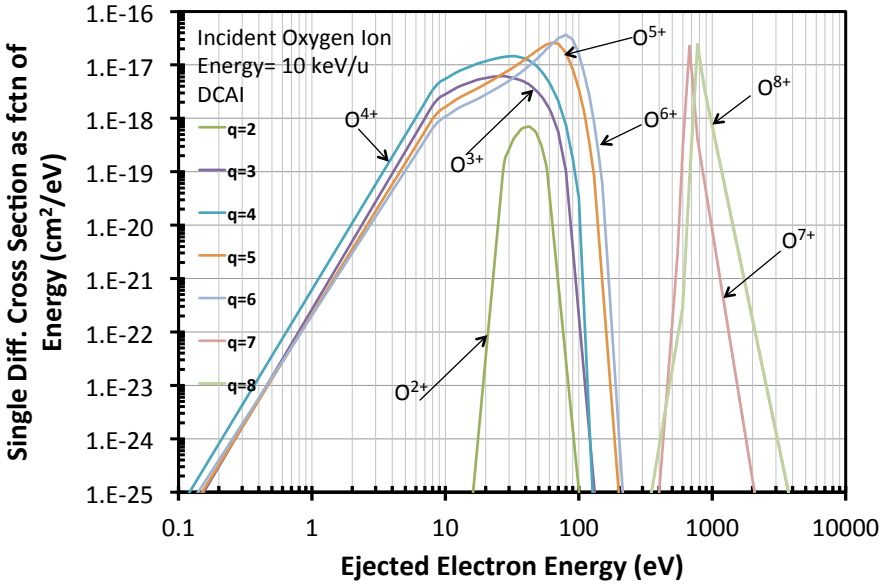

Figure 3.47: Single differential cross section as a function of ejected electron energy for a DCAI collision between an O^{q+} ion and H_2 as a function of ejected electron energy (eV). The ion has an incident energy of 10 keV/u. Each curve represents a different charge state from $q = 2-8$.

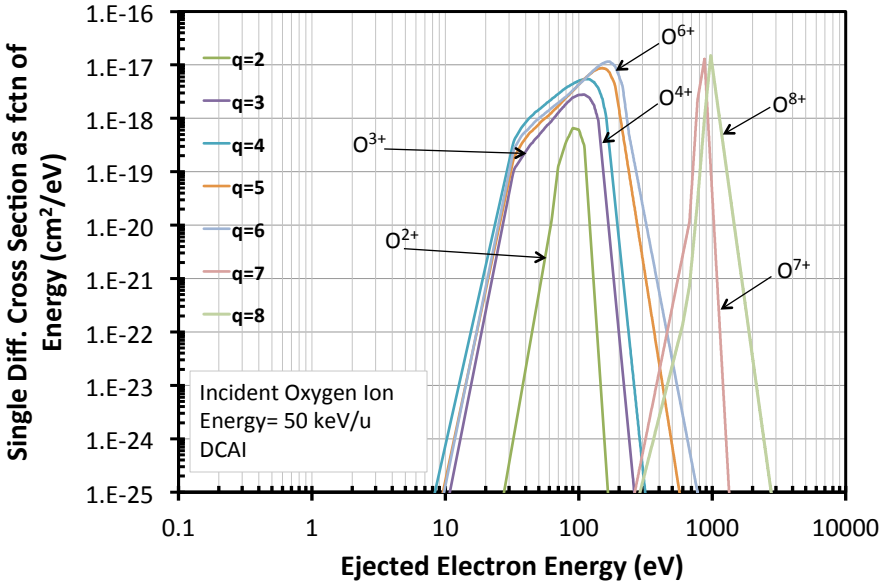

Figure 3.48: Single differential cross section as a function of ejected electron energy for a DCAI collision between an O^{q+} ion and H_2 as a function of ejected electron energy (eV). The ion has an incident energy of 50 keV/u. Each curve represents a different charge state from $q = 2-8$.

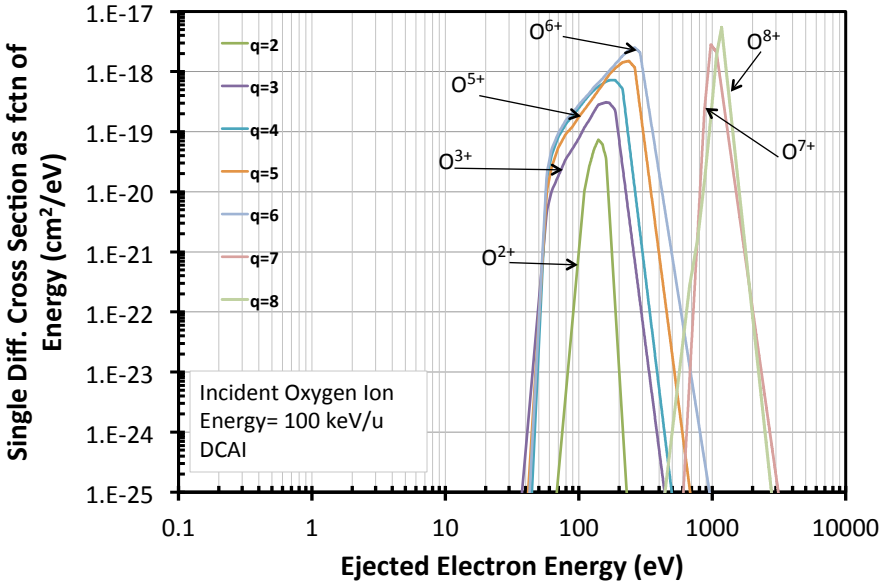

Figure 3.49: Single differential cross section as a function of ejected electron energy for a DCAI collision between an O^{q+} ion and H_2 as a function of ejected electron energy (eV). The ion has an incident energy of 100 keV/u. Each curve represents a different charge state from $q = 2-8$.

Just like with the other processes we have calculated the sdxs as a function of electron ejection angle for a dcai collision. These are shown in Figures 3.50 to 3.53. It is interesting to see that the sdxs as a function of angle exhibit two small peaks around 40-50° and 130°. As we increase the charge state the cross section increases. We also calculated the fraction of electrons that are scattered forward in a dcai collision. Figure 3.54 shows the results. The behavior for this collision is different than for the other ionization collisions. In a DCAI collision, it appears that, in general, in a collision with an ion with a lower charge state tend to have a higher fraction of electrons that scatter forward. Higher charge ions have a higher fraction the is scattered backward. For example, for a 100 keV/u ion at a low charge state (q=2) almost 90% of the electrons are scattered forward. However, for the same ion energy, but at a high charge state (q=7 or 8) only about 65% of the electrons are scattered forward. This behavior can be understood by looking at the plots of the sdxs as a function of angle. As mentioned before, there are two peaks for these cross section curves. One of them is around 130°. This peak is even higher for the high charge states of the ions, which explains why they are more likely to contribute backward scattered electrons than the lower charge states do.

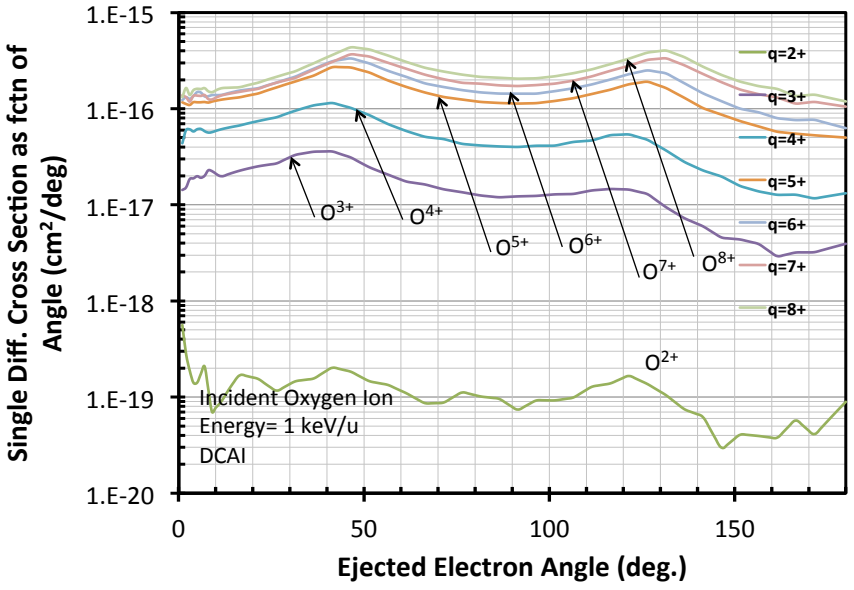

Figure 3.50: Single differential cross section as a function of ejected angle for a DCAI ionization collision between an O^{q+} ion and H_2 as a function of ejected electron energy (eV). The ion has an incident energy of 1 keV/u. Each curve represents a different charge state from $q = 2 - 8$. Higher charge states have a very low sdxs and are not shown.

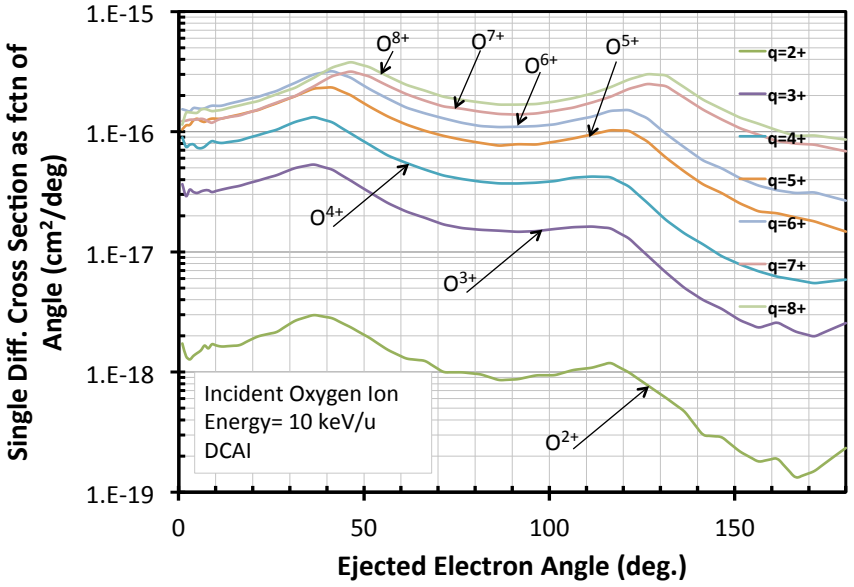

Figure 3.51: Single differential cross section as a function of ejected angle for a DCAI ionization collision between an O^{q+} ion and H_2 as a function of ejected electron energy (eV). The ion has an incident energy of 10 keV/u. Each curve represents a different charge state from $q = 2-8$.

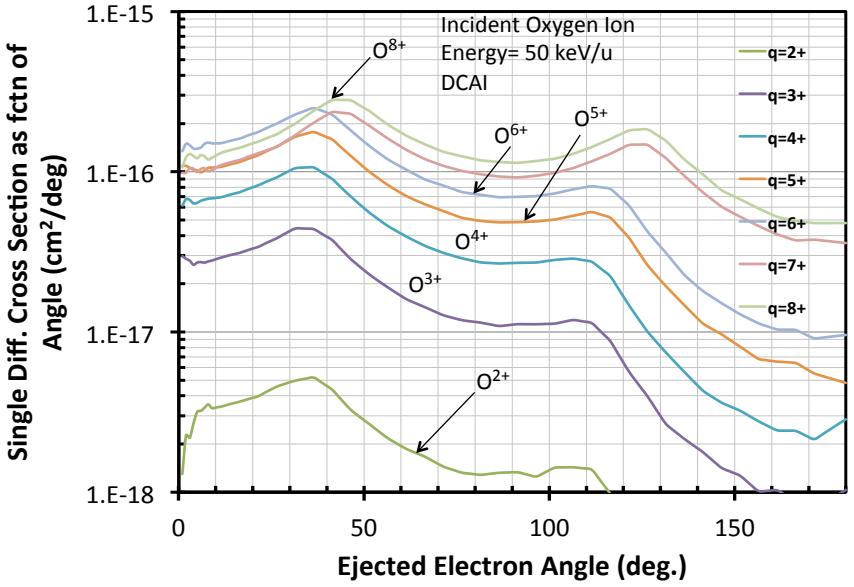

Figure 3.52: Single differential cross section as a function of ejected angle for a DCAI ionization collision between an O^{q+} ion and H_2 as a function of ejected electron energy (eV). The ion has an incident energy of 50 keV/u. Each curve represents a different charge state from $q = 2-8$.

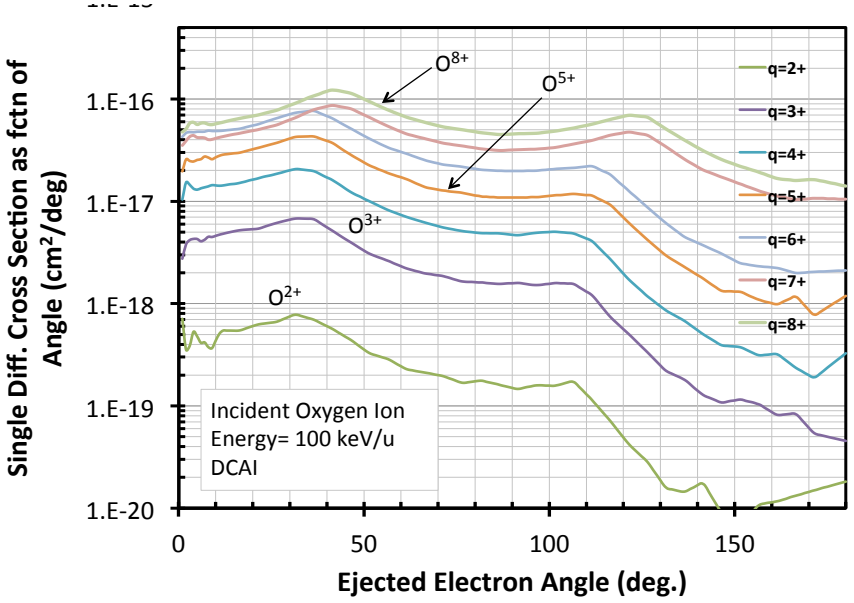

Figure 3.53: Single differential cross section as a function of ejected angle for a DCAI ionization collision between an O^{q+} ion and H_2 as a function of ejected electron energy (eV). The ion has an incident energy of 100 keV/u. Each curve represents a different charge state from $q = 2-8$.

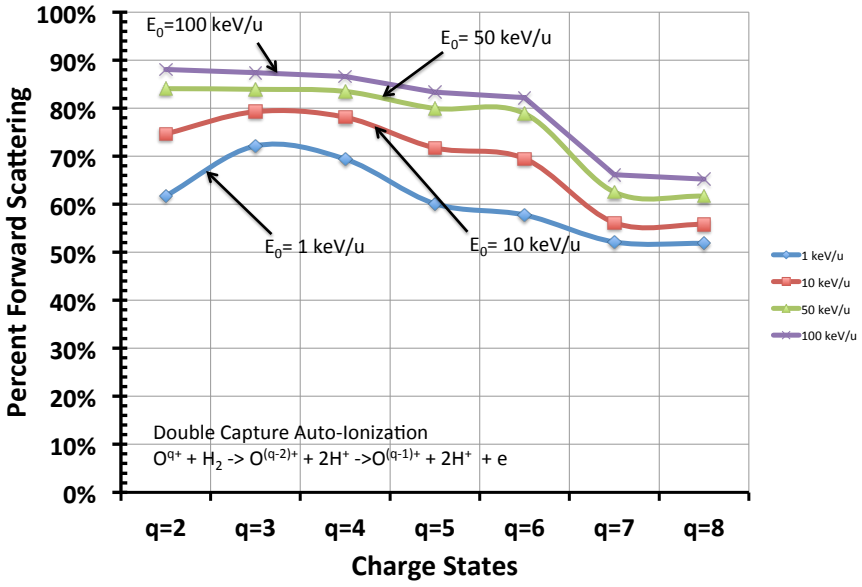

Figure 3.54: Percent of forward scattering for each charge state after a DCAI ionization collision. By forward scattering we mean electron ejection angles less than 90°

3.5.4 Single Differential Cross Section for Stripping Collisions

Calculating the stripping cross sections required multi electron models because for this type of collision the ejected electrons come from the projectile and not the target. This required complicated the calculations and proved to be more time consuming than the ionization cross section calculations. For example, $O^{2+}(1s^2 2s^2 2p^2)$ had to be treated as a 4-electron calculation since the outer four electrons needed to be present in order to get not only the double stripping calculation right, but also the single stripping. The 1s electrons could, in this case, be ignored since they would not be stripped off with any significant probability when there were four more loosely bound electrons. The single stripping cross section is modeled better by having the available electrons with equal binding energies (the so called inCTMC model, "i" independent electron, "n" for n-electrons). Another important remark on the calculation of the stripping sdxs is that the object doing the stripping is modeled as H and not H_2. With the limited experimental data for stripping that exists, we have found this approximation to be reasonable. To make a model taking the full H_2 molecule into account would be a really big project and the code would run so slow that the calculations would be infeasible without using a large computer cluster. Such calculations are not feasible for the present work and will be addressed in a future project.

The single differential cross sections for stripping are considerably smaller than those for ionization collisions. However, they are important to the contribution of higher energy electrons. In a stripping collision, the projectile (in our case the oxygen) is ionized. Therefore, the ejected electrons will have a boost that corresponds to the projectile energy when measured in the lab frame and their sdxs will peak at that corresponding energy. This energy can be found by taking the initial ion energy and then dividing it by the ion to electron mass ratio (1836). For example, the peak for the

sdxs for a 500 keV/u oxygen ion is expected to be at an energy of 272 eV, for a 1 MeV/u ion, the peak is expected at 545 eV, and for a 2 MeV/u ion the peak is expected at 1090 eV. Therefore, the stripping cross sections extend to much higher ejected electron energies than the ionization cross sections, due to the projectile velocity boost. Figures 3.55 to 3.57 present the calculated sdxs for single stripping of oxygen ions in H_2. Similarly to the target ionization, projectile ionization may produce two free electrons after each collision. This is referred to a double stripping collision and is also considered in our models. Because the specifics on the calculations go beyond the topic of this paper, we will only present the results of the CMTC calculation for the double stripping cross sections that are used in our model. Only the charge states $q = 1 - 6$ will undergo double stripping. These single differential cross sections are shown in Figures 3.58 to 3.60. The procedure to calculate these cross sections is more involved than those for ionization, as mentioned earlier. Therefore, the number of ions needed to build enough statistics is very high. Some of the curves obtained have a lower count of statistics and are a little uncertain, especially for the higher charge states and for low energies. However, we have tried our best to obtain a reasonable behavior in the curves.

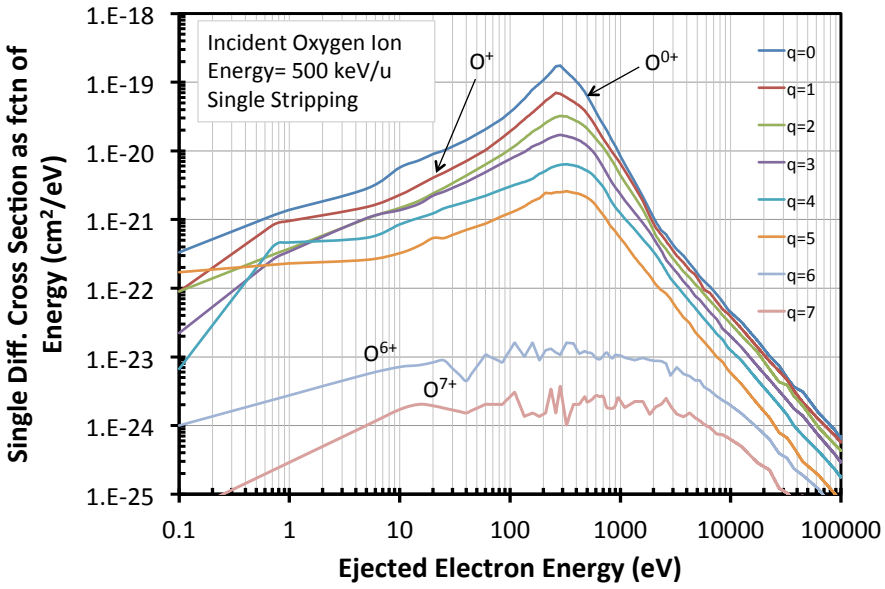

Figure 3.55: Single differential cross section as a function of ejected angle for a single stripping collision between an O^{q+} ion and H_2 as a function of ejected electron energy (eV). The ion has an incident energy of 500 keV/u. Each curve represents a different charge state from $q = 0 - 7$.

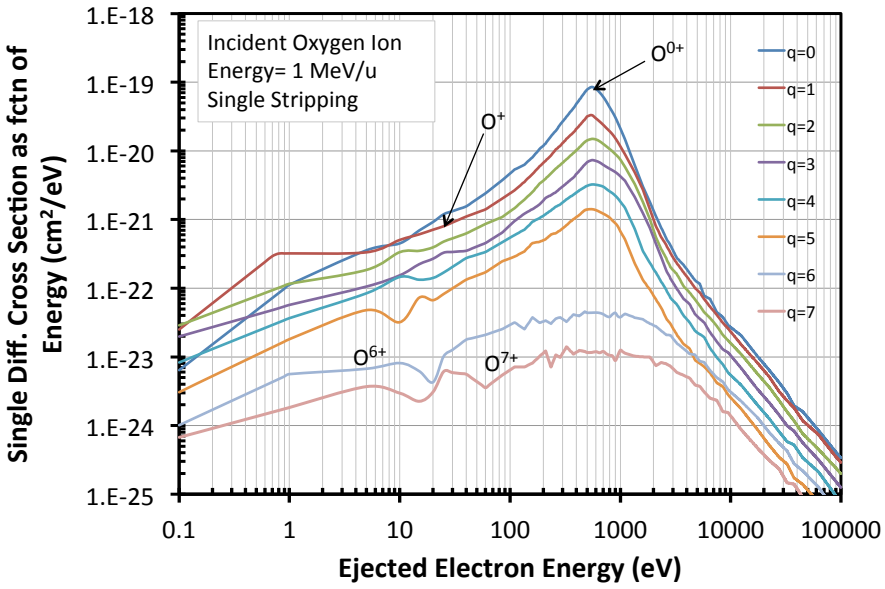

Figure 3.56: Single differential cross section as a function of ejected angle for a single stripping collision between an O^{q+} ion and H_2 as a function of ejected electron energy (eV). The ion has an incident energy of 1 MeV/u. Each curve represents a different charge state from $q = 0 - 7$.

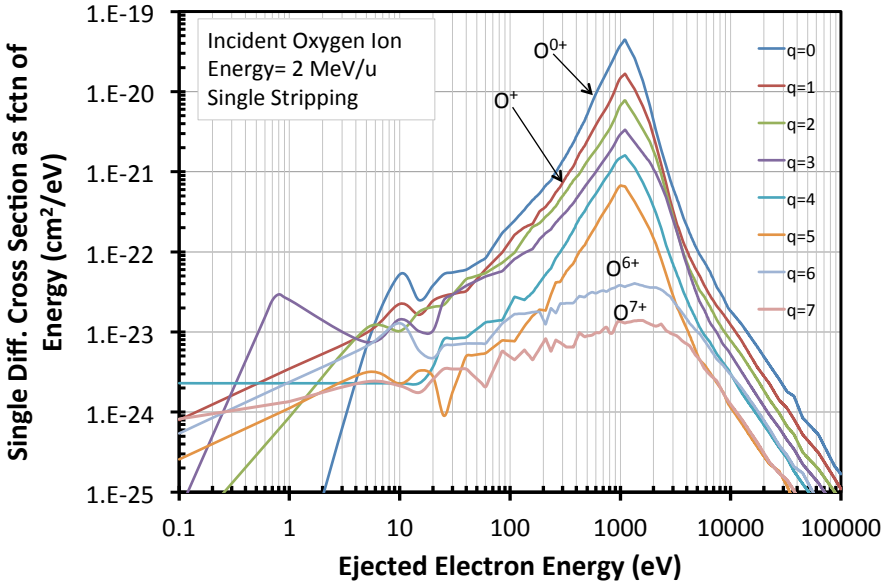

Figure 3.57: Single differential cross section as a function of ejected angle for a single stripping collision between an O^{q+} ion and H_2 as a function of ejected electron energy (eV). The ion has an incident energy of 2 MeV/u. Each curve represents a different charge state from $q = 0 - 7$.

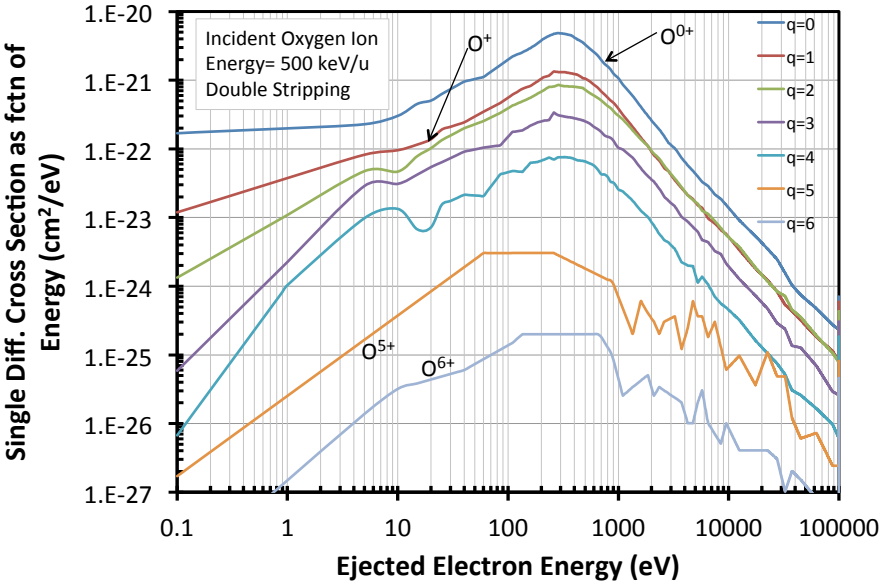

Figure 3.58: Single differential cross section as a function of ejected angle for a double stripping collision between an O^{q+} ion and H_2 as a function of ejected electron energy (eV). The ion has an incident energy of 500 keV/u. Each curve represents a different charge state from $q = 0 - 6$.

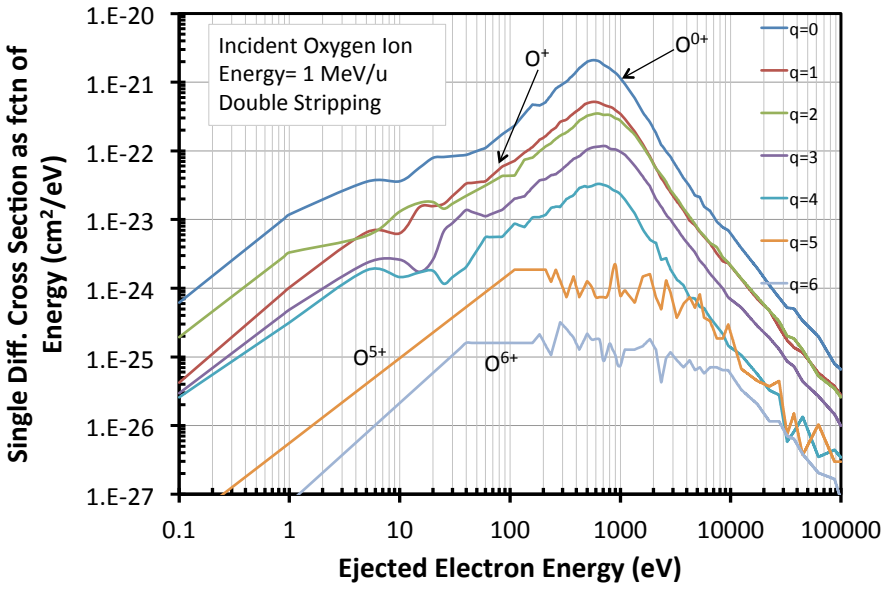

Figure 3.59: Single differential cross section as a function of ejected angle for a double stripping collision between an O^{q+} ion and H_2 as a function of ejected electron energy (eV). The ion has an incident energy of 1 MeV/u. Each curve represents a different charge state from $q = 0 - 6$.

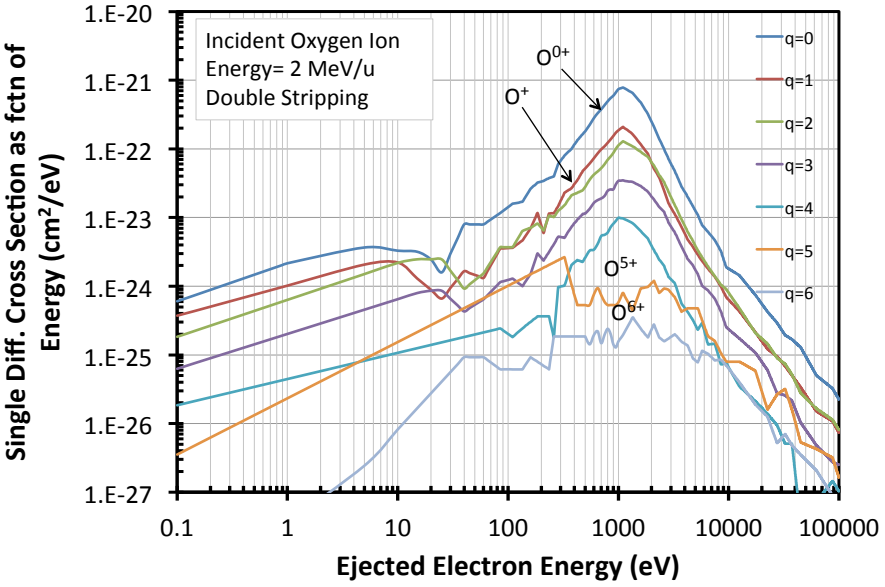

Figure 3.60: Single differential cross section as a function of ejected angle for a double stripping collision between an O^{q+} ion and H_2 as a function of ejected electron energy (eV). The ion has an incident energy of 2 MeV/u. Each curve represents a different charge state from $q = 0 - 6$.

3.5.5 Electron Energy Distributions

The main purpose of calculating the single differential cross sections for the present project is to be able to obtain the energy distribution of the secondary electrons ejected by the ion-neutral collision between the oxygen ions and hydrogen molecules present in the Jovian atmosphere. We calculated the probability of ejecting an electron with an energy greater than or equal to E_s by the following equation:

$$f = 1 - \frac{\int_0^{E_s} (d\sigma/dE) dE}{\int_0^{\infty} (d\sigma/dE) dE}.$$

Here, f is the fraction (or probability) of ejected electrons with energy E_s (or greater). $d\sigma/dE$ is the single differential cross section (for single or double ionization) as a function of ejected electron energy E_s. This fraction is calculated for each charge state and for each incoming oxygen ion energy (1, 10, 50, 100, 500 keV/u, 1 MeV/u and 2 MeV/u) as available from the data. Figures 3.61 to 3.67 show the distributions for single ionization collisions and Figures 3.68 to 3.74 show the distributions for double ionization collisions. The same procedure was used to calculate the distribution of ejected electrons for all other collision processes considered in our model, where one or more electrons are ejected after the collision (see previous section for these processes and their cross section information). The resulting probabilities for transfer ionization are shown in Figures 3.75 to 3.78. For DCAI the distribution is shown in Figures 3.79 to 3.82.For single stripping collisions the distributions are shown in Figures 3.83 to 3.85 and for double stripping collisions are shown in Figures 3.86 to 3.88. Since the distributions depend on the single differential cross sections, the uncertainty in the cross section due to low statistics carries on to the distribution. Therefore, the distributions for 1 keV/u and sometimes even for 10 keV/u do not behave as nicely as those for higher energies.

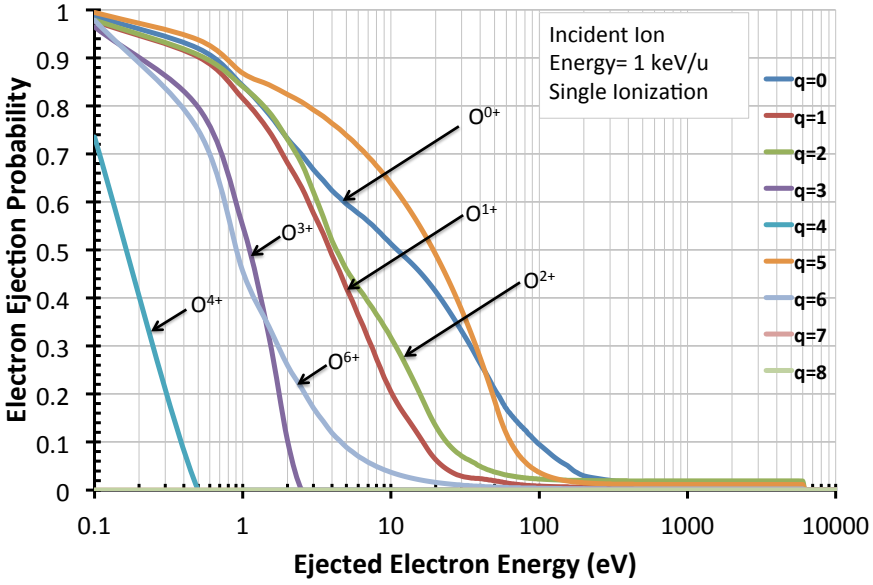

Figure 3.61: Probability of ejecting a secondary electron with energy E_s for an oxygen ion with energy $E_{ion} = 1$ keV/u, after a single ionization collision. Each curve represents a different charge state of oxygen (O^{q+}, q=0-8). See Figure 3.7 for the corresponding single differential cross sections.

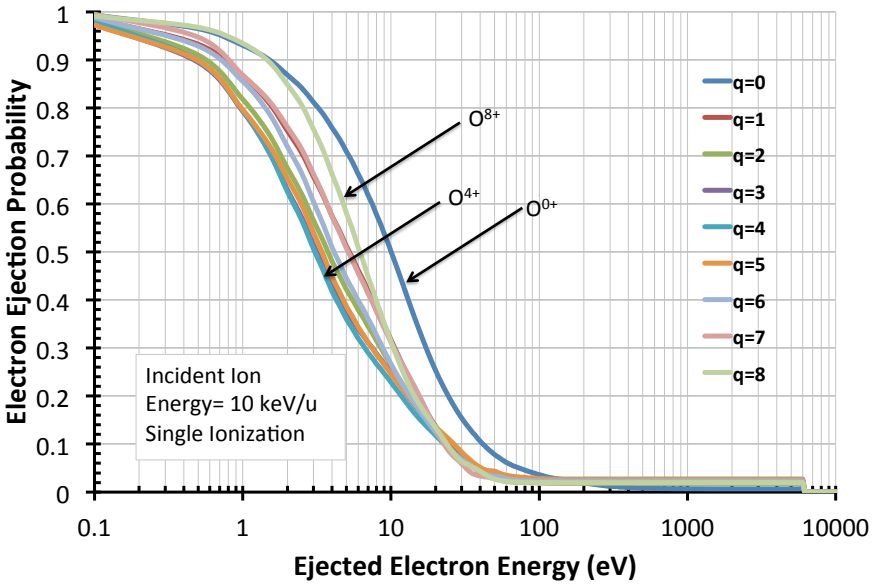

Figure 3.62: Probability of ejecting a secondary electron with energy E_s for an oxygen ion with energy $E_{ion} = 10$ keV/u, after a single ionization collision. Each curve represents a different charge state of oxygen (O^{q+}, q=0-8). See Figure 3.8 for the corresponding single differential cross sections.

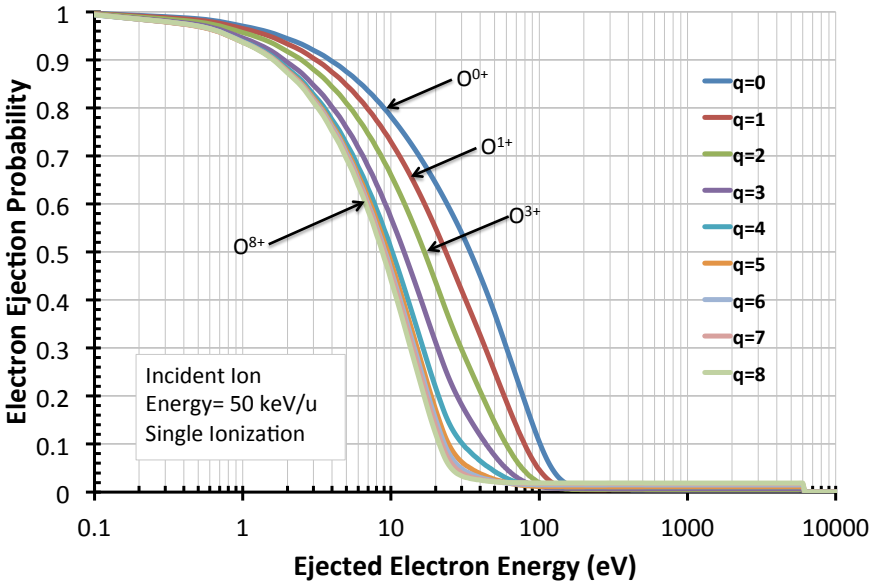

Figure 3.63: Probability of ejecting a secondary electron with energy E_s for an oxygen ion with energy $E_{ion} = 50$ keV/u, after a single ionization collision. Each curve represents a different charge state of oxygen (O^{q+}, q=0-8). See Figure 3.9 for the corresponding single differential cross sections.

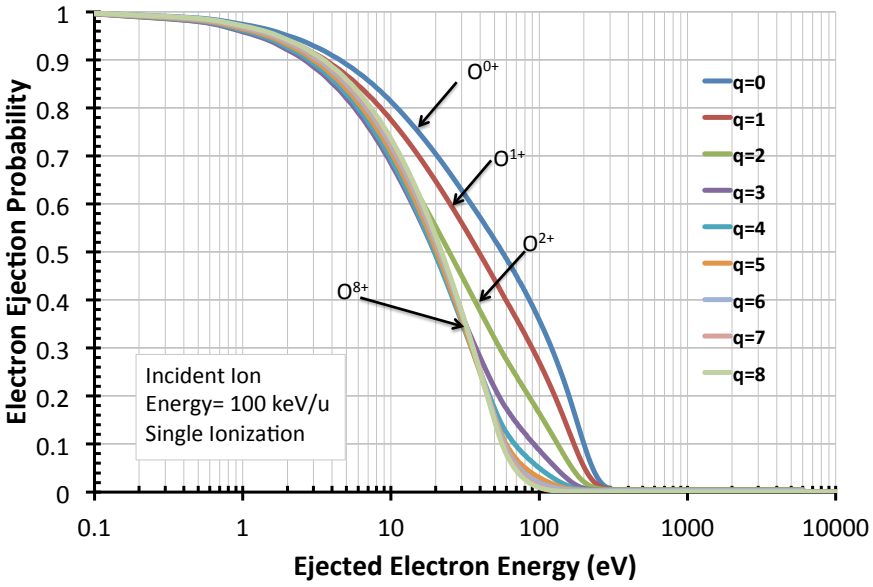

Figure 3.64: Probability of ejecting a secondary electron with energy E_s for an oxygen ion with energy $E_{ion} = 100$ keV/u, after a single ionization collision. Each curve represents a different charge state of oxygen (O^{q+}, q=0-8). See Figure 3.10 for the corresponding single differential cross sections.

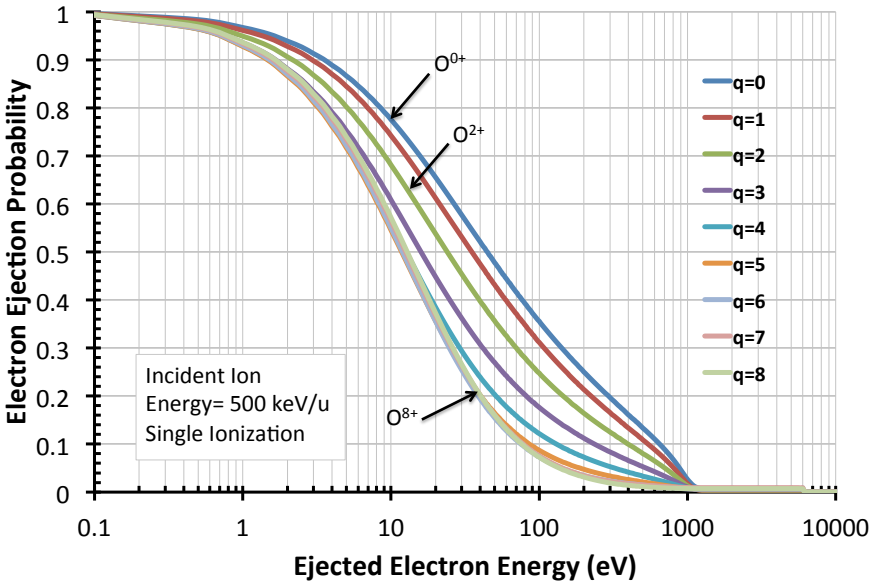

Figure 3.65: Probability of ejecting a secondary electron with energy E_s for an oxygen ion with energy $E_{ion} = 500$ keV/u, after a single ionization collision. Each curve represents a different charge state of oxygen (O^{q+}, q=1-8). See Figure 3.11 for the corresponding single differential cross sections.

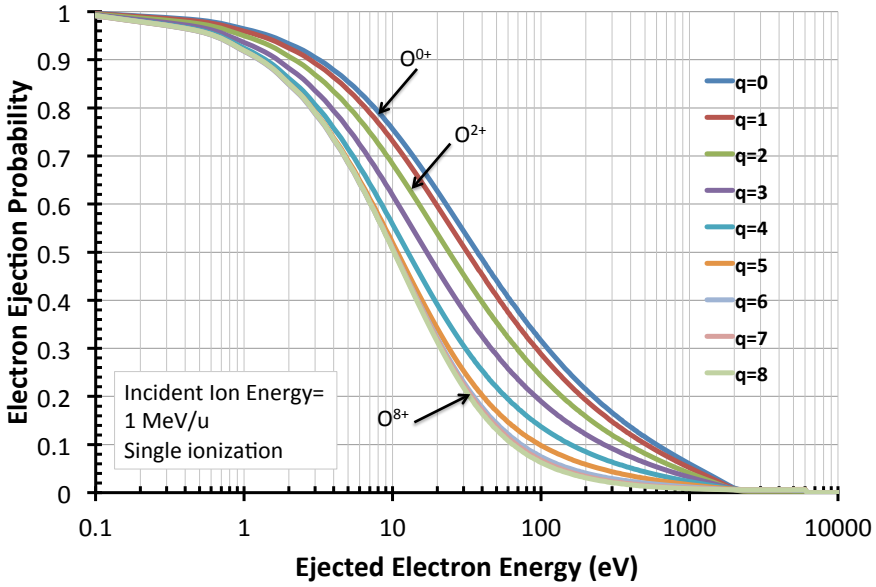

Figure 3.66: Probability of ejecting a secondary electron with energy E_s for an oxygen ion with energy $E_{ion} = 1$ MeV/u, after a single ionization collision. Each curve represents a different charge state of oxygen (O^{q+}, q=0-8). See Figure 3.12 for the corresponding single differential cross sections.

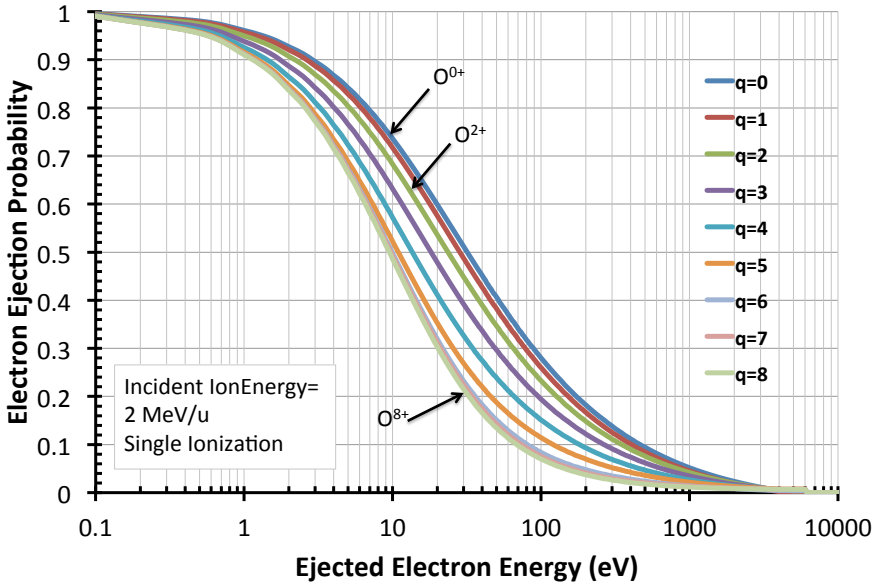

Figure 3.67: Probability of ejecting a secondary electron with energy E_s for an oxygen ion with energy $E_{ion} = 2$ MeV/u, after a single ionization collision. Each curve represents a different charge state of oxygen (O^{q+}, q=0-8). See Figure 3.13 for the corresponding single differential cross sections.

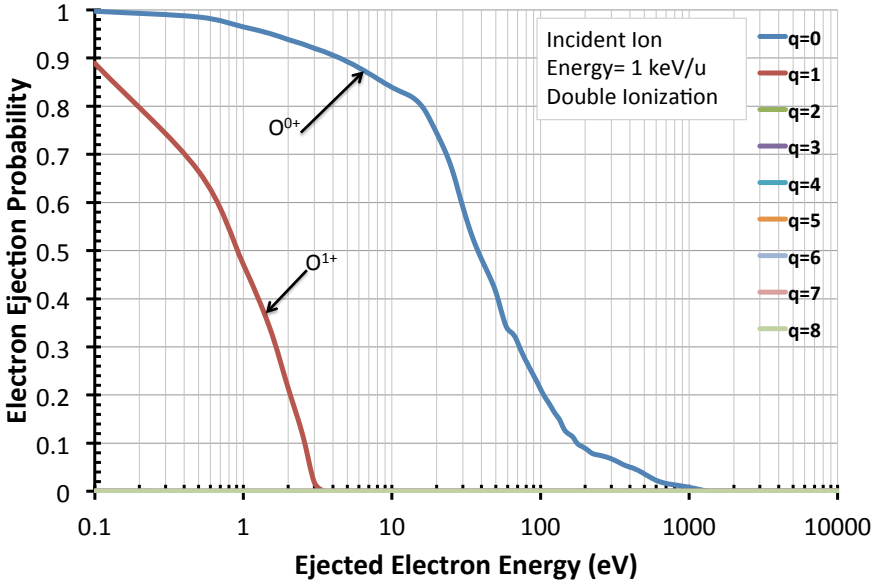

Figure 3.68: Probability of ejecting a secondary electron with energy E_s for an oxygen ion with energy $E_{ion} = 1$ keV/u, after a double ionization collision. Each curve represents a different charge state of oxygen (O^{q+}, q=0-1). See Figure 3.14 for the corresponding single differential cross sections.

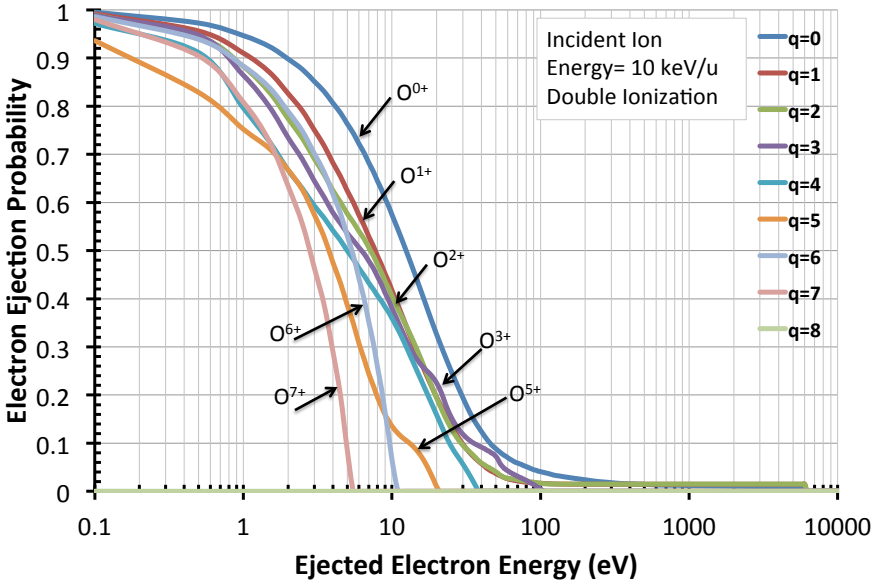

Figure 3.69: Probability of ejecting a secondary electron with energy E_s for an oxygen ion with energy $E_{ion} = 10$ keV/u, after a double ionization collision. Each curve represents a different charge state of oxygen (O^{q+}, q=0-7). See Figure 3.15 for the corresponding single differential cross sections.

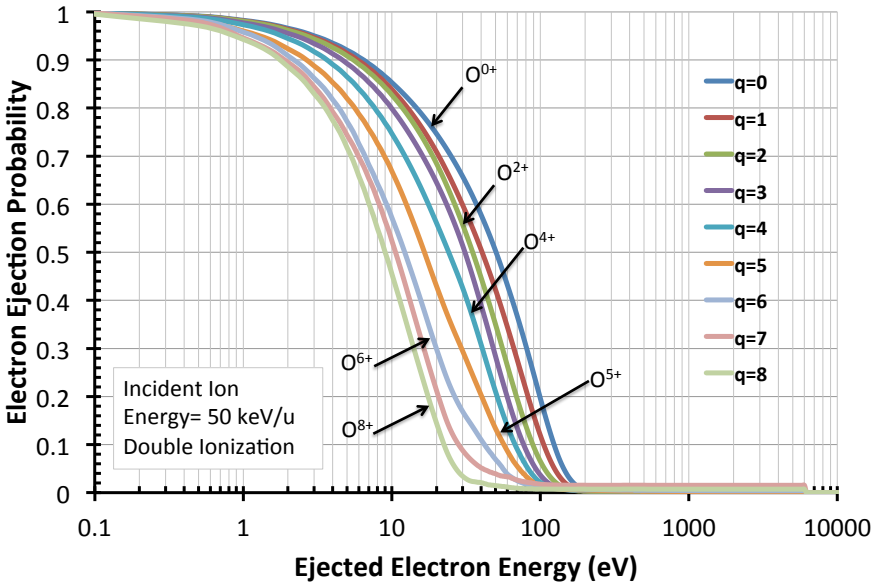

Figure 3.70: Probability of ejecting a secondary electron with energy E_s for an oxygen ion with energy $E_{ion} = 50$ keV/u, after a double ionization collision. Each curve represents a different charge state of oxygen (O^{q+}, q=0-8). See Figure 3.16 for the corresponding single differential cross sections.

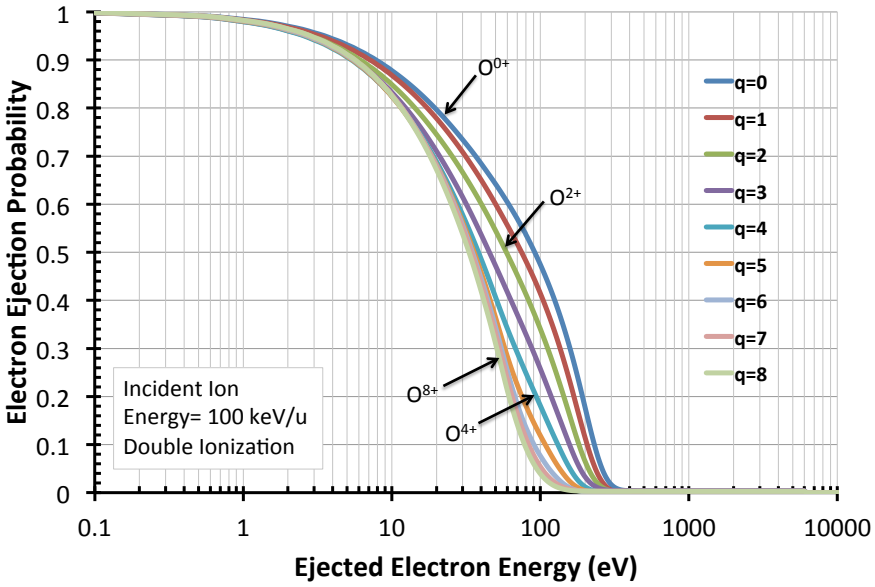

Figure 3.71: Probability of ejecting a secondary electron with energy E_s for an oxygen ion with energy $E_{ion} = 100$ keV/u, after a double ionization collision. Each curve represents a different charge state of oxygen (O^{q+}, q=0-8). See Figure 3.17 for the corresponding single differential cross sections.

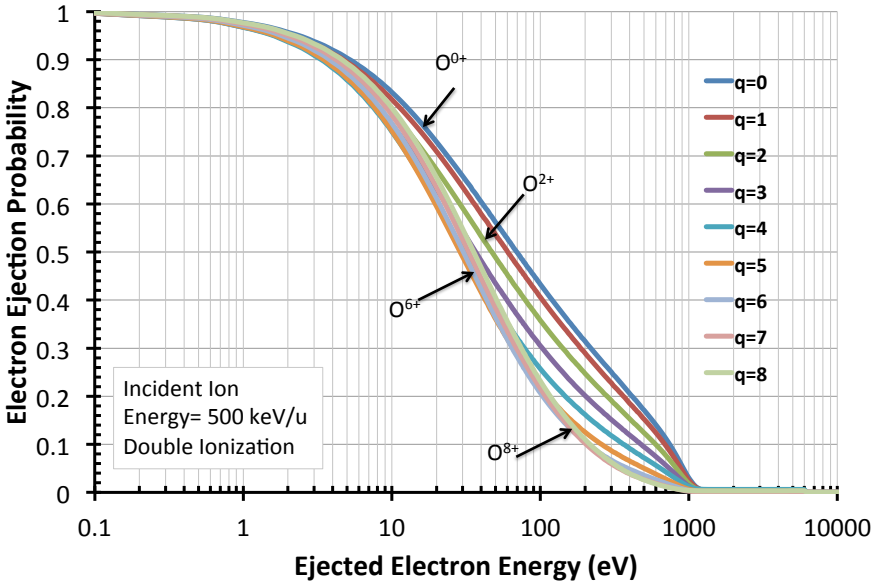

Figure 3.72: Probability of ejecting a secondary electron with energy E_s for an oxygen ion with energy $E_{ion} = 500$ keV/u, after a double ionization collision. Each curve represents a different charge state of oxygen (O^{q+}, q=0-8). See Figure 3.18 for the corresponding single differential cross sections.

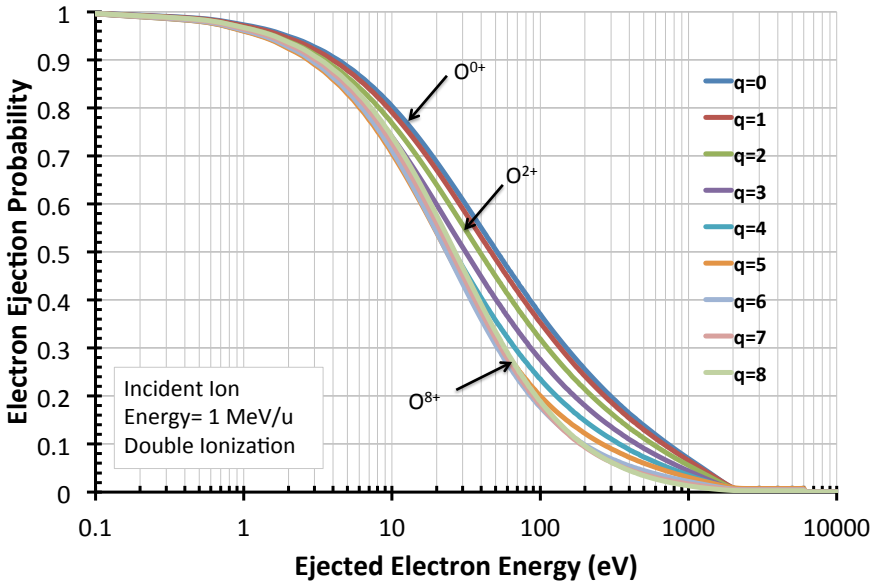

Figure 3.73: Probability of ejecting a secondary electron with energy E_s for an oxygen ion with energy $E_{ion} = 1$ MeV/u, after a double ionization collision. See Figure 3.19 for the corresponding single differential cross sections.

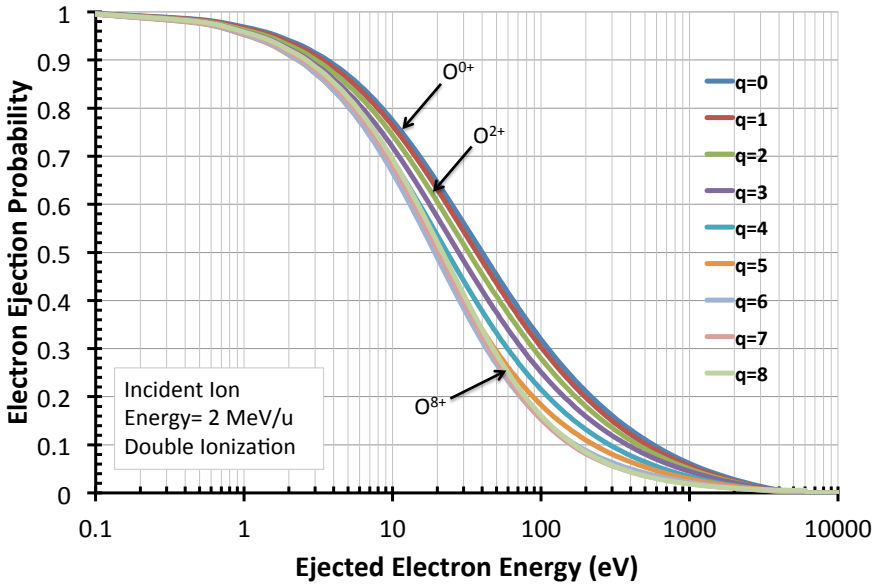

Figure 3.74: Probability of ejecting a secondary electron with energy E_s for an oxygen ion with energy $E_{ion} = 2$ MeV/u, after a double ionization collision. See Figure 3.20 for the corresponding single differential cross sections.

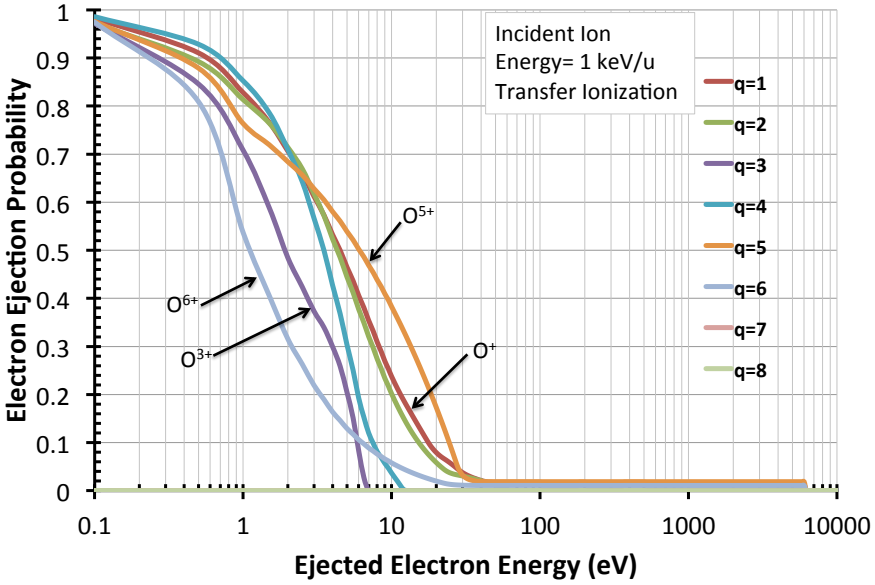

Figure 3.75: Probability of ejecting a secondary electron with energy E_s for an oxygen ion with energy $E_{ion} = 1$ keV/u, after a transfer ionization collision. Each curve represents a different charge state of oxygen (O^{q+}, q=1-8). See Figure 3.37 for the corresponding single differential cross sections.

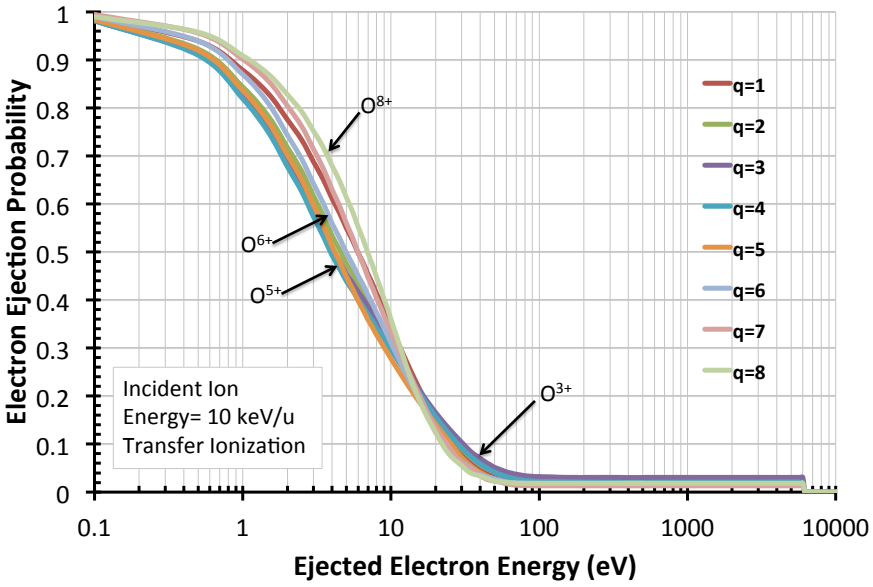

Figure 3.76: Probability of ejecting a secondary electron with energy E_s for an oxygen ion with energy $E_{ion} = 10$ keV/u, after a transfer ionization collision. Each curve represents a different charge state of oxygen (O^{q+}, q=1-8). See Figure 3.38 for the corresponding single differential cross sections.

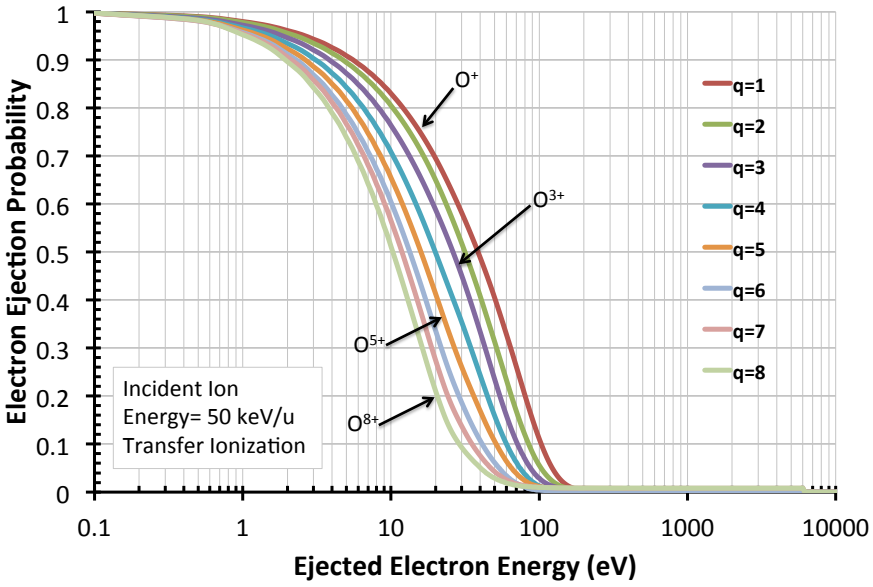

Figure 3.77: Probability of ejecting a secondary electron with energy E_s for an oxygen ion with energy $E_{ion} = 50$ keV/u, after a transfer ionization collision. Each curve represents a different charge state of oxygen (O^{q+}, q=1-8). See Figure 3.39 for the corresponding single differential cross sections.

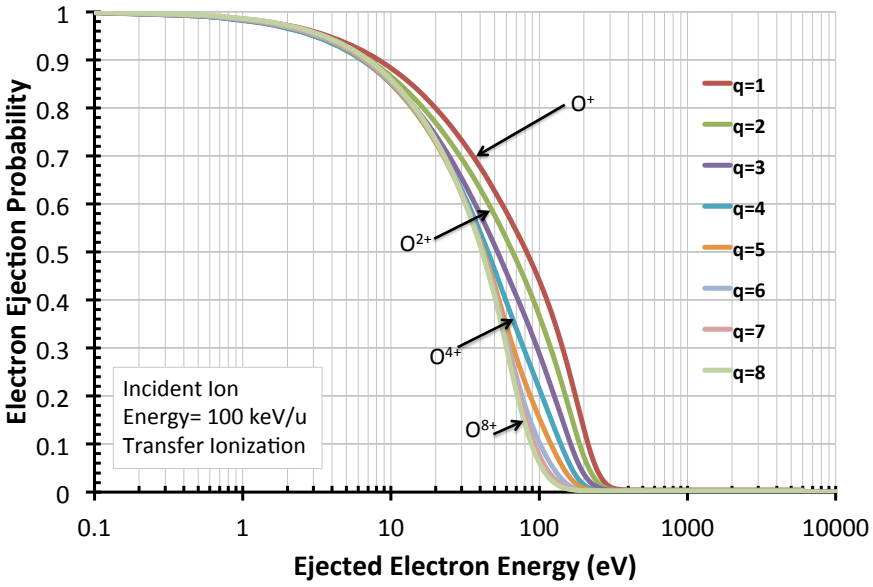

Figure 3.78: Probability of ejecting a secondary electron with energy E_s for an oxygen ion with energy $E_{ion} = 100$ keV/u, after a transfer ionization collision. Each curve represents a different charge state of oxygen (O^{q+}, q=1-8). See Figure 3.40 for the corresponding single differential cross sections.

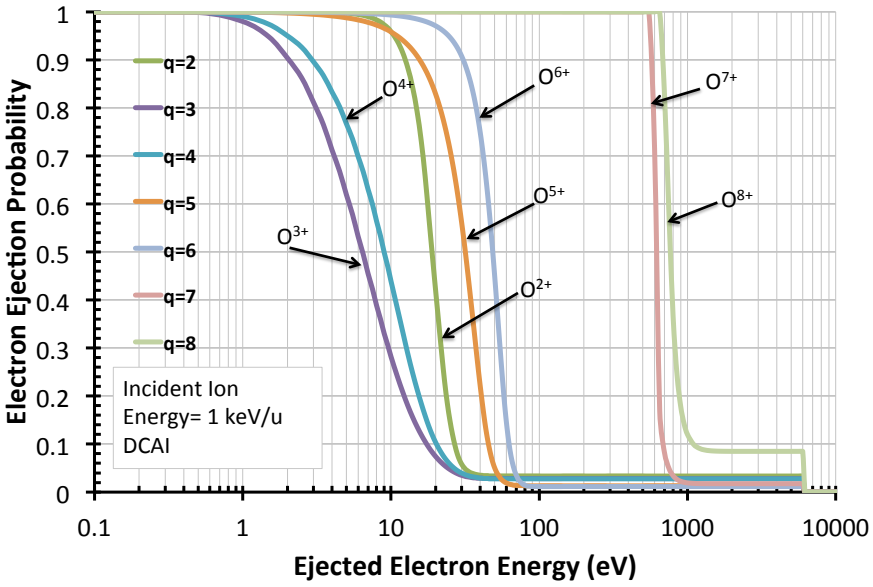

Figure 3.79: Probability of ejecting a secondary electron with energy E_s for an oxygen ion with energy $E_{ion} = 10$ keV/u, after a double capture auto-ionization (DCAI) collision. Each curve represents a different charge state of oxygen (O^{q+}, q=1-8). See Figure 3.46 for the corresponding single differential cross sections.

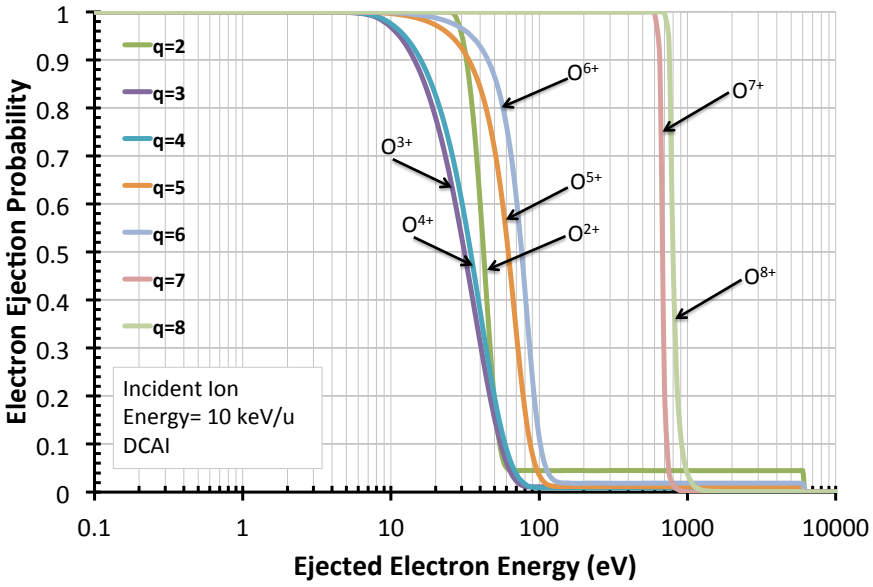

Figure 3.80: Probability of ejecting a secondary electron with energy E_s for an oxygen ion with energy $E_{ion} = 10$ keV/u, after a double capture auto-ionization (DCAI) collision. Each curve represents a different charge state of oxygen (O^{q+}, q=1-8). See Figure 3.47 for the corresponding single differential cross sections.

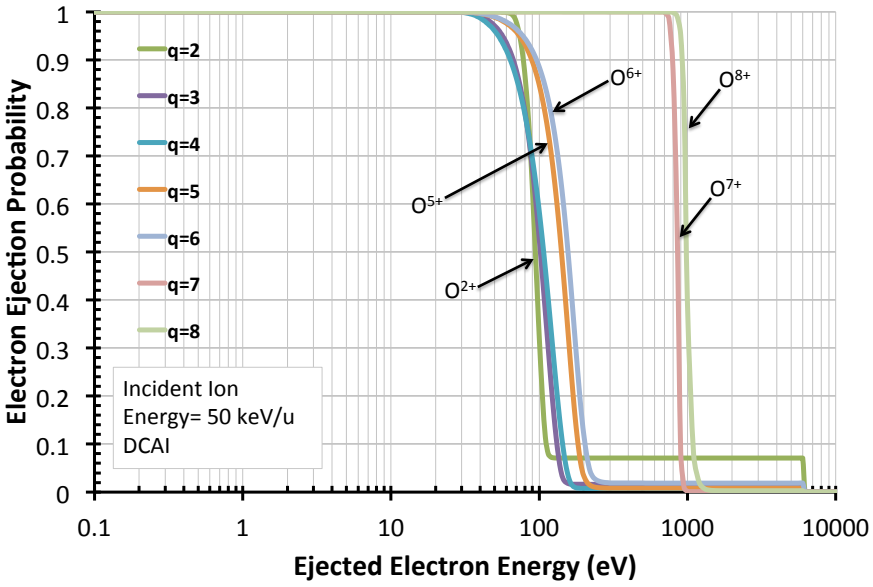

Figure 3.81: Probability of ejecting a secondary electron with energy E_s for an oxygen ion with energy $E_{ion} = 50$ keV/u, after a double capture auto-ionization (DCAI) collision. Each curve represents a different charge state of oxygen (O^{q+}, q=1-8). See Figure 3.48 for the corresponding single differential cross sections.

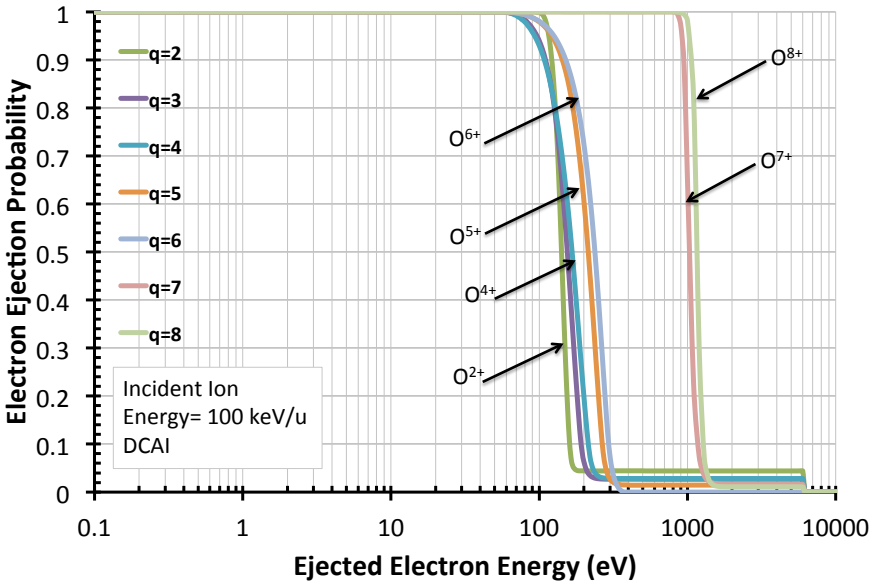

Figure 3.82: Probability of ejecting a secondary electron with energy E_s for an oxygen ion with energy $E_{ion} = 100$ keV/u, after a double capture auto-ionization (DCAI) collision. Each curve represents a different charge state of oxygen (O^{q+}, q=1-8). See Figure 3.49 for the corresponding single differential cross sections.

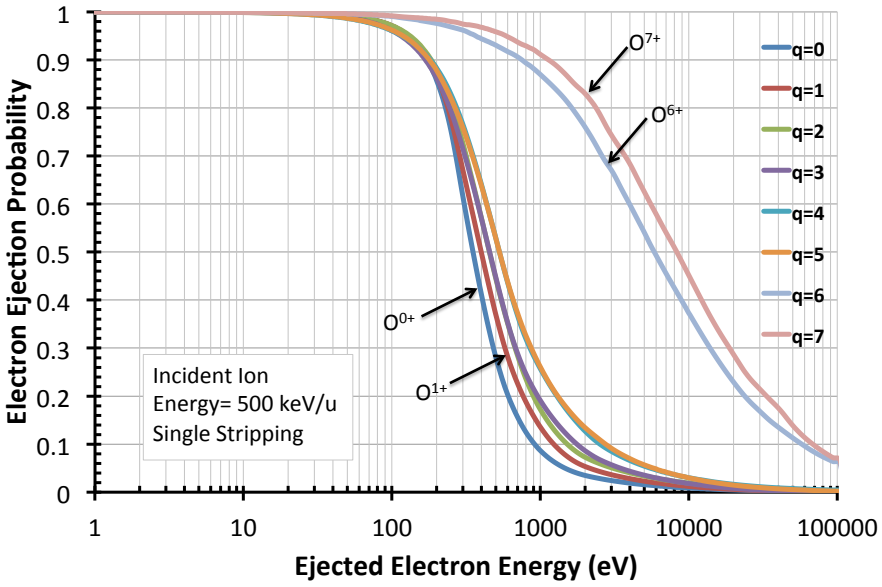

Figure 3.83: Probability of ejecting a secondary electron with energy E_s for an oxygen ion with energy $E_{ion} = 500$ keV/u, after a single stripping collision. See Figure 3.55 for the corresponding single differential cross sections.

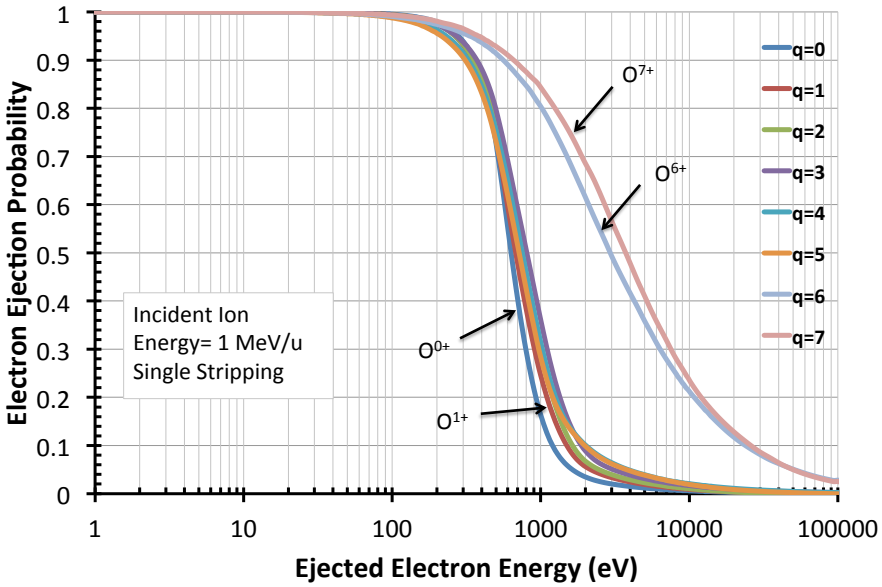

Figure 3.84: Probability of ejecting a secondary electron with energy E_s for an oxygen ion with energy $E_{ion} = 1$ MeV/u, after a single stripping collision. See Figure 3.56 for the corresponding single differential cross sections.

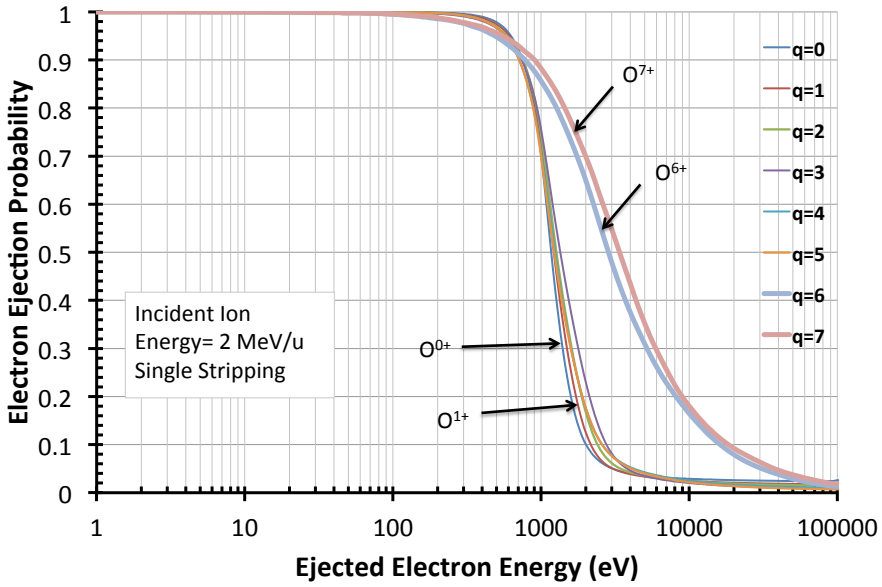

Figure 3.85: Probability of ejecting a secondary electron with energy E_s for an oxygen ion with energy $E_{ion} = 2$ MeV/u, after a single stripping collision. See Figure 3.57 for the corresponding single differential cross sections.

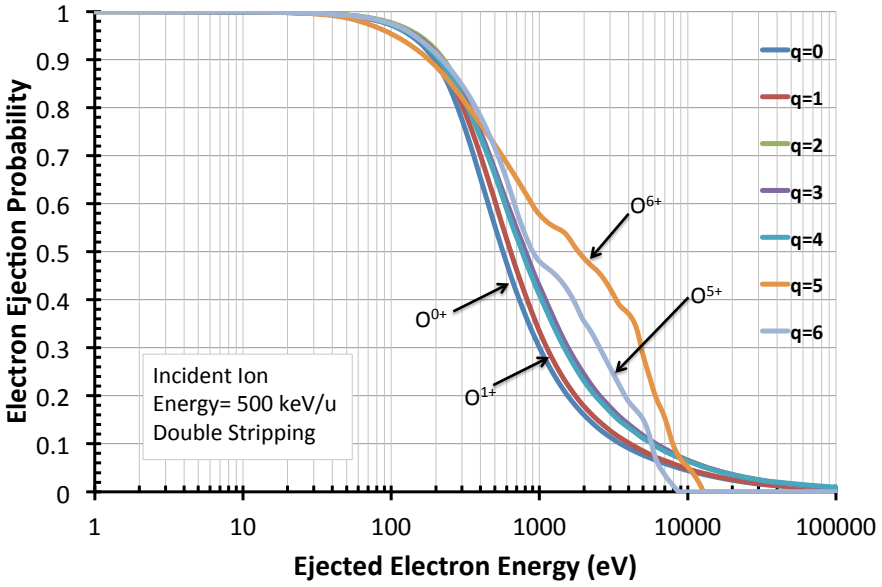

Figure 3.86: Probability of ejecting a secondary electron with energy E_s for an oxygen ion with energy $E_{ion} = 500$ keV/u, after a single stripping collision. See Figure 3.58 for the corresponding single differential cross sections. The higher charge states have lower statistics, giving a different shape in the curve, which may add some uncertainty.

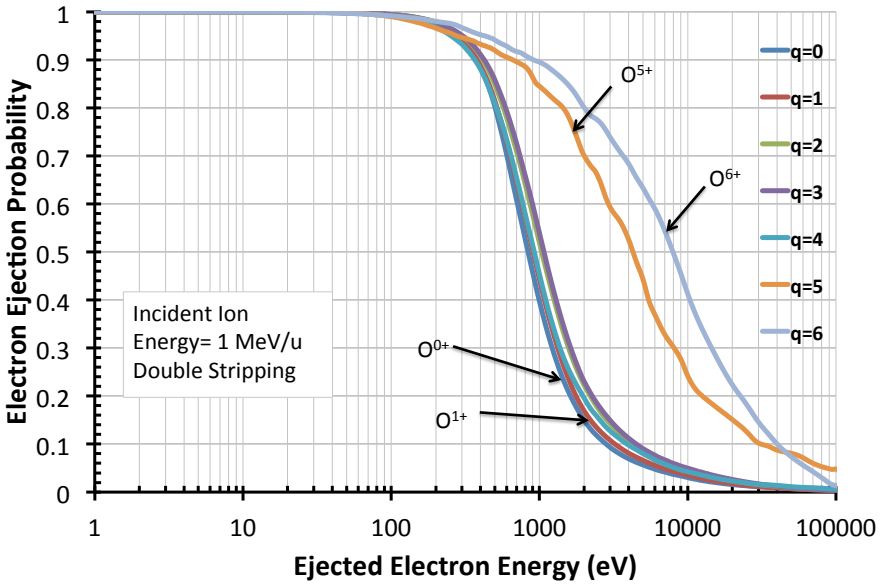

Figure 3.87: Probability of ejecting a secondary electron with energy E_s for an oxygen ion with energy $E_{ion} = 1$ MeV/u, after a single stripping collision. See Figure 3.59 for the corresponding single differential cross sections.

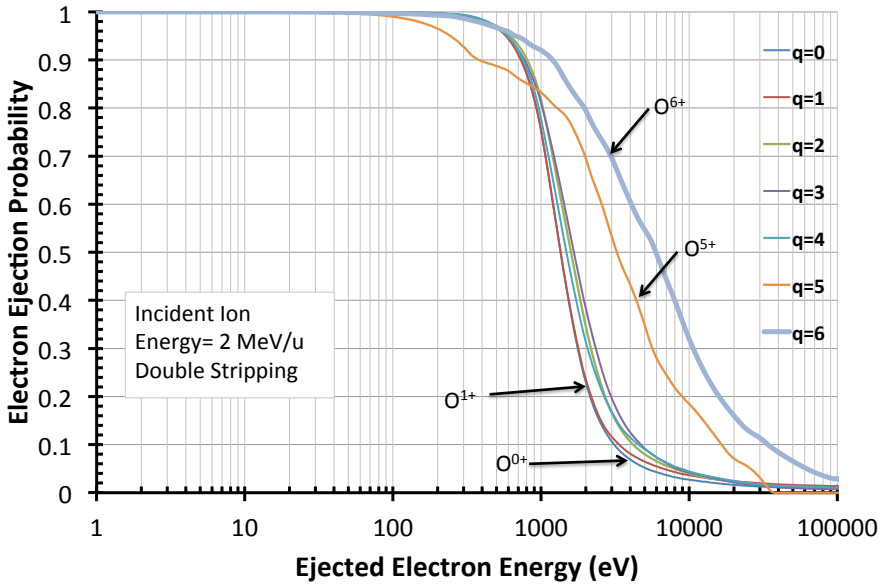

Figure 3.88: Probability of ejecting a secondary electron with energy E_s for an oxygen ion with energy $E_{ion} = 2$ MeV/u, after a single stripping collision. See Figure 3.60 for the corresponding single differential cross sections.

We also compared how the distribution of ejected electrons changes for a single charge state as we vary the energy of the ion in the collision . This allows us to estimate the variation in the electron distribution as we change the initial ion energy, which is helpful for our model since we only have data available for a few initial ion energies. As the ions precipitate in the Jovian atmosphere with an initial energy, they loose energy after every collision and we would need the distribution of the ejected electrons for all ion energies where an ionization or stripping collision occurs. This is of course, impossible to do at this time. However, by comparing the change in the distribution with ion energy, we notice that the difference in the distributions is very small. We show it for two cases in a single ionization collision in Figure 3.89. Therefore, we assume it is appropriate to use the distribution of a 500 keV/u ion as an approximation for the distributions of all ion energies between 250 keV/u to 750 keV/u. Also, we approximate the distributions for ion energies between 750 keV/u to 1375 keV/u by the calculated distribution of a 1 MeV/u ion and the distributions for ion energies between 1375 keV/u and 2 MeV/u by the calculated distribution of a 2 MeV/u ion. For the lower energies, as mentioned above, some of the processes become even more important. Therefore, we also use the distribution of a 100 keV/u ion as an approximation for the distributions of all ion energies between 75 keV/u and 250 keV/u. Also, we approximate lower energies between 75 keV/u and 25 keV/u by the distribution given by ions with energy of 50 keV/u and even lower energies from 25 keV/u down to 5 keV/u with ion energies of 10 keV/u. We also attempted to calculate the single differential cross sections for all the processes for ions with energies as low as 1 keV/u. However, the statistics were extremely low for some cases and some uncertainty exists in these distributions. Only DCAI collisions have a cross section that is significant enough for such low energies. In our model we use the distribution for 1 keV/u ions to approximate processes for energies lower than 5 keV/u.

Figure 3.90 shows a comparison of the distributions obtained for different ion energies in a transfer ionization collision. This allows us to see how the distribution varies to better gage how to approximate the distribution for intermediate values. The change in the probability for the low charge state is small for energies between 1 and 10 keV/u. However, the difference between the 10 keV/u and 50 keV/u is large. The distribution again changes slowly for energies between 50 keV/u and 100 keV/u. On the other hand, for the high charge state, the change between the 10 and 50 keV/u distributions is slow, while the difference between the 50 and 100 keV/u is large. For DCAI we show the comparison in Figure 3.91. We can see that the distributions are shifted in energy (to the left or right), due to the energy boost that the electrons get from the projectile. A similar behavior is seen in the stripping distributions. From the Figure we also note that the difference between the distributions for a highly charge ion at different energies is rather small, while the shift between the distributions is more distinct for the low charge state.

We did the same comparison for a stripping collision. Here we notice that the shape of the distribution remains very similar as we change the energy, but the distribution appears shifted to higher energies. This is attributed to the shift in the cross section peak due to the boost of the ion on the ejected electrons. The difference between the distribution of two consecutive energies with the available data that was calculated with the CTMC is rather large. Therefore, we had to find a way to calculate the distribution for energies in between. To do this, we first calculated new single differential cross sections for the stripping collisions. As we saw in the previous section, there is a peak in the cross section given by the energy boost on the electron by the projectile, i.e. the peak is at the electron energy corresponding to the projectile velocity. The peak energy can be easily calculated by taking the ion energy and diving it by the ion to electron mass ratio (1836). To calculate the cross section for an intermediate energy, we first find

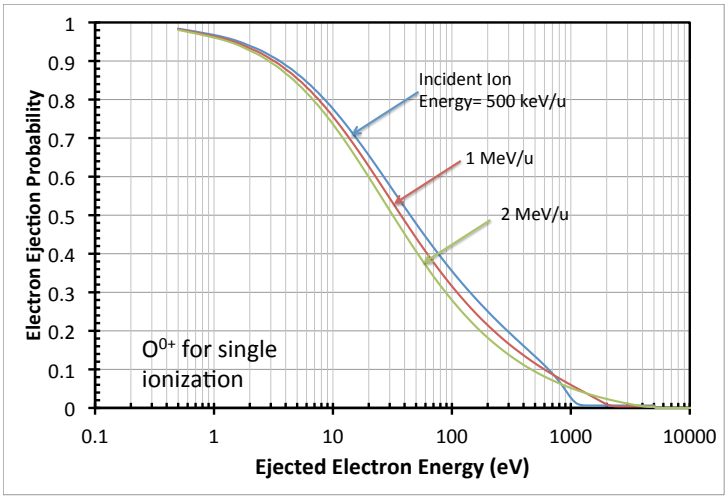

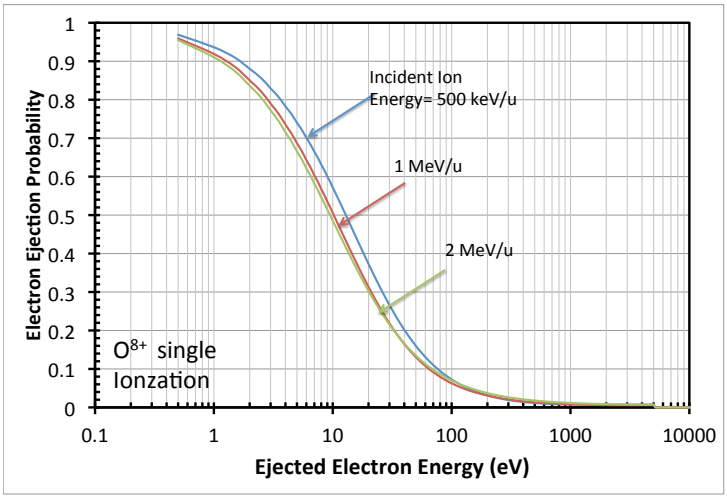

Figure 3.89: Probability of ejecting a secondary electron after a single ionization collision. Each of the curves shows the result for an ion energy of 500 keV/u, 1 MeV/u and 2 MeV/u. The top panel shows the calculated probability for a neutral oxygen (q=0) and the bottom panel shows the probability for a fully stripped oxygen ion (q=8). The change in the probability with ion energy is not very significant.

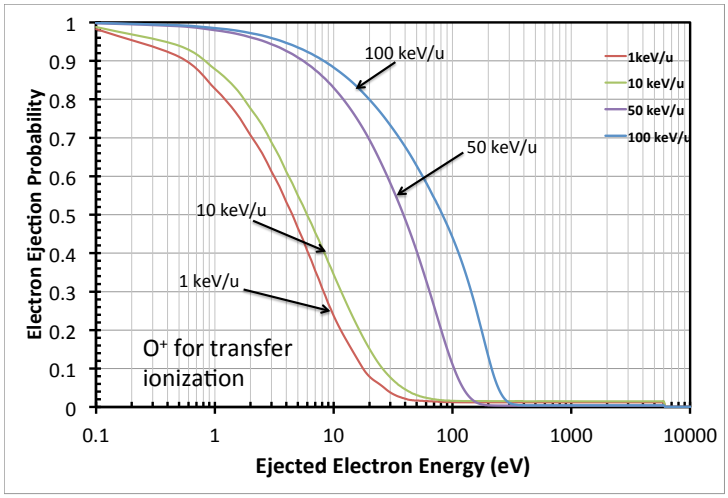

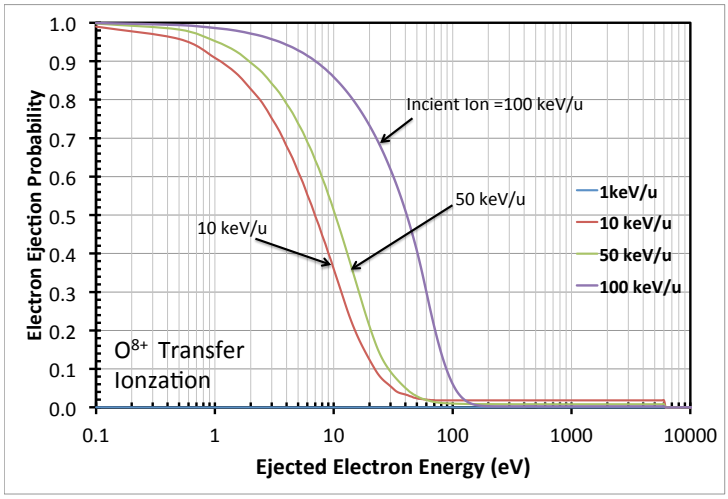

Figure 3.90: Probability of ejecting a secondary electron after a transfer ionization collision. Each of the curves shows the result for an ion energy of 1 keV/u, 10 keV/u, 50 keV/u and 100 keV/u. The top panel shows the calculated probability for a singly charged oxygen (q=1) and the bottom panel shows the probability for a fully stripped oxygen ion (q=8).

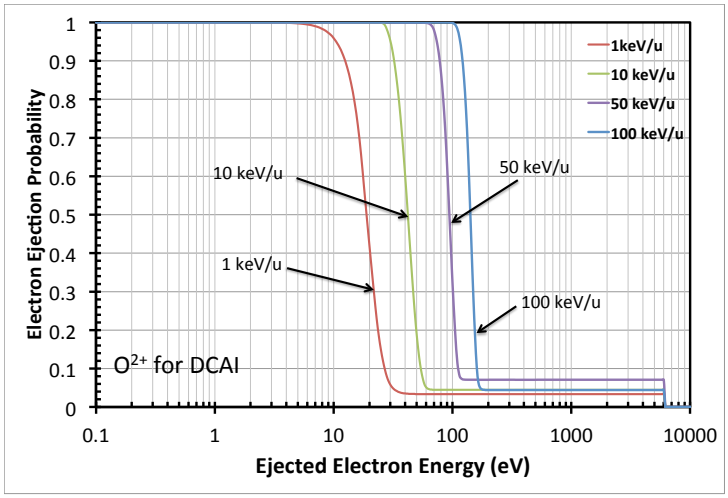

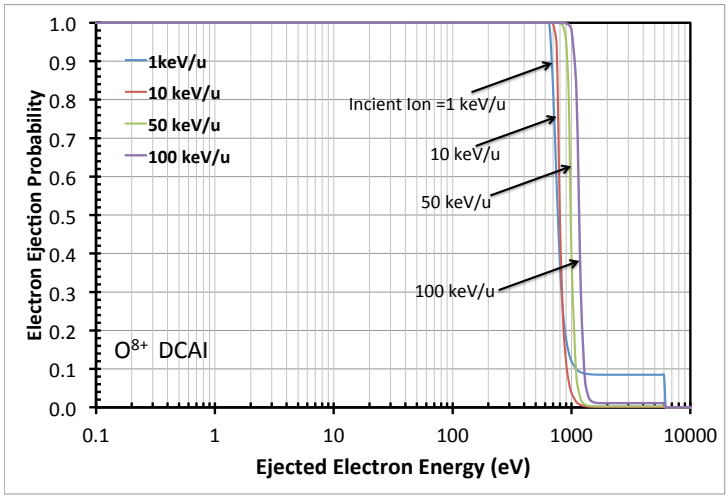

Figure 3.91: Probability of ejecting a secondary electron after a transfer ionization collision. Each of the curves shows the result for an ion energy of 1 keV/u, 10 keV/u, 50 keV/u and 100 keV/u. The top panel shows the calculated probability for a double charged oxygen (q=2) and the bottom panel shows the probability for a fully stripped oxygen ion (q=8).

the new peak energy and shift the known sdxs peak to the new peak location. Then, we normalize the curve by multiplying the known sdxs of the interpolated (or new) cross section to the one from the original curve. With the new sdxs we were able to calculate the distribution for several energies, reducing the gap between the curves. We show our result for the calculated distributions for a neutral oxygen (q=0) for energies from 10 keV/u to 2 MeV/u in Figure 3.93

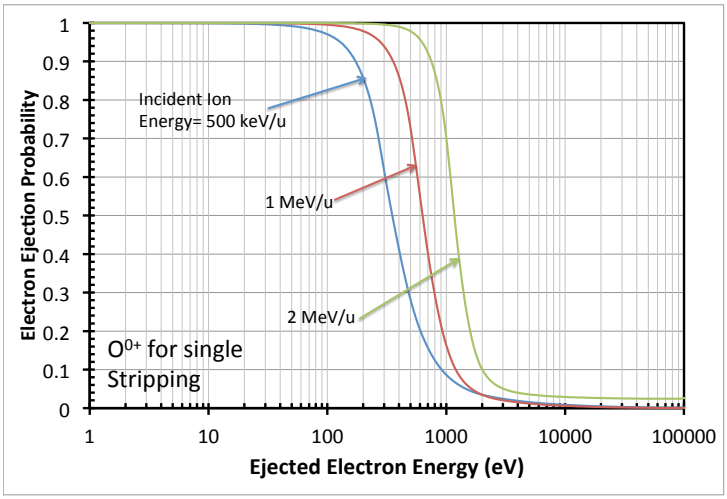

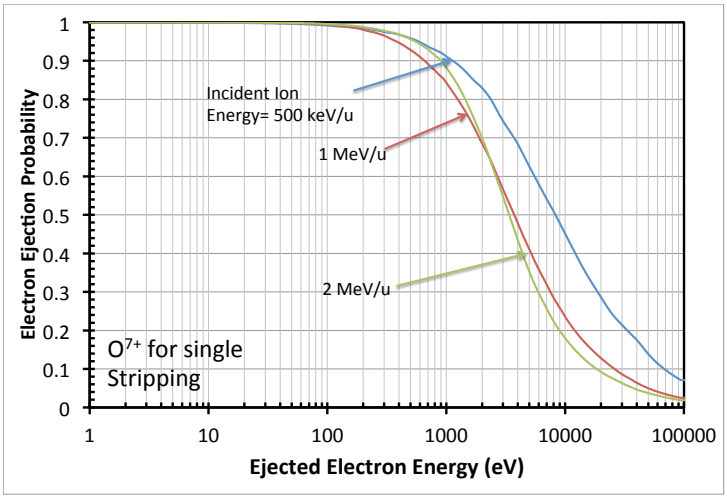

Figure 3.92: Probability of ejecting a secondary electron after a single stripping collision. Each of the curves shows the result for an ion energy of 500 keV/u, 1 MeV/u and 2 MeV/u. The top panel shows the calculated probability for a neutral oxygen (q=0) and the bottom panel shows the probability for a highly stripped oxygen ion (q=7). For the low charge state, the shape of the distribution remains very similar with the change of energy, but it is shifted to higher energies, due to the velocity boost that the electrons have from the projectile.

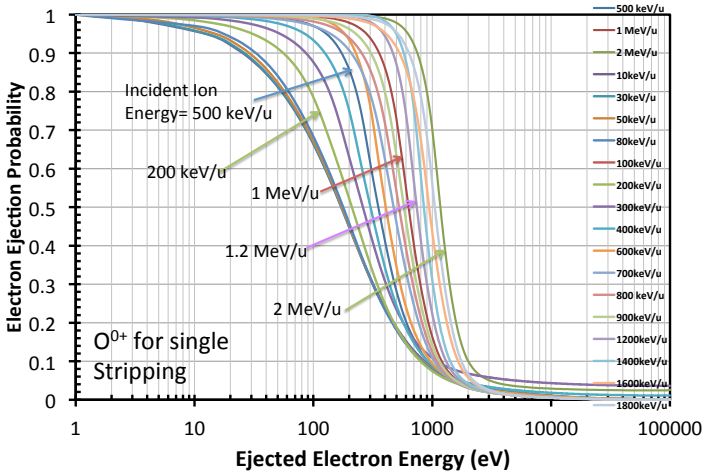

Figure 3.93: Probability of ejecting a secondary electron after a single stripping collision. These distributions were found by interpolating the sdxs from known data by shifting the peak of the cross section and normalizing each curve. This figure shows several curves interpolated from the original curves for 500 keV/u, 1 MeV/u and 2 MeV/u sdxs calculated by the CTMC method.

Chapter 4

Energetic Ion Precipitation and Auroral X-ray Emissions at Jupiter

4.1 Introduction

Energetic ion precipitation at high latitudes in the atmosphere are the source of the x-ray auroral emissions observed in the past decades and recently by XMM-Newton and Chandra X-ray Observatory (CXO). Line emissions from the observations attribute the x-ray emissions to charge exchange collisions between highly ionized sulfur and oxygen ions. We will refer the reader to section 1.3.3 for a review of the x-ray aurora and it's recent development. In this chapter we discuss our model of the x-ray aurora emissions. We compare two models that have been used in the recent years. We have developed a hybrid Monte Carlo method that includes an altitude dependence of the x-ray emissions, making this model the most complete to this date. We show our results in the following sections and discuss why optical effects such as absorption of the emitted x-rays is important for the accurate modeling, representation and understanding of the x-ray aurora.

4.2 Model

To calculate the emitted x-ray intensities in the Jovian polar regions, two different methodologies have been developed: the continuous slow-down method (CSDM) [45, 46], developed for oxygen ion precipitation, and a Monte Carlo method (MCM) [21, 47, 50–52], which included oxygen and sulfur ions. Both methods start with energetic ions that deposit energy into the atmosphere as they precipitate. However, the way in which the ion charge state changes as the particle loses energy is tracked differently for each method. The CSM uses the equilibrium fraction of each charge state as a function of energy, while the MCM follows the ion charge history along its trajectory by recording the charge state after each collision. A more detailed description of these methods will follow in sections below. The previous CSDM models dealt only with oxygen ion precipitation into the atmosphere. In the model presented for this work we arbitrarily chose different initial ion energies to see how each would affect the x-ray spectrum observed. For better comparison between methods as well as to improve our modeling capabilities, this model includes sulfur ions in the CSDM model, as well as opacity and quenching effects on the spectrum.

4.2.1 Neutral Atmosphere

The ion precipitation model requires a background neutral atmosphere in order to account for depth effects and the neutral atmosphere. The Jovian neutral atmosphere presented by [17], based on Galileo probe data [92], [93] and remote observations [94], is adopted for our entire work on Jupiter. The altitude scale is referenced from where the pressure equals 1 bar (approximately the cloud tops), and the densities of methane (CH_4), helium (He) and molecular hydrogen (H_2) are specified (see Figure 4.1). The homopause is the altitude in an atmosphere where molecular and eddy coefficients

become equal. This means that above the homopause diffusion of atmospheric constituents dominates and each species has its own scale height. Below the homopause convection dominates. For our adopted atmospheric model the homopause is located at about 400 km (see figure) and below this altitude the density profiles of CH_4, He, and H_2 have the same scale height. The methane layer located below the homopause plays an important role in the opacity, since carbon in the CH_4 has a large soft x-ray absorption cross section. The temperature and pressure profiles are shown in Figure 4.2 as it may become important for certain parts of the model.

4.2.2 Collision Processes

Auroral x-ray line emission at Jupiter is produced by energetic oxygen and sulfur ions, which undergo charge transfer and/or electron removal collisions as they precipitate into the atmosphere. The product ions from charge transfer collisions are highly excited and emit x-ray photons as part of the radiative decay to the ground state. The collision processes relevant to the Jovian aurora are as follows:

$$\text{Stripping: } O^{(q-1)+} + H_2 \rightarrow O^{q+} + H_2 + e^- \tag{4.1}$$

$$\text{Charge transfer: } O^{q+} + H_2 \rightarrow O^{(q-1)+*} + H_2^+ \tag{4.2}$$

$$\text{X-ray emission: } O^{(q-1)+*} \rightarrow O^{(q-1)+} + \gamma \tag{4.3}$$

$$\text{Ionization: } O^{q+} + H_2 \rightarrow O^{q+} + H_2^+ + e^- \tag{4.4}$$

$$\text{Excitation: } O^{q+} + H_2 \rightarrow O^{q+} + H_2^* \tag{4.5}$$

The same processes will also be relevant for sulfur ions. The literature provides a further discussion of these processes [18, 45–48, 50, 51]. Direct excitation of incoming energetic ions might also be contributing to the x-ray emission; however, we did not

include this process in our calculations because the cross section was not available in the literature. But if other type fast particle collision processes (e.g., electron impact ionization and excitation) are reasonable analogies, then the excitation cross section for fast highly-charged oxygen ions should be some fraction ($\sim 25\%$) of the ionization cross section (i.e., the electron removal or stripping cross section). This fraction can be considered as un uncertainty in our calculations. For the current model we use the cross sections for ion-atom collisions explained in Chapter 3, which cover the above mentioned processes (see Figures 3.1 to 3.6). The cross sections are similar to, but not the same as, those used by [46] and also to those computed and used in [48]. In particular, the present simulations of ion-precipitation require a substantial database of atomic collision cross sections. These cross sections are continuously being improved and worked on by modelers, but the calculation process for even just one of these cross sections can be very time consuming. The data used here are part of an even larger database that will be described in detail in forthcoming work [[18], in preparation]. Please refer to Chapter 3 for a more details on the cross sections.

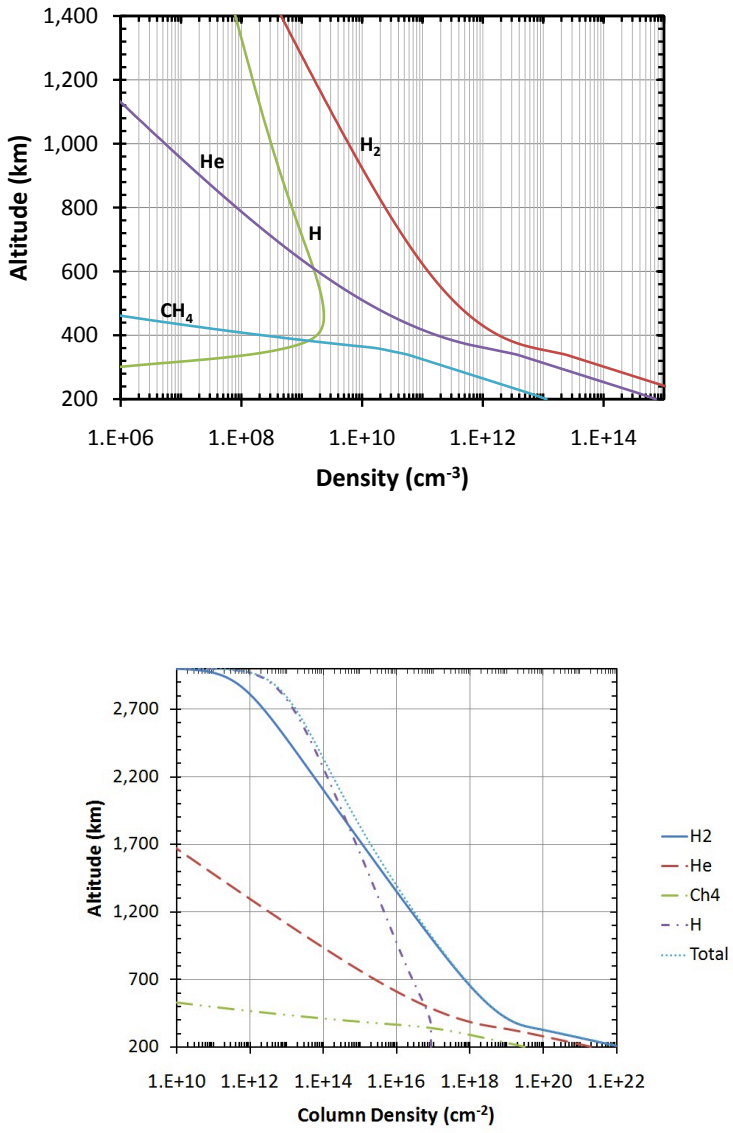

Figure 4.1: Top: Neutral density profiles of H_2, He, H, and CH_4 for Jupiter's upper atmosphere for altitudes between 200 – 1400 km. Data adapted from [17]. Bottom: Column density as a function of altitude for each atmospheric species.

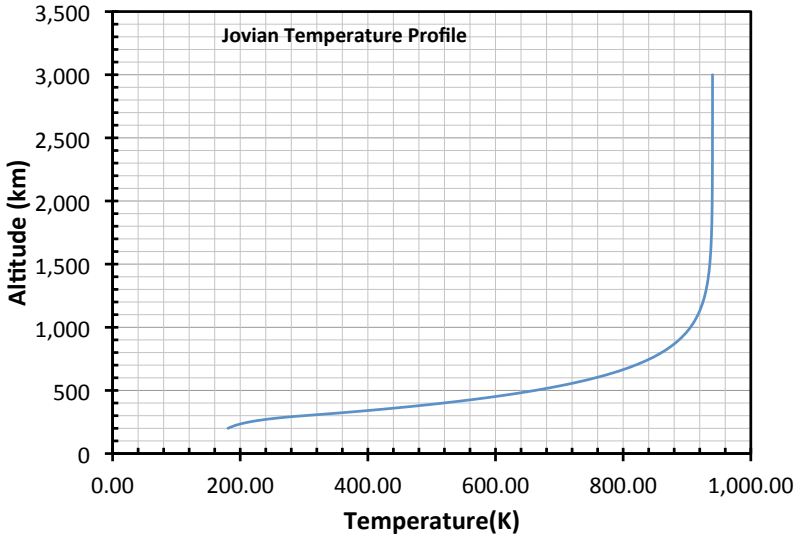

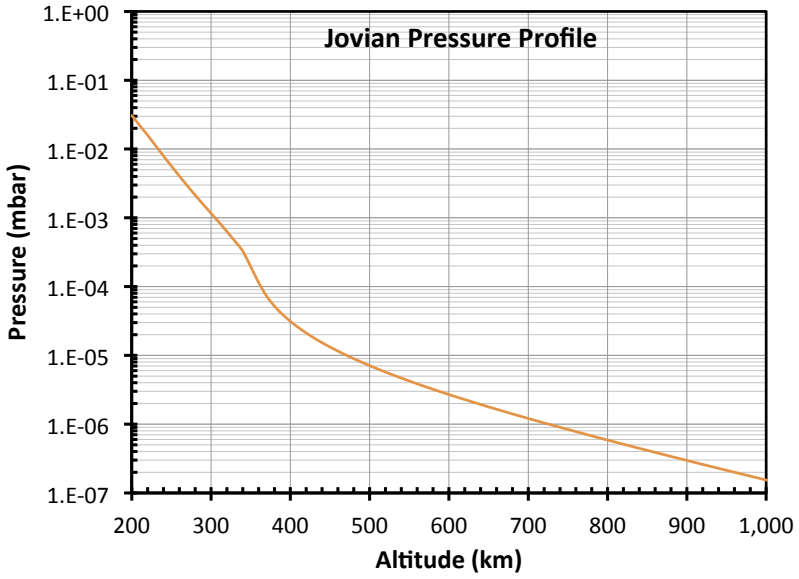

Figure 4.2: Top: Temperature profile for Jupiter's upper atmosphere for altitudes between 200 – 1000 km. Data adapted from [17]. Bottom: Pressure as a function of altitude in the atmosphere.

4.2.3 Charge Distributions

As mentioned above, the main difference between the continuous slow-down method and the Monte Carlo simulations is the way in which each model calculates the charge distributions for the particles as they penetrate the atmosphere.

Equilibrium Fractions

Equilibrium fractions are used in the CSDM to calculate the population distribution of charge states in each beam at a particular energy. It is assumed that a sufficient number of collisions occur for the different charge states to reach equilibrium at each energy under the condition that the density of the target species (H_2) will change in a length scale that is bigger than the collision mean free path [46]. The equilibrium fractions are calculated using transition probabilities P_{ij} by

$$\phi_q P_{q,q+1} = \phi_{q+1} P_{q+1,q}, \tag{4.6}$$

where ϕ_q is the fraction of the beam ions in charge state q at a given energy E, such that the sum of ϕ_q over all charge states equals unity. The flux of ions in a given charge state, q, and at a given energy E, is its equilibrium fraction, ϕ_q, multiplied by the total ion flux regardless of charge state. $P_{q,q+1}$ is the stripping cross section at the energy of interest, $P_{q+1,q}$ is the charge transfer cross section and q is the charge state, which goes from 0 to 8 for oxygen and from 0 to 16 for sulfur. For an example of the equilibrium fraction for oxygen please refer to Figure 4.3 top panel. In general, for energies above 3 MeV/u oxygen is fully stripped ($q = 8$), while for energies between 10 keV/amu and 1.5 MeV/amu an oxygen beam has a mix of all different charge states.

Using the same method, we calculated equilibrium fractions for sulfur as shown in Figure 4.4 bottom panel. For energies up to 100 keV/u there is a mix of charge states for

$q = 0, 1,$ and 2. For higher energies up to 3.5 MeV/u there is a mix of all the different charge states, and above 8 MeV/amu the sulfur ions are fully stripped ($q = 16$).

Monte Carlo calculation of charge distribution

As pointed out by [47], a problem arises from the equilibrium, fraction method due to the fact that it calculates the charge distribution assuming that at a given energy E the production and loss of a charge state q by stripping and charge transfer are the same and it does not take into account the charge state history of the precipitating ions. To address this issue, a Monte Carlo simulation is developed for this paper, based on the model developed by [47, 50, 51], but we added an altitude dependence to improve the current models. Since the spectra is not sensitive to the initial charge state of the ions [51], charge states of O^{2+} and S^{1+} were arbitrary chosen for our model, since they are common magnetospheric ions and as pointed out by fits done by [52] the original sulfur population in the outer magnetosphere appears to be mainly singly charged.

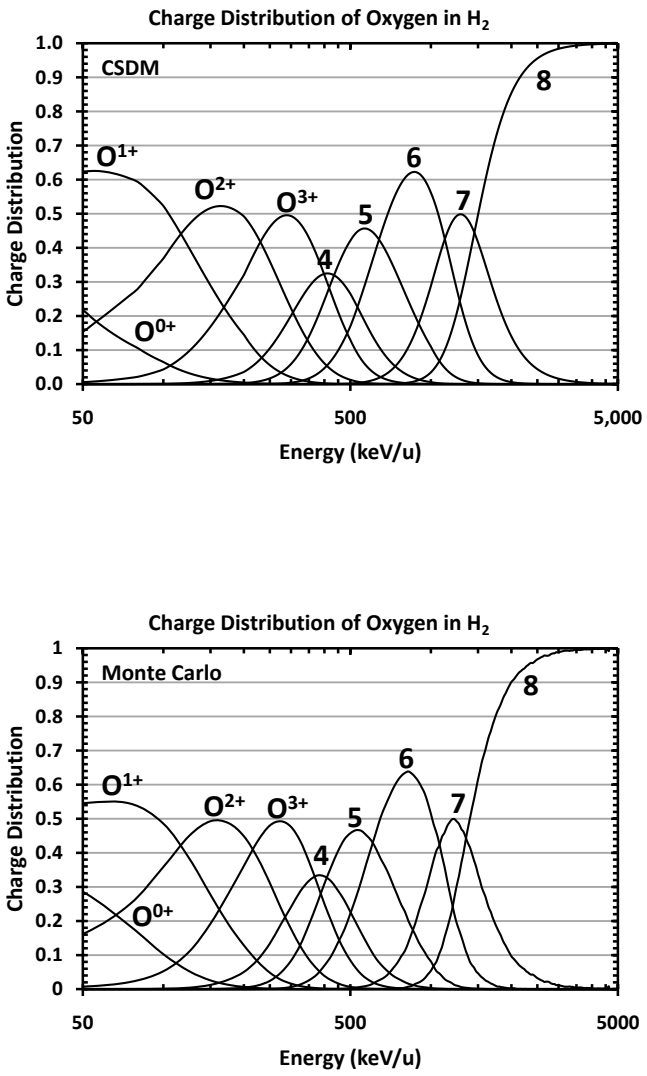

Figure 4.3: Oxygen charge state equilibrium fraction distributions as a function of energy for all oxygen states ($q = 0 - 8$) in molecular hydrogen as calculated by the continuous-slow-down model (CSDM) [top], and by the Monte Carlo model (MCM) [bottom].

Once the ions are introduced into the atmosphere, the probability of having a collision can be found by:

$$P = 1 - \exp^{\sigma_{tot}\Delta N} \tag{4.7}$$

where σ_{tot} is the total cross section given by the sum of the probable collision processes, given in equations 4.1, 4.2, and 4.4 and N is the column density. Therefore, the displacement that each ion will move before a collision can be found randomly by:

$$\Delta N = -\ln(P)/\sigma_{tot}, \tag{4.8}$$

where P is given by a random number between 0 and 1. Once it is established that a collision did occur, the type of collision is also decided randomly. There are three possible outcomes for the charge state of the ion: 1) it can remain the same $\{q \rightarrow q\}$, 2) it can gain one electron $\{q \rightarrow (q-1)\}$, or 3) it can lose an electron $\{q \rightarrow (q+1)\}$. The probabilities for these transitions can be calculated using the cross sections presented earlier by:

$$p_0 = \frac{\sigma_{ionization}}{\sigma_{tot}} \tag{4.9}$$

$$p_+ = \frac{\sigma_{stripping}}{\sigma_{tot}} \tag{4.10}$$

$$p_- = \frac{\sigma_{cx}}{\sigma_{tot}} \tag{4.11}$$

At each collision the ion will lose some energy calculated with the stopping power as explained in the following section. Note that this means that the model is not fully Monte Carlo since a stopping power is used for the energy loss. However, energy loss via ionizing collisions is dominant which makes this a reasonable approximation yet allows the ion charge states to vary randomly during the precipitation. This collision

method is repeated until the ion runs out of energy and its vertical trajectory is followed in the atmosphere by the column density displacement, which can in turn be converted to altitude. By following the ion charge history at each collision, it is possible to build a charge distribution as a function of energy for both oxygen and sulfur ions as shown in Figures 4.3 and 4.4 bottom panels. To accomplish this, one must keep track of the number of ions at each charge state for each energy, independently of the initial ion energy or collision processes that the ions might have undergone during their trajectory.

4.2.4 Stopping Power and Energy Deposition

As the energetic ions penetrate the atmosphere they interact with neutral species by elastic collisions and via electronic transitions and lose energy in these interactions. In order to calculate the energy loss of each collision and be able to find the final depth of the ions we used stopping powers for both oxygen and sulfur with H_2 as a target atom. We have assumed that the stopping power with He as a target is approximately equal to that with H_2 as a target, which leads to a few percent error. The energy loss per particle per path length (s) increment is given by:

$$\frac{dE}{ds} = -n(s) * S(E(Z)) \tag{4.12}$$

where dE/ds is the energy loss per unit length as the beam penetrates the atmosphere $n(z)$ is the total atmospheric density at that altitude z, and $S(E(z))$ is the empirical stopping power at the energy of the beam for that specific altitude. Note that this equation is the same as equation 2.21 rearranged. One can relate the path length s to the altitude z by the pitch angle α, as given by: $dz = ds \cdot \cos\alpha$. We have assumed an isotropic distribution of particles and have chosen the pitch angle randomly. The polar cusp magnetic field is assumed to be radial. The empirical stopping power curves for both oxygen

and sulfur are shown in Figure 4.5 [adapted from [20]]. One can see that the oxygen stopping power peaks at about an energy of 300 keV/u, while the sulfur stopping power peaks at an energy of about 550 keV/u and has a value about 3 times larger than the oxygen stopping power.

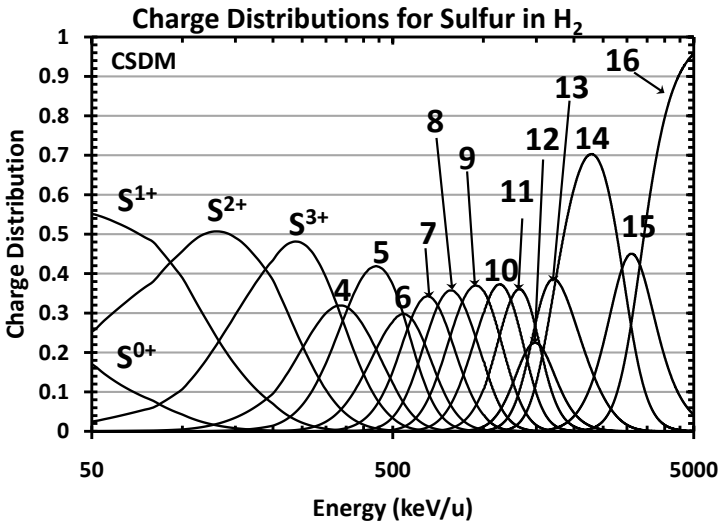

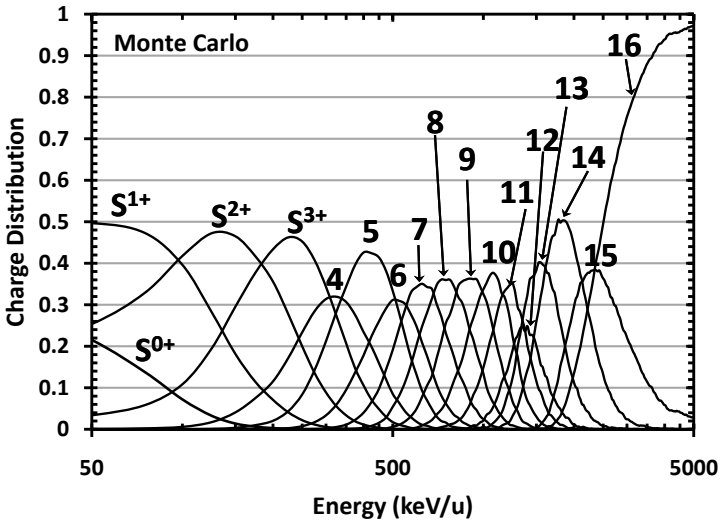

Figure 4.4: Sulfur charge state equilibrium fraction distributions as a function of energy for all oxygen states ($q = 0 - 16$) in molecular hydrogen as calculated by the continuous-slow-down model (CSDM) [top], and by the Monte Carlo model (MCM) [bottom].

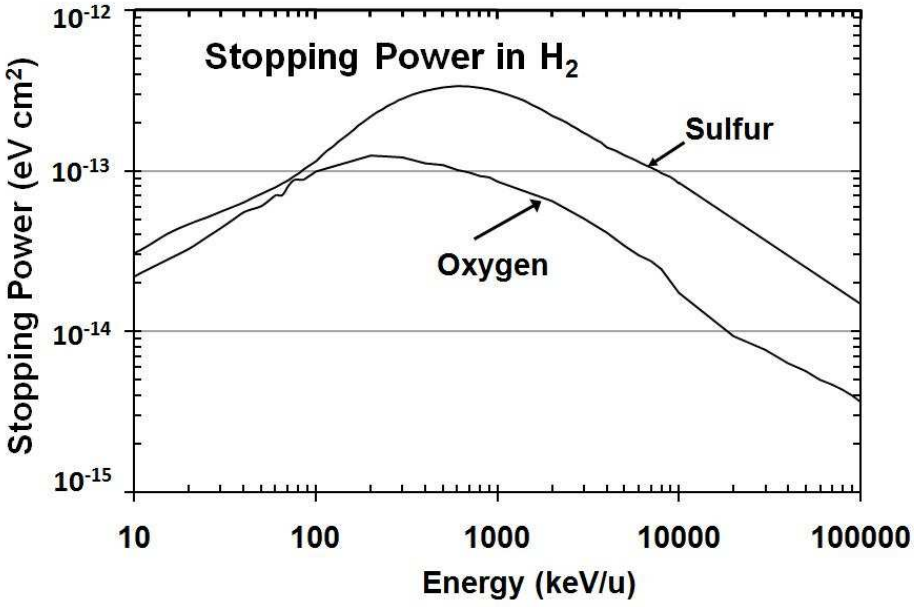

Figure 4.5: Empirical stopping powers for sulfur and oxygen in H_2 as a function of energy. These are used to calculate the energy loss at each ion-neutral collision. Data adapted from [20].

4.2.5 Opacity

To incorporate the opacity of the atmosphere into the model, the optical depth for outgoing photons was calculated for three different path angles with respect to the polar axis (i.e. zenith): 0 degrees, 80 degrees, and 90 degrees. These different angles will give a range of results for the different spatial geometries that might be found in observations. The optical depth is given by:

$$\tau(\lambda, z_0) = Ch(\theta, z) \sum_j \sigma_j^{abs}(\lambda) \int_{z_0}^{\infty} n_j(z) dz \tag{4.13}$$

where $\tau(\lambda, z_0)$ is the optical depth as a function of wavelength (corresponding to each outgoing photon energy) and as a function altitude (z_0) where emission occurs.

We show the optical depth for H_2 for 60, 80 and 90 degrees for an wavelength λ = 34.5 Å, as shown in Figure 4.6. $Ch(\theta, z)$ is the Chapman function for an exit angle θ and altitude z. The sum in equation 4.13 is over all the neutral species j in the atmosphere (H_2, He and CH_4). σ_j^{abs} is the photo-absorption cross section for the given wavelength for a given species j and $n_j(z)$ is the density for species j at altitude z. The absorption cross sections for the different species were adapted from [79] and from NIST tabulations [95] and are shown in Figure 2.21. For example, for a 560 eV photon the absorption cross sections of atomic hydrogen, helium and carbon are 8×10^{-23} cm^2, 2×10^{-21} cm^2 and 2×10^{-19} cm^2, respectively. Since the atmospheric model used has molecular hydrogen, its absorption cross section was approximated by multiplying the atomic hydrogen cross section by a factor of two. We also note that $Ch(\theta, z) \approx \sec\theta$ for $\theta \leq 80^\circ$, but for $\theta = 90^\circ$ the Chapman function is given by

$$Ch\left(\frac{\pi}{2}, z_0\right) = \sqrt{\frac{R_J}{H}\frac{\pi}{2}} \tag{4.14}$$

where R_J is the Jovian equatorial radius (71,492 km) and H is the neutral scale height ($\sim$ 30 km for altitudes of between 370 – 380 km, which is where the ions are emitting most of the x-rays). Figure 4.7 shows the different scale heights for each neutral component considered in our atmospheric model. The scale height is determined by:

$$H(z) = \frac{kT(z)}{m_{neutr}g(z)}; \tag{4.15}$$

where k is the Boltzmann constant (1.38×10^{-23} J/K), T is the temperature at a given altitude z, m_{neutr} is the molecular mass of the given atom or molecule, and $g(z)$ is the acceleration of gravity at the given altitude. We also calculated the Chapman function at a 90° angle for each atmospheric, see Figure 4.8.

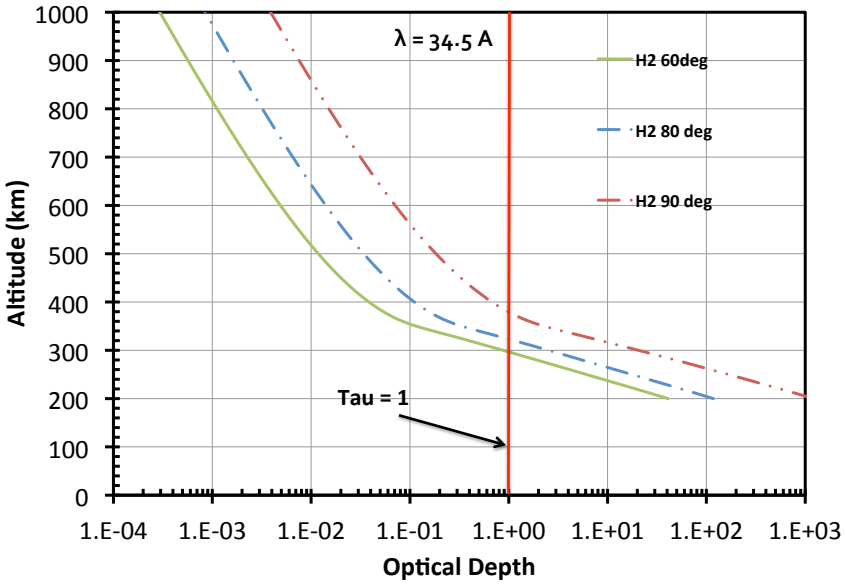

Figure 4.6: Optical depth for H_2 as a function of altitude in the upper atmosphere, according to our model, for a wavelength of $\lambda = 34.5$ Å. Please see equation 4.13. The solid green line shows τ for an angle of 60°. The blue dash-dotted line shows τ for an angle of 80°, and the red dash-double dot line shows τ for an angle of 90°.

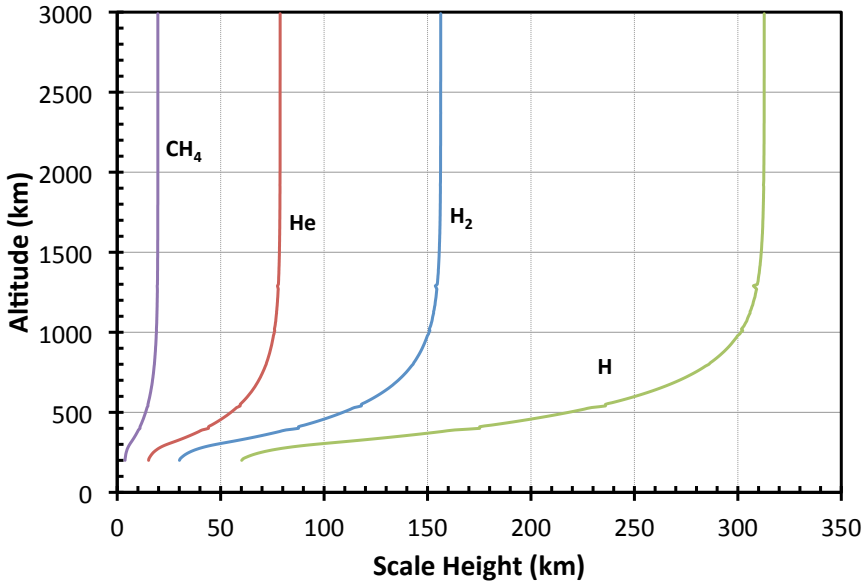

Figure 4.7: Scale height $H = \frac{kT}{mg}$ for the neutral constituents of the jovian upper atmosphere for each altitude

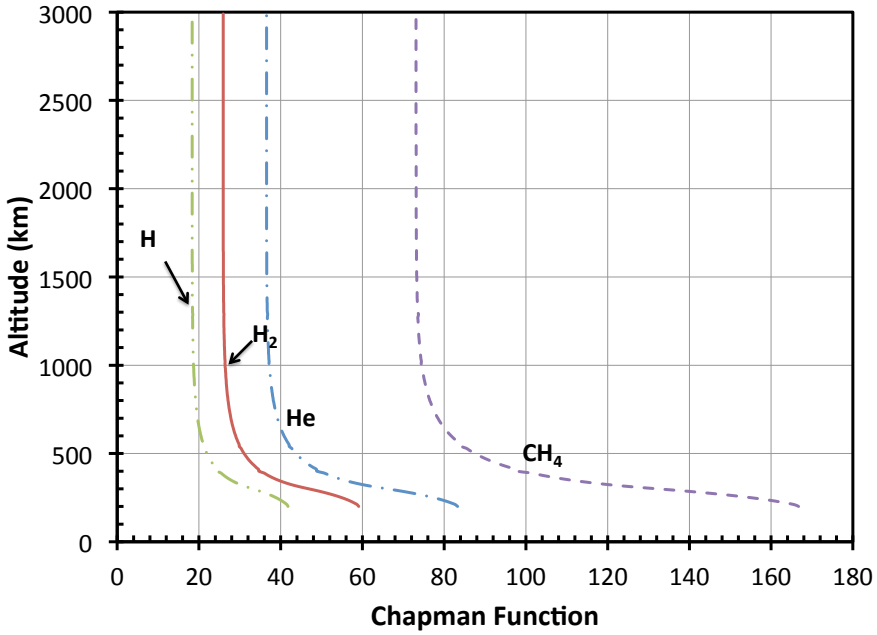

Figure 4.8: Chapman function as a function of height z for each atmospheric neutral considered in our model of the upper atmosphere.

4.2.6 Quenching

Some states of the helium-like O^{6+} ion can have long lifetimes and it is possible for a collision to occur before these ions de-excite. The quenching rate used in the model was estimated by assuming that any collision that changes the charge state of the ion (e.g. charge transfer, stripping, transfer ionization) will prevent the ion from radiating. To calculate how much emission would be lost, the total charge transfer and stripping cross sections for O^{6+} were used as an approximation for the quenching cross section. The quenching rate was calculated as:

$$R(z) = v \cdot \sigma_{quench}(z) \cdot n(z), \tag{4.16}$$

where $R(z)$ is the quenching rate in units of $\sec^{-1}$ at a given altitude z, $v = \sqrt{2E(z)/M}$ is the speed of the particle, and $n(z)$ is the neutral density at a given altitude z. $\sigma_{quench}(z)$ is the quenching cross section approximated by the O^{6+} total charge transfer cross section $(\sigma_{q,q-1}(E(z)))$ added to the O^{6+} stripping cross section $(\sigma_{strip}(E(z)))$ for the energy E at the altitude z. This approximation gives a lower limit estimate for the quenching cross section, which is presently unknown, and it compares in order of magnitude to quenching cross sections reported by [96].

4.3 Results

4.3.1 Charge Distribution Differences Across Methods

The charge distribution as a function of energy determined with both methods was found to be almost identical for oxygen ions. The largest difference found was about 8% difference in the fraction for the O^{1+} charge state (see Figure 4.3 and Figure 4.10.

However, since the x-ray emission comes from the higher charge states O^{7+} and O^{6+} the difference between the two methods should not affect the oxygen x-ray spectra.

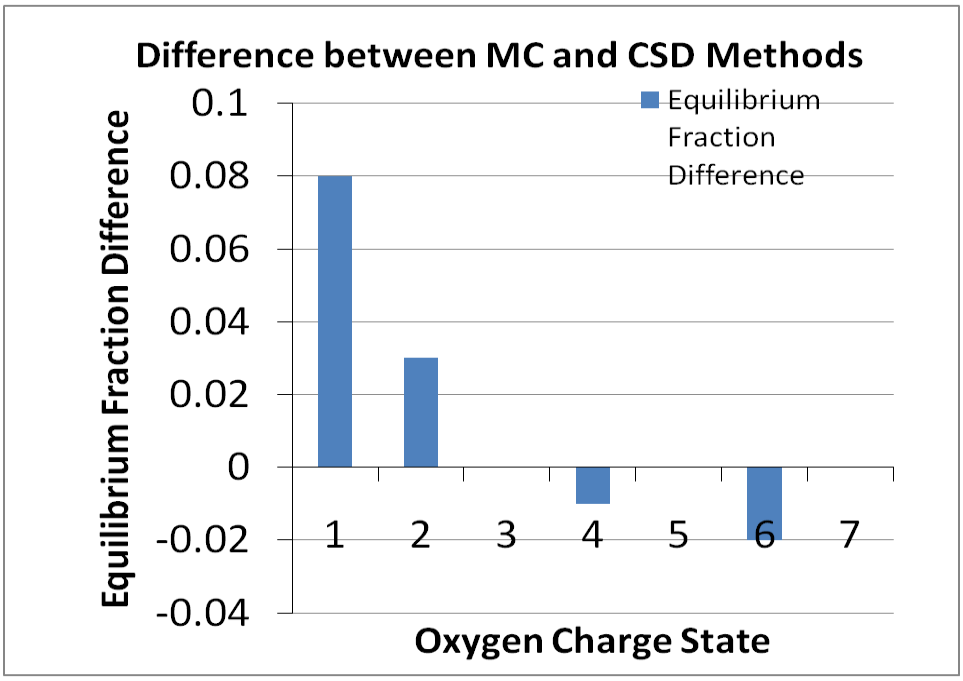

Figure 4.9: Difference in the equilibrium fraction calculated by each method (CSDM or MCM) for each charge state of oxygen.

The same comparison was carried out for sulfur and a bigger difference was found between the two methods especially for the higher charge states (see Figure 4.4). The biggest discrepancy between the two methods was found for S^{14+}, which has a 20% difference in the charge distribution, having a smaller value in the MC methodology. A difference of about 8% was also found for the S^{15+} charge state as well. These discrepancies between the methods can be attributed to a bottleneck in the charge states, where the smallest stripping or charge transfer cross sections, as explained by [47]. Since the differences occur at high charge states that produce x-rays, some differences between modeled spectra calculated with each method would be expected.

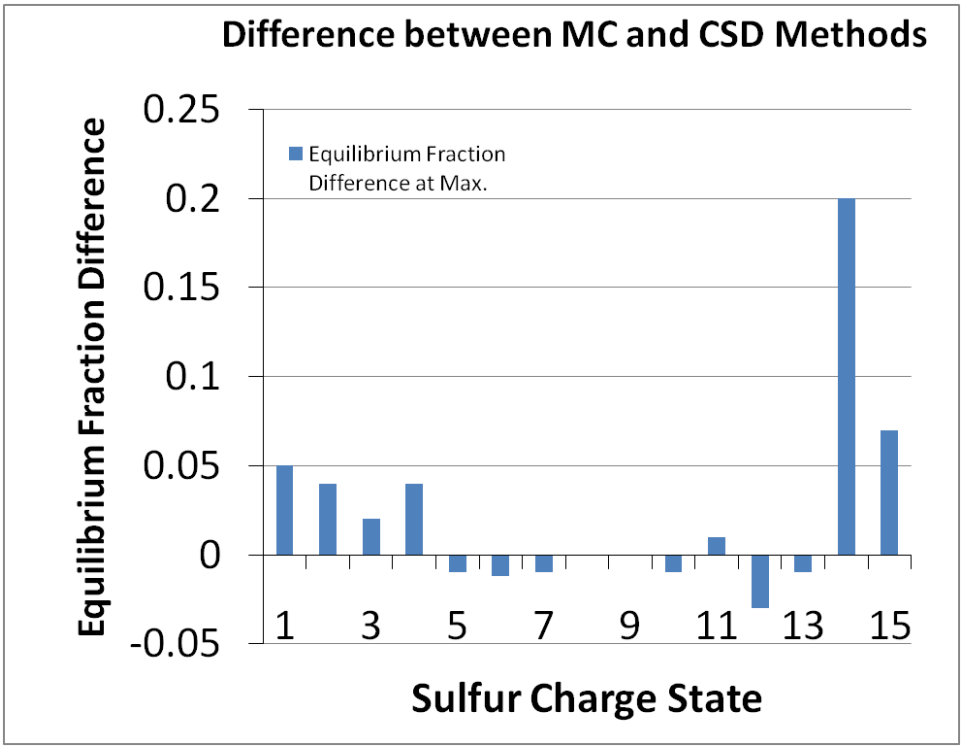

Figure 4.10: Difference in the equilibrium fraction calculated by each method (CSDM or MCM) for each charge state of sulfur.

4.3.2 Ion Production Rate

In general,the production rate $P(z)$ of a given charge state $q-1$ can be calculated for the ECM method using the cross sections described earlier by:

$$P(z) = \int_z^\infty n(z') \left\{ \sigma_{q,q-1}(E(z')) \right\} \phi_q(E(z')) \Phi_{beam} dz' \tag{4.17}$$

for the product ion species (O^{7+} or O^{6+} for example) at altitude z', and $n(z')$ is the atmospheric density at that altitude. $\sigma_{q,q-1}$ is the total charge transfer cross section for the energy E that the beam has at the specified altitude z' and is given by adding the cross sections for single charge transfer, transfer ionization and double-capture autoionization for an initial state q into a state $q-1$. $\phi_q(E(z'))$ is the equilibrium fraction of the

initial charge state q (O^{8+} or O^{7+} for example) and Φ_{beam} is the total flux of the beam. But for the Monte Carlo method we keep track for each ion of the charge exchange collisions in a set of altitude bins and determine the production rate of a given charge state from a large number of incident ions. We normalize the results by the number of incident ions chosen. For the altitude bin with the maximum production rate the statistical error was calculated. For O^{7+} production and energies below 1 MeV/u the statistical error is large (between 10 – 20%), due to the small production rate for these low energies. However, for energies equal and above 1 MeV/u the error decreased to values between 0.5 – 2% dependent on the initial beam energy. For O^{6+} and S^{8+} the production rates are much larger and the statistical error calculated is less than 2% for all initial energies at the altitude where maximum production occurs.

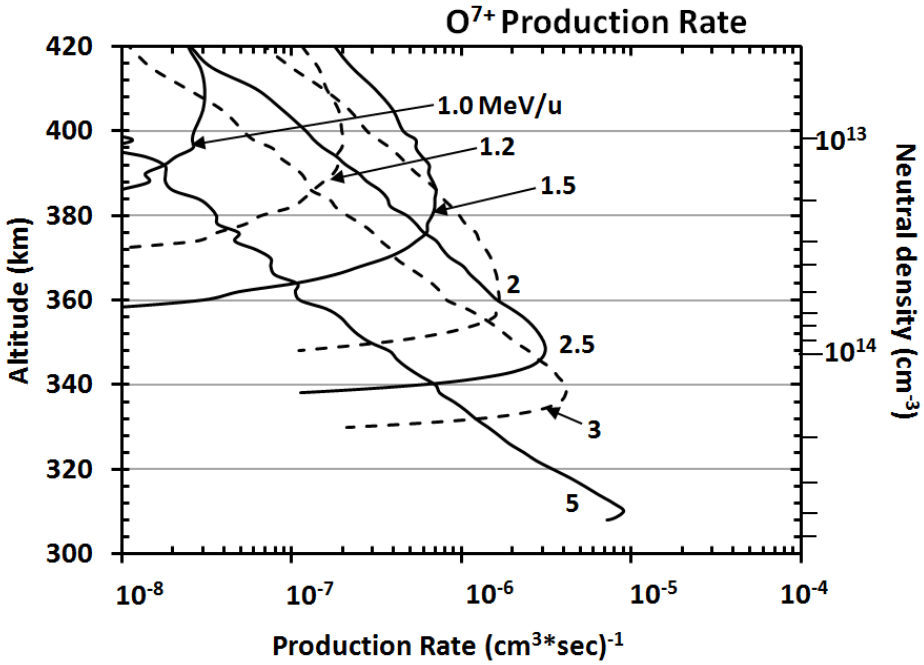

Figure 4.11: O^{7+} production rates. The curves represent the production rate for different incident ion energies (E_0 = 1.0, 1.2, 1.5, 2.0, 2.5, 3.0, and 5.0 MeV/u) as a function of altitude in km.

The product ion species O^{7+} and O^{6+} created by charge transfer emit x-ray photons as the excited ions de-excite via radiative cascading to the ground level [2,21,46,47,50–52, 54, 56]. Using our hybrid Monte Carlo method for a number of incident ions (N> 10,000 for each initial energy) with different initial energies (0.75, 0.85, 1.0, 1.2, 1.5, 2.0, 2.5, 3.0, 5.0 MeV/u chosen arbitrarily) we track the number of O^{7+} and O^{6+} ions that are produced by charge transfer collisions at each altitude in the atmosphere. The production rates for different incident energetic oxygen ions are shown in Figures 4.11 and 4.12, and Figure 4.13 shows the S^{8+} production rate calculated for the initial ion energies shown in the figures in units of MeV/u. This sulfur charge state was chosen as an example because it has the highest intensity of all charge states.

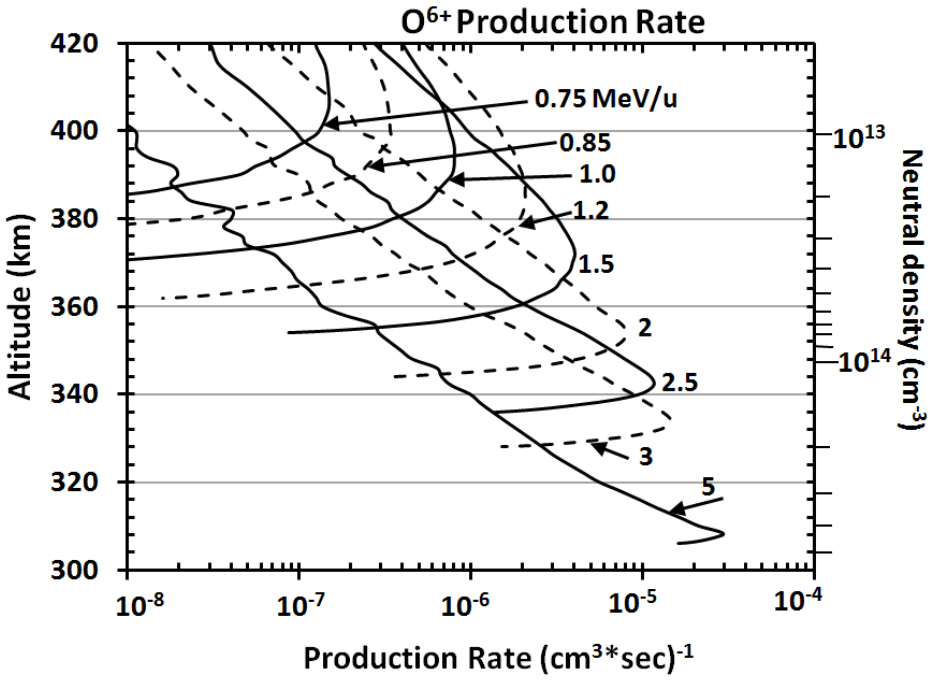

Figure 4.12: O^{6+} production rates. The curves represent the production rate for different incident ion energies (E_0 = 1.0, 1.2, 1.5, 2.0, 2.5, 3.0, and 5.0 MeV/u) as a function of altitude in km.

We assume an isotropic downward distribution of ions (in pitch-angle) at the top of the atmosphere and choose an individual ion's pitch-angle randomly. Pitch-angle affects the depth of ion penetration and energy deposition. Having a range of pitch-angles widens the altitude width of the energy deposition profiles or production rate profiles. As expected, with higher incident ion energies the ions reach deeper into the atmosphere. For example, the peak production rate for O^{6+} is at an altitude z = 380 km for a 1 MeV/u ion, and it is at z = 356 km for a 2 MeV/u ion. Table 4.1 shows a summary of the altitudes and neutral densities for which the O^{7+}, O^{6+}, and S^{8+} production rates peak.

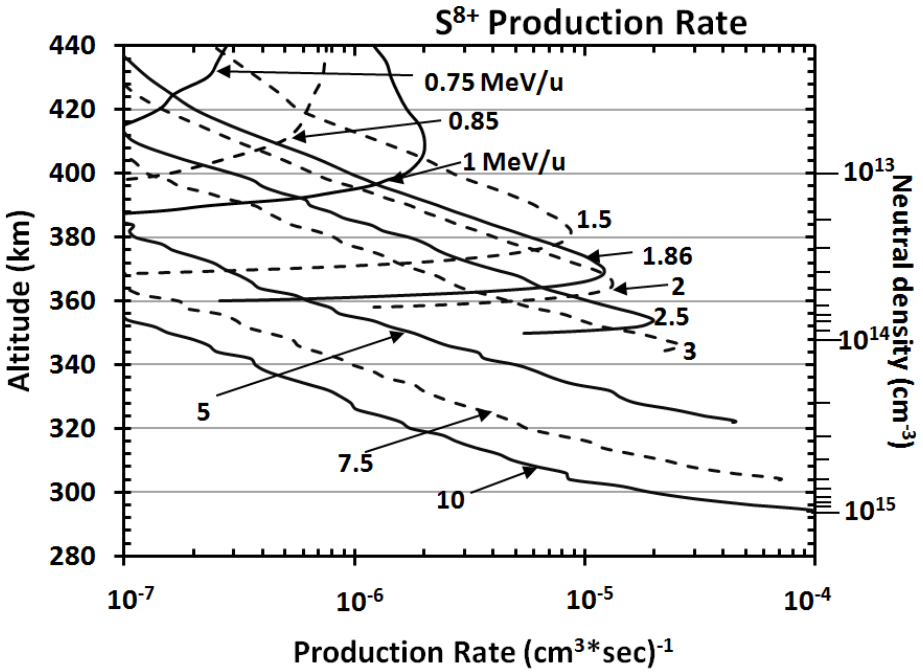

Figure 4.13: S^{8+} production rates. The curves represent the production rate for different incident ion energies (E_0 = 0.75, 0.85, 1.0, 1.5, 2.0, 2.5, 3.0, 5.0, 7.5, and 10.0 MeV/u) as a function of altitude in km.

Table 4.1: Altitude and Corresponding Atmospheric Neutral Density for Peak Ion Production. Numbers in parenthesis correspond to powers of ten.

Initial Ion Energy (MeV/u)	Altitude (km)	Neutral Density (cm^{-3})	Statistical Error
Transition:	$O^{8+} \rightarrow O^{7+}$		
0.75	445	1.89 (12)	18%
0.85	410	5.58 (12)	10%
1.0	410	5.58 (12)	5%
1.2	398	1.09 (13)	3%
1.5	386	1.99 (13)	2%
2.0	360	3.88 (13)	1%
3.0	338	1.54 (14)	1%
5.0	310	4.02 (14)	0.5%
Transition:	$O^{7+} \rightarrow O^{6+}$		
0.75	425	3.09(12)	2%
0.85	398	1.09 (13)	2%
1.0	390	1.66 (13)	2%
1.2	388	3.81 (13)	1%
1.5	372	3.61 (13)	1%
2.0	354	8.20 (13)	0.6%
3.0	334	1.73 (14)	0.4%
5.0	308	4.34 (14)	0.3%
Transition:	$S^{9+} \rightarrow S^{8+}$		
0.75	475	1.09 (12)	2%
0.85	465	1.30 (12)	1.5%
1.0	410	5.58 (12)	1%
1.5	380	2.58 (13)	1%
2.0	366	4.49 (13)	0.6%
3.0	346	1.13 (14)	0.4%
5.0	322	2.54 (14)	0.3%
7.5	304	5.09 (14)	0.3%
10.0	294	1.10 (15)	0.3%

The production rates computed with the MC methodology are very similar to those calculated with the CSDM, especially for oxygen but a stopping power is used for the energy loss so this is not entirely surprising (see Figure 4.14). The same figure shows the difference that the choice of pitch angle has for the production rate. For example, a beam with a pitch angle of 0°goes deeper and has a higher production rate peak than a beam of the same initial energy with an average pitch angle of 60°. One can also see that the Monte Carlo method with a random pitch angle distribution has a production rate that is somewhere in between.

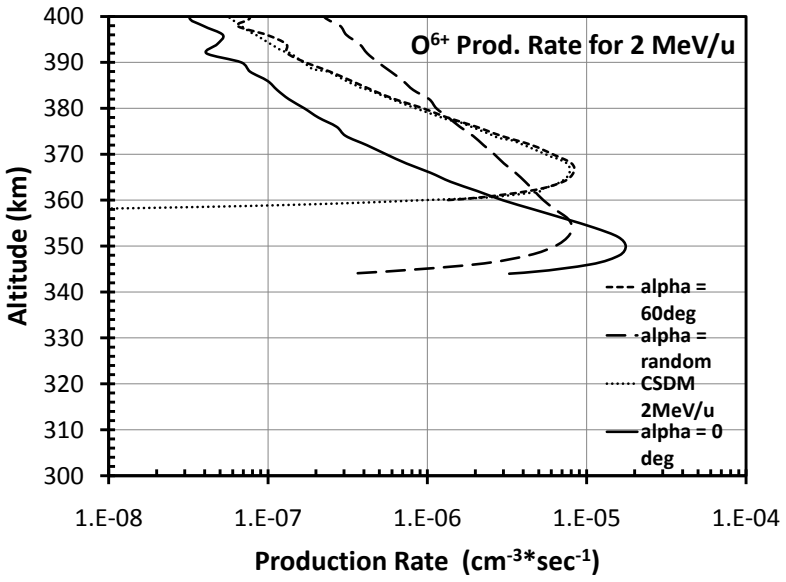

Figure 4.14: O^{6+} production rate for a beam with initial energy of 2.0 MeV/u for different initial pitch angles. The solid line gives the production rate as calculated by the MCM for a 0° pitch angle. The long dashed line represent the same production rate but with random pitch angles. The short dashed line gives the production rate calculated with the MCM for a pitch angle of 60°. The dotted line gives the production rate calculated with the CSDM. Notice how this line is almost identical to the production rate calculated by the MCM with a 60° pitch angle.

The production rate for each of these ions can be used to obtain the emitted photon flux as given by:

$$4\pi \cdot I = \int_{z_0}^{\infty} P(z) \cdot \exp^{-\tau(z)} dz \tag{4.18}$$

where I is the intensity in units of $\mathrm{cm}^{-2}\mathrm{s}^{-1}\mathrm{sr}^{-1}$, $4\pi I$ is the emitted photon flux in units of $\mathrm{cm}^{-2}\mathrm{s}^{-1}$, z_0 is the deepest altitude the beam reaches in the atmosphere before running out of energy, z is the altitude of the ion beam, $P(z)$ is the production rate that was previously calculated, and τ is the optical length at a specific altitude for a particular photon energy. The calculated photon flux rapidly increases for ion energies less than 2 MeV/u, but grows almost at a constant rate for higher energies.

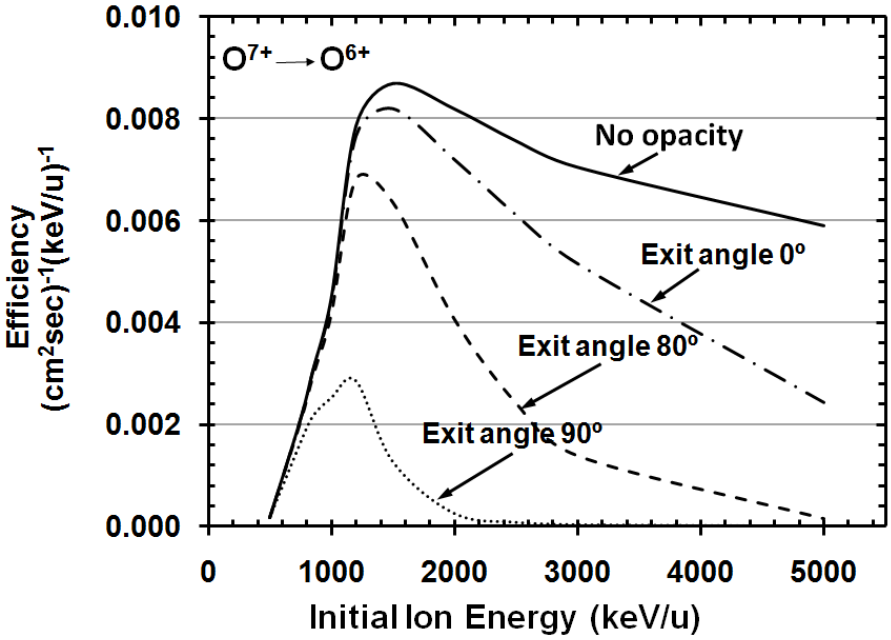

Figure 4.15: Outgoing x-ray photon flux efficiency as a function of initial ion energy for O^{6+} production. The solid line shows the efficiency without any opacity effects. Opacity effects are represented by the other curves. The dot-dashed line shows the photon flux efficiency if opacity if considered for a 0° angle. The dashed line shows the photon flux efficiency for an exit angle of 80° with respect to the pole. The dotted line shows the photon flux efficiency for an exit angle of 90° with respect to the pole.

An emission efficiency was found by dividing $4\pi I$ by the value of the initial ion energy. The efficiency for each oxygen charge state (O^{6+} and O^{7+}) is shown in Figures 4.15 and 4.16 (solid line, no opacity effects considered), and the S^{8+} efficiency is shown in Figure 4.17.

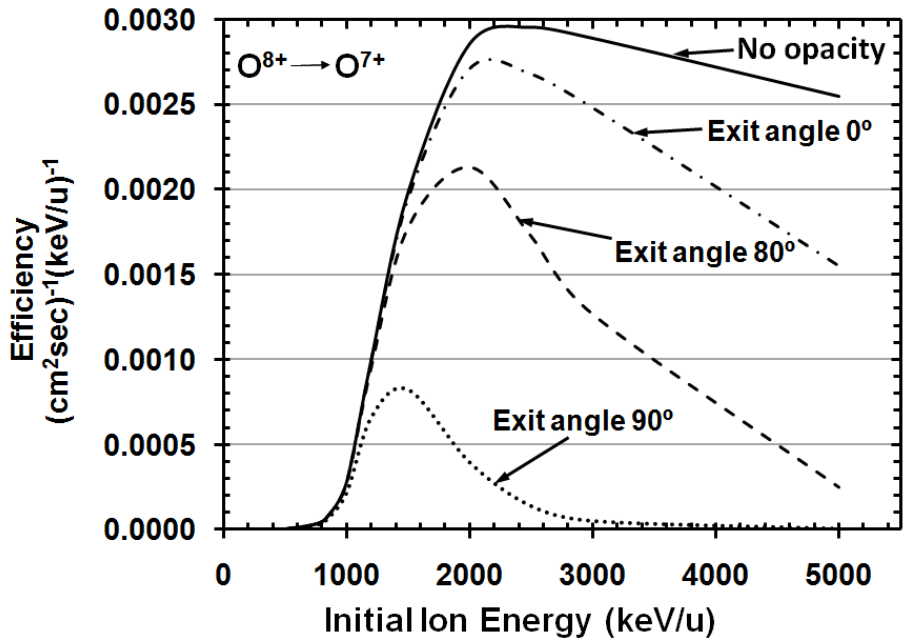

Figure 4.16: Outgoing x-ray photon flux efficiency as a function of initial ion energy for O^{7+} production. The solid line shows the efficiency without any opacity effects. Opacity effects are represented by the other curves. The dot-dashed line shows the photon flux efficiency if opacity if considered for a 0° angle. The dashed line shows the photon flux efficiency for an exit angle of 80° with respect to the pole. The dotted line shows the photon flux efficiency for an exit angle of 90° with respect to the pole.

The most efficient x-ray production from O^{6+} ions occurs for incident ions with energies of about 1.5 MeV/u and from O^{7+} ions for incident ions with initial energies of 2.5 MeV/u.For incident sulfur ions with energies of about 1 MeV/u are the most efficient in producing S^{8+}. The maximum production efficiency of O^{6+} ions is about

three times greater than the production efficiency of O^{7+} ions. However, the maximum production efficiency of S^{8+} ions is about 1.5 times that of the O^{6+} ions.

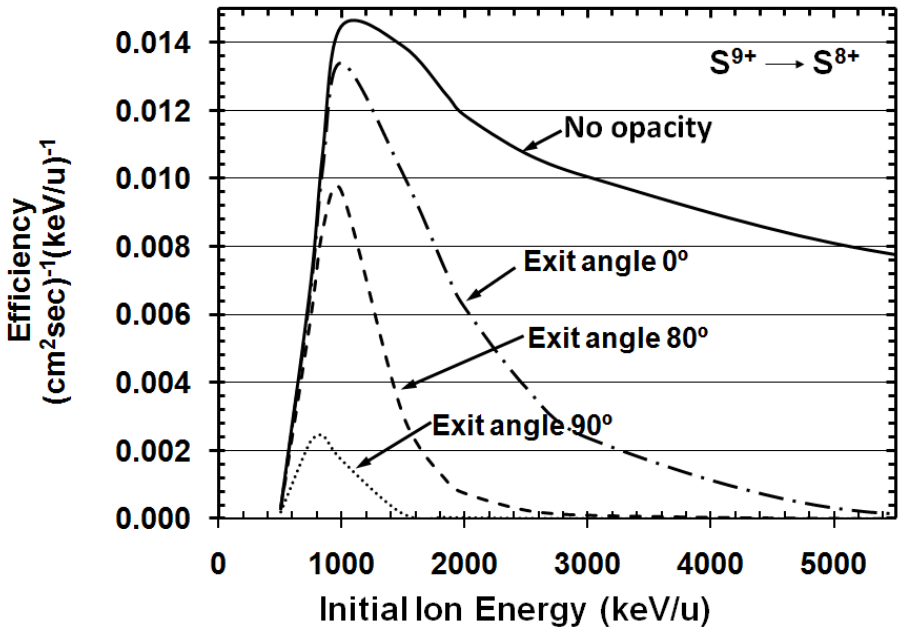

Figure 4.17: Outgoing x-ray photon flux efficiency as a function of initial ion energy for S^{8+} production. The solid line shows the efficiency without any opacity effects. Opacity effects are represented by the other curves. The dot-dashed line shows the photon flux efficiency if opacity if considered for a 0° angle. The dashed line shows the photon flux efficiency for an exit angle of 80° with respect to the pole. The dotted line shows the photon flux efficiency for an exit angle of 90° with respect to the pole.

4.3.3 Opacity Effects

Opacity effects due to atmospheric absorption of outgoing photons should be taken into account. The optical depths were calculated with equation 4.13, as explained in section 4.2.5, and then used in equation 4.18 to calculate a new photon flux for O^{6+}, O^{7+} ions and S^{8+} ions. As an approximation, equation 4.18 was calculated by using the outgoing photon energies of 560.984 eV, 652.723 eV, and 223.218 eV for O^{6+},

O^{7+}, and S^{8+} ions respectively, which are the photon energies for the most intense emission lines. The results are plotted in Figures 4.15, 4.16, 4.17, where the calculated photon emission efficiency without any opacity effects is shown (solid line) and can be compared to the opacity effects given by 0° (dash-dotted line), 80° (dashed line) and 90° (dotted line) exit angles. Opacity effects become significant for incident ion energies higher than 2 MeV/u for O^{7+} ions, 1.2 MeV/u for O^{6+} ions and 1 MeV/u for S^{8+} ions, especially for angles greater than 80°. For energies higher than 5 MeV/u the atmosphere becomes almost opaque to outgoing x-rays for these greater angles.

4.3.4 X-ray Spectra

To simulate a prototypical spectrum the branching ratios for each spectral line (photon energy) were calculated based on the relative photon yields for each ion species and charge state (e.g., O^{q+}) given by [21], which is the most complete spectra available to date. We have used a total of 354 emission lines that correspond to photon energies above 200 eV to fit the x-ray spectra and which include both sulfur and oxygen charge states. See the Appendix tables A.15 to A.19 for the photon count per incident ion obtained by [21] that is used as the compared synthetic spectra. Here we use our calculations to provide the production rate of a given ion species and charge state. In their paper, Hui et al. fit their calculated spectra to Chandra X-ray Observatory (CXO) observations made by [54] for both north and south auroral emissions. We have chosen the best fits achieved by Hui et al. for the CXO observation ID 3726 reported and we used their parameters in our model. For the north auroral observation, initial energies of 1.2 MeV/u for oxygen and 501 keV/u for sulfur were taken as optimal fits [Hui private conversation]. For the south auroral observation, initial energies of 2 MeV/u for oxygen and 1.860 MeV/u for sulfur were taken as optimal for the fit. We then calculated the

emitted photon flux for all 354 energies by using our Monte Carlo methodology and combined them with the corresponding branching ratios given by [21].

For the northern spectrum a sulfur to oxygen ratio of 204 was used for the calculation, as suggested by [21] Table 2, for the best fit. The emissions were then smoothed with Gaussian line profiles with a half-width of 24.5 eV to match those used by models developed, like [51] and [52]. We must note that [21] uses half-widths of 55 eV in order to match instrumental response functions and to speed up the fitting procedure. Our spectra (solid line in Figure 4.18) matched the calculated one by Hui et al. reasonably well (excellent in shape of the spectrum but differences in absolute intensity). However, the absolute intensity of the observations was not considered by Hui et al., just the relative intensity versus photon energy. Our model, which differs from the Hui et al. energy deposition methods, might be expected to have different absolute intensities for an ion species overall (but not the relative line strength within an ion species which we took from Hui et al.).

Opacity effects depend on the viewing geometry which is different for different observations and for the North and South aurora. We used equation 4.18 and calculated the optical depth for each different line (photon energy) separately. Considering the polar cap x-ray emission area for the North aurora observations of [54] (see his image of the auroral emission – Figure 2 of that paper), the exit angle of a path from the emission region to the Earth is 80° with respect to the vertical (zenith). For the South the emission appears to be on the limb or an emission angle of about 90°. Since the initial energy chosen for sulfur in this fit is less than 1 MeV/u, its contribution to the spectrum is a lot smaller than that of oxygen.

For the southern spectrum a sulfur to oxygen ratio of 0.94 was chosen, again to follow the modeled observations by [21]. This result is shown in Figure 4.19 by the solid line, which does not consider any opacity or quenching effects. The viewing

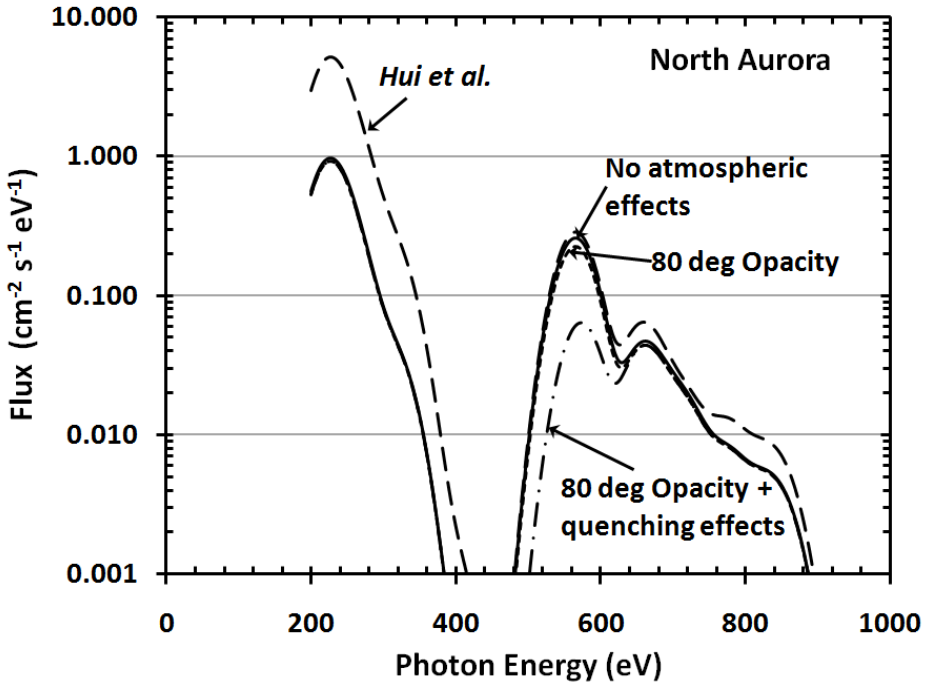

Figure 4.18: Spectra calculated for the north aurora by using [21] as a proxy to the observational data. Initial energies considered for this calculation are 1.2 MeV/u for oxygen and 0.51 MeV/u for sulfur. A sulfur to oxygen ratio of 204 was taken. The long dashed curve shows the proxy data from [21] as a comparison. The solid line shows our current model without any opacity or quenching effects. The small dashed line shows the current model with opacity effects. Note that it is almost overlapping the current model line (solid line). The dashed-dotted line shows the current model with opacity and quenching effects.

geometry for the southern auroral oval is different than the northern one and an exit angle of 90° is chosen for the calculations. As shown in Figure 4.19 by the dotted line, this opacity effect is quite large on the spectrum. This is to be expected, since the initial energies chosen for this fit are well above the point where opacity has a large effect, as shown by the efficiency calculations (Figures 4.15, 4.16, 4.17).

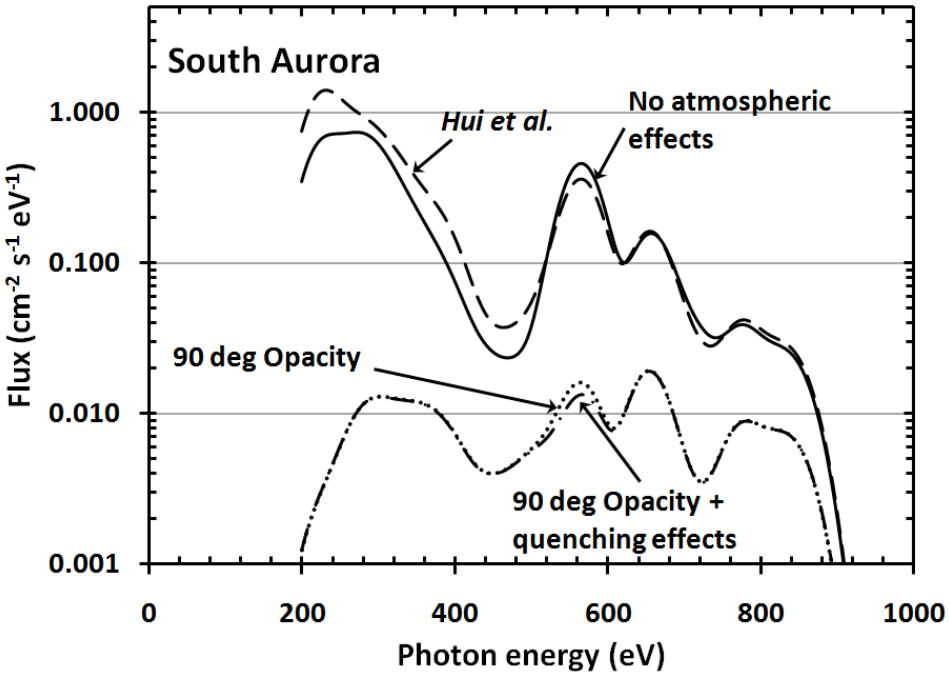

Figure 4.19: Spectra calculated for the north aurora by using [21] as a proxy to the observational data. Initial energies considered for this calculation are 2.0 MeV/u for oxygen and 1.86 MeV/u for sulfur. A sulfur to oxygen ratio of 0.94 was taken. The long dashed curve shows the proxy data from [21] as a comparison. The solid line shows our current model without any opacity or quenching effects. The small dashed line shows the current model with opacity effects. Note that it is almost overlapping the current model line (solid line). The dashed-dotted line shows the current model with opacity and quenching effects.

4.3.5 Quenching Effects

Quenching of some long-lived O^{6+} states also affects x-ray production and the spectrum. For an O^{6+} ion there are two transitions of interest to us: the $1s2s\ -\ 1s^2$ ($^3S\ -\ ^1S$) transition (forbidden) and the $1s2p\ -\ 1s^2$ ($^3P^0\ -\ ^1S$) transition (intercombination), with Einstein A coefficients equal to 1.04×10^3 s^{-1} and 3.31×10^5 s^{-1} respectively [97]. Once the quenching rate was found with equation 4.16, the corresponding quenched photon flux emitted (for the transition in question) was calculated

by modifying equation 4.18, as described by the following equation:

$$4\pi \cdot I = \int_{s_0}^{\infty} P(z) \cdot \exp^{-\tau(z)} \frac{A}{A + R(z)} dz \tag{4.19}$$

where $P(z)$ is the production rate for O^{6+} ions in this case multiplied by the fraction ending up in the metastable state (i.e., ^3S or $^3P^0$) in question, A is the Einstein A-coefficient for the specific forbidden transition, and $R(z(s))$ is the quenching rate. The opacity factor was calculated for each of the 354 photon energies as explained in the previous section and the production rate of the O^{6+} quenched ions is normalized to that of the unquenched.

This quenching effect was included in the north and south spectra for these two emission features. The results are shown by the dash-dotted line shown in Figures 4.18 and 4.19. It can be seen that the effect in the spectrum is considerable, especially in the north. In the south the opacity effect is already quite large, so in comparison, the quenching effect is smaller.

4.4 Discussion

The calculations carried out here demonstrate that most x-ray photons are produced by 1.5 – 2 MeV/u oxygen ions and 1 – 2 MeV/u sulfur ions, which is consistent with recent model spectrum comparisons with observations [21, 50–52]. Higher energy ions can contribute to the x-ray auroral emissions but with lower efficiency. These ions are mainly ionizing the atmosphere.

Our calculations demonstrate that opacity effects do not significantly impact the emitted x-ray spectrum for initial ion energies below $\sim$ 1 MeV/u, but for larger ion energies opacity should be taken into account, especially for exit angles with respect

to the zenith greater than about 80°. For such emission geometries opacity becomes important for those ion energies most efficient in producing x-rays. The effects of opacity depend somewhat on the atmospheric model used and, in particular, on the homopause altitude because the methane abundance falls off rapidly above this transition altitude and because methane's photoabsorption cross section for soft x-rays is quite large [98], [99]. Unfortunately, the structure of the polar thermosphere and ionosphere is not well known (the Galileo probe entered the equatorial atmosphere).

We estimated the effects on auroral x-ray emission of the quenching of the metastable n=2 states of O^{6+}. Significant quenching effects were found for the ${}^3P^0 - {}^1S$ and ${}^3S - {}^1S$ n=2 transitions (i.e., the intercombination and forbidden transitions, respectively), and particularly for the ${}^3S - {}^1S$ transition. The forbidden line is almost completely quenched for energies greater than about 1 MeV/u, as earlier recognized by [51]. Quenching is not strongly sensitive to the details of the atmospheric model used.

When comparing our synthetic spectrum with that of [21], it was evident that the opacity effects are very important for the south aurora where the observation angle is roughly 90° and not so important for the north. For the southern auroral emissions the opacity/geometry becomes the dominating factor in diminishing the intensity of the emissions. In fact, the geometry could be such that much of the x-ray emitting region might not be visible to the Earth due to the planetary tilt and location of the magnetic polar cap. After considering how opacity and quenching effects diminish the spectrum, one might have to consider a much larger flux of incoming oxygen and sulfur ions (but Hui et al. did not model the absolute intensities of the observed aurora) and different sulfur to oxygen ratios to actually match the observations. The Hui et al. spectrum, when altered with the CXO instrument response function, gives a good fit to the observed spectrum both in the north and south polar regions. For our spectra to match the observations (i.e., the Hui et al. spectra) a larger sulfur to oxygen ratio

would be required. In particular, for the north this ratio should be ≈ 1.25, although the quenched lines would still show a smaller intensity. The south opacity has such a large effect on sulfur that it distorts the spectrum. An exact sulfur to oxygen ratio is hard to estimate, but an increase in sulfur to oxygen ratio of $\sim$10 times would be sufficient to match Hui et al. The difference in the intensities between those given by Hui et al. and our model shows that our model is less efficient in producing x-rays mostly due to quenching as well as the difference in the energy deposition methods used.

We also estimate a "global" efficiency for Jovian x-ray emission, which we define as the total x-ray luminosity divided by the total incoming power of precipitating ions. This can be determined by dividing the outgoing power per unit area (integrated over all x-ray energies) by the net incoming power per unit area for the incident ions. We neglect opacity and quenching effects for this estimate, since we are assuming the total luminosity emitted from the planet (including radially outgoing photons) and not just the observed luminosity. For the north aurora, as discussed above, the best fit was found for initial oxygen ion energies of 1.2 MeV/u and initial sulfur energies of 0.51 MeV/u (based on [21]), as well as a sulfur to oxygen ratio of 204. For a net downward oxygen flux of 1/cm^2/s and a net downward sulfur flux 204 times that, we obtain outward photon intensities assumed to be over 2π steridians and estimate an outgoing energy flux of about 3 keV/(cm^{2}s) for combined sulfur and oxygen emissions. Considering the sulfur to oxygen ratio mentioned above, the downward/incoming energy flux for all ions is 6.7 GeV/(cm^{2}s), giving the north aurora an efficiency of $\varepsilon \approx 4.7 \times 10^{-7}$. A typical observed total x-ray luminosity is $\approx$ 1 GW [53], [42]. Using the estimated efficiency for the north aurora this observed x-ray luminosity implies an auroral ion input power of $\sim\ 2 \times 10^{15}$ W, which is about 10 times larger than the total auroral input for electrons as estimated from the observed UV aurora [100], [101], [1]. Such a large input power from ion precipitation seems unlikely and we note that this is due

to the low initial energy of the sulfur ions (510 keV/u), which as a consequence also required a very high sulfur to oxygen ratio to match the observations. Such low initial energy sulfur ions are not very efficient in x-ray production (please refer to Figure 4.17) and this lack of emission must be compensated by a high ratio with respect to oxygen. If a higher initial energy for sulfur were considered (e.g., 1.0 – 1.5 MeV/u) a much lower sulfur to oxygen ratio would be required, which in turn would increase the global efficiency and decrease the input power needed.

For the south aurora the best fit values were found for an initial oxygen energy of 2 MeV/u and an initial sulfur energy of 1.86 MeV/u and a sulfur to oxygen ratio of 0.94. For these higher energies the opacity effect for a 0° angle has some effect (refer to Figures 4.15, 4.16 and 4.17) and was considered in the calculations. The net outgoing energy flux for both ion species is $\approx$ 12.5 keV/cm^2/s) and the downward/incoming energy flux is $\approx$ 175 MeV/cm^2/s). These values give the south aurora a global efficiency of $\varepsilon \approx 7.13 \times 10^{-5}$, which is much larger than the one found for the north. Again, if we consider a typical observed luminosity of about 1 GW, the required auroral ion input power is 1.4×10^{13} W, which is about a factor of 5 – 10 less than expected UV emission observed from electron precipitation [101]. This result also supports the possibility that for the northern aurora higher initial sulfur energies and a lower sulfur to oxygen ratio would give a more reasonable global x-ray emission efficiency.

Chapter 5

Primary Electron Precipitation and Photoelectrons in the Auroral Region

5.1 Primary Electron Precipitation

As we have mentioned in previous chapters, the precipitation of energetic charged particles in a planetary atmosphere (in our case Jupiter) produces aurora. These auroral emissions are the product of collisions between these charged particles and the neutrals in the atmosphere. Although our study concentrates on the energetic ion precipitation in the Jovian atmosphere, energetic electron precipitation at Jupiter is also a very important process. The electron precipitation originates with the coronation breakdown that occurs in the middle magnetosphere due to mass loading (see section 1.4.1 for a review on this topic). This torque creates a current system that couples the mid-magnetosphere to the ionosphere of the planet (MI-coupling system). The Birkeland currents in this MI-coupling accelerate the electrons to high energies ($\geq$ 100 keV in some cases). The bulk of the observed electrons have energies ranging between 1 – 30 keV. The energetic electrons are the source of the UV emissions that are observed as the auroral oval (for a review on the UV aurora and the auroral oval at Jupiter we refer the reader to [1]).

Spectroscopic observations of the UV emissions suggest a total auroral particle input flux of the order of $10^{13} - 10^{14}$ W in each hemisphere, which is about three orders of magnitude stronger than the particle input flux for Earth [101]. Models assume that most of this energy input is due to electrons, instead of protons or heavy ions. The reason is that so far, there is no evidence for strong proton precipitation in the Ly-α profiles and the oval spectrum also shows no indication of the line emission expected for the oxygen and sulfur ion precipitation, as observed in the x-ray aurora.

The energy flux being input by the electrons in the atmospheric auroral region is about 100 times that of the global extreme ultraviolet due to solar radiation. This large energy input from the electrons has major consequences in the upper atmosphere due to ionization of the neutral species present, radiation, and particle heating. This heating is capable of maintaining large exospheric temperatures that are observed at the mid- and high latitudes of the planet [101]. According to models, about 50% of the electron energy is converted to heat in the neutral atmosphere [22, 101]. The excitation to the $b^3\Sigma_u^+$ state and the ionization of H_2 (see Chapter 2 for the cross section information) are among the most important processes for heating the atmosphere. Rotational and vibrational excitation of H_2 are, very efficient for cooling the thermal electrons, ultimately heating the atmospheric neutrals via collisions. In order to model the primary electron transport in an atmosphere (in our case for Jupiter), energy degradation models have been developed in the past 30 years. A commonly used model assumes a mean pitch angle for the transported electrons, which allow to approximate their distribution by an upward and downward flux. This method is called the two-stream approach and will be explained in the next section.

5.1.1 Suprathermal Electron Transport

Suprathermal electrons (1 eV $<$ E $<$ 200 eV) in a magnetic field will follow helical trajectories along the field line consisting of gyration around a so called gyro-center as well as a motion of the gyro-center parallel to the field line [26, 71]. If these electrons are moving in a non-uniform magnetic field that varies slowly compared to the gyro-frequency or at long scales compared to the gyroradius and are moving in a parallel magnetic field, one may write their Boltzmann equation as:

$$\frac{\partial f}{\partial t} + v_z \frac{\partial f}{\partial z} - e/m \cdot E_{\parallel} \left\{ \mu \frac{\partial f}{\partial v} + \frac{1+\mu^2}{v} \frac{\partial f}{\partial \mu} \right\} - \frac{v(1-\mu^2)}{2B} \frac{\partial B}{\partial z} \frac{\partial f}{\partial \mu} = (\frac{\delta f}{\delta t})_{coll.} \quad (5.1)$$

In equation 5.1, the distribution function in phase space is $f = f(\vec{x}, \vec{v}, t) = f(z, v, \mu, t)$. Here $\mu = \cos\theta$, where θ is the pitch angle for the electron. z is the distance along the field line, i.e, parallel to the field, and v is the velocity component along the field line. From this equation, we can also notice that the only effect of the magnetic field on the distribution is on the pitch angle distribution. The parallel electric field, $E_{\parallel}$, changes the pitch angle distribution and accelerates the electrons. If the magnitude of the magnetic field is roughly constant along the field line, the divergence term $\frac{\partial B}{\partial z}$ on equation 5.1 may be neglected.

The flux up (Φ^+) or down (Φ^-) a field line, in units of $\mathrm{cm}^{-2}\mathrm{s}^{-1}\mathrm{eV}^{-1}$ at a distance s for a particular energy $\varepsilon = 1/2 m_e v^2$ is defined by [102] as:

$$\Phi^+(s, \varepsilon) = \int_0^{\pi} \frac{2\pi v^2}{m_e} f(s, v, \theta) \sin\theta d\theta \quad (5.2)$$

$$\Phi^-(s, \varepsilon) = \int_{\pi/2}^{\pi} \frac{2\pi v^2}{m_e} f(s, v, \theta) \sin\theta d\theta \quad (5.3)$$

Now, let $\Phi = 2\varepsilon/m^2 f$, where ε is the kinetic energy of the particle. Then we can rewrite the transport equation as:

$$\sqrt{m/(2\varepsilon)}\frac{\partial\Phi}{\partial t}+\mu\frac{\partial\Phi}{\partial r}+e/mE_{\parallel}\varepsilon\mu\frac{\partial}{\partial\varepsilon}(\frac{\Phi}{\varepsilon})+(\frac{eE_{\parallel}}{E}-\frac{1}{B}\frac{\partial B}{\partial r})\frac{1-\mu^2}{2}\frac{\partial\Phi}{\partial\mu}=\sqrt{m/(2\varepsilon)}\frac{\delta\Phi}{\delta t} \tag{5.4}$$

If we assume steady state ($\partial\Phi/\partial t = 0$), neglect external electric fields E, and assume that the change in B is negligible, then the previous equation simplifies to:

$$\mu\frac{\partial\Phi}{\partial r}=\sqrt{m/(2\varepsilon)}\frac{\delta\Phi}{\delta t} \tag{5.5}$$

These sets of equations were originally solved by [103] and [104] for transport of photoelectrons in Earth's ionosphere. The solution is known as the two-stream approach (or two-stream equations), since they approximate the electron transport along the field line in two directions (or streams): upward and downward. The two-stream equations are [71]:

$$\langle\mu\rangle\frac{\partial\Phi^+}{\partial r}=-n_k\sigma_s^t\Phi^+ +\frac{n_s\sigma_s^e}{2}(\Phi^+ +\Phi^-)+\frac{Q_0}{2} \tag{5.6}$$

for the upward flux, and:

$$\langle\mu\rangle\frac{\partial\Phi^-}{\partial r}=-n_k\sigma_s^t\Phi^- +\frac{n_s\sigma_s^e}{2}(\Phi^+ +\Phi^-)+\frac{Q_0}{2} \tag{5.7}$$

for the downward flux. Here, n_k is the neutral density for a given species k, σ_s^t is the total cross section and σ_s^e is the elastic scattering cross section. As previously shown, the upward and downward fluxes (Φ^+ and Φ^-) may be calculated by integrating the distribution function as function of angle and position $(r,\mu\phi)$. In the previous equations

the last term is given by the supra-thermal electron production:

$$Q_0(r) = \int_0^{2\pi} d\phi \int_{-1}^{1} P_e(\phi, \mu, r) d\mu \tag{5.8}$$

where P_e is the electron production rate. In our model, we solve the set of transformed Boltzmann equations to a steady state. After some manipulation, the two-stream equations solved by the code are:

$$\frac{d\Phi^{\mp}}{ds} = -\sum_k n_k(s)(\sigma_a^k + p_s^k \sigma_s^k)\Phi^{\mp}(\varepsilon, s) + \sum_k n_k(s) p_e^k \sigma_e^k \Phi^{\pm}(\varepsilon, s) + \frac{q(\varepsilon, s)}{2} + q^{\mp}(\varepsilon, s). \tag{5.9}$$

Here, σ_a^k is the total inelastic cross section for a neutral species k, p_s^k and σ_s^k are the electron backscatter probability and cross section, respectively. Therefore, the first term of the equation accounts for the loss of electrons from the flux in a given direction due to absorption or backscatter (change in the direction, therefore showing up in the opposite flux). In the second term, p_e^k and σ_e^k are the elastic probability and cross section, respectively. The third term accounts for the photoelectron production rate due to direct photoionization, and the last term gives the electron production due to cascading and is given by:

$$q^{\mp}(\varepsilon, s) = \sum_k n_k(s) \sum_{i, E>\varepsilon} \{p_{aj}^k(E)\sigma_{aj}^k(E \to \varepsilon)\Phi^{\pm}(E, s) + (1 - p_{aj}^k(E))\sigma_{aj}^k(E \to \varepsilon)\Phi^{\mp}(E, s)\}. \tag{5.10}$$

The cascading terms involve book-keeping the electrons as they move from one energy bin to another bin. This may happen for the flux in one direction (either up- or downward) or it may also occur between the fluxes (an electron may cascade from the upward flux to the downward flux via backscatter collision).

5.1.2 Our Two–Stream Code: Validation of the Code

All the cross sections that we use to solve the two-stream equations for our model are found in Chapter 2. Without an extensive compilation of the appropriate cross sections it would not be possible to solve the two-stream equations. As the electrons travel along the field line, they undergo elastic and inelastic collisions with the atmospheric neutrals (H_2, H, He, and CH_4). One can see that the two-stream calculation takes into account electron-electron collisions, electron neutral collisions, as well as the production and loss of electrons along the field line. The total flux calculated at each energy bin includes the primary production from photoionization, the production of electrons by inelastic collisions with neutrals and the cascade of electrons by energy degradation due to inelastic collisions from higher energy electrons. The two-stream code that we use calculates the evolution of the electron energy as a function of altitude (i.e., the transport of the electrons and their energy) by using a set of discrete energy bins. The energy bins have widths ranging from 0.5 eV for low energies (less than 10 eV) and increase to 200 eV widths for the highest energies (reaching 200 keV).

In order to validate our code and make sure that the results are reasonable, we tested it by inputing electron beams of a given flux and initial energy used in the models of [22] and compared our results. The main differences between the two models are the updated cross sections and the atmospheric model that we are using. Both models use the two-stream approach implemented for the electron transport. In their paper, *Waite et al.* present calculations by injecting electron beams of initial energy of 1 and 10 keV, which correspond to 950 and 9800 eV on their energy grid, and with an initial flux of 10 ergs/cm^2/s. In our code, due to the difference in energy bins between the two modes, the corresponding energies are 975 eV and 9900 eV, respectively. A good way to compare the two models is by looking at the ion production rates calculated. We

look at the ion production of H_2^+ and H^+ due to each auroral electron beam (one with 1 keV electrons and another with 10 keV electrons). The ion production rate of any ion species at a given altitude is calculated in the two-stream code by:

$$P^{n_k}(s) = \sum_E \sigma_{ion}^{n_k} \cdot (\Phi^+(s) + \Phi^-(s))\Delta E; \tag{5.11}$$

where $\sigma_{ion}^{n_k}$ is the ionization cross section for a given ion species n_k, at a given electron energy E and $\Phi^{\pm}$ is the upward/downward electron flux at the given altitude s along the field line.

Our results for a mono-energetic beam with initial energy of 1 keV (975 eV) are shown in Figure 5.1 and for a beam with initial energy of 10 keV (9900 eV) are shown in Figure 5.2. As a comparison, we show the calculated production rates for H_2^+ and H^+ from [22] in Figure 5.3. We can see that our production rate is not identical to that shown by [22]. This was to be expected because, as mentioned earlier, our cross sections and atmosphere are not the same. However, the location and value of the peak production rate for both ions (H_2^+ and H^+) in both models is at a very similar value for the 10 keV electron beam. For the 1 keV beam our model has a larger production rate, but the peak is located at the same altitude. This validates the energy deposition process, as it appears that the electrons are loosing most of their energy in the same region of the atmosphere.

As reviewed in Chapter 2 there is no data available for inelastic backscatter cross sections. Therefore, in our model we assume that they are equal to the elastic backscatter cross sections. Also, the backscatter probabilities of H and He are taken to be equal. In order to see what kind of effect this would have in our calculations, we have computed the ion production rate as explained in the previous paragraph, but without any backscatter probability, i.e., $p_s^k = 0$. The result is shown in Figure 5.4. From the figure

we can see that the difference in the production rate by ignoring backscatter of electrons is less than 10 %. This is a very small effect considering the uncertainties in the other cross sections.

We calculate the average energy for the creation of an ion pair, which allows us to check that the code is calculating the electron fluxes, energy degradation and ion production rates properly. It is known from the literature that the average energy for ion pair production is $\sim$ 35 – 40 eV [26, 71, 105]. We calculate the average ion pair energy by introducing mono-energetic electron beams with energies ranging from 25 – 180,000 eV with a flux of 1000 $\mathrm{cm^2 s^{-1} eV^{-1}}$. We then calculate the electron density n_e by adding the total ion production for all possible ion species considered. The average energy per pair is given by:

$$\langle E_{pair} \rangle = \Phi_{init} \langle \mu_{avg} \rangle E_{init} n_e^{-1} dE. \tag{5.12}$$

For incident electron energies greater than 50 eV the average energy needed for an ion pair is $\approx$ 35 eV. However, as the input energy decreases, this energy rapidly increases, showing an asymptotic behavior as the energy approaches the threshold energy. Our results for the average energy per ion pair as a function of incoming electron energy are shown in Figure 5.5.

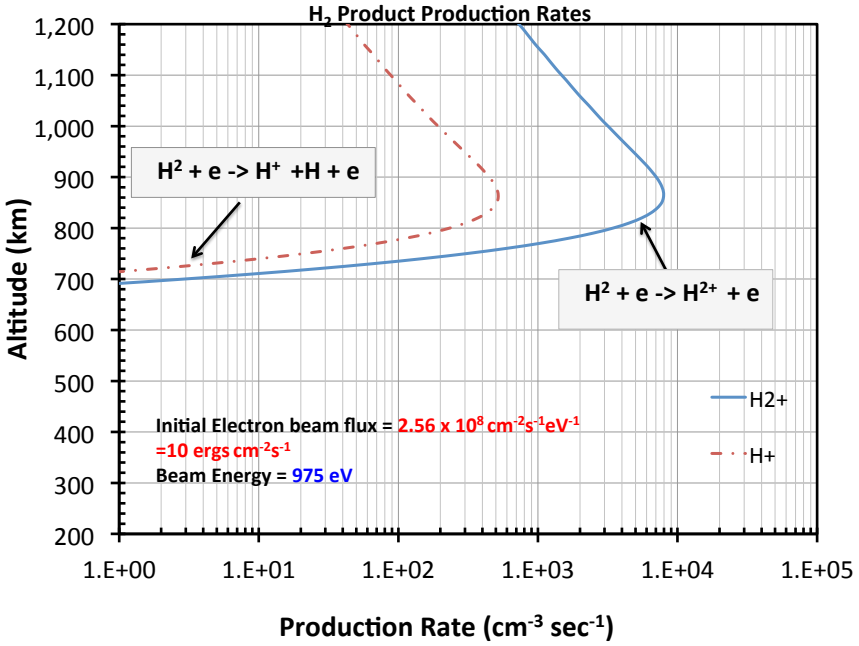

Figure 5.1: A mono-energetic beam of electrons with a flux of 1 erg/cm^2/s and energy of $\sim$ 1 keV is injected at the top of the atmosphere. As a consequence, the neutral species may become ionized. Here we show the ion production rate [cm^{-3}s^{-1}] for H^{2+} and H^+ production by electron impact ionization of H_2.

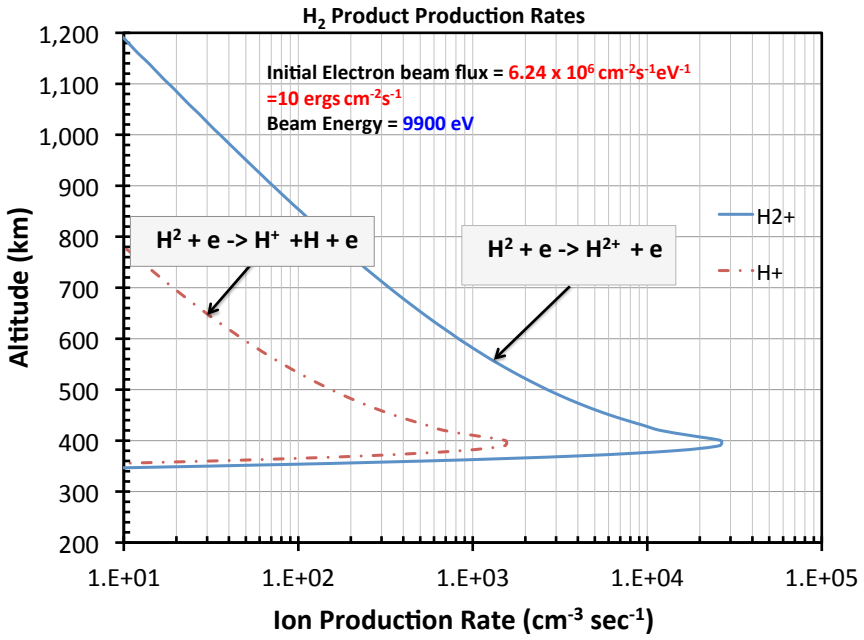

Figure 5.2: A mono-energetic beam of electrons with a flux of 1 erg/cm^2/s and energy of $\sim$ 10 keV is injected at the top of the atmosphere. As a consequence, the neutral species may become ionized. Here we show the ion production rate [cm^{-3}s^{-1}] for H^{2+} and H^+ production by electron impact ionization of H_2.

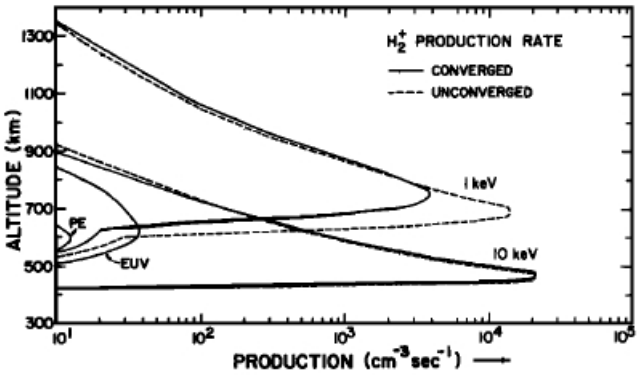

Fig. 7. H_2^+ ion production rate as a function of altitude for the 1- and 10-keV electron precipitation cases, as well as the solar EUV production rates.

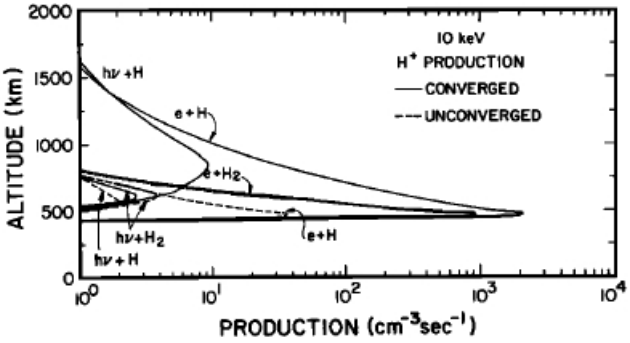

Fig. 8. H^+ production rates as a function of altitude for the 10-keV auroral cases. Note the dramatic increase in the e + H process in the converged (solid line) versus the unconverged (dashed line) auroral atmospheres.

Figure 5.3: H^+ production rates as a function of altitude for a 1keV and a 10 keV electron beam as calculated by [22]. Taken from Figure 8 in [22].

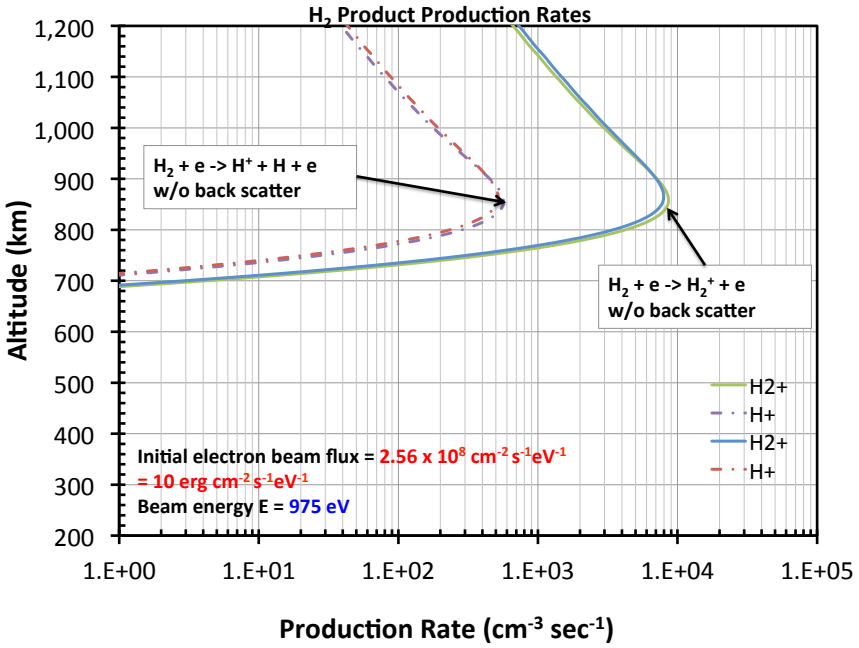

Figure 5.4: A mono-energetic beam of electrons with a flux of 1 erg/cm^2/s and energy of $\sim$ 1 keV is injected at the top of the atmosphere. Here we show the ion production rate [cm^{-3}s^{-1}] for H^{2+} and H^+ production by electron impact ionization of H_2. We have calculated the production rate with and without backscatter collisions as labeled in the plot. No significant difference was found.

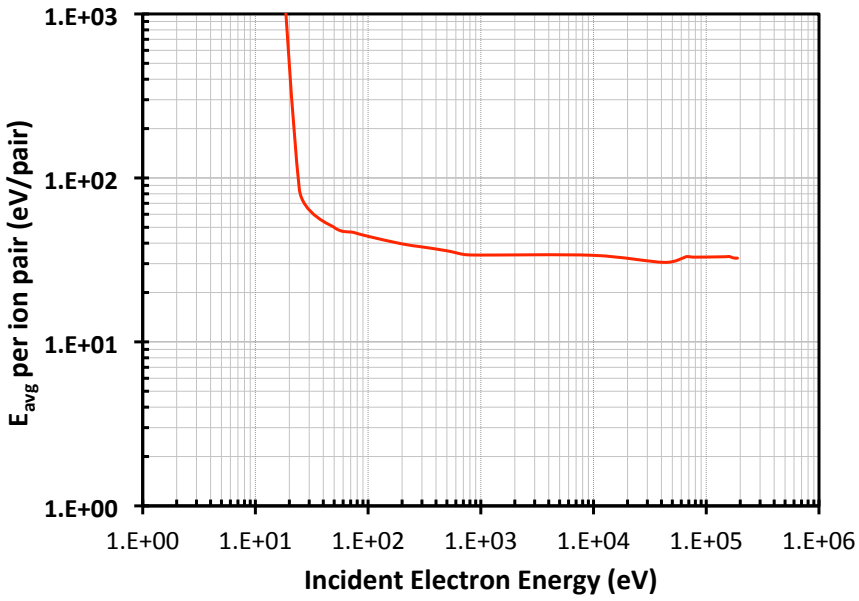

Figure 5.5: Average energy per ion pair produced by the precipitation of mono energetic electrons with a flux of 1000 $cm^{-2}s^{-1}eV^{-1}$.

5.1.3 Primary Electron Precipitation

With the two stream code we calculate the electron fluxes along the field line for monoenergetic auroral electron beams with energies of 20 and 50 keV with a total energy input each of 10 ergs/cm^2/s. This electron flux is "injected" at the top of the atmosphere (z = 3000 km) in order to simulate the effect of an electron aurora. We show the upward and downward electron fluxes at different altitudes for each beam in Figures 5.6 and 5.7. For the downward flux, we can see that for high altitudes, the highest flux is at the beam energy. This is to be expected, since all the electrons injected at the top of the atmosphere have such high energy. However, as the electrons penetrate deeper in the atmosphere, they will collide with the neutrals and cascade down to lower energies as well as produce secondary electrons at lower energies. Therefore, the flux for electron energies between 20 – 1000 eV starts to increase as we go deeper in the atmosphere. It is also interesting to see that in the vicinity of the ion production peak, the behavior of the flux curve is rather different than that for the higher altitudes, in that it increases for energies greater than 1 keV, while the other curves decreased. From the figures we can also see that the flux for electron energies between 20 – 1000 eV is established at altitudes around 750 km and varies very little for lower altitudes until the ion production peak is reached, where the electron beam loses most of his energy. The upward flux figures show that the flux for high energies doesn't re-establish. This means that the energetic electron beam thermalizes as it penetrates the atmosphere and there are no sources in the atmosphere to replenish such high energy electrons. The upward flux for energies greater than 25 eV also remains almost unchanged as we change altitude. The thermal electron flux increases as we go lower in altitude as more and more electrons thermalize by Coulomb collisions. The same characteristic behaviors are seen in both auroral beams.

We also show the flux for specific energies as a function of altitude in Figures 5.8 and 5.9. This figures show the buildup of electron fluxes for energies much lower than the beam energy. For example, for the suprathermal energies chosen in the figures, the downward flux is very low at the highest altitudes. However, as the electron beam is transported deeper in the atmosphere, it loses energy due to collisions and produces secondary electrons. We can see how the flux for the lower energies rapidly increases for altitudes between 3000 – 1000 km. Around 1000 km the flux becomes almost constant for energies between 20 – 100 eV, where a balance between production and loss is reached. However, at the lower energies (9.75 eV in our case) the flux continues to increase as the electrons continue to themalize due to electron-electron collisions. We can see a peak in the fluxes at a deeper altitude where the beam penetrates and where the ion production peaks occur. This peak occurs around 350 km (or neutral density of 8×10^{13} cm^{-3}) for the 20 keV electron beam and around 300 km (or neutral density of 10^{15} cm^{-3}) for the 50 keV electron beam. The upward electron fluxes show a similar behavior as the downward fluxes at low altitudes, i.e., they also have a small peak in the flux. In fact, for these low altitude the flux is isotropic, i.e., the upward and downward fluxes are approximately equal to each other. However, as the flux moves upward in the atmosphere it remains almost constant for energies greater than 50 eV. This tells us that the flux and loss processes for these energies are in equilibrium and the electrons are able to escape the atmosphere. For lower energies there is a slow decrease up to altitudes of around 2000 km before the flux remains constant.

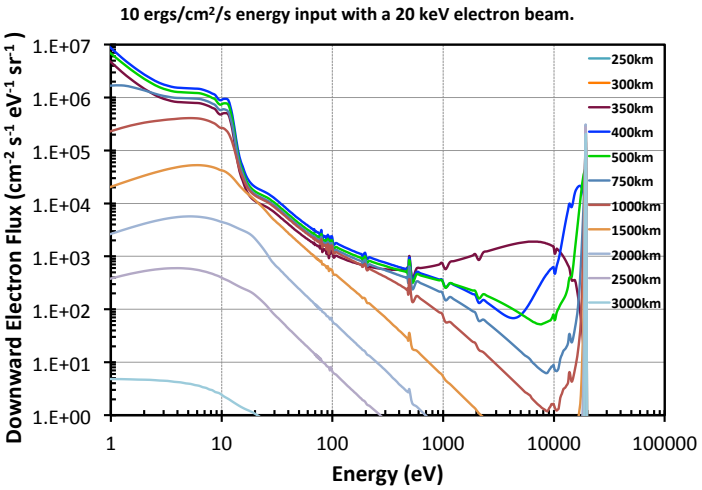

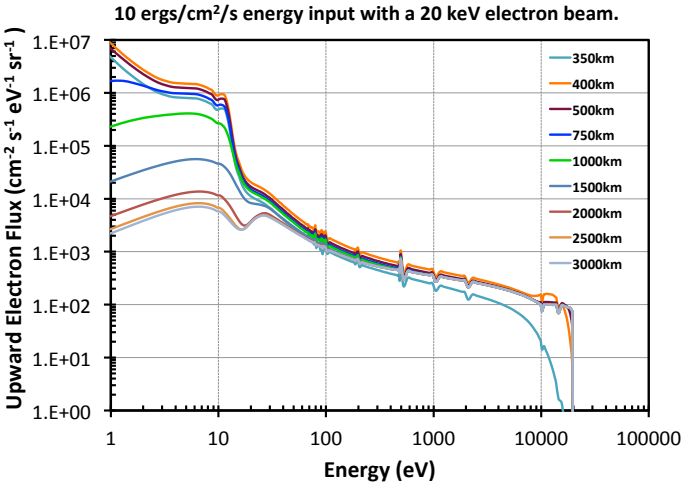

Figure 5.6: Downward (top) and upward (bottom) electron fluxes due to a monoenergetic beam of 20 keV electrons with a total input of 10 ergs/cm^2/s at different altitudes along the field line. No photoelectrons are considered in the calculations.

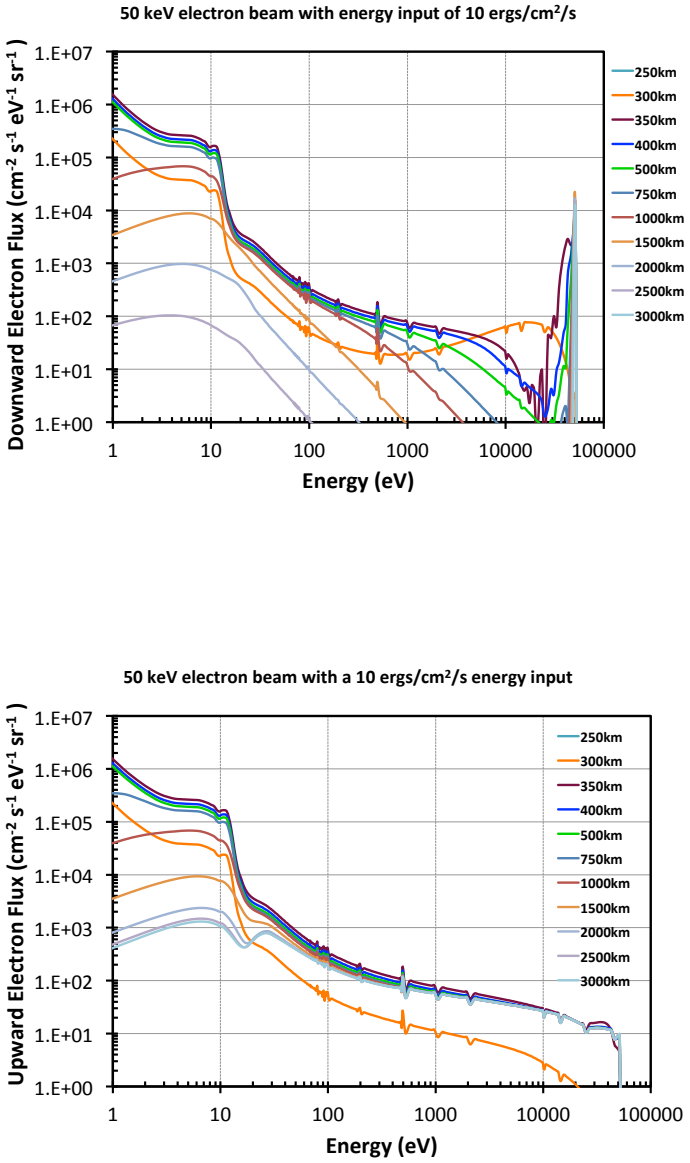

Figure 5.7: Downward (top) and upward (bottom) electron fluxes due to a monoenergetic beam of 50 keV electrons with a total input of 10 ergs/cm^2/s at different altitudes along the field line.No photoelectrons are considered in the calculations.

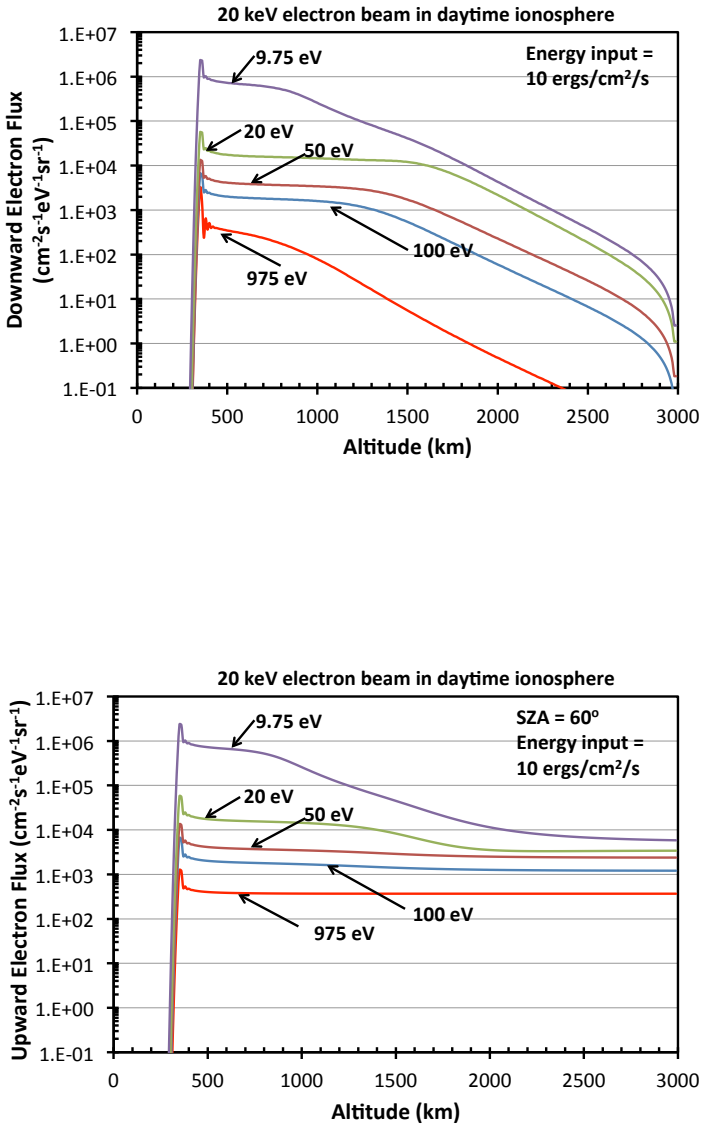

Figure 5.8: Downward (top) and upward (bottom) electron fluxes due to a monoenergetic beam of 20 keV electrons with a total input of 10 ergs/cm^2/s for different electron energies as a function of altitude along the field line.No photoelectrons are considered in the calculations.

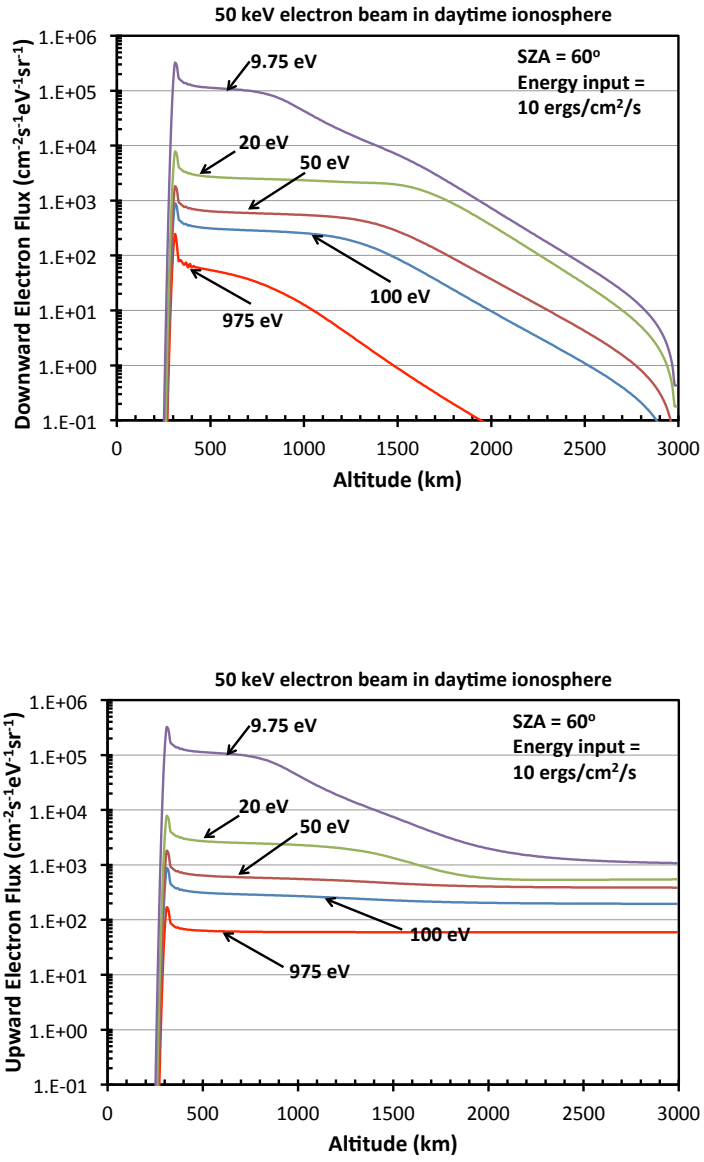

Figure 5.9: Downward (top) and upward (bottom) electron fluxes due to a monoenergetic beam of 20 keV electrons with a total input of 10 ergs/cm^2/s for different electron energies as a function of altitude along the field line. No photoelectrons are considered in the calculations.

We also calculate the ion production rates for the different ion species due to the electron aurora. We choose monoenergetic beams with electron energies of 1, 20 and 50 keV. The ion production due to the primary beam and the subsequent secondary electrons is calculated by equation 5.11 in the two-stream code. We don't include any photoelectrons in the calculation. The ion production due to each monoenergetic beam is shown in Figures 5.10 to 5.12. The figures label this production rate as secondary production. This means that this is the ion production rate due to the monoenergetic electron beam its secondary electrons as they collide with the neutrals, ionizing them. We label primary ion production rate the ion production rate due to the photoionization of the neutrals, as it will be explain in a later section.

From the figures we can see that the higher the electron energy of the beam the further in the atmosphere it will penetrate, as it is to be expected. The same behavior occurred with the energetic ion precipitation in the atmosphere. In the cases where the electron beam stops above the homopause, for example with the 1 keV electron beam, there are very little hydrocarbon ions produced. Since the electrons do not penetrate very deep in the atmosphere, they only interact with the neutrals in the region where the CH_4 density is very low (see Figure 4.1 for the neutral densities). The other two beams that we have considered are energetic enough to reach below the homopause and production of hydrocarbon ions is observed at altitudes below 400 km.

Table 5.1 summarizes the column production rates of the different ions for each electron beam considered in our calculation. We can see that the column production rate of the hydrocarbons is extremely low for the 1 keV electron beam as compared to the other two beams. However, the 1 keV electron beam and the 50 keV electron beam have the same column production rate of H_2^+. Higher energy electrons have much lower ionization cross sections, as the tail of the cross section decreases rapidly at higher energies (see Figure 2.9). So increasing the electron energy does not necessarily

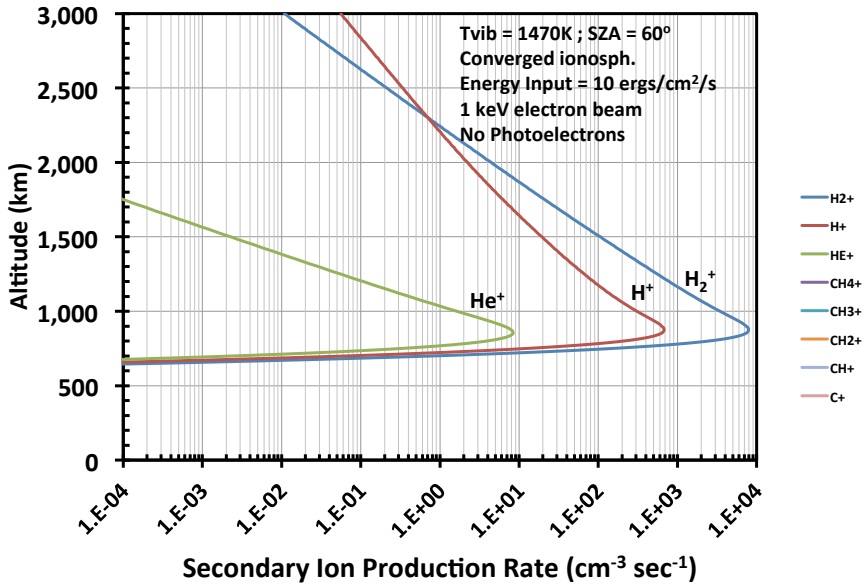

Figure 5.10: Ion production rate due to the precipitation of 1 keV electrons with a flux of 10 erg/cm^2/s in the jovian atmosphere due to secondary electrons. No solar input is considered in the calculations. The ionization is solely produced by the electron-neutral collisions as electrons penetrate the atmosphere.

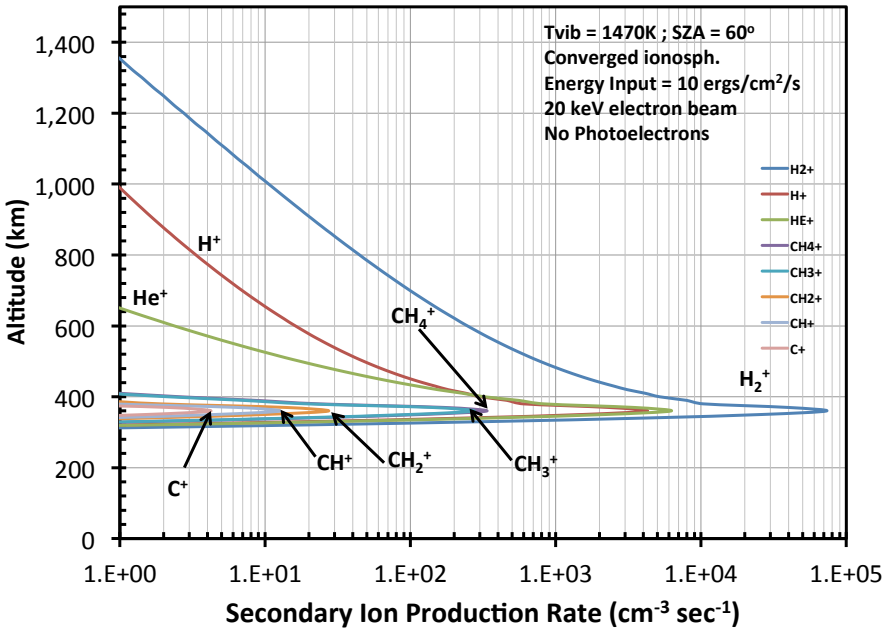

Figure 5.11: Ion production rate due to the precipitation of 20 keV electrons with a flux of 10 erg/cm^2/s in the jovian atmosphere due to secondary electrons. No solar input is considered in the calculations. The ionization is solely produced by the electron-neutral collisions as electrons penetrate the atmosphere.

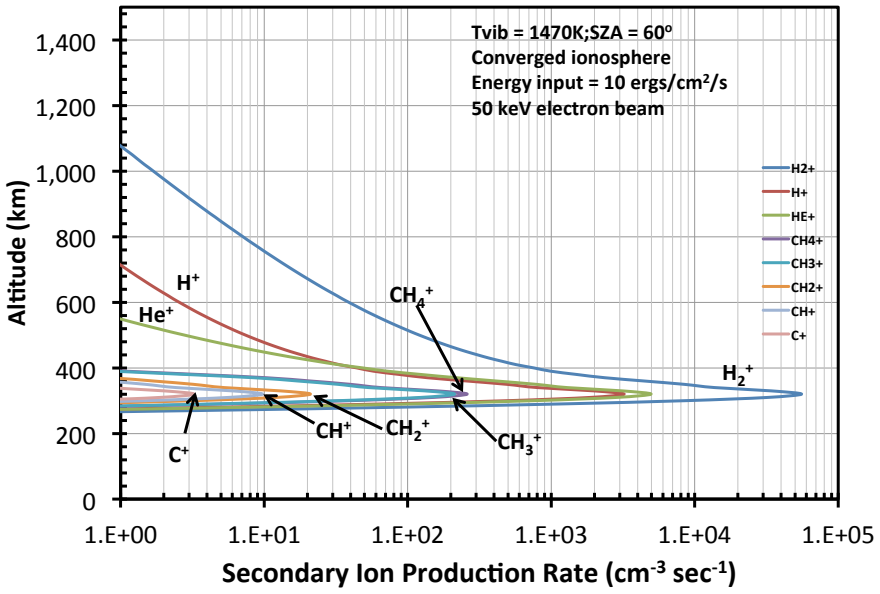

Figure 5.12: Ion production rate due to the precipitation of 50 keV electrons with a flux of 10 erg/cm^2/s in the jovian atmosphere due to secondary electrons. No solar input is considered in the calculations. The ionization is solely produced by the electron-neutral collisions as electrons penetrate the atmosphere.

Table 5.1: Column ion production rates due to a 1, 20 and 50 keV electron beams each with an energy input of 10 erg/cm^2/s. The table shows our results for the main ions produced in a column of the atmosphere by electron-neutral collisions.

Ion Produced	1 keV	20 keV	50 keV
Column production rate	($cm^{-2}s^{-1}$)	($cm^{-2}s^{-1}$)	($cm^{-2}s^{-1}$)
H_2^+	1.69×10^{11}	1.92×10^{11}	1.68×10^{11}
H^+	1.56×10^{10}	1.13×10^{10}	9.76×10^{9}
He^+	1.28×10^{8}	1.48×10^{10}	1.49×10^{10}
CH_4^+	1.21×10^{-3}	6.82×10^{8}	7.57×10^{8}
CH_3^+	9.36×10^{-4}	5.56×10^{8}	6.19×10^{8}

increase the ionization production. On the other hand, the 50 keV electron beam has the highest column production rate of hydrocarbon ions because it is able to penetrate deeper in the atmosphere, where the hydrocarbon neutral density is highest.

5.1.4 Airglow Emission due to Electron Precipitation

Energetic precipitation in the Jovian upper atmosphere leads to the excitation of the neutrals by inelastic collisions. Airglow emissions in Jupiter are in the UV, composed of Ly-α lines and bands as well as Werner bands. Some of the processes leading to these airglow emissions are:

$$H_2(B,C) \rightarrow H_2(X) + h\nu(Ly,W) \tag{5.13}$$

$$e + H_2(X) \rightarrow H(2p) + H(n,l) + e \tag{5.14}$$

$$H_2(2p) \rightarrow H(1s) + h\nu(H\ Ly-\alpha)[1215.67nm] \tag{5.15}$$

The last process shows the dissociation of H_2, which leaves it in an excited state, which then produces H Ly-α emission when it de-excites to the ground state (dissociative excitation of H_2). The dissociative excitation process of H_2 is the dominating contributor for Ly-α line emission. CH_4 may also undergo dissociative excitation to produce Ly-α emissions. However, its contribution is negligible [23] and we exclude it from our calculations.

Another important contribution to the airglow originates from cascading processes from higher to lower states. For example, the $B^1\Sigma_u^+$ state has a large cascade contribution. It is mostly populated by cascading from the $E,F^1\Sigma_g^+$. It is estimated that about $\sim$95% of the H_2 that is in the $v_j = 0$ level of the $B^1\Sigma_u^+$ state arises from the $E,F^1\Sigma_g^+$ cascade [106]. The $C^1\Pi_u$ state cascade doesn't appear to be very important ($<$ 10% effect) [107].

Measurements of the cascading cross sections are very hard to develop. Emission that is attributed to both, direct and cascade, excitation is observed, however, it cannot be differentiated [106]. According to experimental work by [107] the $E,F^1\Sigma_g^+ \rightarrow B^1\Sigma_u^+$

Table 5.2: Column production rate of Lyman band emission due to cascading from the $E,F^1\Sigma_g^+ \rightarrow B^1\Sigma_u^+$ state and then to the ground state. This is calculated for three different electron beam energies that are injected at the top of the atmosphere. The percent emission indicates the percent of the band emission that is due to the cascade.

Electron Energy	Column rate ($cm^{-2}s^{-1}$)	Percent of Ly band emission
1keV	5.82×10^9	9.25%
20 keV	6.18×10^9	8.56%
50 keV	5.43×10^9	8.85%

cascade contributes 24% $\pm$ 10% of the total Lyman band emission intensities at high energies (100 – 300 eV) and 50% $\pm$ 20% at 20 eV. Because there are no concrete calculations or measurements available in the literature for the cascading processes implicated in the airglow emissions, we have estimated the cross section of the $E,F^1\Sigma_g^+ \rightarrow B^1\Sigma_u^+$ cascade to be 0.95 times the cross section for the $E,F^1\Sigma_g^+ \rightarrow X^1\Sigma_g$ transition. The cross sections for other transitions pertinent to the airglow emissions are reviewed in Chapter 2. One may calculate the airglow production rate as a function of altitude $P(s)$ by:

$$P^i(s) = \sum_E \sigma^i_{airglow} \cdot (\Phi^+(s) + \Phi^-(s))\Delta E; \tag{5.16}$$

where, $\sigma^i_{airglow}$ is the airglow cross section for a specific process or outcome i (H-Ly α, H_2 Lyman and Werner, dissociative excitation of H_2, and cascading processes). For the H_2 Lyman band due to cascading we have considered only 95% of the production, because of arguments explained above. We have calculated the airglow production as a function of altitude for monoenergetic electron beams with initial energies of 1 keV, 20 keV and 50 keV and a flux of 10 erg/cm^2/s. No solar input was considered in the calculation. The results are shown in Figures 5.13 to 5.15. For each of the beams, the column production rate of Lyman bands is shown in Table 5.2.

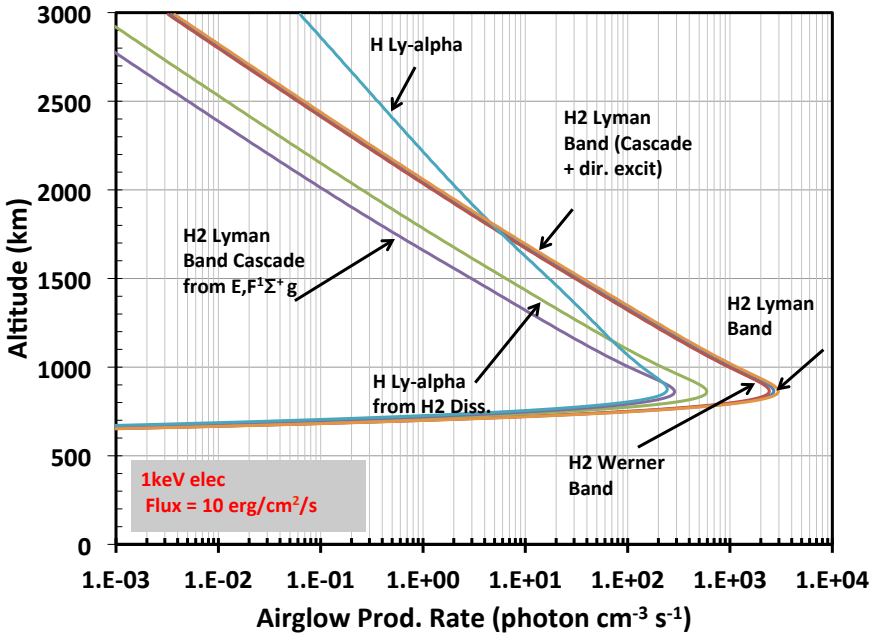

Figure 5.13: Production rate of airglow emissions due to different production mechanisms due to the precipitation of 1 keV electrons with a flux of 10 erg/cm^2/s in the jovian atmosphere. No solar input is considered in the calculations. The emissions are solely produced by the electron-neutral collisions as they penetrate the atmosphere.

We compare our results from the airglow calculations to similar results done by [22] (see Table 6.7). A summary of the airglow emissions results from our calculations for the three beams (energies 1, 20 and 50 keV) are shown in Table 5.4. For most processes the emission rate appears to be somewhat constant with the increase in electron energy. However, the emission of Lyman alpha by direct excitation of H increases as the electron beam energy decreases. This may be explained by the fact that a higher energy electron beam will penetrate lower in the atmosphere, where the hydrogen density dramatically decreases (see Figure 4.1).

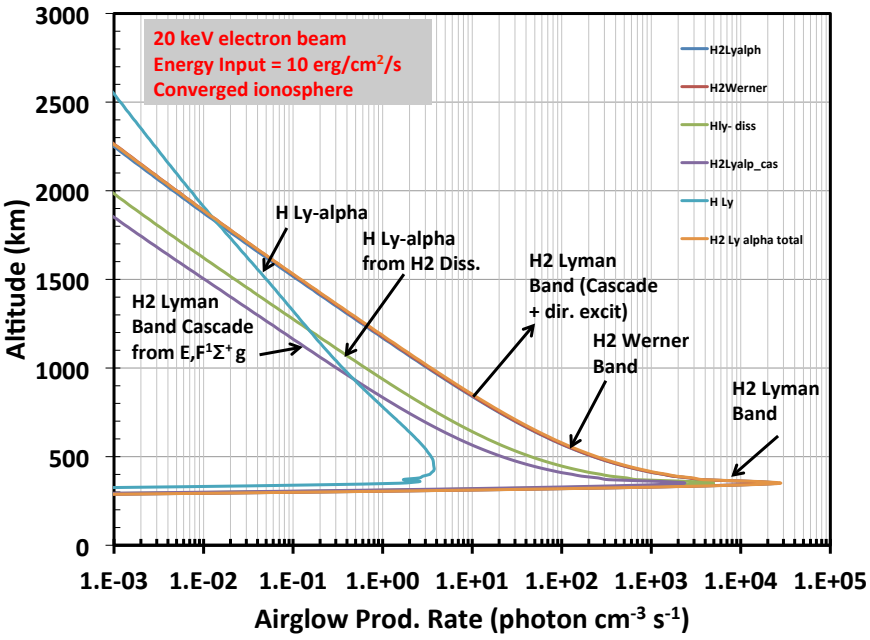

Figure 5.14: Production rate of airglow emissions due to different production mechanisms due to the precipitation of 20 keV electrons with a flux of 10 erg/cm^2/s in the jovian atmosphere. No solar input is considered in the calculations. The emissions are solely produced by the electron-neutral collisions as they penetrate the atmosphere.

Table 5.3: Airglow emissions for a 1 keV electron beam with an energy input of 10 erg/cm^2/s. The table shows our results for a **column rate (cm^{-2}s^{-1})** compared to those in [22] Table 4b in their paper.

Process	This paper	Waite et al. 1983
Lyman bands	6.29×10^{10}	1.91×10^{10}
Werner bands	1.52×10^{10}	5.17×10^{10}
Lyman alpha	1.94×10^{10}	3.25×10^{10}

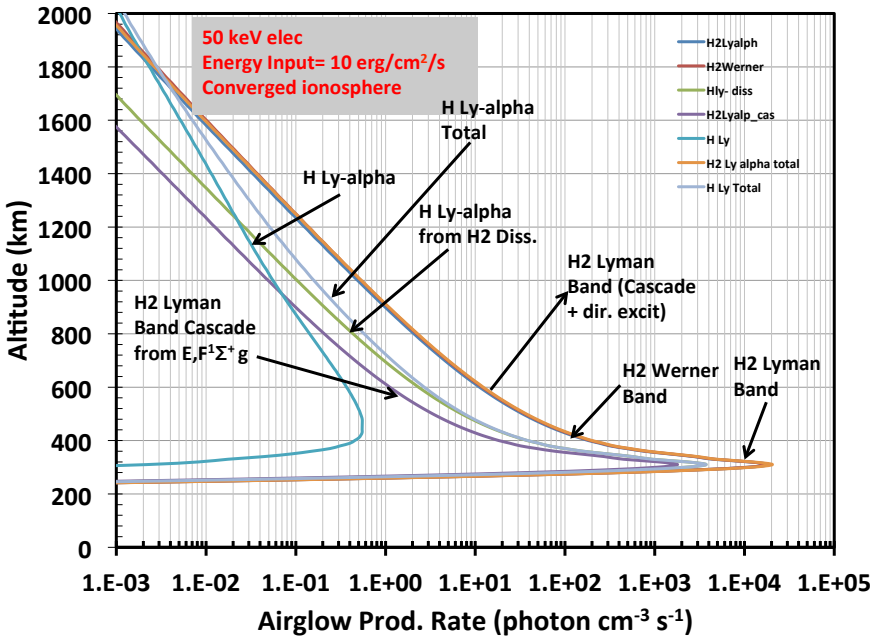

Figure 5.15: Production rate of airglow emissions due to different production mechanisms due to the precipitation of 50 keV electrons with a flux of 10 erg/cm^2/s in the jovian atmosphere. No solar input is considered in the calculations. The emissions are solely produced by the electron-neutral collisions as they penetrate the atmosphere.

Table 5.4: Airglow emissions for a 1, 20 and 50 keV electron beams each with an energy input of 10 erg/cm^2/s. The table shows our results for the different emissions in a column of the atmosphere.

Process	1 keV	20 keV	50 keV
Column rate	(cm^{-2}s^{-1})	(cm^{-2}s^{-1})	(cm^{-2}s^{-1})
Lyman bands (direct excit.)	5.70×10^{10}	6.60×10^{10}	5.59×10^{10}
Lyman bands (cascade)	5.82×10^{9}	6.18×10^{9}	5.43×10^{9}
Werner bands	5.17×10^{10}	6.36×10^{10}	5.62×10^{10}
Lyman alpha (from H_2 diss.)	1.21×10^{10}	1.29×10^{10}	1.13×10^{10}
Lyman alpha (from H)	7.27×10^{9}	1.30×10^{8}	1.94×10^{7}

5.2 Photoelectrons in the Jovian Ionosphere

Photoelectrons are important in the dynamics of the ionosphere. Just like the primary electrons, they will have collisions with the neutrals leading to excitation and emission of radiation, they may recombine with the ions present, or they may undergo election-electron Coulomb collisions. In general, if a primary electron and a photoelectron have the same energy, it is not possible to tell the difference between them, as they will not hold any information on how they were created. However, we know that the primary electron population that is responsible for the UV aurora is more energetic than the secondary electron population. In our work, we concentrate in a three electron populations that will affect the ionosphere in Jupiter. The one of them is populated by photoelectrons created by photoionization of the atmospheric neutrals by solar EUV and x-ray photons. We will review the photoelectrons in this section by analyzing the photoelectron transport and energy deposition using the two-stream approach, explained in detail in section 5.1.1.

When solar radiation interacts with an atmosphere it creates an ionosphere or modifies an existing one. Observations have shown that the day- and night sides of a planetary atmosphere have different structures. The solar photons interact with the neutrals present and will create new ions, electrons, atoms (by photodissociation) and excited neutrals. This will change the density or vertical profiles of the ion and neutral species present. Jupiter is no exception. Therefore we have included the effect of the solar photons by calculating the photoelectron production due to the solar EUV and x-ray radiation that reaches Jupiter. This is handled by our photoelectron code.

To calculate the photoelectron production in the Jovian ionosphere, we first obtain the solar photon fluxes from the solar irradiance proxy code EUV97 from [108]. This solar flux is then scaled using the 10.7 cm radio flux proxy (F10.7) measured in 10^{22} W

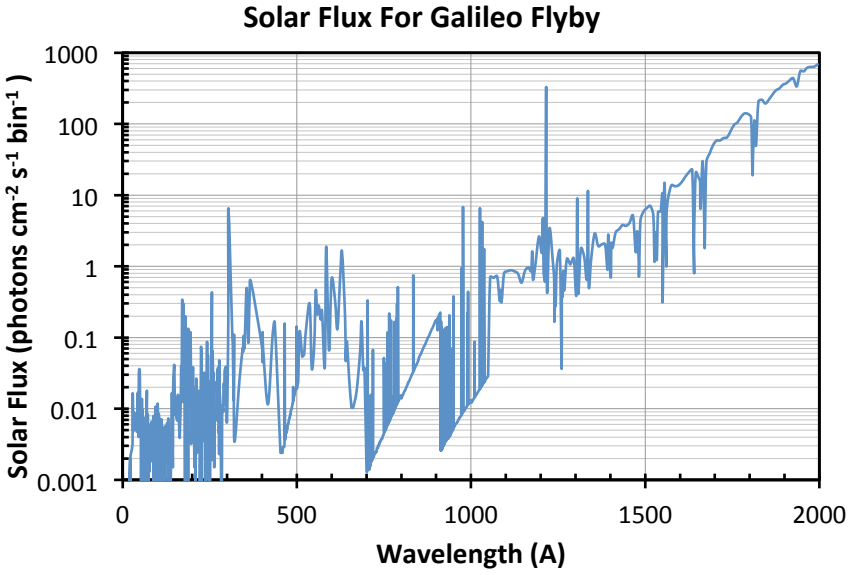

Figure 5.16: Solar flux adapted

m^{-2} Hz^{-1} to obtain the solar minimum conditions at the time of the Galileo encounter (see [109] for more details). The solar flux adopted in our code for all solar input calculations is shown in Figure 5.16 and takes a value of F10.7= 75. The solar spectrum and the cross sections are used in 950 wavelength bins. We calculate photoionization production rates by:

$$P(z) = n(z) \cdot \sigma_{ph.ion} \cdot \Phi_{solar} \exp^{-\tau}; \tag{5.17}$$

where $\sigma_{ph.ion}$ is the photoionization cross section, Φ_{solar} is the solar flux at $\sim$ 5 A.U. and τ is the optical depth as given by equation 4.13. All the photoionization and photoabsorption cross sections needed for our calculations are given in Section 2.5. We calculate the ion production rate due to each neutral species considered in our model

(H_2, H, He and CH_4). Because the amount of solar light that reaches the atmosphere depends on the solar zenith angle, we have chosen to calculate the ion production rate for three angles: 0°, 60° and 90°. We show two types of results. Figures 5.17 to 5.18 show the production rate for each individual ion species that is a product of photoionization. Figures 5.19 to 5.20 show the total ion production rate that results from each neutral species. In the figures we can see that as we increase the solar zenith angle, the ion production rate decreases. This is to be expected, since a larger solar zenith angle means a larger absorption of the solar flux by the atmosphere due to the opacity effect, i.e., there are less photons available to ionize the neutral atmosphere. In Figure 5.17 we compare our model results for a solar zenith angle of 0° with a model developed by [23]. Their model also calculates photoionization rates in the upper atmosphere of Jupiter. Although the atmospheric model, the cross sections and the solar activity index used in the models are not the same, the production rate values and peak altitudes calculated are very similar (please refer to the figure) for H_2^+ and CH_4^+ but are different for H^+ and He^+. The difference in the H^+ production is attributed to our differences in the atmospheric profiles, as the H density in their model is higher than in our model, especially at low altitudes, where the ion production peaks. The smaller difference in the He^+ ion production rate may be attributed to the difference in the cross sections used in our models.

The photoelectrons produced by the photoionization of the neutrals will in turn have further collisions in the atmosphere. Our photoelectron code calculates the photoelectron production rate at each altitude, binned by electron energy. This output is then input in the two-stream code (see sections 5.1.1 and 5.1.2 for details) which then calculates the electron transport in the atmosphere, considering collisions between electrons and neutrals or other electrons present in the ionosphere. Figures 5.21 to 5.22 show the ion production rates due to the photoelectron collisions for four solar zenith angles

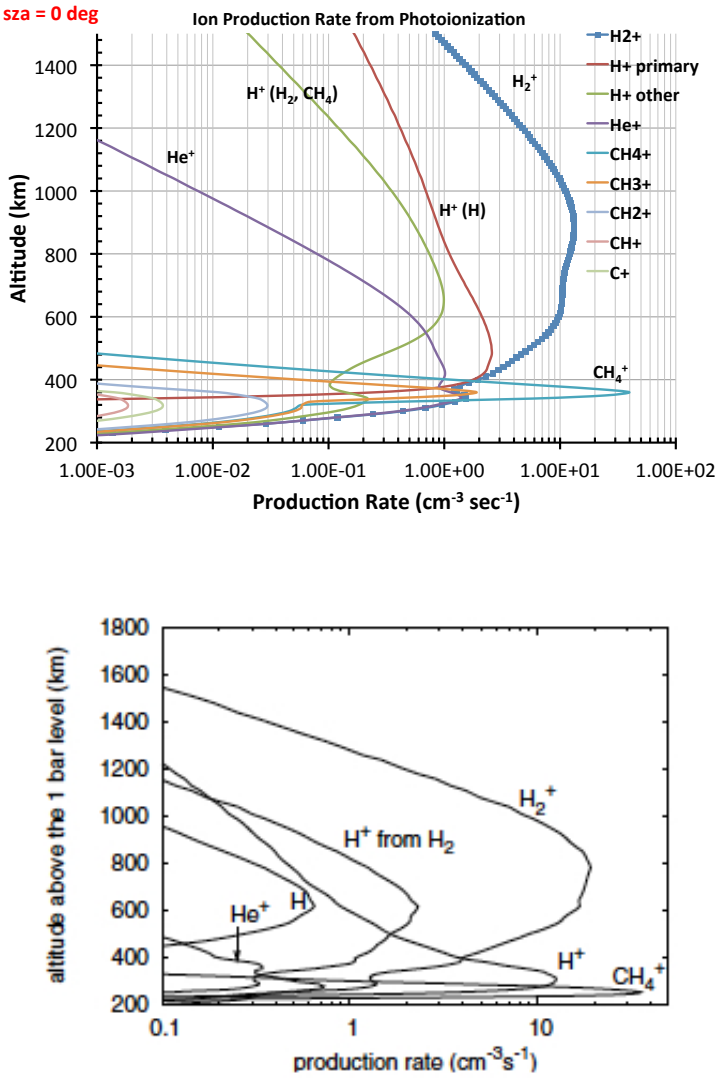

Figure 5.17: Photoionization production rate for each ion species considered in our model (top) are compared to those calculated by [23] (bottom) for F10.7=100. The solar flux for both cases is coming at a solar zenith angle of 0°. Species in parenthesis denote parent species.

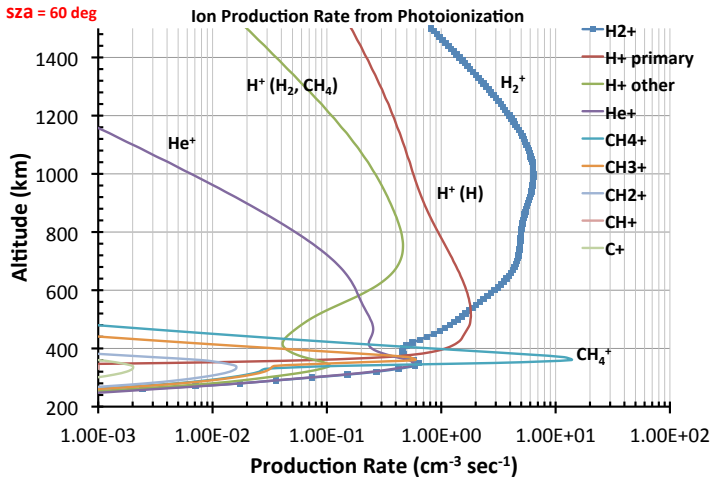

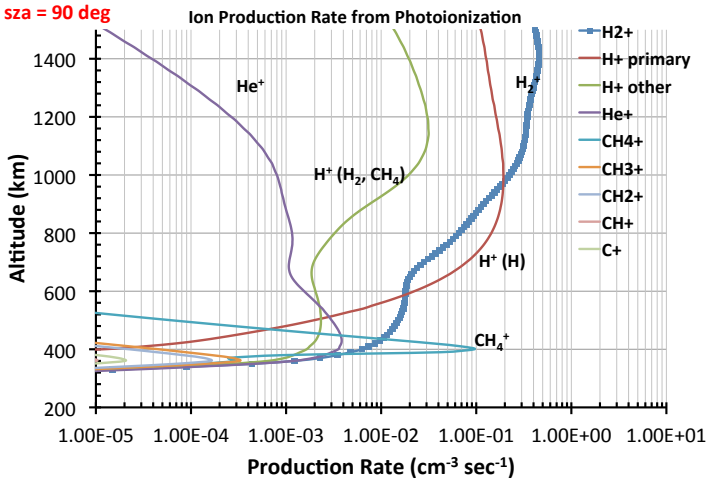

Figure 5.18: Photoionization production rate for each ion species considered in our model. The solar flux is coming at a solar zenith angle of 60°(top) and 90°(bottom). Species in parenthesis denote parent species.

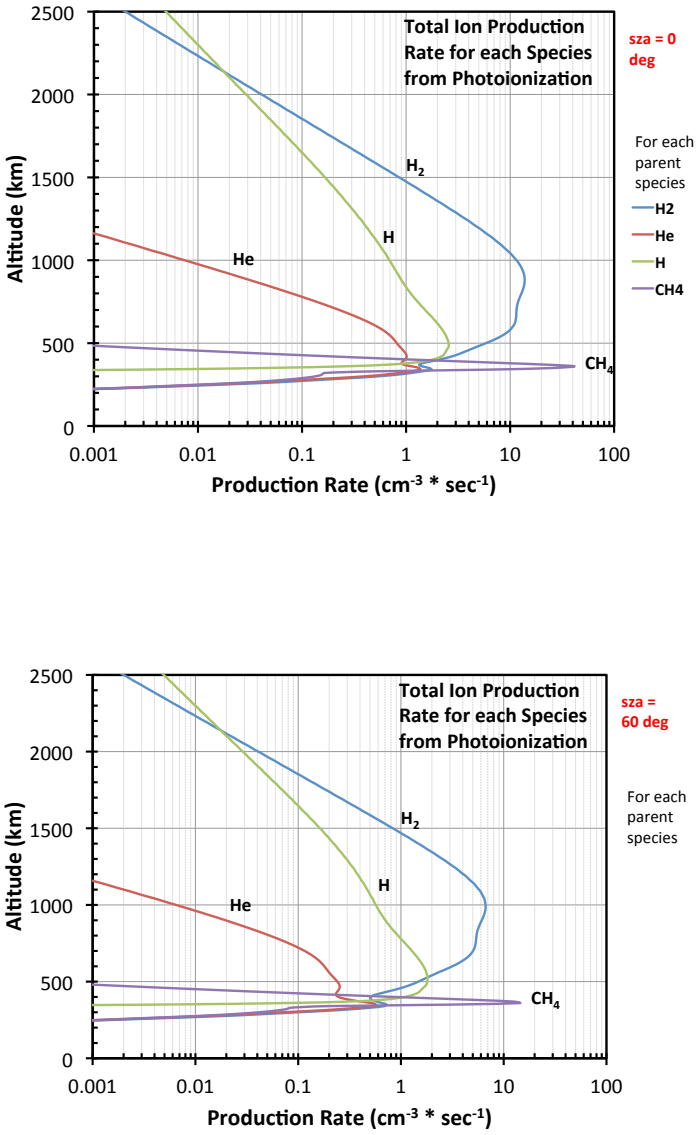

Figure 5.19: Total photoionization production rate for each neutral species considered in our model. The solar flux is coming at a solar zenith angle of 0°(top) and 60°(bottom). Each line represents the parent species.

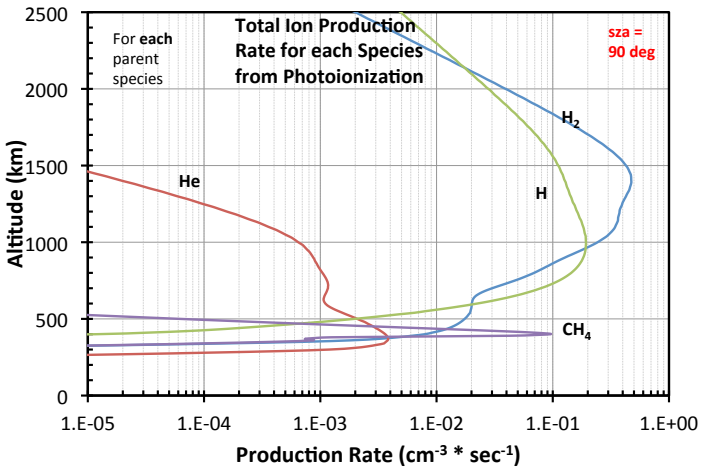

Figure 5.20: Total photoionization production rate for each neutral species considered in our model. The solar flux is coming at a solar zenith angle of 90°. Each line represents the parent species.

Table 5.5: Column production rates for a solar case. All cases are for solar minimum conditions. The table shows our results for the main ions produced in a column of the atmosphere. It includes photoionization and electron-neutral ionization collisions

Ion Produced	0°	60°	80°	90°
Column production rate	($cm^{-2}s^{-1}$)	($cm^{-2}s^{-1}$)	($cm^{-2}s^{-1}$)	($cm^{-2}s^{-1}$)
H_2^+	1.17×10^9	5.89×10^8	2.05×10^8	4.34×10^7
H^+	1.88×10^8	1.31×10^8	6.33×10^7	2.00×10^7
He^+	4.00×10^7	1.43×10^7	2.93×10^6	1.80×10^5
CH_4^+	1.06×10^8	3.77×10^7	6.09×10^6	2.74×10^5
CH_3^+	5.70×10^6	1.91×10^6	1.85×10^5	1.55×10^3

of interest: 0°, 60°, 80° and 90°. This ion production rate is due to the photoelectron transport along the field line and their interactions with the neutrals. The total (primary and secondary) ion production rates calculated by the two-stream code due to the photoelectron transport are shown in Figures 5.23 to 5.24. In agreement with the previous figures, the production rate at higher solar zenith angle decreases. The figures also show a secondary production peak at lower altitudes for each ion species. This peak is created by the photoelectrons created deep in the atmosphere by high energy solar photons. These photons create higher energy photoelectrons, which ionize the neutrals in the lower atmosphere producing a secondary peak at lower altitudes. Table 5.5 summarizes the total column production rate for the main ions due to the photoelectrons produced at different solar zenith angles. As observed earlier, higher solar zenith angle has a lower ion production rate, especially for hydrocarbon species located deep in the atmosphere, where not many solar photons are able to reach.

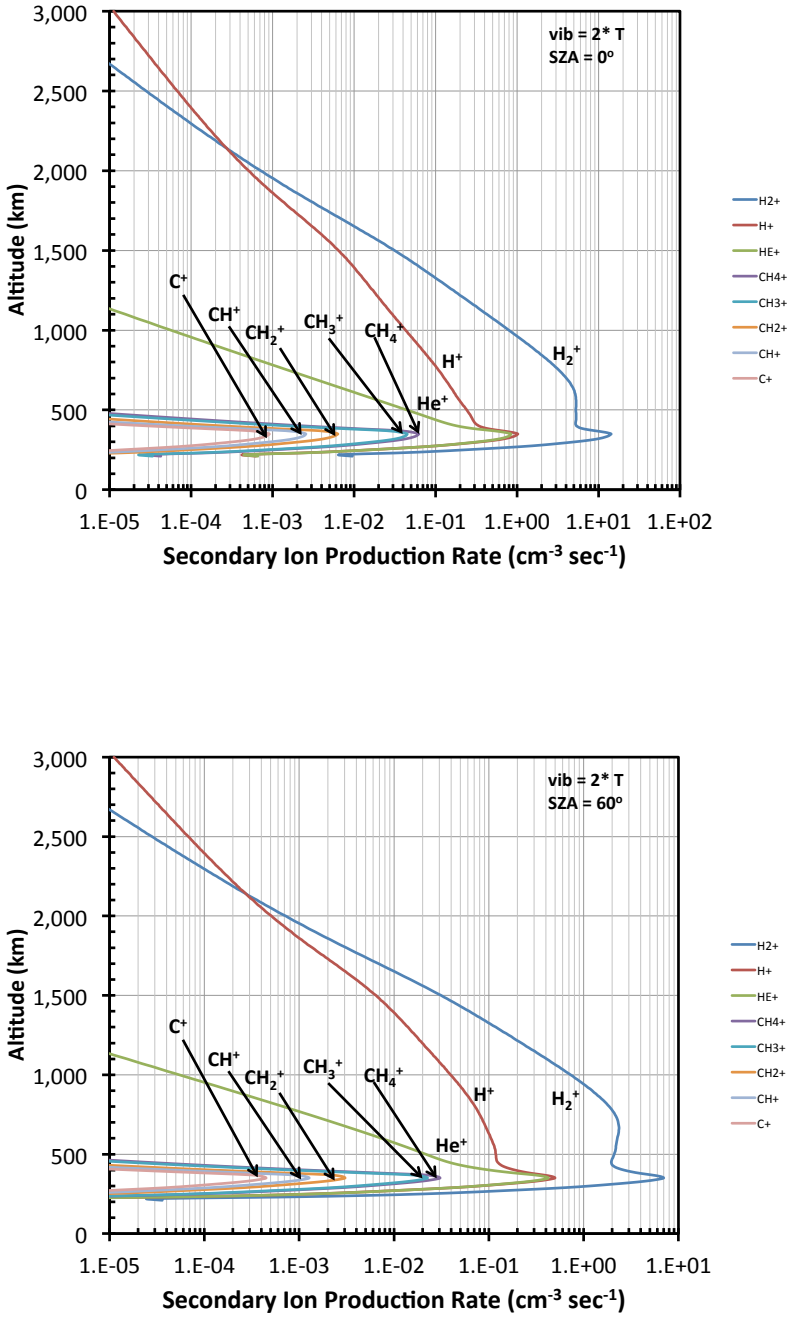

Figure 5.21: Secondary ionization production rate for each ion species considered in our model due to photoelectrons and secondary electrons produced in the atmosphere. The solar flux is coming at a solar zenith angle of 0°(top) and 60°(bottom). Each line represents the total ion production, no matter the parent species.

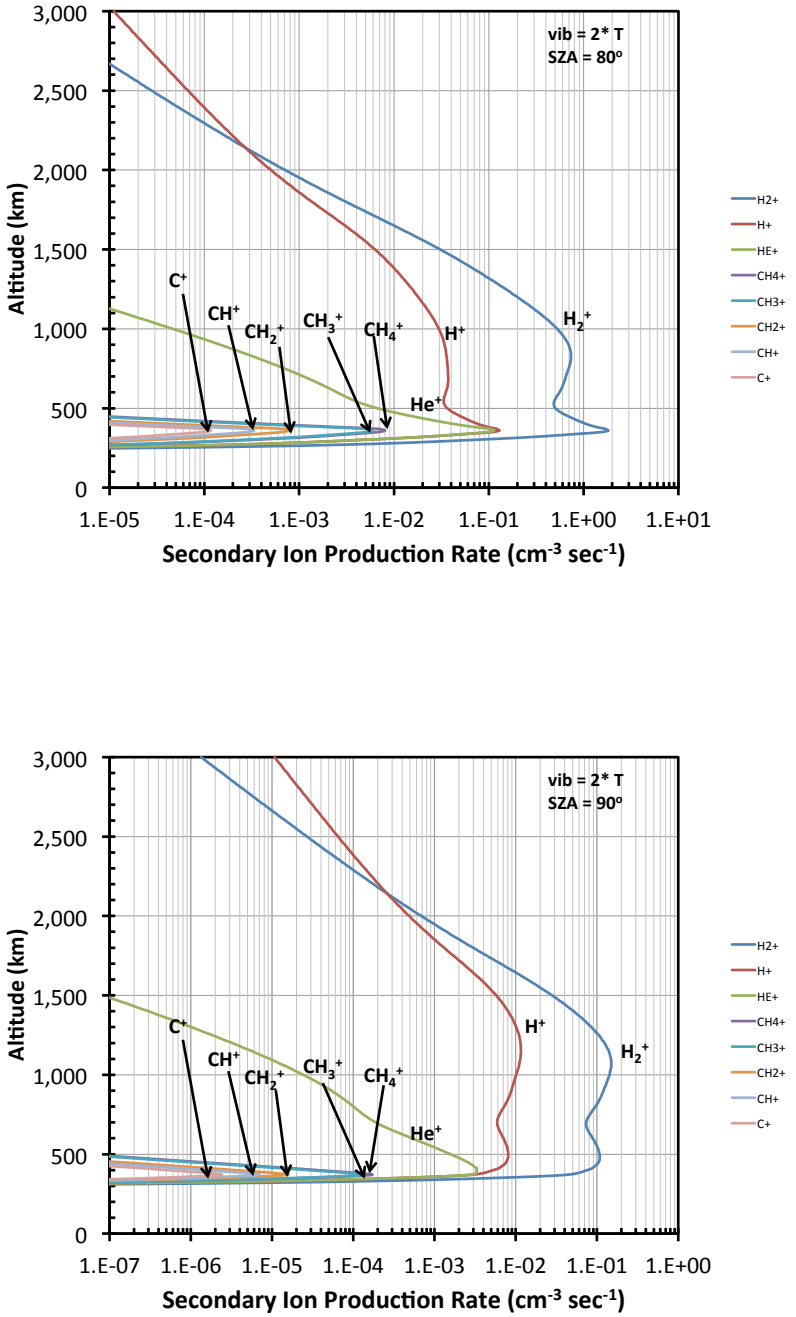

Figure 5.22: Secondary ionization production rate for each ion species considered in our model due to photoelectrons and secondary electrons produced in the atmosphere. The solar flux is coming at a solar zenith angle of 80°(top) and 90°(bottom). Each line represents the total ion production, no matter the parent species.

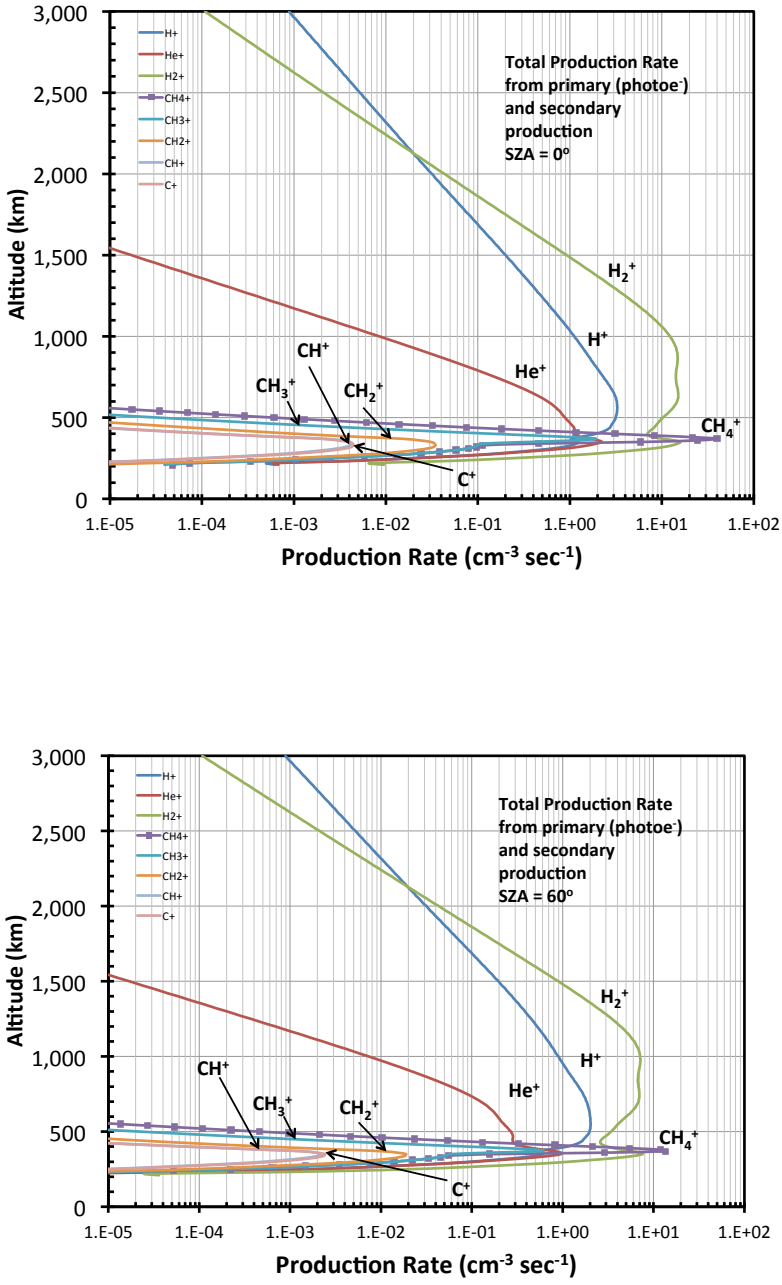

Figure 5.23: Total ion production rate for each ion species considered in our model due to photoionization, photoelectrons and secondary electrons produced in the atmosphere. The solar flux is coming at a solar zenith angle of 0°(top) and 60°(bottom). Each line represents the total ion production, no matter the parent species.

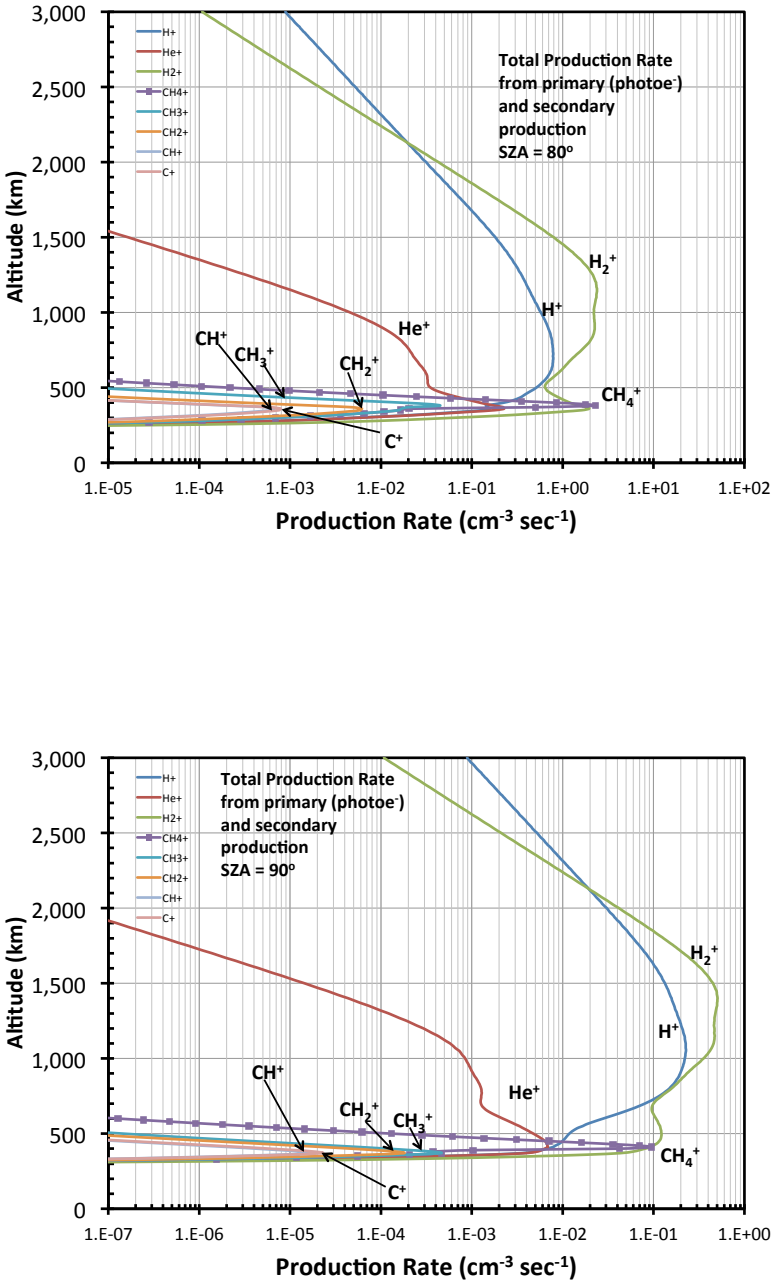

Figure 5.24: Total ion production rate for each ion species considered in our model due to photoionization, photoelectrons and secondary electrons produced in the atmosphere. The solar flux is coming at a solar zenith angle of 80°(top) and 90°(bottom). Each line represents the total ion production, no matter the parent species.

With the two-stream equations we calculate the transport of the photoelectrons along the magnetic field line, taking into account cascading and secondary electrons produced by photoelectron collisions with neutrals. The electron fluxes are calculated for each solar zenith angle of 0°, 60°, 80°and 90°at altitude bins of 10 km from 200 – 3000 km above the cloud tops. We have chosen three important altitudes to illustrate the fluxes:

- 3000 km (the top of the atmosphere) (Figure 5.25): this altitude is important for the escape of electrons from the atmosphere (upward fluxes), as well as the input electron fluxes that may penetrate the atmosphere (downward fluxes).

- 1000 km (Figure 5.26): we chose this altitude because it is the approximate location of the main ion production peak, as shown in Figures 5.17 to 5.24.

- 350 km (Figure 5.26): we chose this altitude because this is the approximate location of the secondary ion production rate peak, as shown in Figures 5.21 to 5.24.

Figure 5.25 shows the difference in the downward and upward electron fluxes at the top of the atmosphere. The downward fluxes are very small, since we are just assuming photoelectrons as our input. Because the atmosphere is tenuous at high altitudes, the photoelectron production is low and the solar zenith angle has almost no effect in the electron production. However, the upward fluxes are much higher, as they include electrons produced in the lower parts of the atmosphere that have been transported upward by collisions. The escaping energy flux in an atmospheric column is $\sim 1.27 \times 10^7$ eVcm^{-2}s^{-1}.

As the electrons are transported further along the field line toward the planet, we begin to see more differences in the photoionization. As we look further down the

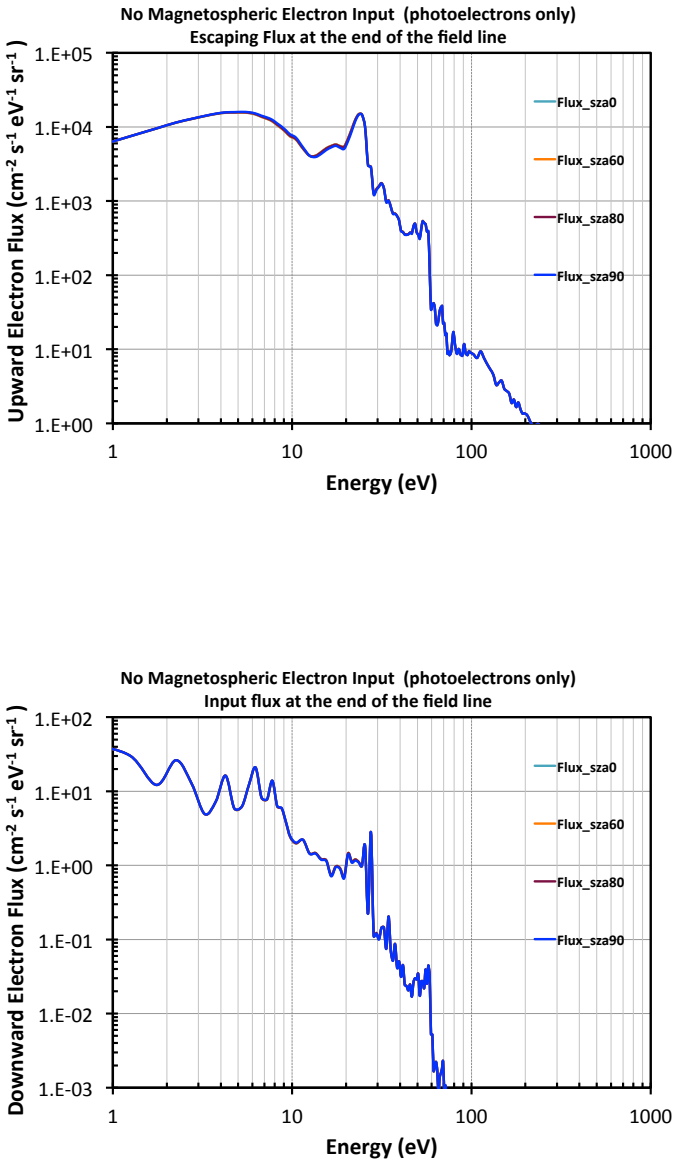

Figure 5.25: Upward (top) and downward (bottom) electron fluxes calculated with the two-stream transport equations at the top of the atmosphere (z=3000 km) for three different SZA (0°, 60°, 80°and 90°). There is no external input of electrons, i.e., no magnetospheric electron beams are considered here. The fluxes for the different angles overlap because the atmosphere is very tenuous at this altitude and no considerable effects due to geometry are seen.

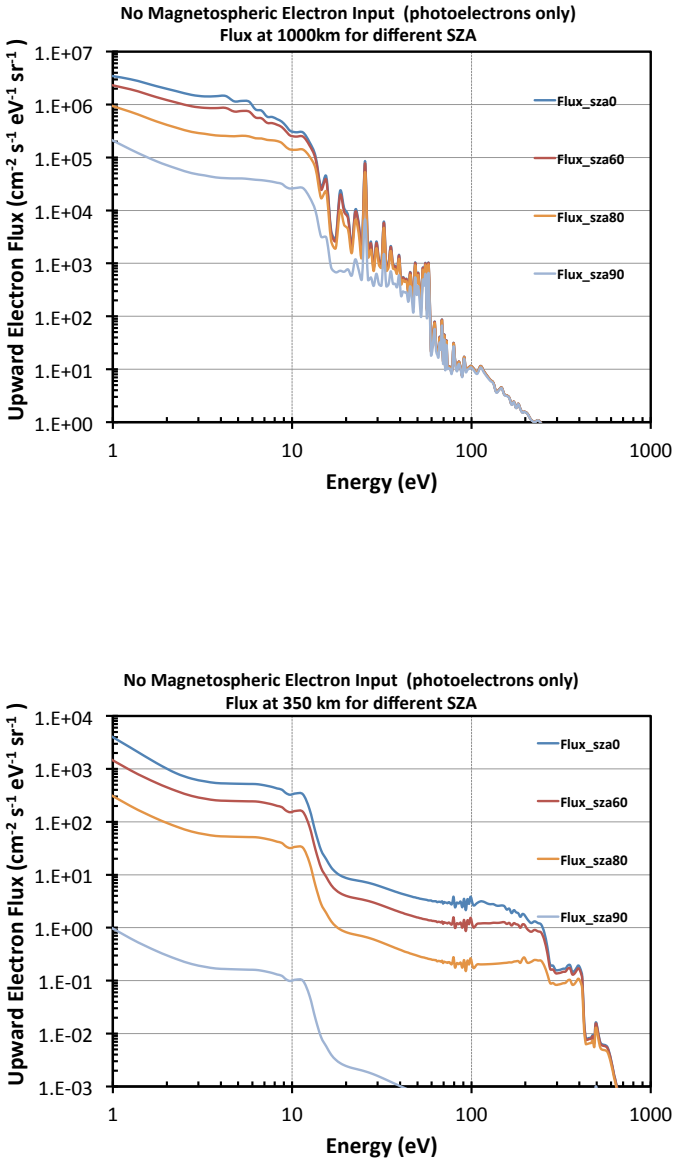

Figure 5.26: Upward electron fluxes calculated with the two-stream transport equations for three different SZA (0°, 60°, 80°and 90°). The fluxes shown are for an altitude of 1000 km (top) and 350 km (bottom) along a vertical field line. There is no external input of electrons, i.e., no magnetospheric electron beams are considered here. The difference in the curves shows the effect of atmospheric opacity to the solar photons depending on the solar zenith angle. The downward fluxes are not shown because they are almost identical to the upward fluxes in all cases.

magnetic field line at lower altitudes, the atmosphere becomes denser and the photoelectron population begins to form. If we continue to lower altitudes, it becomes much denser and at the same time more opaque to the incoming solar photons. Therefore, less photoelectrons will be produced and the fluxes up and down the field line will also be smaller. Figure 5.26 clearly shows this effects. For example, the fluxes are much higher at 1000 km compared to the fluxes at the top of the atmosphere. This shows the buildup of photoelectrons as we penetrate down the atmosphere. However, the bottom panel shows that at altitudes of 350 km the fluxes are again lower. As explained above, this is due to the opacity to the solar photons as we increase the atmospheric density in the lower altitudes. Another important observation is that once we penetrate the atmosphere, the fluxes become isotropic, i.e., the upward and downward fluxes are identical. We can conclude that the electron population seen at these lower altitudes is mostly created locally. Another important feature shown in these figures are the peaks that appear in the flux at about 25 and 35 eV. These can be seen for the upward fluxes at the top of the atmosphere and 1000 km, but are lost at the 350 km fluxes. The peaks are characteristic for photoionization and have been seen in planetary atmospheres [71] and are due to photionization of the atmospheric neutrals by the solar HeII resonance line at 30.4 nm [110] . This can be considered a "fingerprint" of the photoelectron production. The peaks are not observed are lower altitudes, where the solar photons are mostly absorbed and photoionization becomes inefficient.

Another way to look at our results is by looking at the flux of a given energy as a function of altitude. We chose to display the results for 25 eV, as it is a characteristic photoelectron energy and as seen in Figures 5.25 and 5.26 the flux due to photoelectron is higher for lower energies. The downward flux as a function of altitude for a 25 eV electron is shown in Figure 5.27. This was calculated for the different solar zenith angles, as explained earlier. The figure shows how the electron flux builds up as we go

down in the atmosphere peaking at altitudes between 1500 km (SZA=90°) and 1000 km (SZA=0°). This coincides with the ion production rate peaks shown in Figures 5.17 and 5.18. Below these altitudes, the fluxes rapidly drop as the atmosphere becomes denser and more opaque and less photoelectrons are being produced.

Figure 5.28 shows the upward electron fluxes as a function of altitude also for 25 eV electrons. As with the downward electrons, the upward electron flux peaks at altitudes between 1000 – 1500 km depending on the solar zenith angle used. However, as we go to higher altitudes, the upward fluxes decrease a little and then remain constant and escape the atmosphere. We tried a special case where we assumed an electron density of 10^4 cm^{-3} at the top of the atmosphere for a solar zenith angle of 0° to see the effect that a high electron density would have in the flux. We chose this value as it was speculated that such electron densities would be observed in the upper atmosphere of Jupiter [29]. However, this density is too low to have any observable effect in the flux as is shown in the figure.

Figures 5.29 to 5.32 show the upward and downward fluxes as a function of altitude for different electron energies. Each figure shows the electron fluxes obtained for the different solar zenith angles. As we go deeper in the atmosphere the neutral density increases and the downward electron fluxes increase as there are more neutrals that are being ionized. However, once the atmosphere becomes opaque to the solar photons there is no further photoionization and the electron fluxes rapidly drop at low altitudes. As expected and seen above, lower energy electrons have higher fluxes. When the solar zenith angle is increased, the peak of the electron flux occurs at higher altitudes, as the photons are not able to reach as far down in the atmosphere before being absorbed. Also they are less efficient in producing electrons. Therefore, the electron fluxes at higher solar zenith angles are also lower. For high solar zenith angles there is a secondary peak that is observable at lower energies. This is due to the secondary electron process

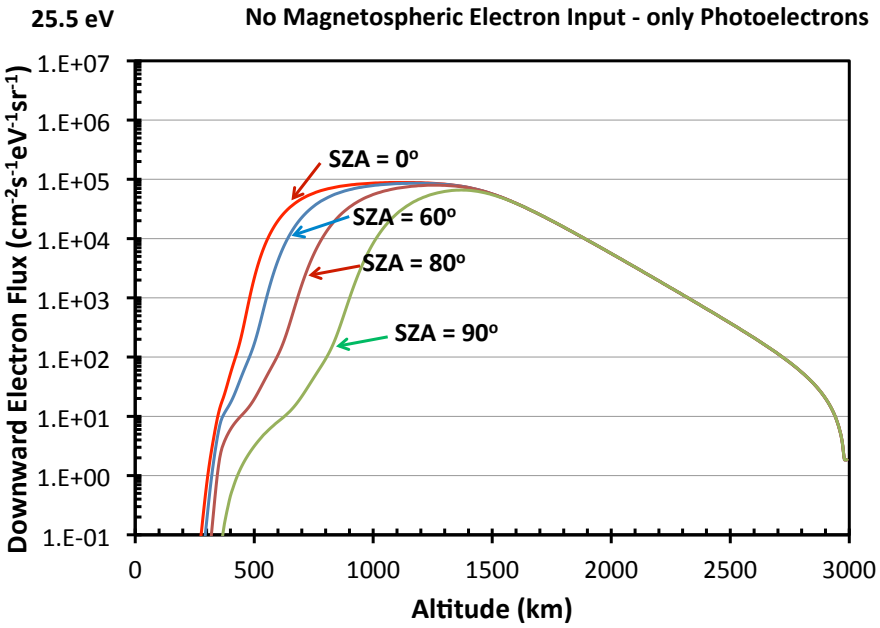

Figure 5.27: Downward electron flux as a function of altitude for 25 eV electrons. Each curve represents a different solar zenith angle (0°, 60°, 80°and 90°). No external electron input in considered, i.e., only photoelectrons and their secondary electrons are considered in the flux.

that occur lower in the atmosphere, as there is very little, if any, photoionization in this region.

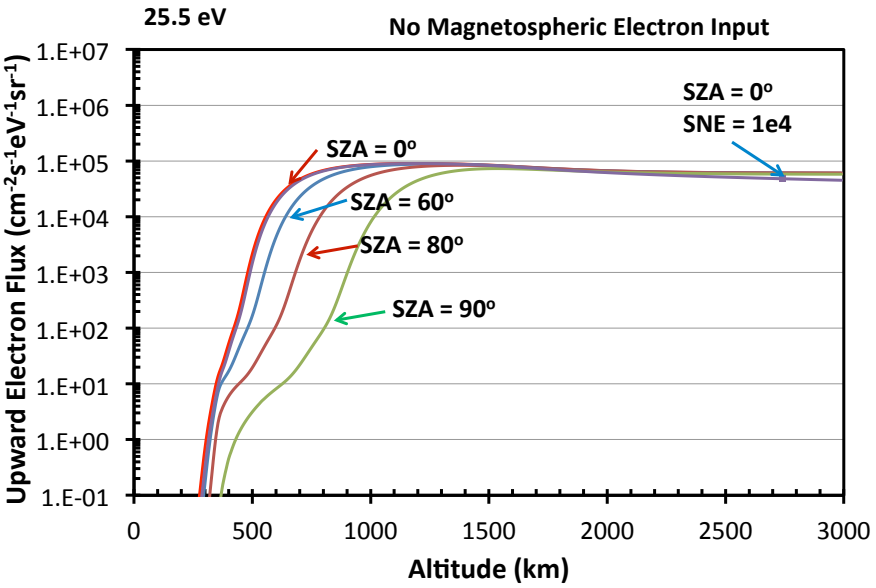

Figure 5.28: Upward electron flux as a function of altitude for 25 eV electrons. Each curve represents a different solar zenith angle (0°, 60°, 80°and 90°). No external electron input in considered, i.e., only photoelectrons and their secondary electrons are considered in the flux. A special case was tried out with an electron density of 10^4 cm^{-3} at the top of the atmosphere. However, this density is too low to have an effect on the flux.

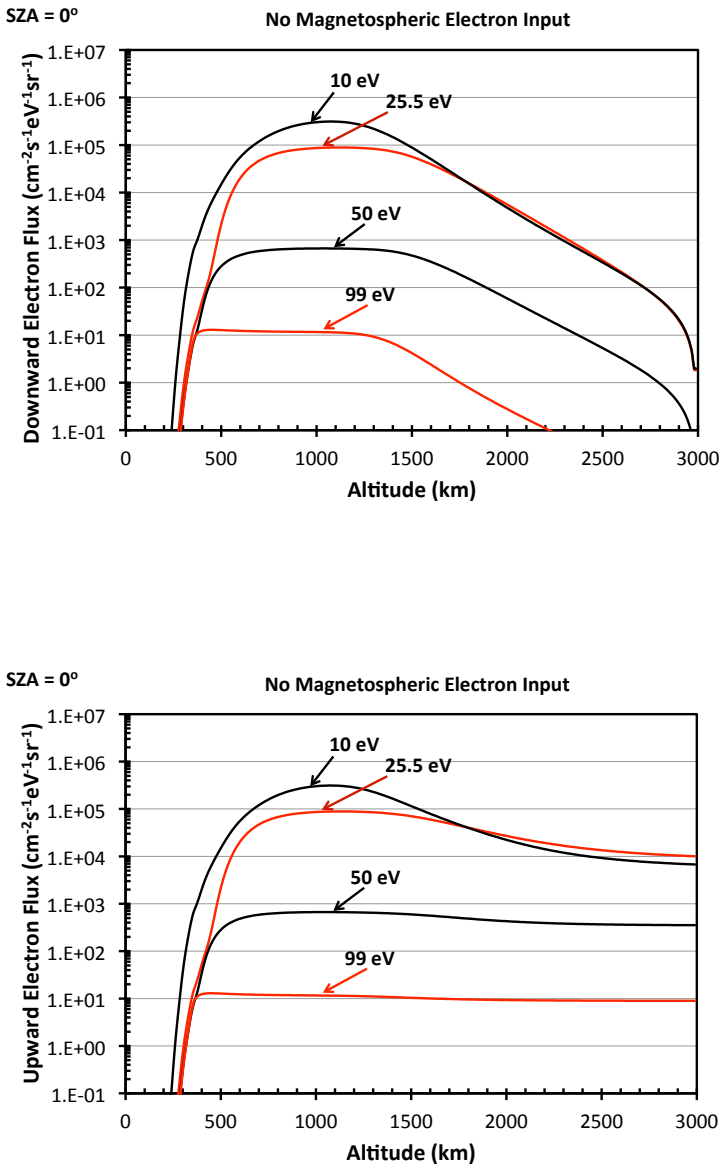

Figure 5.29: Downward (top) and upward (bottom) electron fluxes as a function of altitude calculated with the two-stream transport equations for specific electron energies as labeled in the figure. This figure shows the fluxes due to photoelectrons at a 0° solar zenith angle. There is no external input of electrons, i.e., no magnetospheric electron beams are considered here.

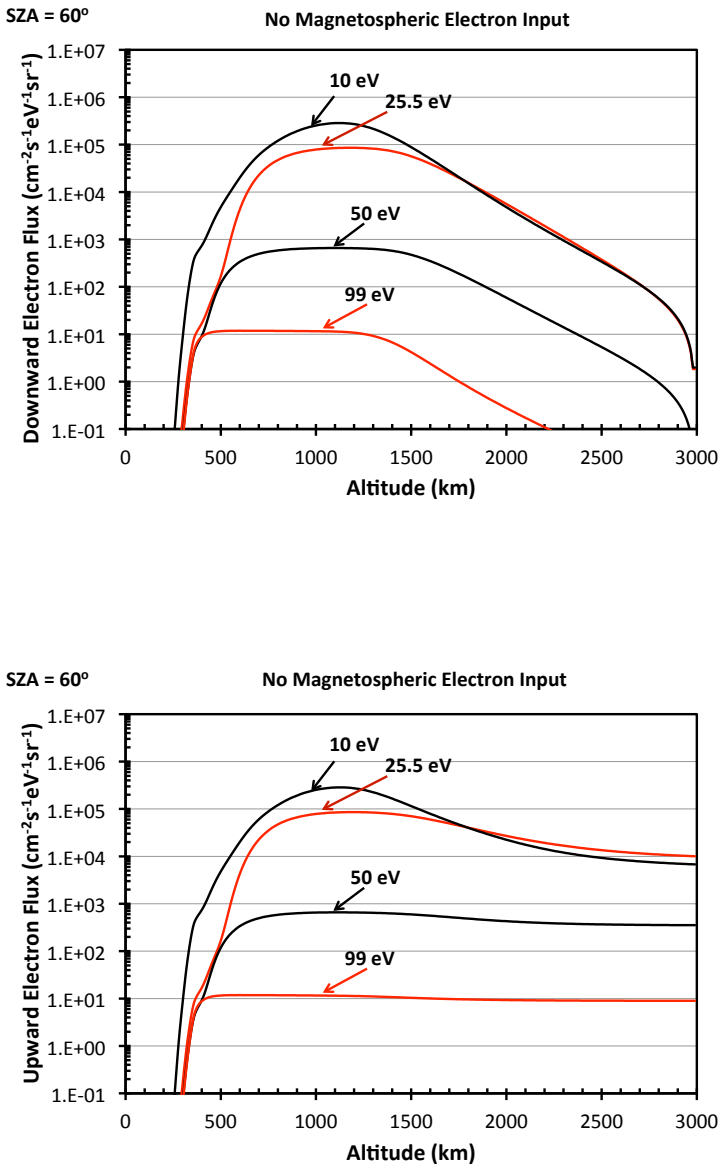

Figure 5.30: Downward (top) and upward (bottom) electron fluxes as a function of altitude calculated with the two-stream transport equations for specific electron energies as labeled in the figure. This figure shows the fluxes due to photoelectrons at a 60° solar zenith angle. There is no external input of electrons, i.e., no magnetospheric electron beams are considered here.

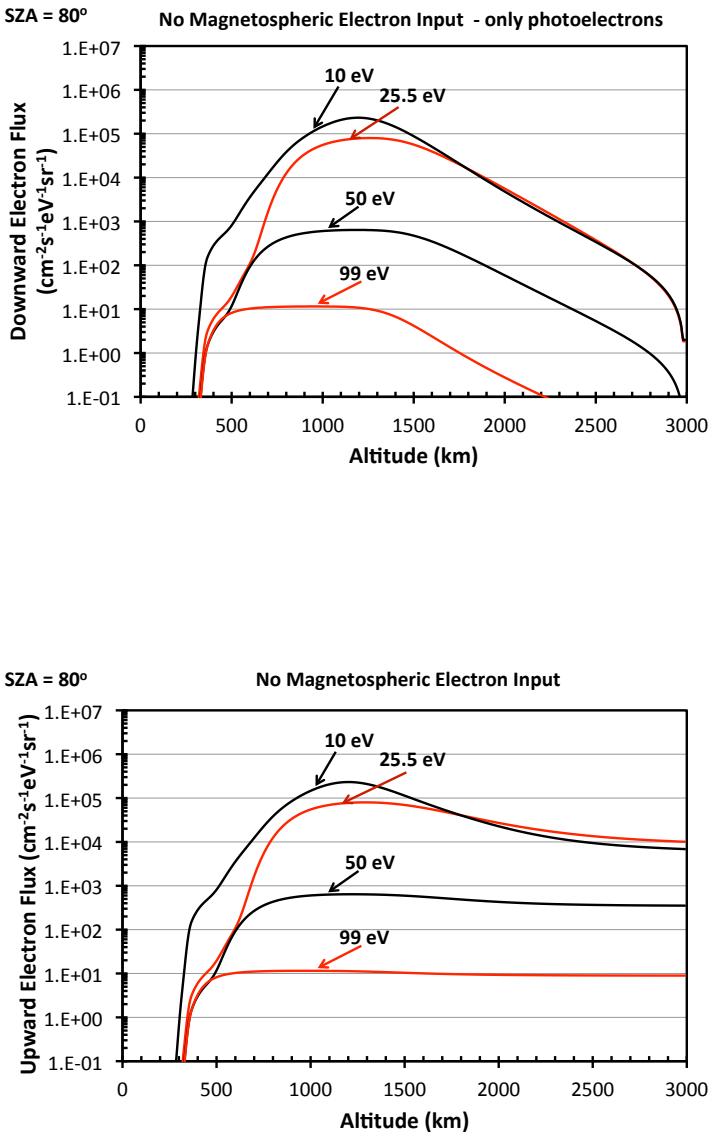

Figure 5.31: Downward (top) and upward (bottom) electron fluxes as a function of altitude calculated with the two-stream transport equations for specific electron energies as labeled in the figure. This figure shows the fluxes due to photoelectrons at a 80° solar zenith angle. There is no external input of electrons, i.e., no magnetospheric electron beams are considered here.

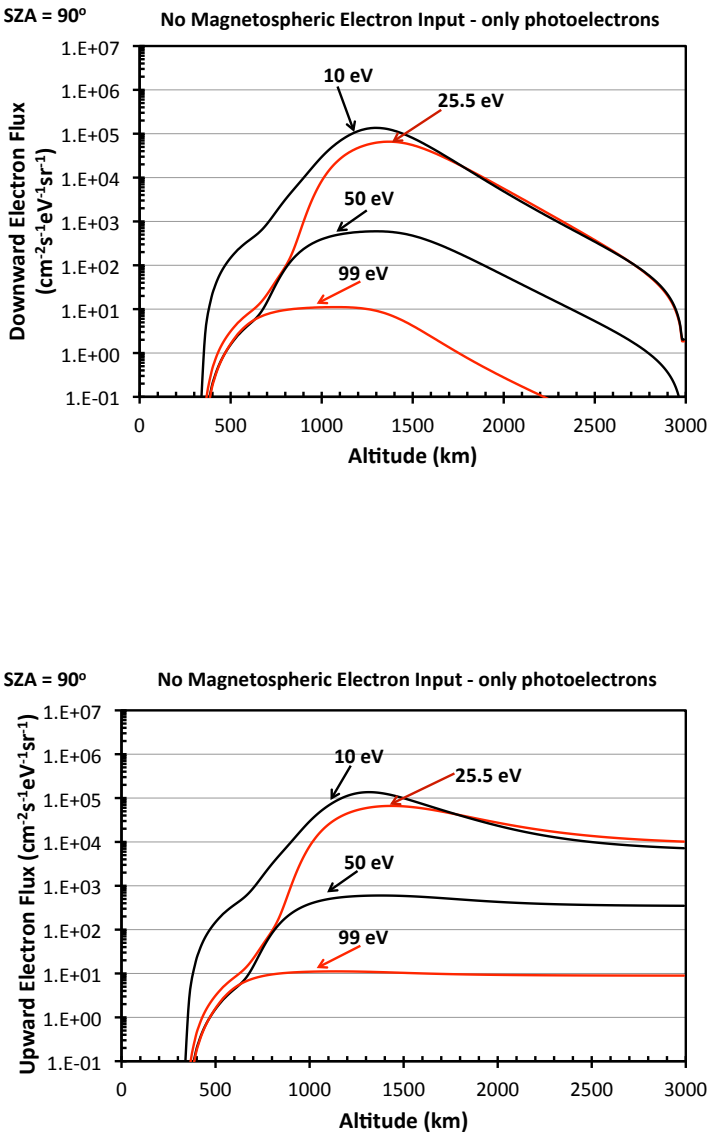

Figure 5.32: Downward (top) and upward (bottom) electron fluxes as a function of altitude calculated with the two-stream transport equations for specific electron energies as labeled in the figure. This figure shows the fluxes due to photoelectrons at a 90° solar zenith angle. There is no external input of electrons, i.e., no magnetospheric electron beams are considered here.

5.2.1 Airglow Emissions in the Daytime Ionosphere

When only photoelectrons are considered, there are still airglow emissions produced as the photoelectrons collide with the neutrals in the atmosphere while they are transported up and down a magnetic field line. Please see section 5.1.4 for a review of the processes that give rise to airglow emissions and Chapter 2 for the needed cross sections. We calculate the airglow emissions using equation 5.16 and the upward and downward fluxes calculated by the two-stream code and shown in the previous section. We calculate the airglow production rates for the different solar zenith angles to observe the effect that the photoelectron fluxes will have in these observable emissions. Our results are shown in Figures 5.33 to 5.34. The figures show also a double peak in the emissions just like the one seen for the ion production rates. Harder solar photons are able to penetrate deeper in the atmosphere and photo ionize the neutrals present, a second population of photoelectrons are produced that will give rise to the secondary peak observed in the airglow emissions. Only H Ly-α emissions don't show this double peak. This emissions originate from H atoms, which are less abundant in the lower atmosphere and not enough to create any significant emissions. We can also see how as the solar zenith angle increases the primary airglow emission peak altitude rises in the atmosphere, as the photons are absorbed at higher altitudes. The secondary peak also becomes smoother broader as the solar zenith angle increases. It is also important to notice that the secondary peak in the airglow emissions for all energies is larger than the primary peak. We summarize our results in Table 5.6 by calculating the column emission rates.

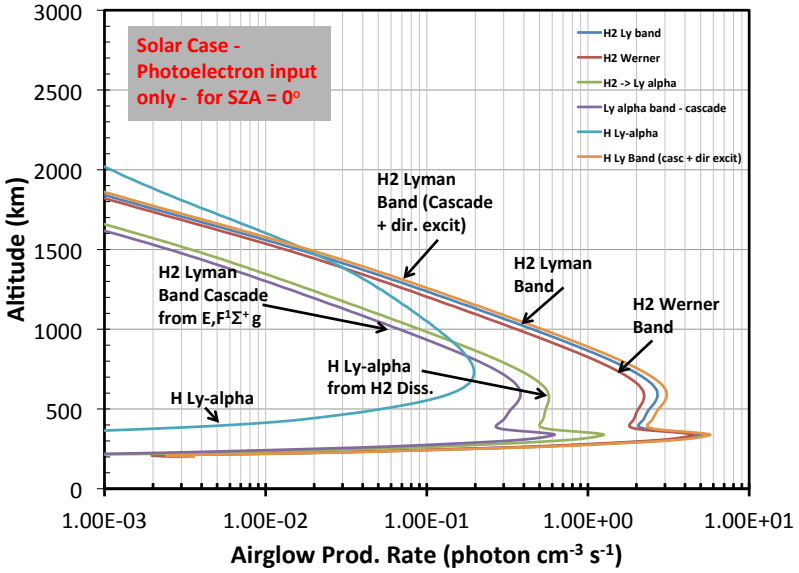

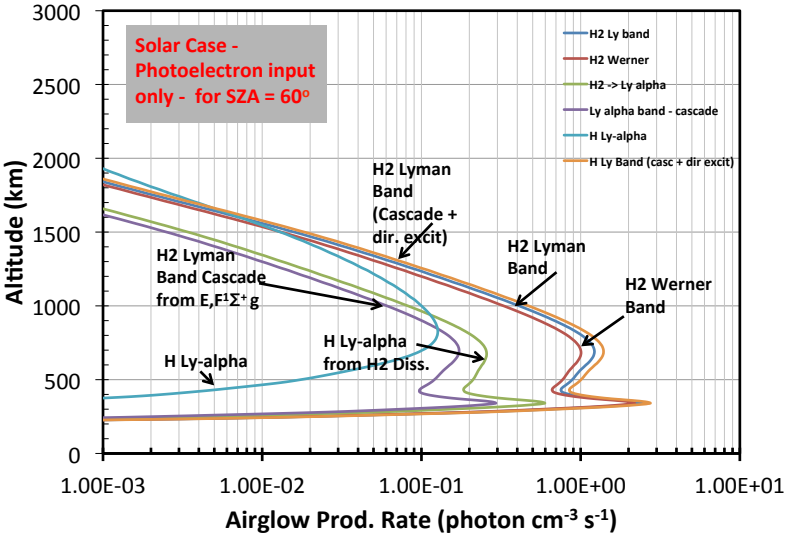

Figure 5.33: Production rate for airglow emissions due to the transport of photoelectrons in the ionosphere. The solar flux is coming at a solar zenith angle of 0°(top) and 60°(bottom).

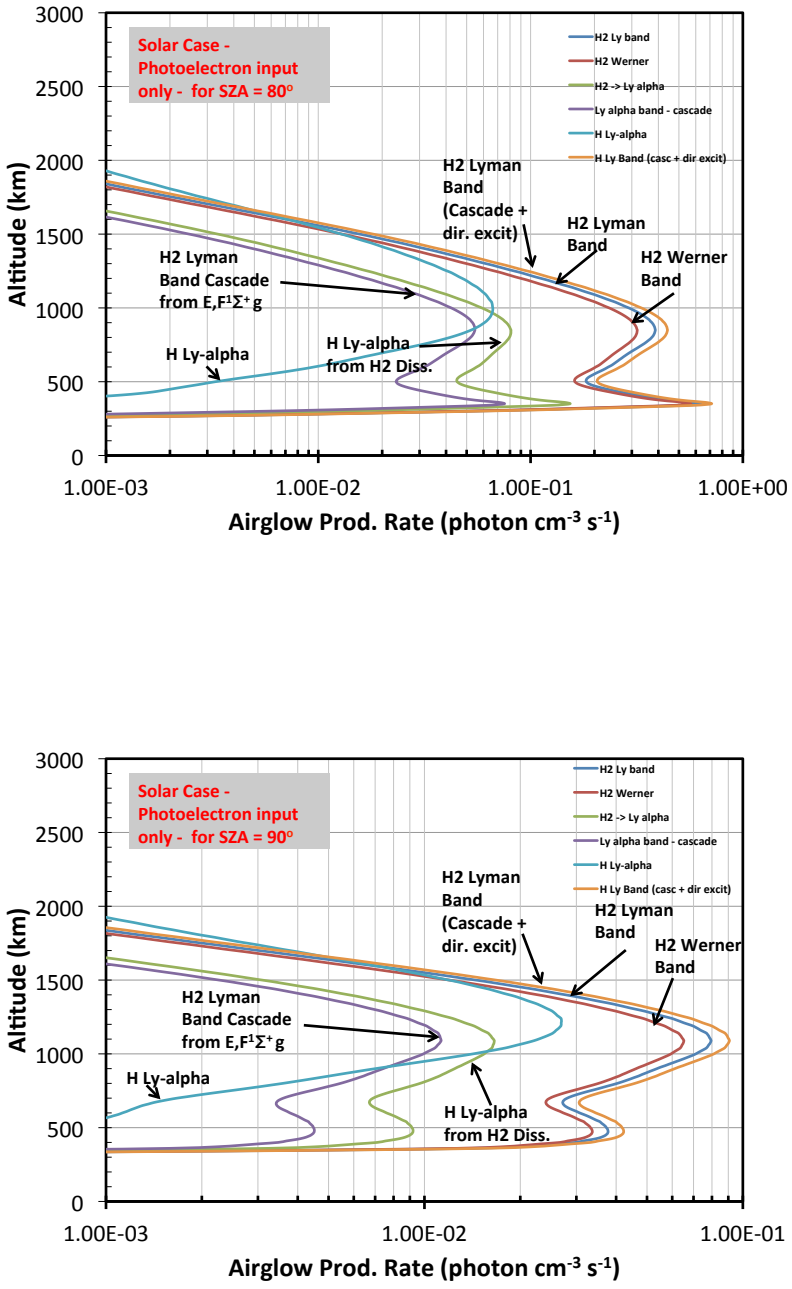

Figure 5.34: Production rate for airglow emissions due to the transport of photoelectrons in the ionosphere. The solar flux is coming at a solar zenith angle of 80°(top) and 90°(bottom).

Table 5.6: Airglow emissions due to photoelectrons for different solar zenith angles. The table shows our results for the different emissions in a column of the atmosphere.

SZA	0°	60°	80°	90°
Process	($cm^{-2}s^{-1}$)	($cm^{-2}s^{-1}$)	($cm^{-2}s^{-1}$)	($cm^{-2}s^{-1}$)
Lyman bands (direct excit.)	1.55×10^8	7.80×10^7	2.71×10^7	5.37×10^6
Lyman bands (cascade)	2.13×10^7	1.07×10^7	3.72×10^6	7.45×10^5
Werner bands	1.31×10^8	6.58×10^7	2.29×10^7	4.54×10^6
Lyman alpha (from H_2 diss.)	3.43×10^7	1.73×10^7	6.02×10^6	1.19×10^6
Lyman alpha (from H)	1.11×10^7	7.35×10^6	3.96×10^6	1.49×10^6

5.3 Auroral Electrons in a Daytime Ionosphere

The same codes can be used to calculate the ion production rates and electron fluxes for an electron aurora in a daytime ionosphere. We chose a solar zenith angle of 60° to calculate the ionosphere densities (see Section 5.4). We use three monoenergetic beams each with 1, 20 and 50 keV electrons, which are injected at the top of the ionosphere (that is z = 3000 km) with a total energy input of 10 ergs/cm^2/s as done for the auroral electron calculations seen above. In this case we also include photoelectrons produced for a solar zenith angle of 60° as were calculated in the previous section. We calculate the total ion production rates that are obtained in this case due to the monoenergetic beam and the photoelectrons as they will be important in order to determine the ionospheric densities in the next section. The calculated ion production rates are shown in Figures 5.35 to 5.37. From the figures it is clear the the ion production due to the monoenergetic beams dominates. However, at lower altitudes, where the beam does not penetrate, the photoelectrons are still ionizing the neutrals creating a secondary ion production peak at lower altitudes that only very energetic electrons would be able to reach. Table 5.7 summarizes the ion production rate in a column of the atmosphere. Comparing this results to those shown in Table 5.1, which contains the column production rate due to the auroral beams without including photoelectrons, we can see that the only noticeable increase is for the hydrocarbon production rate for the 1 keV beam. This means that for beams energetic enough to reach altitudes below the homopause, their effect in the ionosphere dominates over the photoelectrons. However, for less energetic electron beams the photoelectrons have have a greater effect. We calculate the UV airglow emissions due to ion precipitation in Chapter 6.

Table 5.7: Column production rates for a 1, 20 and 50 keV electron beams each with an energy input of 10 erg/cm^2/s and photoelectrons produced for a daytime ionosphere (SZA = 60°). The table shows our results for the main ions produced in a column of the atmosphere.

Ion Produced	1 keV	20 keV	50 keV
Column production rate	($cm^{-2}s^{-1}$)	($cm^{-2}s^{-1}$)	($cm^{-2}s^{-1}$)
H_2^+	1.69×10^{11}	1.93×10^{11}	1.68×10^{11}
H^+	1.56×10^{10}	1.13×10^{10}	9.77×10^{9}
He^+	7.17×10^{8}	1.54×10^{10}	1.55×10^{10}
CH_4^+	3.77×10^{7}	7.20×10^{8}	7.95×10^{8}
CH_3^+	1.91×10^{6}	5.58×10^{8}	6.21×10^{8}

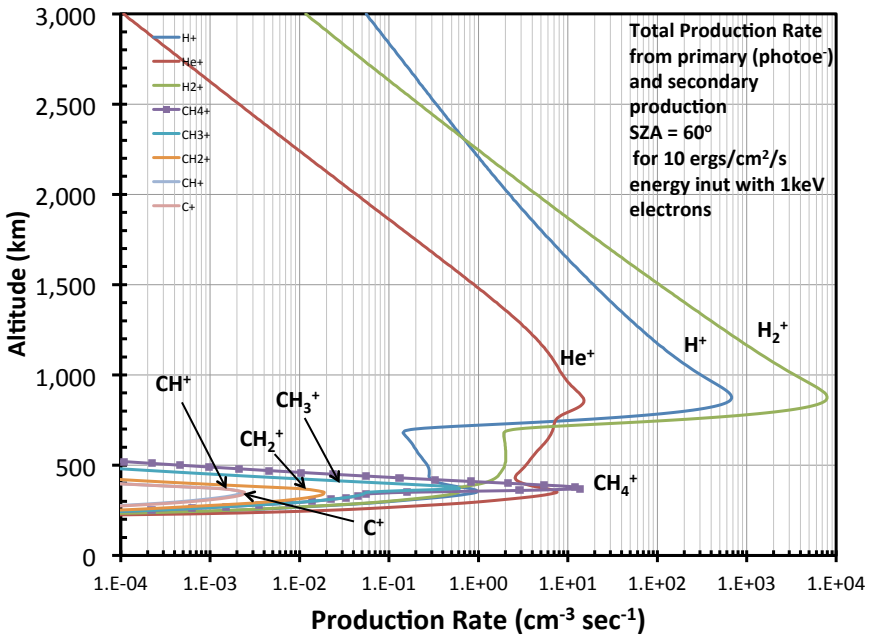

Figure 5.35: Total ion production rates due to photoionization and a monoenergetic beam with 10 ergs/cm^2/s energy input of 1 keV electrons. The solar flux is coming at a solar zenith angle of 60°, to simulate a daytime ionosphere. The production rate due to the monoenergetic electron dominates.

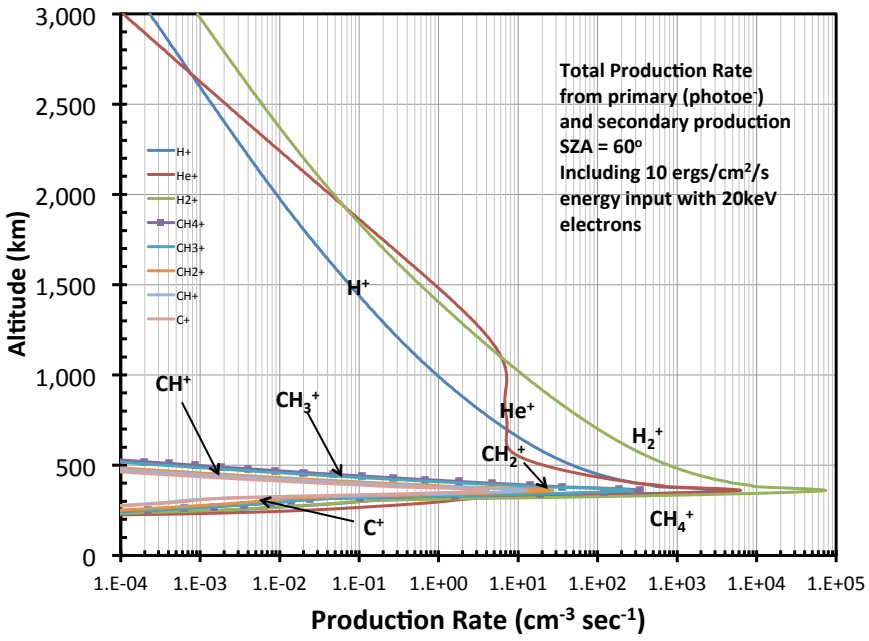

Figure 5.36: Total ion production rates due to photoionization and a monoenergetic beam with 10 ergs/cm^2/s energy input of 20 keV electrons. The solar flux is coming at a solar zenith angle of 60°, to simulate a daytime ionosphere. The production rate due to the monoenergetic electron dominates.

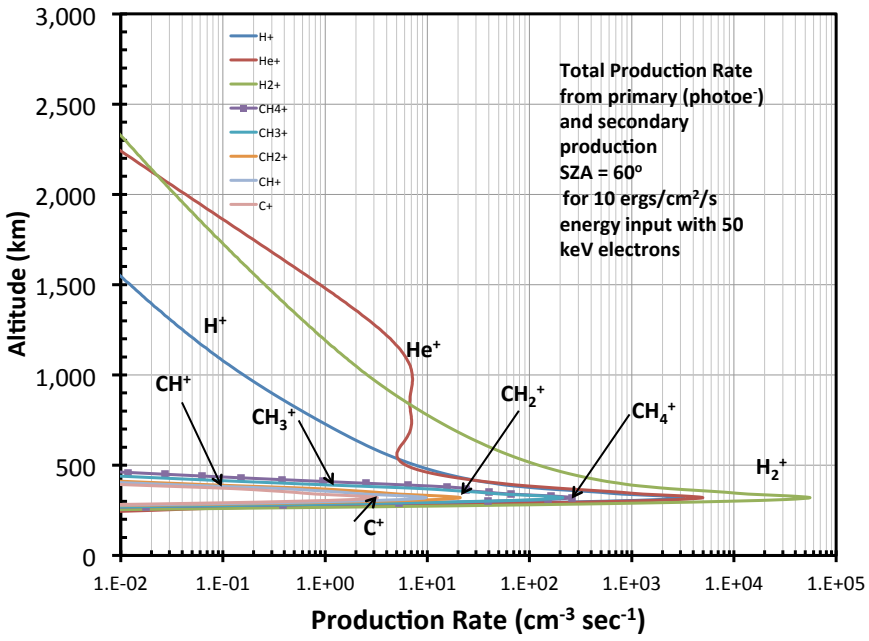

Figure 5.37: Total ion production rates due to photoionization and a monoenergetic beam with 10 ergs/cm^2/s energy input of 50 keV electrons. The solar flux is coming at a solar zenith angle of 60°, to simulate a daytime ionosphere. The production rate due to the monoenergetic electron dominates.

5.4 Ionospheric Effects

In this section we calculate the ion densities and the effects that different ionospheric conditions present to the ion profiles. For example, for a daytime ionosphere, the effect of solar zenith angle is important for photoionization and will affect the resultant equilibrium in the ion densities. In an auroral region, where electron beams are injected at the top or when secondary electrons created at different altitudes in the ionosphere are taken into account, the ion density profiles will be modified as the electrons have collisions and chemical reactions while they are transported in the ionosphere. We use a photochemical model in order to calculate the ion densities for a steady state ionosphere ($\partial n/\partial t = 0$), by solving the continuity equations:

$$\frac{\partial n_e}{\partial t} + \frac{\partial \phi_e}{\partial z} = P_e - \alpha n_e^2 \tag{5.18}$$

for the electrons, and

$$\frac{\partial n_i}{\partial t} + \frac{\partial \phi_i}{\partial z} = P_i - L_i n_i^2 \tag{5.19}$$

for the ions. Since the ionosphere is electrically neutral, the condition that $n_e = \sum_i n_i$ must be true. The second term on the left hand in the equations is due to vertical transport by molecular diffusion and is neglected in our model, as we are assuming hydrostatic equilibrium. The loss mechanism for the electrons is electron recombination. There are 35 electron recombination reactions that we consider in our model. They are listed in the Appendix Table A.20 with the corresponding recombination coefficient α, where $\tau = (\alpha n_e)^{-1}$ gives the chemical time constant due to electron recombination processes. The loss mechanism for the ions include the ion-electron recombination, as well as ion neutral reactions. We have included 163 ion-neutral reactions in our model, which are listed in the Appendix Table A.21 with their reaction rates, k_i. The char-

acteristic time constant for the reaction is given by $\tau = (k_i n)^{-1}$. The photochemical code calculates the densities for 27 ions that we chose: H^+, He^+, H_2^+, H_3^+, HeH^+, CH_5^+, CH_4^+, CH_3^+, CH_2^+, CH^+, C^+, $C_2H_5^+$, $C_2H_4^+$, $C_2H_3^+$, $C_2H_2^+$, $C_3H_7^+$, $C_3H_5^+$, $C_3H_4^+$, $C_3H_2^+$, C_3H^+, $C_3H_3^+$, $C_2H_6^+$, $C_2H_7^+$, $C_nH_m^+$, $C_3H_6^+$, $H_2C_3H^+$ and C_2H^+. We use the ion production rates due to photoionization (shown in Figures 5.23 to 5.24) for solar zenith angles of 0°, 60°, 80°and 90°. These will determine the production term for the equations. Please refer to section 2.5 for the relevant photoionization cross sections and to section 5.2 for the details on the ion production rate calculation. Our code solves the coupled equations for each altitude on the grid, starting at 200 km increasing by 10 km until an altitude of 3000 km, using a Newton-Raphson iterative technique, until chemical equilibrium is achieved.

For our photochemical model we have included C_2H_2, C_2H_4, C_2H_6, C_4H_6 and $H_{2(vib\geqslant 4)}$ in the neutral density profiles, in addition to H_2, He, H, and CH_4, because these hydrocarbon species are important for the ion-neutral chemistry in the lower atmosphere. We calculated the neutral density of the hydrocarbons for altitudes above the homopause (350 km in our model) by assuming hydrostatic equilibrium:

$$n_i(z) = n_{0,i} \exp^{-z/H} \tag{5.20}$$

where $H = k_B T/m_i g$ is the scale height for each species and $n_{0,i}$ is the density at height z_0=350 km (see Figure 4.7 for the scale heights). For the altitudes below the homopause, we have calculated the neutral densities for the hydrocarbons based on

mixing ratios between the hydrocarbon and H_2. The following values were used:

$$n_{C_2H_2}(z) = n_{H_2}(z) \cdot (3 \times 10^{-5}) \text{from ref. [111]} \tag{5.21}$$

$$n_{C_2H_4}(z) = n_{H_2}(z) \cdot (2 \times 10^{-6}) \text{from ref. [111]} \tag{5.22}$$

$$n_{C_2H_6}(z) = n_{H_2}(z) \cdot (1 \times 10^{-6}) \text{from ref. [112]} \tag{5.23}$$

Figure 5.38 shows the neutral profiles used in the photochemical model.

A common issue when modeling the Jovian ionosphere is determining the density of H^+ ions. An effective loss mechanism for the H^+ ions is by charge transfer with a vibrationally excited H_2 molecule via the reaction:

$$H^+ + H_{2(vib)} \rightarrow H_2^+ + H \tag{5.24}$$

Therefore, in the model, we try different vibrational temperatures to calculate the $H_{2(vib)}$ density and see the effect on the H^+ production. By varying the vibrational temperature we attempt to bring the electron density in agreement to other models and observations, for example, [29,111,113]. We calculate the density of vibrationally excited $H_{2(vib)}$ by:

$$n_{H_{2(vib)}}(z) = n_H(z) \cdot \exp^{-21960/T_{vib}} \tag{5.25}$$

In auroral regions, the electron-neutral collisions may increase the vibrational temperature considerably [113]. We vary the vibrational temperature T_{vib} in equation 5.25 to obtain different profiles until one is reached that is closest to the measurements or other models based on measurements. We calculated the density profiles by setting T_{vib} = T(z), 1.5T(z), 2T(z) or 3T(z), where T(z) is the temperature as a function of altitude in our atmospheric model as shown in Figure 4.2. The results for the $H_{2(vib)}$ density

profiles (Figure 5.39) show that as we increase the vibrational temperature, the $H_{2(vib)}$ peak density rapidly increases by several orders of magnitude, from 0.2 cm^{-3} for T_{vib} = T(z) to almost 10^7 cm^{-3} for T_{viib} = 3T(z). The peak density also occurs at lower altitudes in the atmosphere. For T_{vib} = T(z) the peak altitude is about 800 km, while for T_{vib} = 3T(z) the peak density is at about 550 km. Therefore, the vibrational temperature for H_2 is a very sensitive parameter in the model and it is also not exactly known.

As we increase the $H_{2(vib)}$ density in the atmosphere, H^+ losses will also increase by the reaction shown in equation 5.24, which is a very efficient sink mechanism for these ions. This same reaction will increasingly produce H_2^+ which in turn undergoes the reaction:

$$H_2^+ + H_2 \rightarrow H_3^+ + H. \tag{5.26}$$

This reaction is very important in the jovian ionosphere, as it has a very small time constant and is a dominant chemistry process. It also explains why H_3^+ is the main ion species in regions of the ionosphere. Figures 5.40 to 5.41 show the effect that the change in $H_{2(vib)}$ density with vibrational temperature has on the ion densities of H^+, H_2^+ and H_3^+.

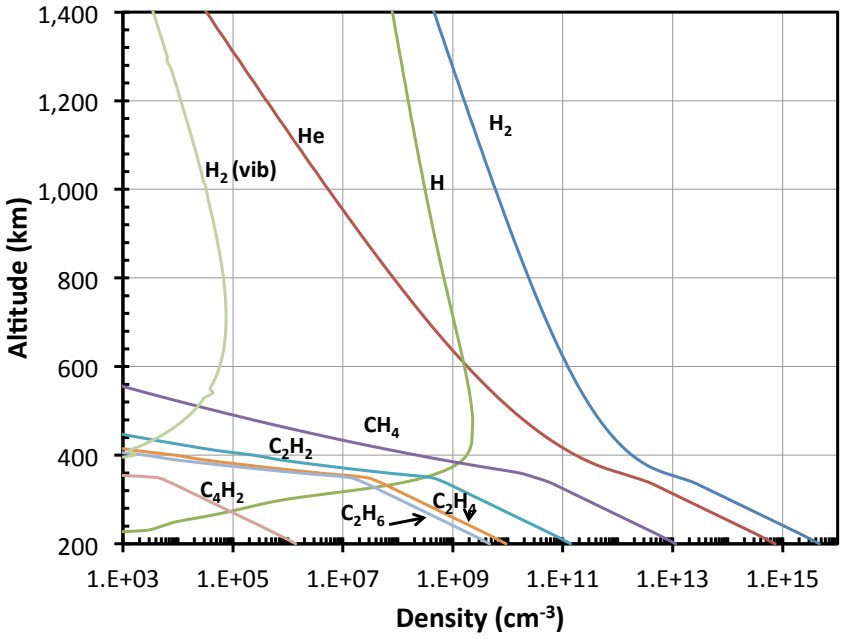

Figure 5.38: Neutral atmosphere profiles used in the photochemical model. Extra hydrocarbons were added because they become important for the chemical reactions occurring at low altitudes.

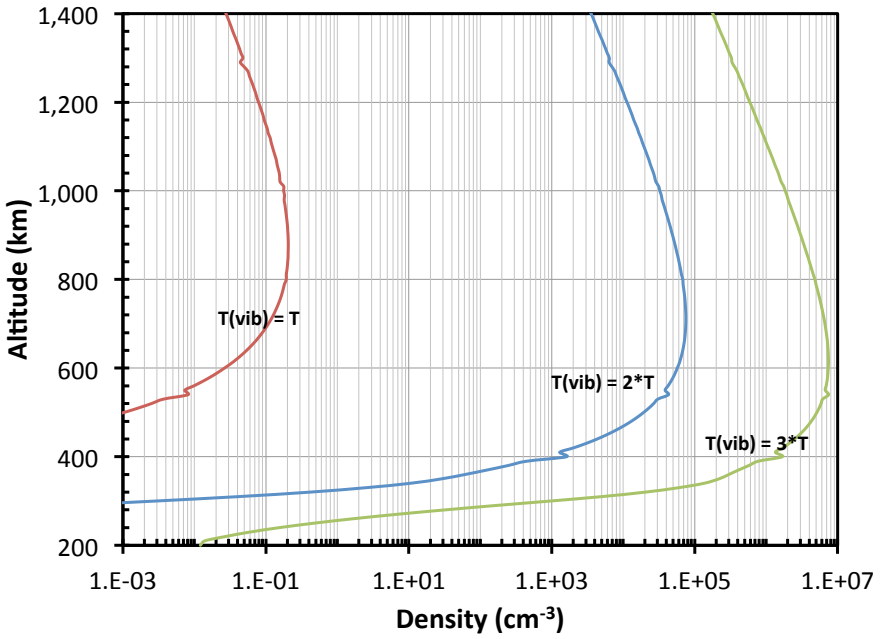

Figure 5.39: $H_{2(vib)}$ density profiles for $T_{vib}(z) = T(z)$, $2T(z)$ and $3T(z)$.

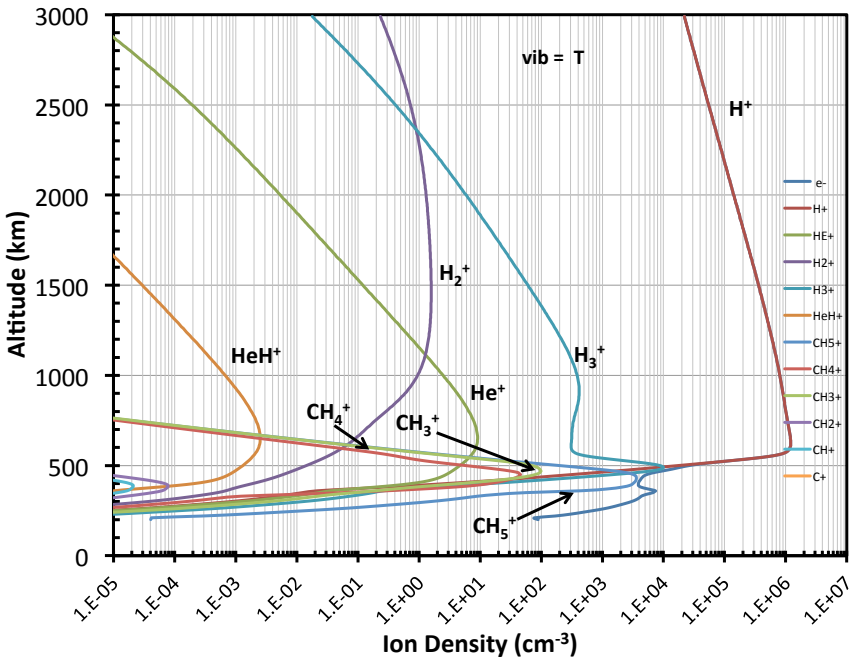

Figure 5.40: Ion densities calculated by our photochemical model. The density of $H_{2(vib)}$ is modified by setting the vibrational temperature $T_{vib}(z)= T(z)$.

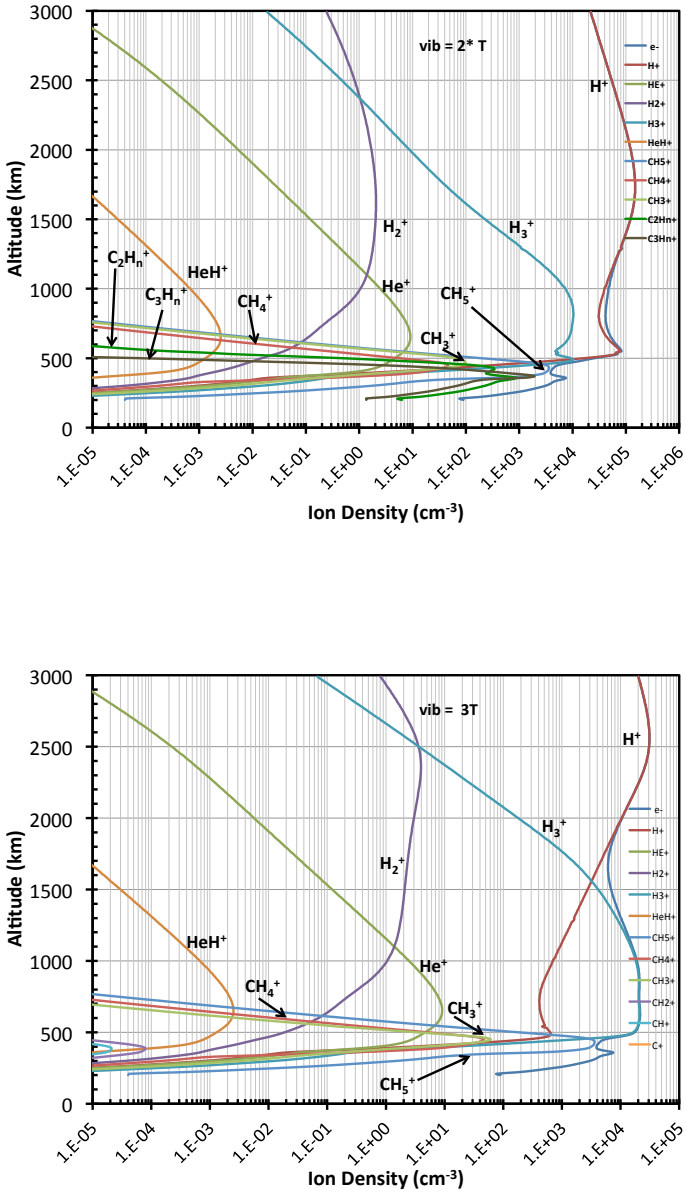

Figure 5.41: Ion densities calculated by our photochemical model. The density of $H_{2(vib)}$ is modified by setting the vibrational temperature $T_{vib}(z)= 2T(z)$ (top) and $T_{vib}(z)= 3T(z)$.

The figures show, as it was expected, that the H^+ and H_2^+ densities decrease for altitudes below 1500 km when the vibrational temperature is increased. At the same time, the H_3^+ peak density also increases from 4×10^2 to $\sim 2 \times 10^4$ cm^{-3}. It becomes the main ion for altitudes below 1500 km, where both the electron and ion precipitation that causes the UV and x-ray aurora deposit their energy. Measurements of ionospheric densities by Pioneer [29], as well as other model results [22, 114] show the electron densities that generally peak for values of 10^5 cm^{-3}. We therefore chose our results with a vibrational temperature of $T_{vib}(z) = 2T(z)$ to be the most appropriate to match the expected results, as the other two temperatures give densities that are either too high or too low to match the observations.

We have also calculated the ion densities at equilibrium for the species of interest as we change the solar zenith angle. The increase in the solar zenith angle has most effect at lower altitudes, which means the hydrocarbon ion species are most affected. At large solar zenith angle the photons are absorbed in the atmosphere at higher altitudes and don't have a chance to reach the lower altitudes and photoionize the neutrals present. The dominant hydrocarbon ion species is CH_5^+, due to the major production reaction:

$$CH_4^+ + H_2 \rightarrow CH_5^+ + H. \tag{5.27}$$

For example, the density of CH_5^+ ions (the dominant hydrocarbon ion) decreases from 3×10^3 cm^{-3} at SZA = 0° to 4×10^2 cm^{-3} at SZA = 90°. We use a value of $T_{vib}(z) = 2T(z)$ for all the cases. The results are shown in Figures 5.42 and 5.43.

Ref. [114] uses a vibrational temperature of 1470 K, which gives a constant gas kinetic coefficient of 2×10^{-9} cm^{3}s^{-1}. It gives results very close to our choice of $T_{vib}(z) = 2T(z)$ and it is also in accordance with [22] and [113]. Therefore, we have chosen this temperature to calculate the ionospheric model for an incoming electron beam with an

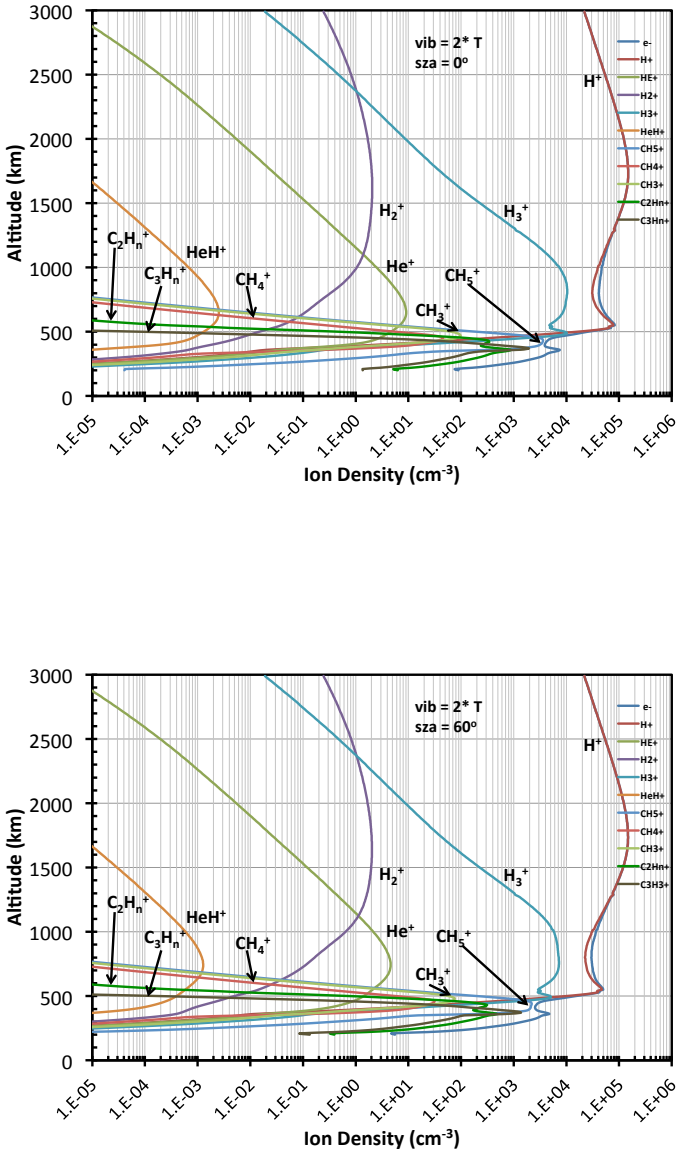

Figure 5.42: Ion densities calculated by our photochemical model. The density of $H_{2(vib)}$ is calculated by setting the vibrational temperature $T_{vib}(z)= 2T(z)$. We calculate the densities for a solar zenith angle of 0° (top) and 60° (bottom).

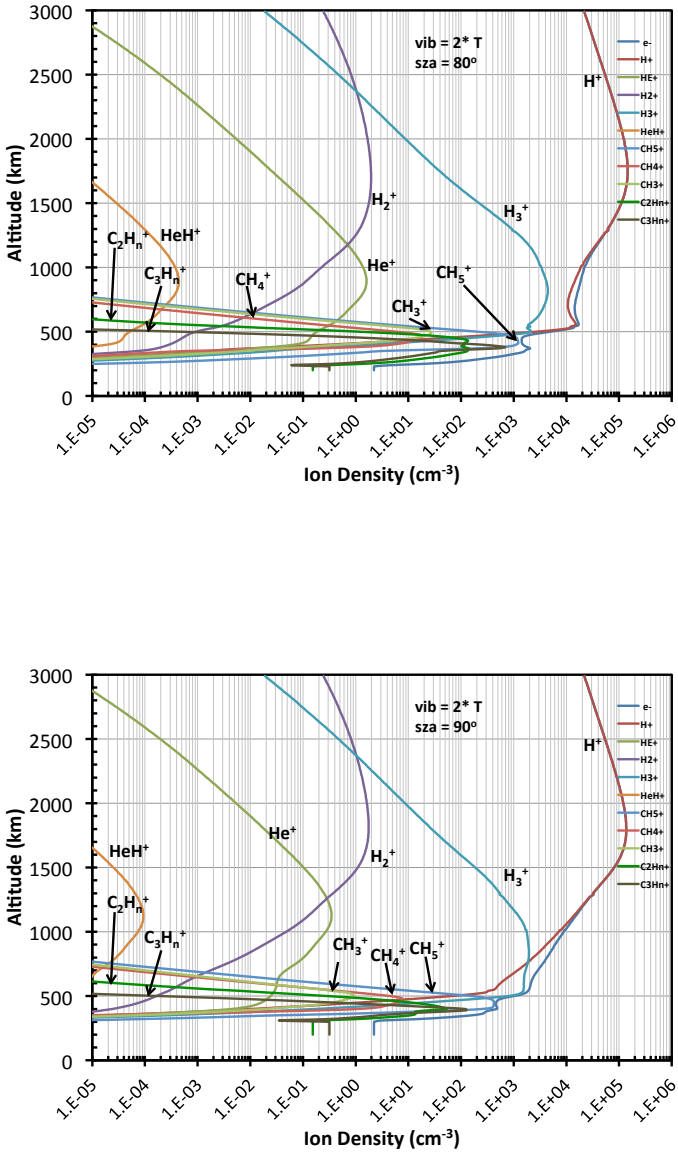

Figure 5.43: Ion densities calculated by our photochemical model. The density of $H_{2(vib)}$ is calculated by setting the vibrational temperature $T_{vib}(z)= 2T(z)$. We calculate the densities for a solar zenith angle of 80° (top) and 90° (bottom).

energy flux of 10 ergs with electrons of energies of 20 keV and 50 keV. The ion densities are shown in Figures 5.44 to 5.47. Because the chemistry in the lower atmosphere is more complicated due to the hydrocarbons present, the code requires more iterations to achieve equilibrium. To speed up the process, we divided the altitude grid and did the calculations for altitudes greater than 500 km separately. This is possible, because the equilibrium calculation of one altitude grid does not depend on the other ones and it allows the code to converge faster.

The ion density at higher altitudes is not very affected by the increase in the electron energy. However, the hydrocarbon ion densities increase in the lower atmosphere, especially the minor species.

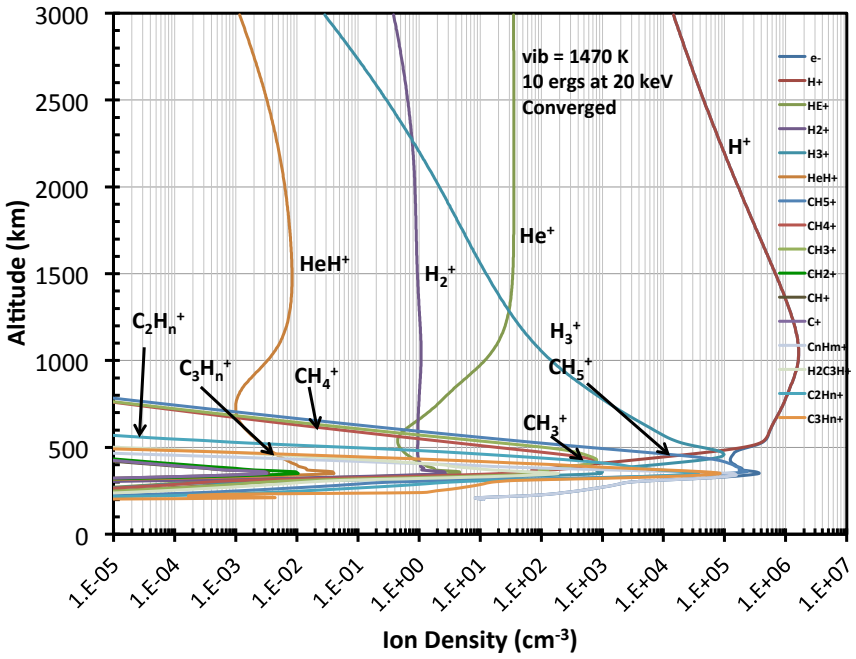

Figure 5.44: Ionospheric profiles for a night time auroral case with a 20 keV electron beam with a flux of 10 ergs. The density of $H_{2(vib)}$ is modified by setting the vibrational temperature T_{vib}(z)= 1470 K.

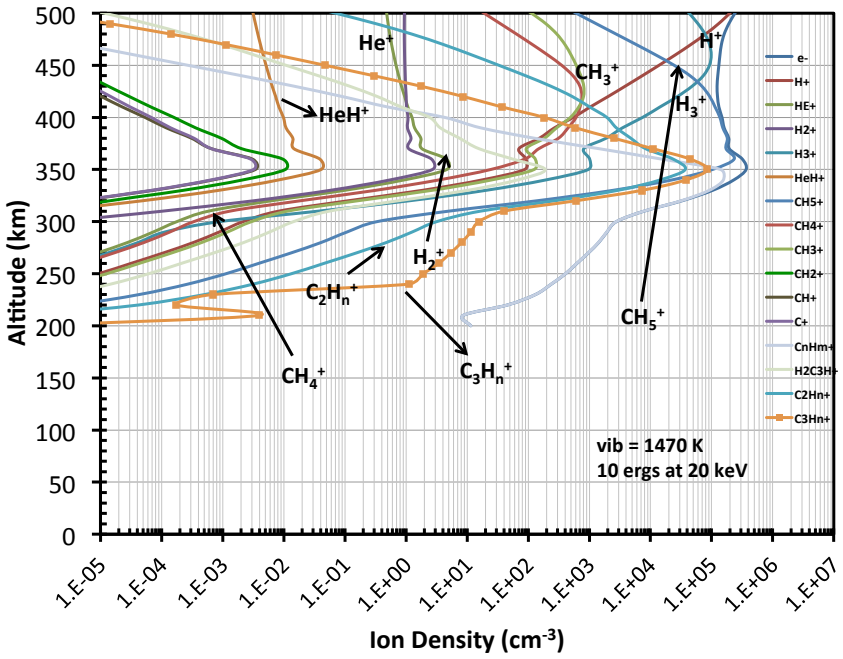

Figure 5.45: Ionospheric profiles for a night time auroral case with a 20 keV electron beam with a flux of 10 ergs, as shown in Figure 5.44. Here we emphasize the lower altitude to better show the hydrocarbon ions.

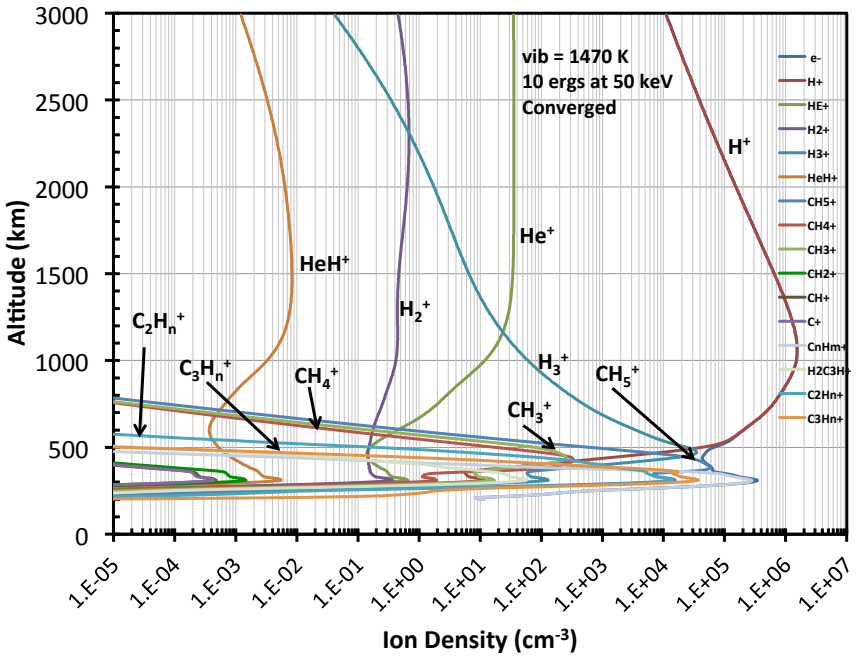

Figure 5.46: Ionospheric profiles for a night time auroral case with a 50 keV electron beam with a flux of 10 ergs. The density of $H_{2(vib)}$ is modified by setting the vibrational temperature T_{vib}(z)= 1470 K.

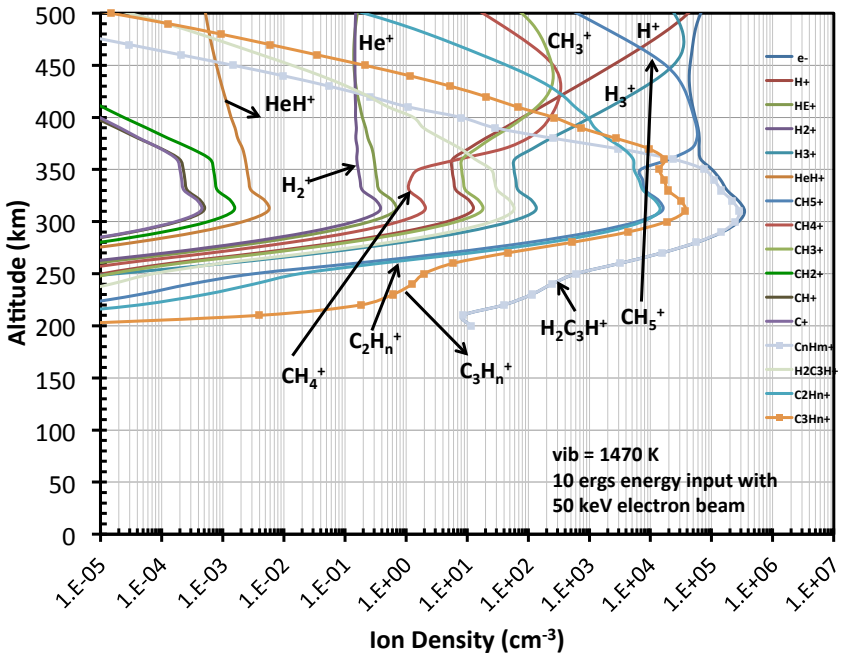

Figure 5.47: Ionospheric profiles for a night time auroral case with a 50 keV electron beam with a flux of 10 ergs, as shown in Figure 5.46. Here we emphasize the lower altitude to better show the hydrocarbon ions.

Chapter 6

Effects of Auroral Ion Precipitation

6.1 Secondary Electrons from Energetic Ion Precipitation

In the previous chapter, we have calculated the ion production rates and electron fluxes due to primary electron beams penetrating the atmosphere and for photoelectrons produced in the atmosphere. These calculations were done with a two-stream model of electron transport along the magnetic field lines (see section 5.1.1). We have compared our model results with those obtained by [22] and [23] in order to validate our calculations. Considering the use of new cross section information and atmospheric model in our calculations, we are within a reasonable difference with the previous models and our model is suitable to handle the transport of electrons along a magnetic file line in the atmosphere.

In the past decade a lot of work has been done to improve the modeling of the primary electron precipitation and the UV aurora. For example, the work of [22] has been further developed for the primary UV aurora by [101] to include thermal effects in the upper atmosphere. However, not much work has been done to model the sec-

ondary electrons resulting from the ion precipitation that leads to the x-ray aurora. [45] did some estimates regarding the secondary electron distributions resulting from low oxygen charge states precipitating into the upper atmosphere. This model is not very accurate, as it approximates the secondary electron ejection cross section to those of secondary electrons in proton-neutral collisions. Due to the lack of cross section data available tho model was (and still is) the most accurate model available for secondary electrons ejected by the precipitating ions. With the present work we make an enormous contribution to this research area by calculating for the first time the secondary electron distributions due to the precipitation of oxygen ions in the jovian upper atmosphere. We use the most up-to-date single differential cross sections that are available (see Chapter 3) and combine them with the most complete ion precipitation model (see Chapter 4) to obtain secondary electron distributions at different altitudes in the atmosphere. This chapter will review secondary electron production model and show the electron fluxes in the ionosphere obtained by applying the two-stream model that was covered in the previous chapter (see sections 5.1.1 and 5.1.2). We also calculate the ion production rates and airglow production due to the secondary electrons from the ion aurora.

6.2 Model Description

In order to model the production rates of secondary electrons from the energetic ion precipitation, we adapt our existing ion Monte Carlo model (see Chapter 4) to handle the ejected electrons. We use the same neutral atmosphere (see Figure 4.1) as well as the same ion neutral cross sections for ionization, stripping and charge transfer collisions that are used in the ion Monte Carlo model (see Chapter 3 for the cross sections used and Section 4.2.2 for a review of the collision processes considered in the ion precipitation model). We then incorporate all the processes that involve the ejection of a secondary

electron by using the single differential cross sections and processes given in Chapter 3.

Let's describe the process in a little more detail. We have selected three initial ion energies 1 MeV/u, 1.5 MeV/u and 2 MeV/u for our sampling model. We chose these energies based on the fact that they are the energies that are most effective in producing the x-ray auroral emissions observed in the polar cap (see Chapter 4). We use only oxygen ions for this model, as the single differential cross sections available at the time are only for oxygen and none are available for sulfur. We start at the top of the atmosphere (3000 km over the cloud tops) with a low charge state (q=2) and let the ion precipitate along a radial field line at the polar cap, i.e., with zero inclination. The ion will penetrate a random distance or depth in the atmosphere measured in column density, dN, as shown in equation 4.8. At that point it will have a collision, also chosen at random by the probabilities shown in equaltions 4.9 to 4.11. There are three types of collisions that are possible: 1. Ionization, 2. Stripping and 3. Charge transfer (see section 4.2.2 for a review of these collisions). In this new model, we have added more possible collision outcomes, as they are important for the secondary electrons. For instance, if we have an ionization collision, the code randomly decides weather it is a single or double ionization collision. This is done by calculating a probability for each process with the total cross sections at the collision energy for the processes involved, in this case single or double ionization, just as it is done in equaltions 4.9 to 4.11. If the ion has a stripping collision, the code randomly decides wether it was a single or a double striping collision. And last, if we have a charge transfer collision, the code will randomly decide between three different outcomes: transfer ionization, double capture auto-ionization or charge transfer (which does not have an ejected electron). A summary of the decision process can be seen in a flow chart on Figure 6.1.

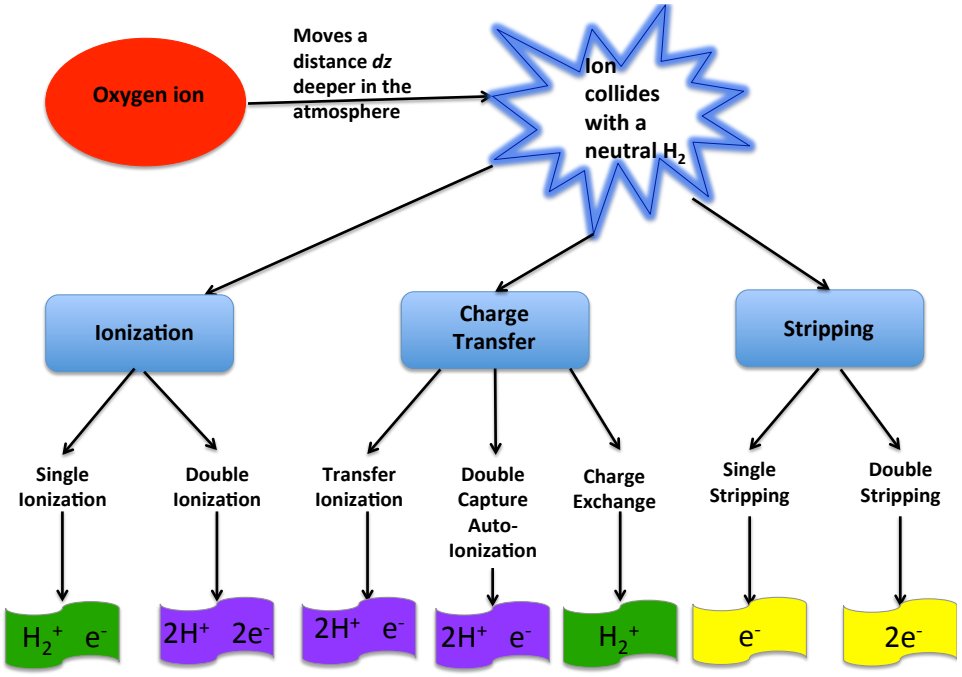

Figure 6.1: Representation of the ion precipitation model and the possible outcomes that it may have after a collision with a neutral hydrogen molecule in the atmosphere. Each collision is chosen randomly by the code using the appropriate cross sections. The product ions and electrons after each collision are shown.

In Figure 6.1 we can see that the different collisions will give different products which are important for our model. For example, double ionization and double stripping collisions will produce two electrons, single ionization and stripping as well as transfer ionization and double capture auto-ionization will produce a single electron and charge exchange collisions will produce no electrons. For the ionospheric effects of the ion precipitation we are also interested in the H_2^+ and H^+ ions that are produced in these collisions, since they are important for the atmospheric chemistry, as we review in Section 5.4. The code in our numerical model keeps track of the altitude where the collisions occur and therefore, we are also able to track the production rate of electrons and ions at each altitude bin. There are 150 altitude bins in this code, which vary in size from 100 km for very high altitudes (3000 km – 1100 km) down to 2 km for the low altitudes (400 km – 250 km), where the ions deposit most of their energy. In this section we will concentrate on the secondary electrons that are ejected in the above mentioned collisions and we will discuss their effects in the ionosphere.

When a collision occurs, we calculate the energy of the ejected electron by using the ejected electron probability distributions given in Section 3.5.5. At each collision, the code finds the appropriate ejected electron probability distribution for the given energy of the ion, the charge state at the time of the collision and the type of collision that occurred. Because we don't have a way to calculate the distribution of the ejected electron for all possible ion energies we approximate the distribution to that of the closest available ion energy, as explained in Chapter 3. At each collision we find the energy of the ejected electron randomly from the distribution. To do this, first, we calculate the ejection probability for the highest and lowest energies that make up each energy bin in our two-stream code. Then, we take a random number between 0 and 1 and find the distribution values in which the random number lies between. This will

give us the energy bin to which the ejected electron corresponds to, i.e., the energy of the secondary electron.

As a test of this procedure before utilizing it in the ion precipitation model, we have used the ejected electron probability for all initial ion energies available from the data for all processes and charge states (see Chapter 3) and have used 10^5 random numbers for each case to find the corresponding energy of the ejected electron. The code keeps track of the number of electrons produced at each energy bin. This number is normalized by dividing the total counts at each bin by the total number of electrons, 10^5, and the size of the energy bin, dE. The normalized counts correspond to the production rate of electrons for a particular collision type and initial ion energy and charge state and the resulting shape should model the shape of the single differential cross section used to calculate the probability distribution. The magnitude of the normalized counts vary from the single differential cross sections because of the different energy bin sizes by which we are dividing. For example, at higher energies the bin size is bigger and the resulting normalized production rate is smaller than for the low energies, where the bin sizes are small (e.g. 0.5 eV). Figures 6.2 to 6.14 show the resulting production rates or normalized counts for the different collision processes for 10^5 ejected electrons in each case. We chose to show only the charge states with the highest cross sections to represent the results.

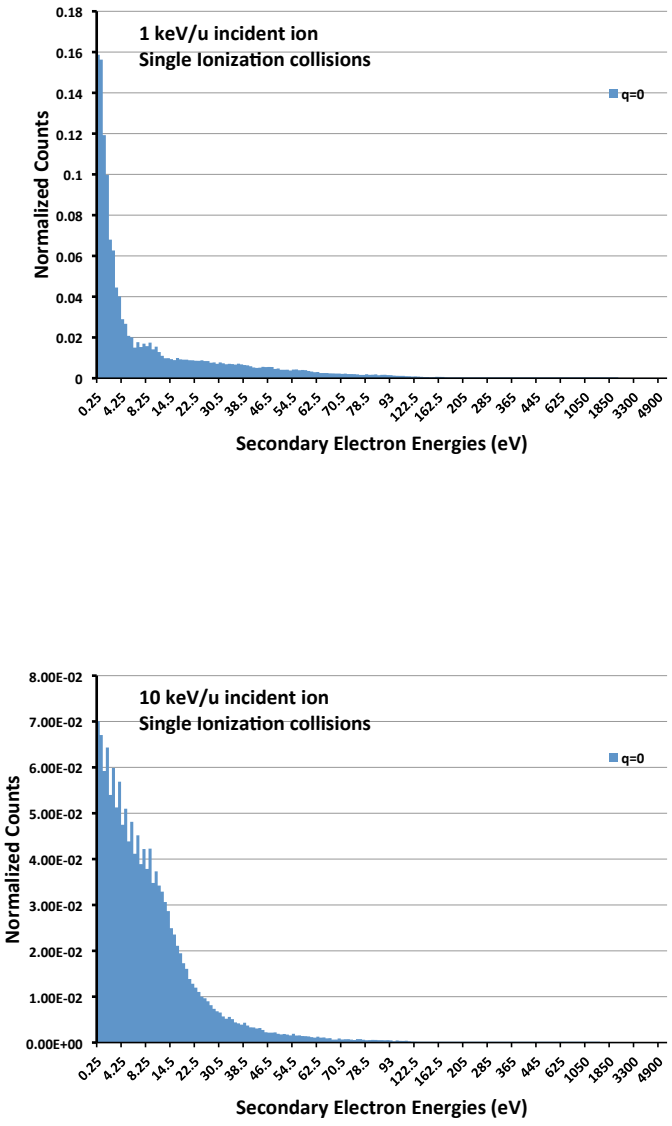

Figure 6.2: Normalized counts of secondary electrons ejected calculated randomly by using the distributions given in Section 3.5.5. The collision type is single ionization and the initial ion energies are 1 keV/u (top) and 10 keV/u (bottom).

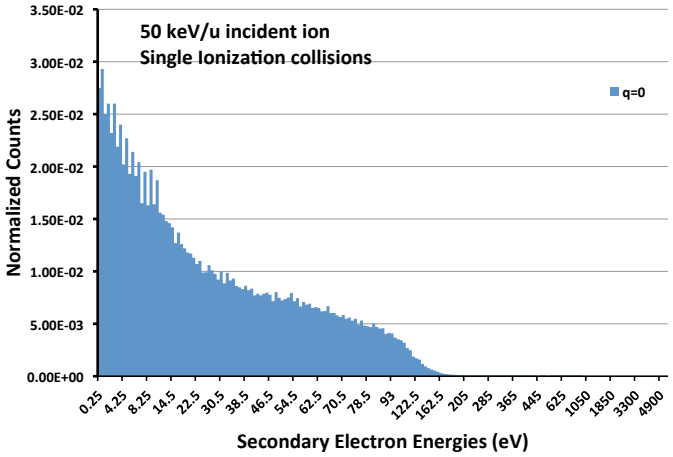

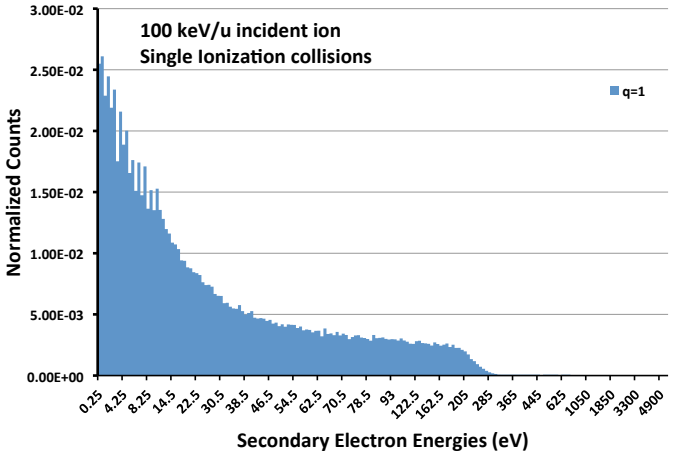

Figure 6.3: Normalized counts of secondary electrons ejected calculated randomly by using the distributions given in Section 3.5.5. The collision type is single ionization and the initial ion energies are 50 keV/u (top) and 100 keV/u (bottom).

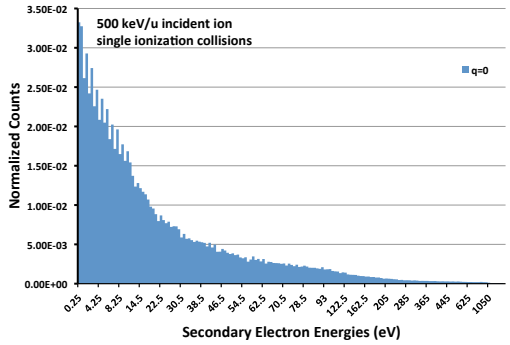

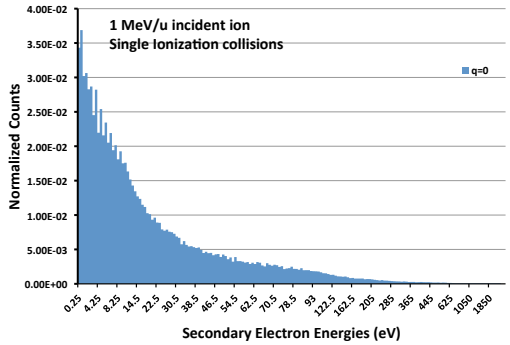

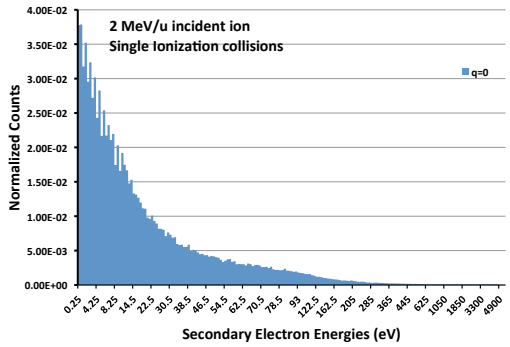

Figure 6.4: Normalized counts of secondary electrons ejected calculated randomly by using the distributions given in Section 3.5.5. The collision type is single ionization and the initial ion energies are 500 keV/u (top) and 1 MeV/u (center) and 2 MeV/u (bottom).

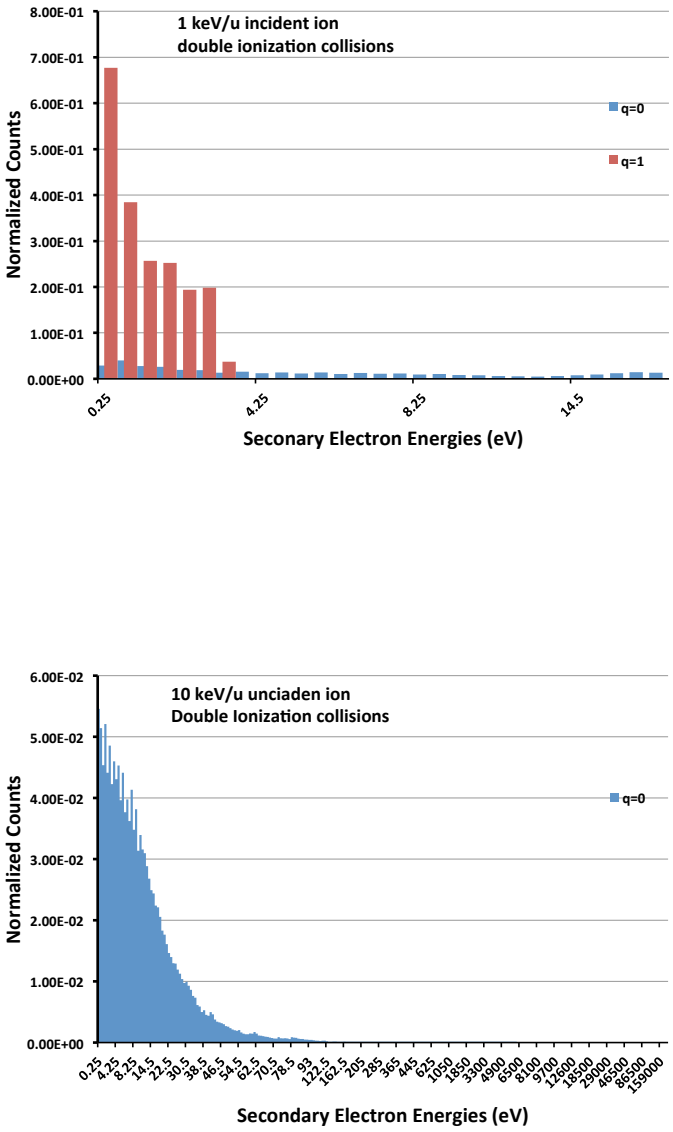

Figure 6.5: Normalized counts of secondary electrons ejected calculated randomly by using the distributions given in Section 3.5.5. The collision type is double ionization and the initial ion energies are 1 keV/u (top) and 10 keV/u (bottom).

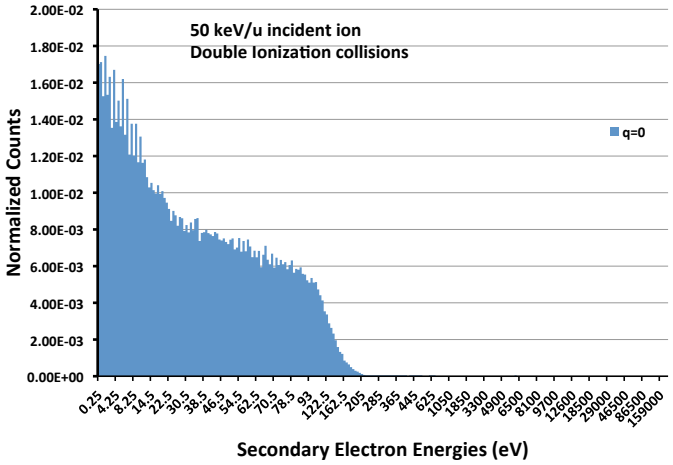

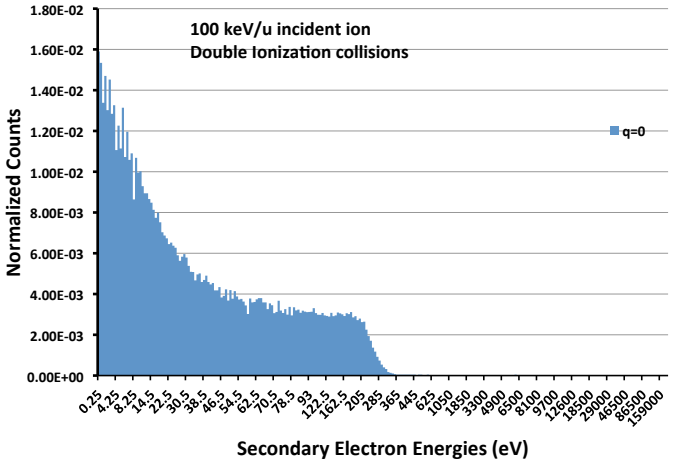

Figure 6.6: Normalized counts of secondary electrons ejected calculated randomly by using the distributions given in Section 3.5.5. The collision type is double ionization and the initial ion energies are 50 keV/u (top) and 100 keV/u (bottom).

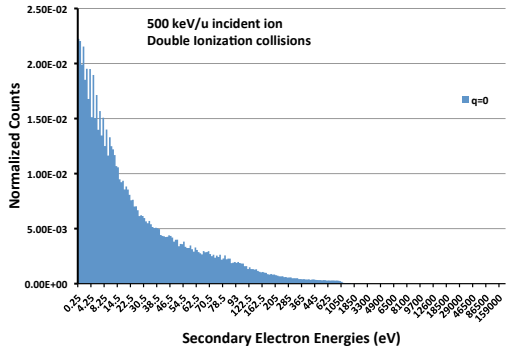

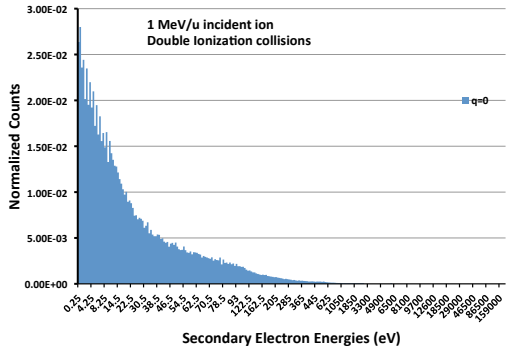

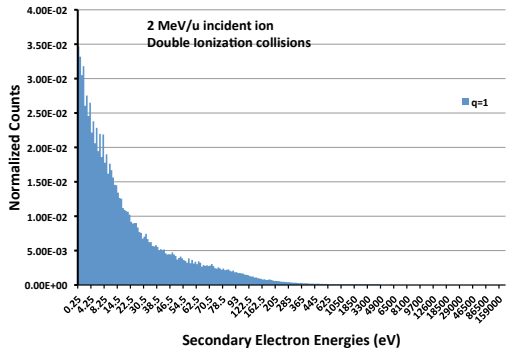

Figure 6.7: Normalized counts of secondary electrons ejected calculated randomly by using the distributions given in Section 3.5.5. The collision type is double ionization and the initial ion energies are 500 keV/u (top) and 1 MeV/u (center) and 2 MeV/u (bottom).

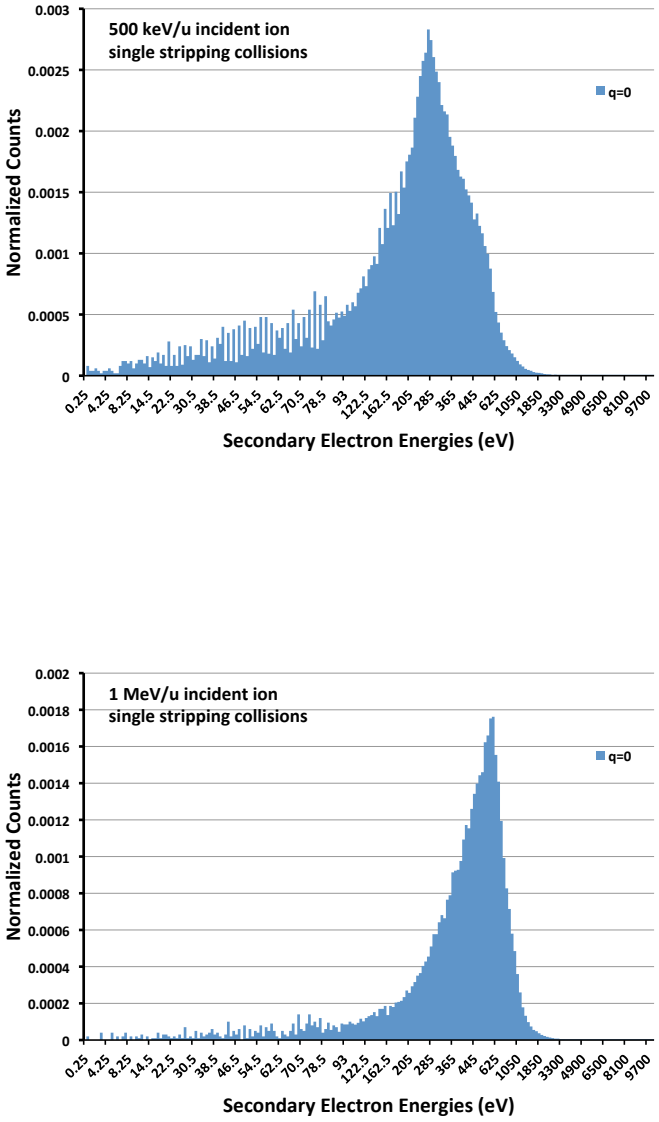

Figure 6.8: Normalized counts of secondary electrons ejected calculated randomly by using the distributions given in Section 3.5.5. The collision type is single stripping and the initial ion energies are 500 keV/u (top) and 1 MeV/u (bottom). Note that the peak of the produced electrons is at the boosted electron energy, due to the fact that the electron is ejected from the projectile and not the target.

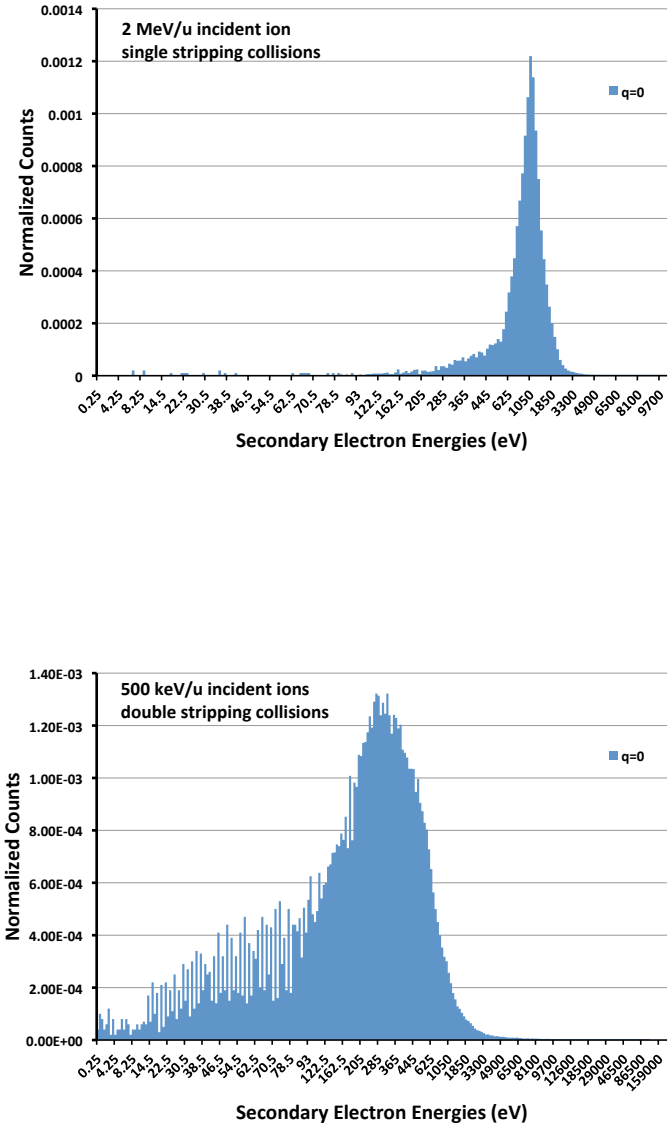

Figure 6.9: Normalized counts of secondary electrons ejected calculated randomly by using the distributions given in Section 3.5.5. The collision type is single stripping with an initial ion energy of 2 MeV/u (top) and a double stripping collision for a 500 keV/u ion (bottom). Note that the peak of the produced electrons is at the boosted electron energy, due to the fact that the electron is ejected from the projectile and not the target.

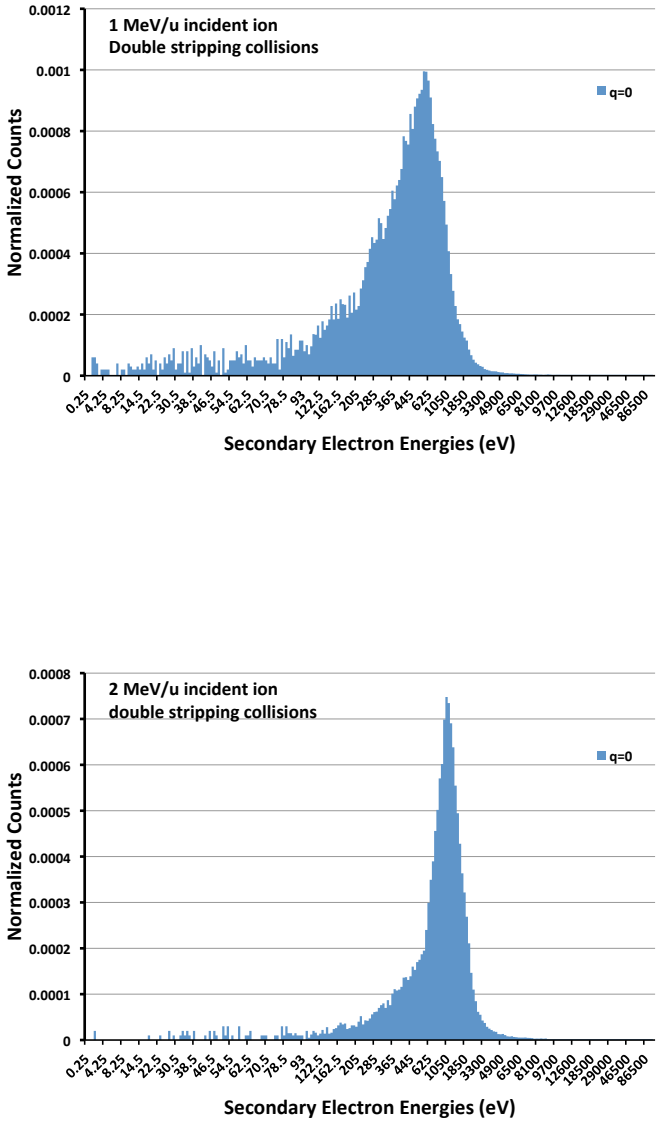

Figure 6.10: Normalized counts of secondary electrons ejected calculated randomly by using the distributions given in Section 3.5.5. The collision type is double stripping and the initial ion energies are 1 MeV/u (top) and 2 MeV/u (bottom). Note that the peak of the produced electrons is at the boosted electron energy, due to the fact that the electron is ejected from the projectile and not the target.

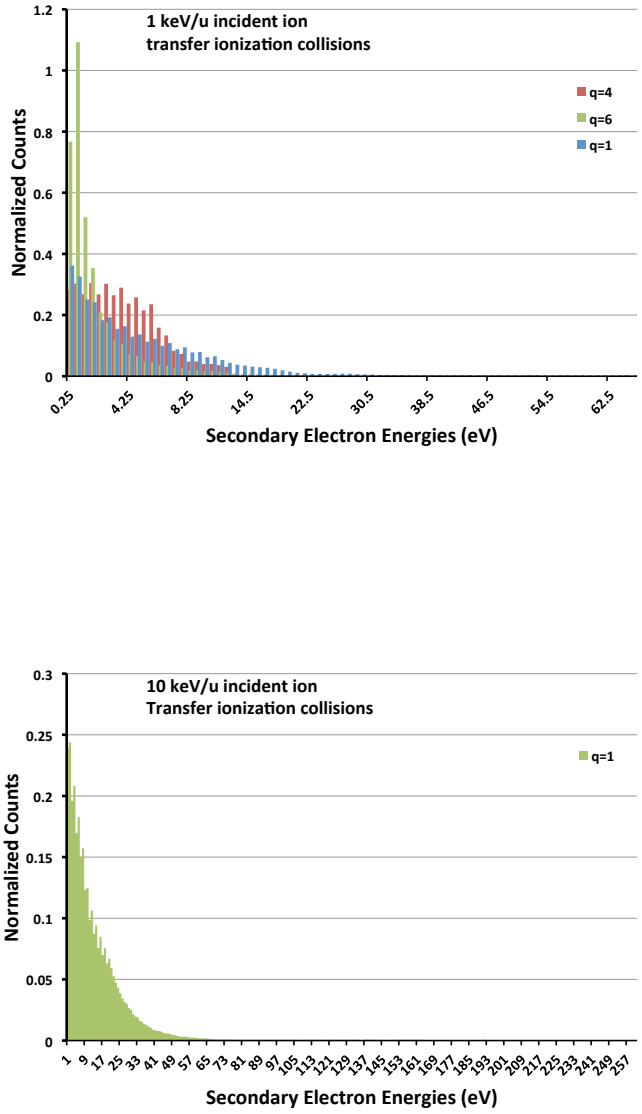

Figure 6.11: Normalized counts of secondary electrons ejected calculated randomly by using the distributions given in Section 3.5.5. The collision type is transfer ionization and the initial ion energies are 1 keV/u (top) and 10 keV/u (bottom).

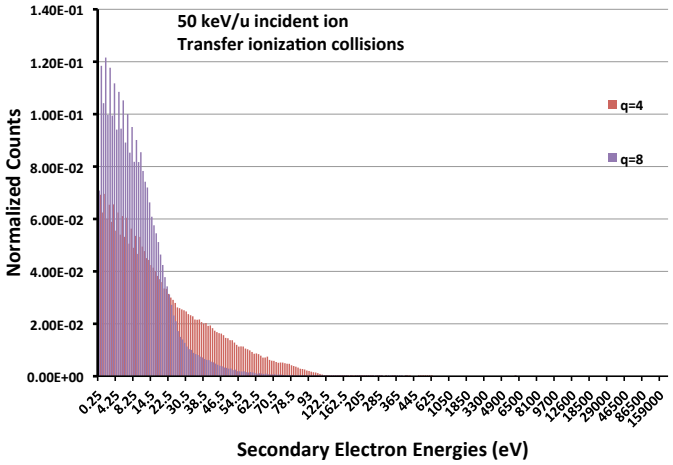

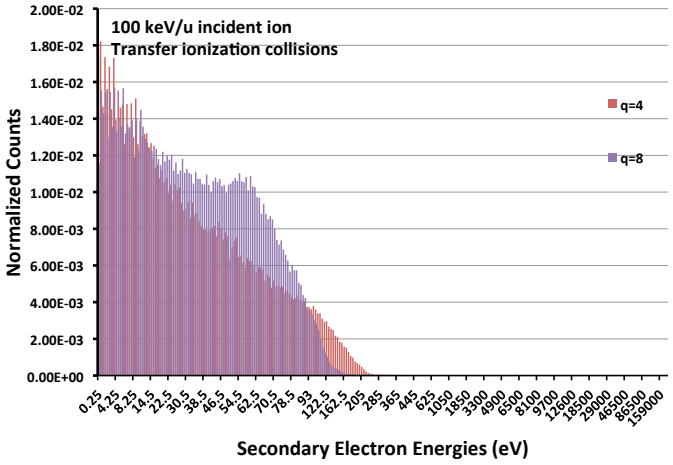

Figure 6.12: Normalized counts of secondary electrons ejected calculated randomly by using the distributions given in Section 3.5.5. The collision type is transfer ionization and the initial ion energies are 50 keV/u (top) and 100 keV/u (bottom).

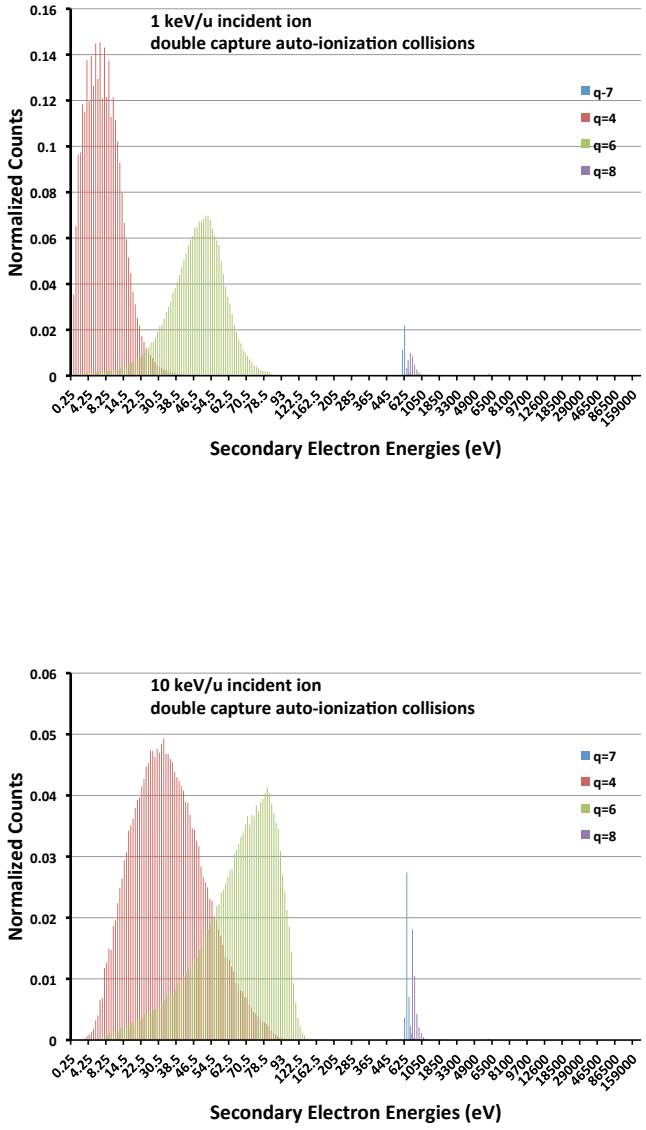

Figure 6.13: Normalized counts of secondary electrons ejected calculated randomly by using the distributions given in Section 3.5.5. The collision type is double capture auto-ionization and the initial ion energies are 1 keV/u (top) and 10 keV/u (bottom). The peaks on the counts are due to an energy boost to the electrons as they are emitted from the projectile.

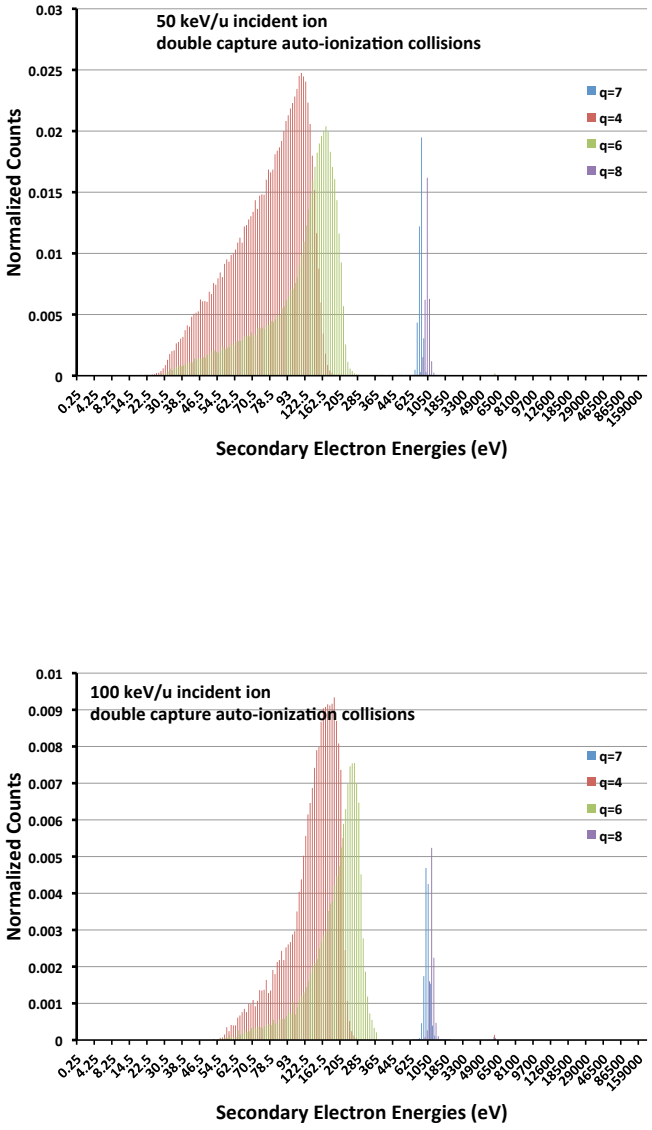

Figure 6.14: Normalized counts of secondary electrons ejected calculated randomly by using the distributions given in Section 3.5.5. The collision type is double capture auto-ionization and the initial ion energies are 50 keV/u (top) and 100 keV/u (bottom). The peaks on the counts are due to an energy boost to the electrons as they are emitted from the projectile.

We implement this procedure in the ion precipitation model to determine the energy of the ejected electrons. After the collision type is determined, the ejected electron energy is picked at random from the ejection probability for the given process as explained above. In Chapter 3 we also calculated the angular dependence of the ejected electrons. We have used the precent forward scattering calculated and shown in Figures 3.35, 3.36, 3.45, and 3.54 to randomly decide if the electron will scatter forward or backward after the collision. All the electrons ejected from a stripping collision are assumed to scatter forward, due to the high cross section for the forward scattering angles in this collision type.

In order to build enough statistics we use 10,000 - 15,000 incident ions at each initial energy chosen (1 MeV/u, 1.5 MeV/u or 2 MeV/u) and collect the production rates of forward and backward scattered secondary electrons independently as well as the product H^+ and H_2^+ at each altitude bin. The electron production rates at each altitude that we obtain from the ion Monte Carlo model are used as an input in the two-stream code. The two-stream code uses altitude bins of 10 km in size. Therefore, we must adjust our results from the ion precipitation model to match the altitudes in the two-stream code. For example, if we have an altitude bin with a size of 100 km in the ion precipitation model, we divide the production rates for this altitude by 10 and put the result in each of the corresponding 10 altitude bins in the two-stream code. If the altitude bin in the ion precipitation model is only 2 km, we add the production rate of five consecutive bins an match them to the corresponding altitude bin in the two-stream code.

6.3 Results

6.3.1 Secondary Electron Production and Fluxes

Our first important result in this model is the production rate of secondary electrons due to the ion precipitation. Figures 6.15 to 6.17 show the forward and backward electron production rates at different altitudes in the atmosphere due to the precipitation of a single oxygen ion with an initial energy at the top of the atmosphere of either 1, 1.5 or 2 MeV/u, respectively. From the figures we can see that as we go deeper in the atmosphere the electron production increases. The peak electron production occurs where the ion beam reaches a maximum depth. The majority of the electrons are produced in ionization collisions. Therefore, the shape of the production rate resembles the single differential ionization cross section. There is a drop in the production around 2 MeV, just as seen in the cross section. Some of the electrons come from the stripping collisions. These electron production gives rise to a secondary peak seen in the production rate at lower altitudes around 1 MeV.

We also show the production rate as a function of altitude for certain electron energies of interest. These are shown in Figures 6.18 to 6.20 for forward and backward scattered electrons. In these figures we can clearly see that the production rate peak for all the different electron energies occurs at the same altitude. For the 1 MeV/u oxygen ion the peak electron production rate occurs at an altitude between 330 – 340 km as seen in the figure. The highest electron production is for low energy electrons, as expected from the cross sections. The production rate for low energy electrons scattered forward is about 50 times larger than for those scattered backward. For higher electron energies ($\sim$1 keV) the production rate of forward scattered electrons is about 25 times larger than those scattered backward. For a 2 MeV/u oxygen ion the peak electron rate occurs at an altitude between 300 – 310 km. As it is to be expected, the 2 MeV/u oxygen ions

reach deeper in the atmosphere than the lower energy ions, depositing most of their energy low in the atmosphere.The forward electron production rate is 12.5 times larger than the backward electron production for low energy electrons and 20 times larger for the high energy electrons and overall it is larger than the electron production rate of the 1 MeV/u ion.

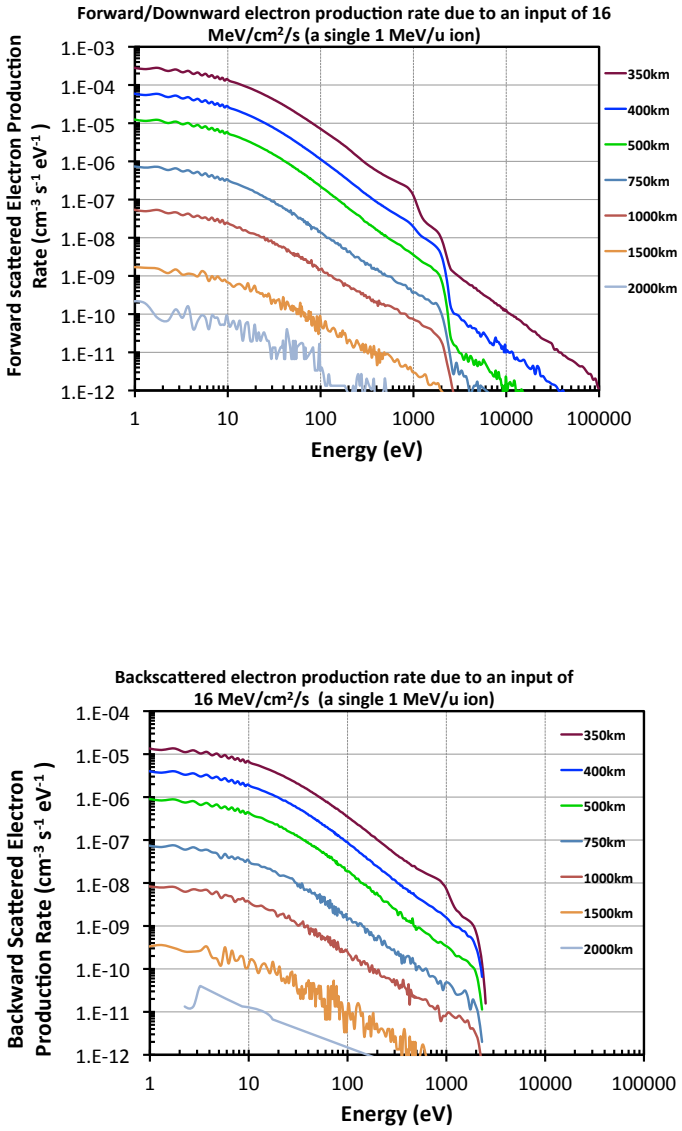

Figure 6.15: Secondary electron production rates at different altitudes in the atmosphere due to the precipitation of an oxygen single ion with an initial energy of 1 MeV/u at the top of the atmosphere (energy flux = 16 MeV/cm^2/s). The top figure shows the forward scattered electron production and the bottom figure shows the backward scattered electron production.

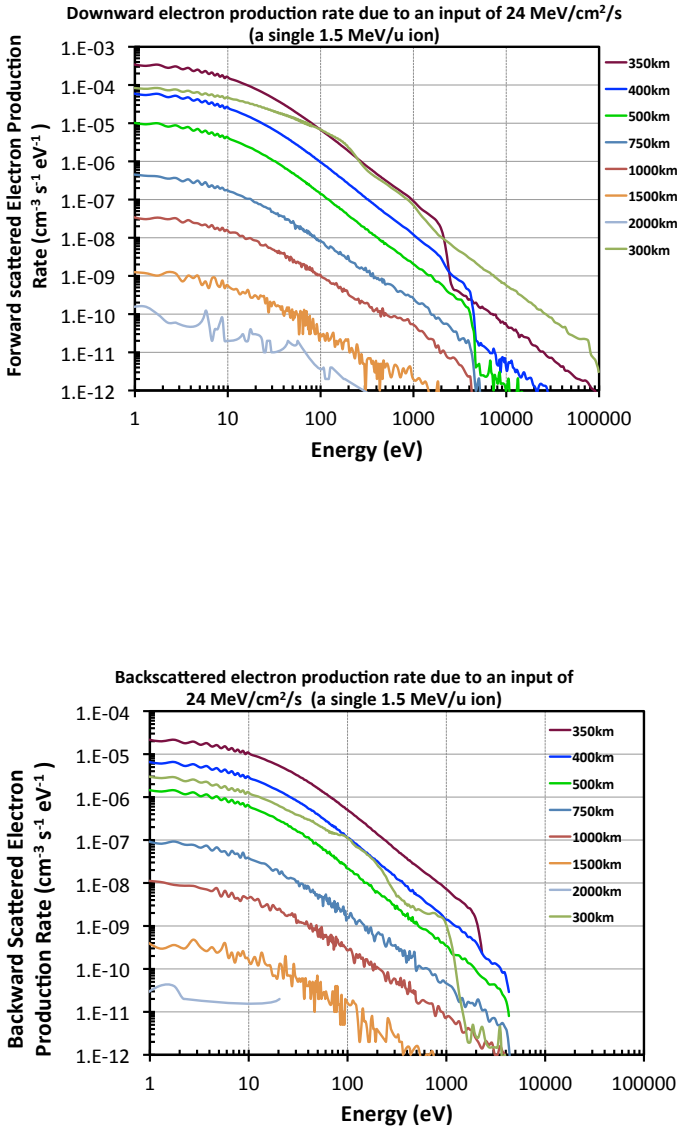

Figure 6.16: Secondary electron production rates at different altitudes in the atmosphere due to the precipitation of an oxygen single ion with an initial energy of 1.5 MeV/u at the top of the atmosphere (energy flux = 24 MeV/cm^2/s). The top figure shows the forward scattered electron production and the bottom figure shows the backward scattered electron production.

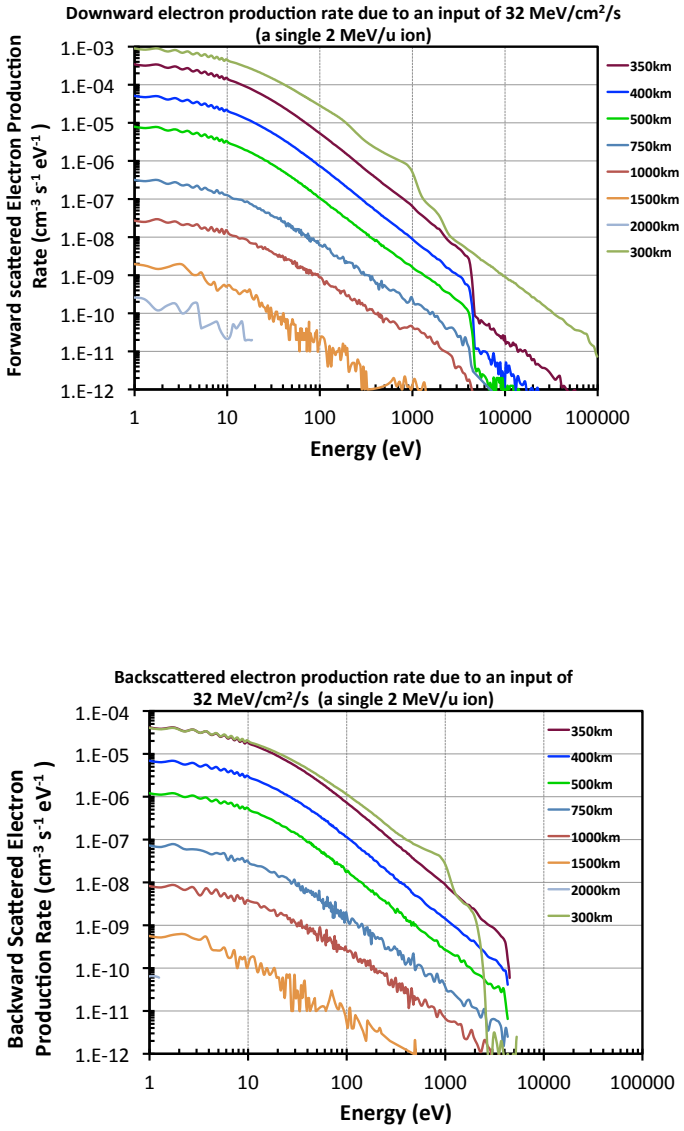

Figure 6.17: Secondary electron production rates at different altitudes in the atmosphere due to the precipitation of an oxygen single ion with an initial energy of 2 MeV/u at the top of the atmosphere (energy flux = 32 MeV/cm^2/s). The top figure shows the forward scattered electron production and the bottom figure shows the backward scattered electron production.

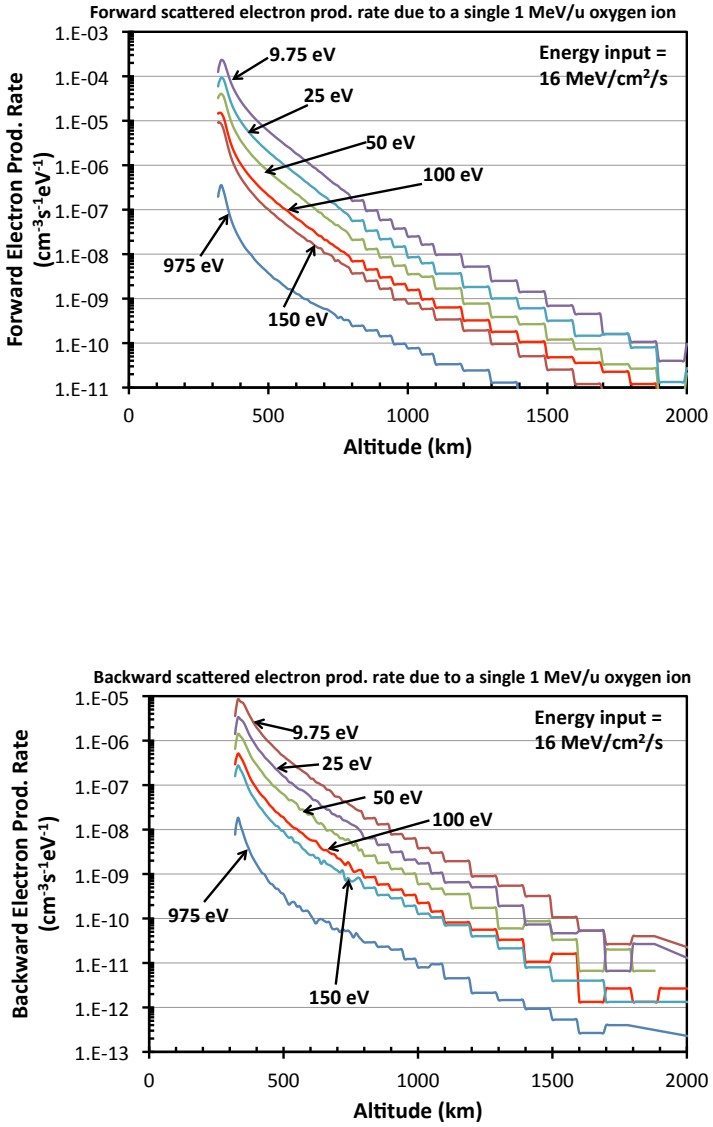

Figure 6.18: Secondary electron production rates as a function of altitude for different secondary electron energies due to the precipitation of an oxygen ion with an initial energy of single 1 MeV/u at the top of the atmosphere (energy flux = 16 MeV/cm^2/s). The top figure shows the forward scattered electron production rate and the bottom figure shows the backward scattered electron production rate.

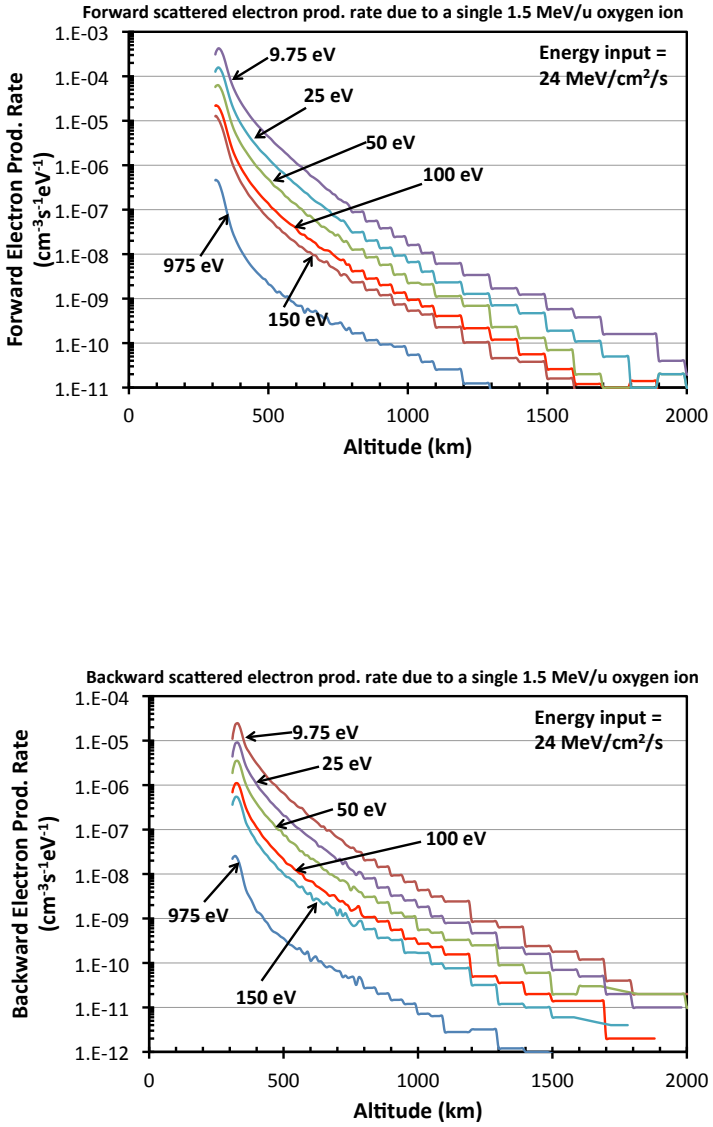

Figure 6.19: Secondary electron production rates as a function of altitude for different secondary electron energies due to the precipitation of an oxygen ion with an initial energy of single 1.5 MeV/u at the top of the atmosphere (energy flux = 24 MeV/cm^2/s). The top figure shows the forward scattered electron production rate and the bottom figure shows the backward scattered electron production rate.

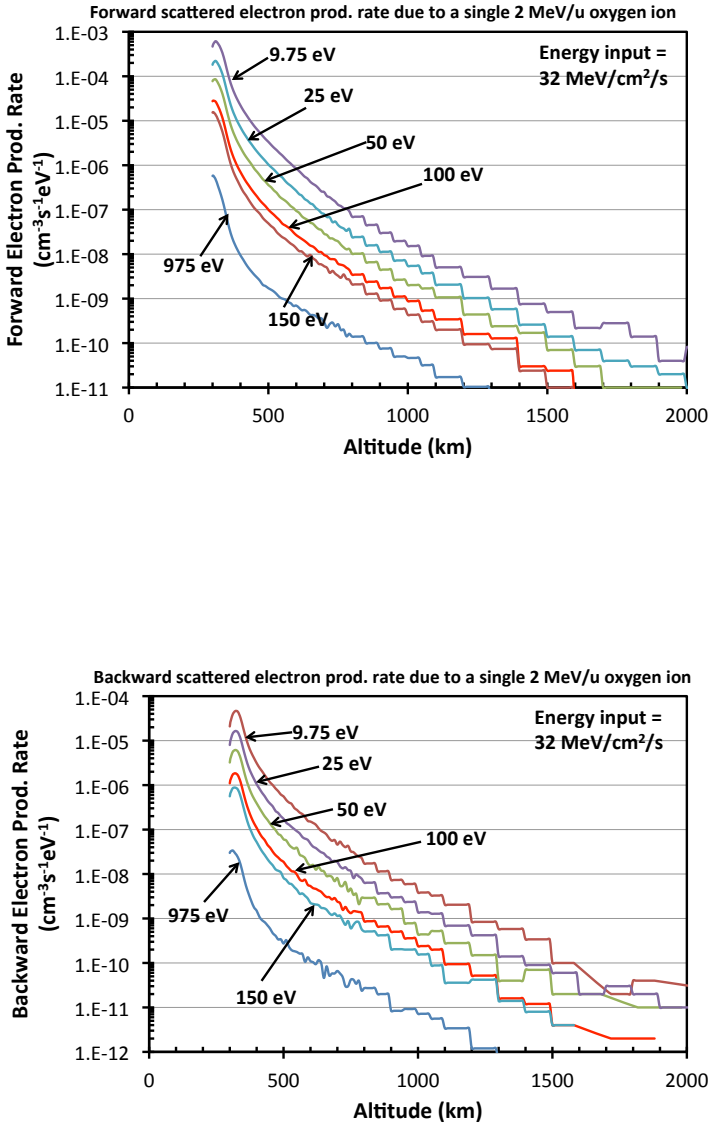

Figure 6.20: Secondary electron production rates as a function of altitude for different secondary electron energies due to the precipitation of an oxygen ion with an initial energy of single 2 MeV/u at the top of the atmosphere (energy flux = 32 MeV/cm^2/s). The top figure shows the forward scattered electron production rate and the bottom figure shows the backward scattered electron production rate.

The forward scattered electrons are included as a production term in the two-stream equations for the downward flux and similarly the backward electron production is included as a production term for the upward electron flux. This is done by changing the third term on the right hand side of equation 5.9. In the previous chapter, this term included half of the photoelectron production calculated, as it was assumed that these photoelectrons were isotropic. However, the ion Monte Carlo precipitation model calculates upward and downward electron production rates separately. Therefore, the forward scattered electron production is used in the third term of the two-stream equation to calculate the downward flux and similarly the backward scattered electron production is used to calculate the upward fluxes. We solve the equations for the fluxes along the field line as explained in the above sections and show the results in Figures 6.22 to 6.23. We use an initial electron density in the ionosphere calculated for a solar zenith angle of 80°, as shown in section 5.4 Figure 5.43, and an electron temperature equal to the neutral density temperature as shown in Figure 4.2.

The downward electron fluxes build up as we go further in the atmosphere. There is very little electron production due to the ion collisions at high altitudes because of the low neutral density. However, the flux builds up at lower altitudes, as more secondary electrons are produced. However, at very low altitudes, the electron flux drops quickly again, since the ion beam that produces the secondary electrons doesn't penetrate such low altitudes. The upward and downward electron fluxes are very comparable and almost equal for altitudes close to the production peak location. The fluxes for electron energies between 20 – 1000 eV remain almost constant at high altitudes and there is not a high loss of these electrons once they are produced lower in the atmosphere, allowing them to escape the ionosphere. The same behavior is observed for the three cases explore. However, as we increase the ion energy, the variation in the fluxes close to the peak altitude becomes smaller.

In Figures 6.24 to 6.26 we can see how the downward electron fluxes build up as we go to lower altitudes. There is very little difference between the upward and downward electron fluxes for 10 eV electrons for altitudes below 1000 km, suggesting that the flux for this low energy becomes isotropic below this altitude. However, for 20 eV electrons the upward flux is larger than the downward flux at these lower altitudes. This can be explained by production of upward electrons by backscatter collisions that occur locally due to the electron transport. For higher energies the downward electron fluxes are a larger. Fewer electrons are able to backscatter at these higher electron energies and the electron production in the upward direction is initially low. For all energies we can see that the electron flux reaches a steady value at altitudes above 1500 – 2000 km, depending on the electron energy. This indicates that there is a balance in their production and loss of electrons at high altitudes where the neutral density is low. For high energies this equilibrium is reach low in the atmosphere and the electrons are able to escape. For lower energy electrons this equilibrium is only reached at altitudes higher than 2000 km. In the previous chapter we saw a similar behavior in the fluxes of auroral electrons and photoelectrons.

At the top of the atmosphere (z = 3000 km) we can use the flux calculated by the two-stream code to identify the upward and downward energy flux and electron flux. The upward flux at the top of the atmosphere is very important, as it gives us information regarding the escaping energy flux and/or electrons, which in turn contribute to the downward current. This current is very important for the ionosphere-magnetosphere coupling mechanism. Table 6.1 summarizes the upward and downward electron and energy fluxes at the top of the atmosphere due to a single oxygen ion with an initial energy of either 1, 1.5 or 2 MeV/u.

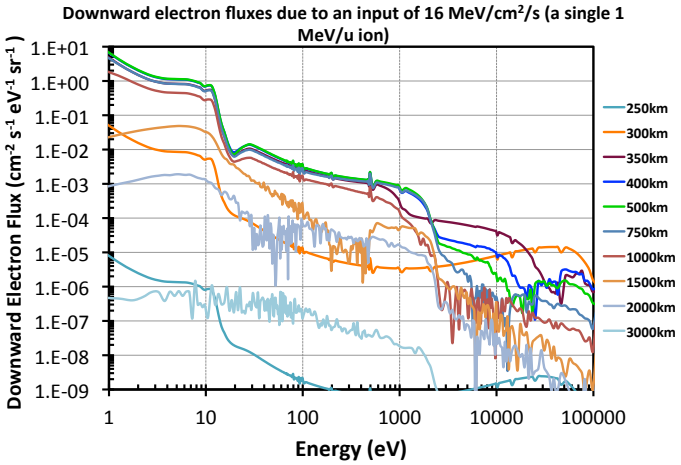

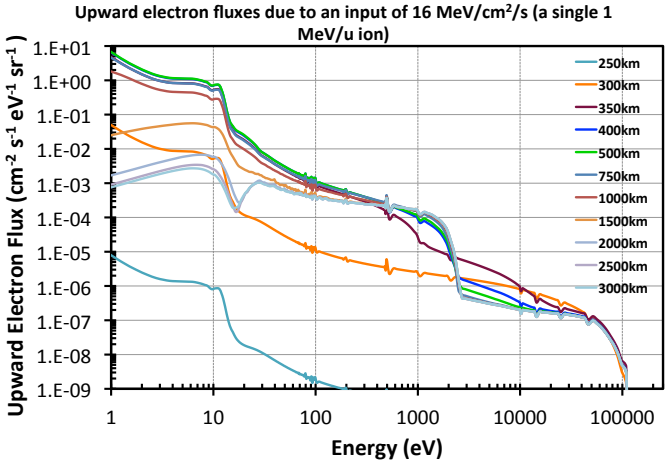

Figure 6.21: Downward (top) and upward (bottom) electron fluxes at different altitudes in the atmosphere calculated with the two-stream transport equations for specific electron energies as labeled in the figure. This figure shows the fluxes due to secondary electron fluxes from a single 1 MeV/u oxygen ion (energy flux = 16 MeV/cm^2/s). There is no other external input of electrons, i.e., no magnetospheric electron beams or photoelectrons are considered here.

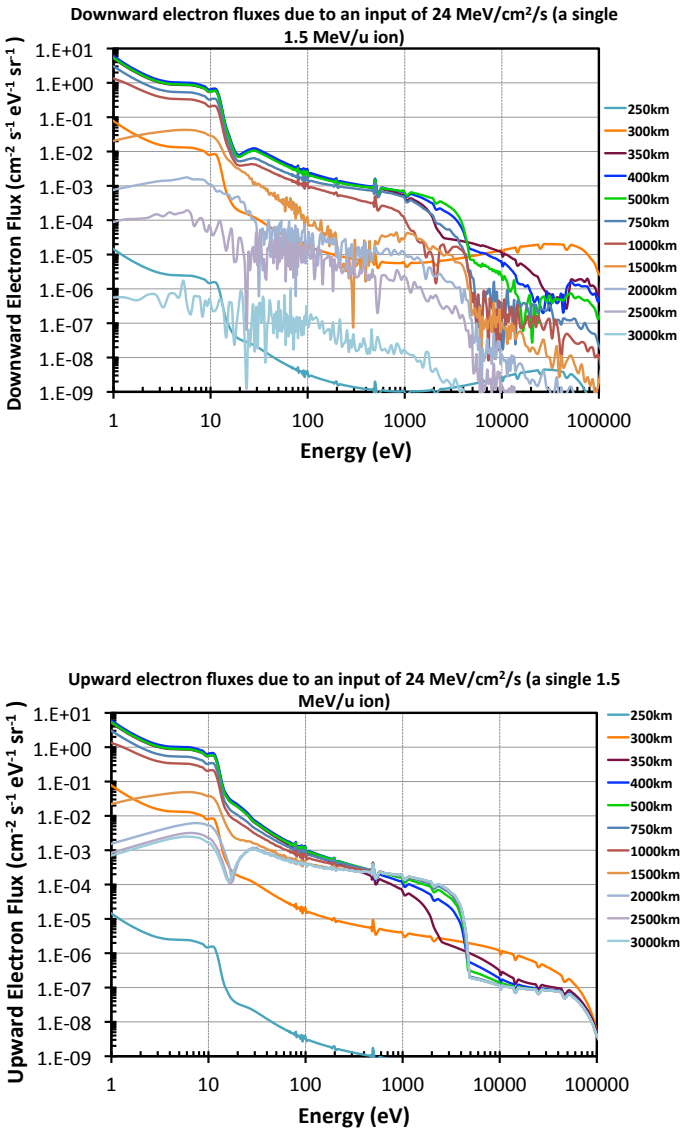

Figure 6.22: Downward (top) and upward (bottom) electron fluxes at different altitudes in the atmosphere calculated with the two-stream transport equations for specific electron energies as labeled in the figure. This figure shows the fluxes due to secondary electron fluxes from a single 1.5 MeV/u oxygen ion (energy flux = 24 MeV/cm^2/s). There is no other external input of electrons, i.e., no magnetospheric electron beams or photoelectrons are considered here.

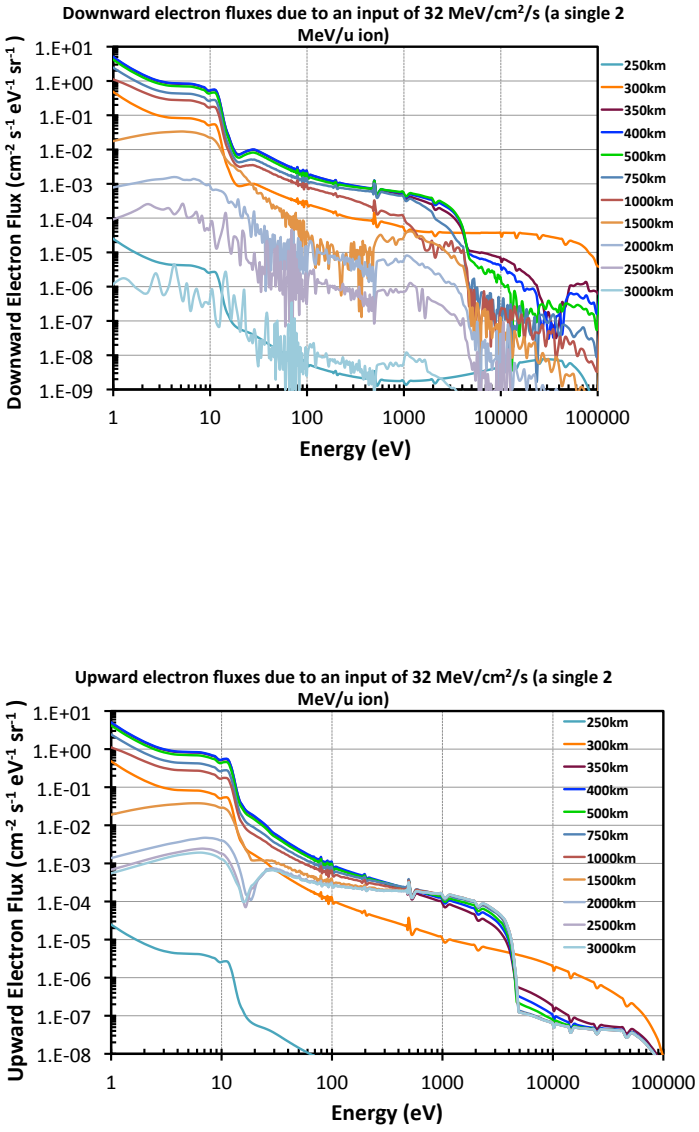

Figure 6.23: Downward (top) and upward (bottom) electron fluxes at different altitudes in the atmosphere calculated with the two-stream transport equations for specific electron energies as labeled in the figure. This figure shows the fluxes due to secondary electron fluxes from a single 2 MeV/u oxygen ion (energy flux = 32 MeV/cm^2/s). There is no other external input of electrons, i.e., no magnetospheric electron beams or photoelectrons are considered here.

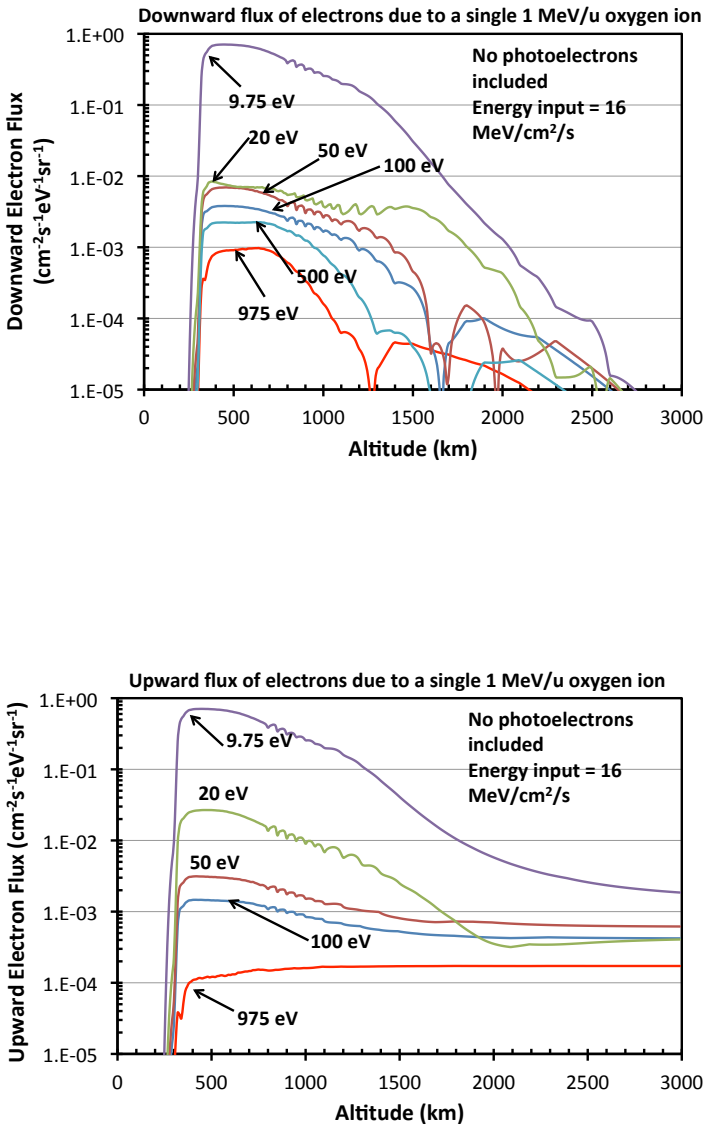

Figure 6.24: Downward (top) and upward (bottom) electron fluxes as a function of altitude calculated with the two-stream transport equations for specific electron energies as labeled in the figure. This figure shows the fluxes due to secondary electron fluxes from a single 1 MeV/u oxygen ion (energy flux = 16 MeV/cm^2/s). There is no other external input of electrons, i.e., no magnetospheric electron beams or photoelectrons are considered here.

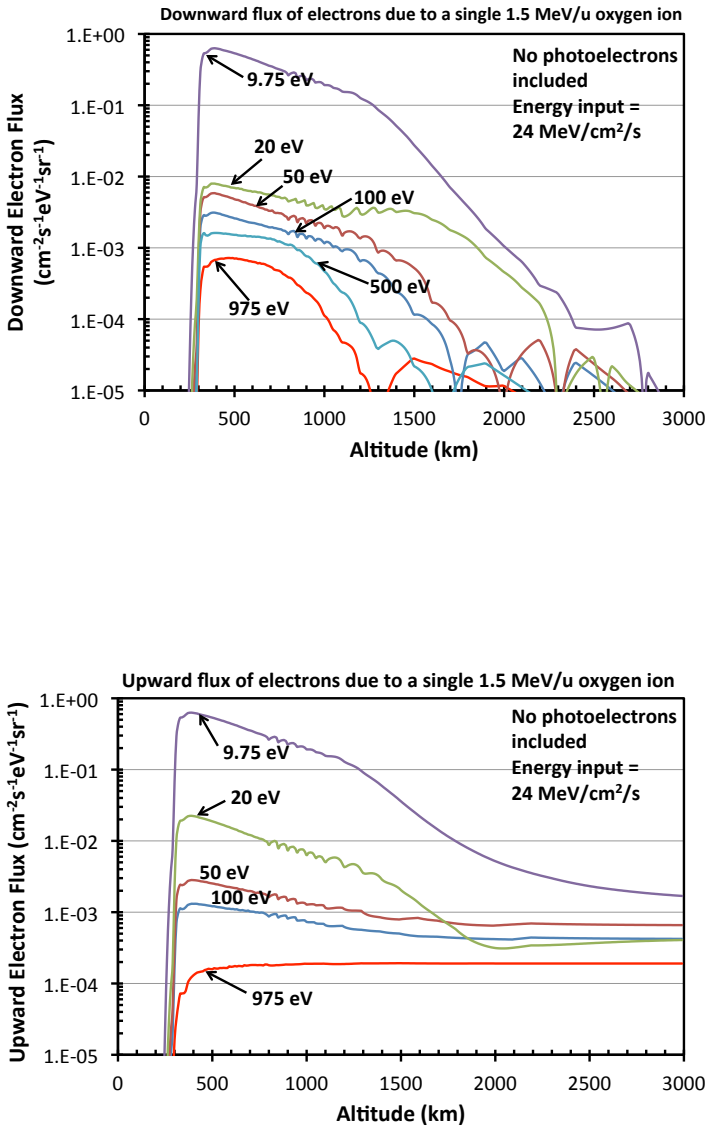

Figure 6.25: Downward (top) and upward (bottom) electron fluxes as a function of altitude calculated with the two-stream transport equations for specific electron energies as labeled in the figure. This figure shows the fluxes due to secondary electron fluxes from a single 1.5 MeV/u oxygen ion (energy flux = 24 MeV/cm^2/s). There is no other external input of electrons, i.e., no magnetospheric electron beams or photoelectrons are considered here.

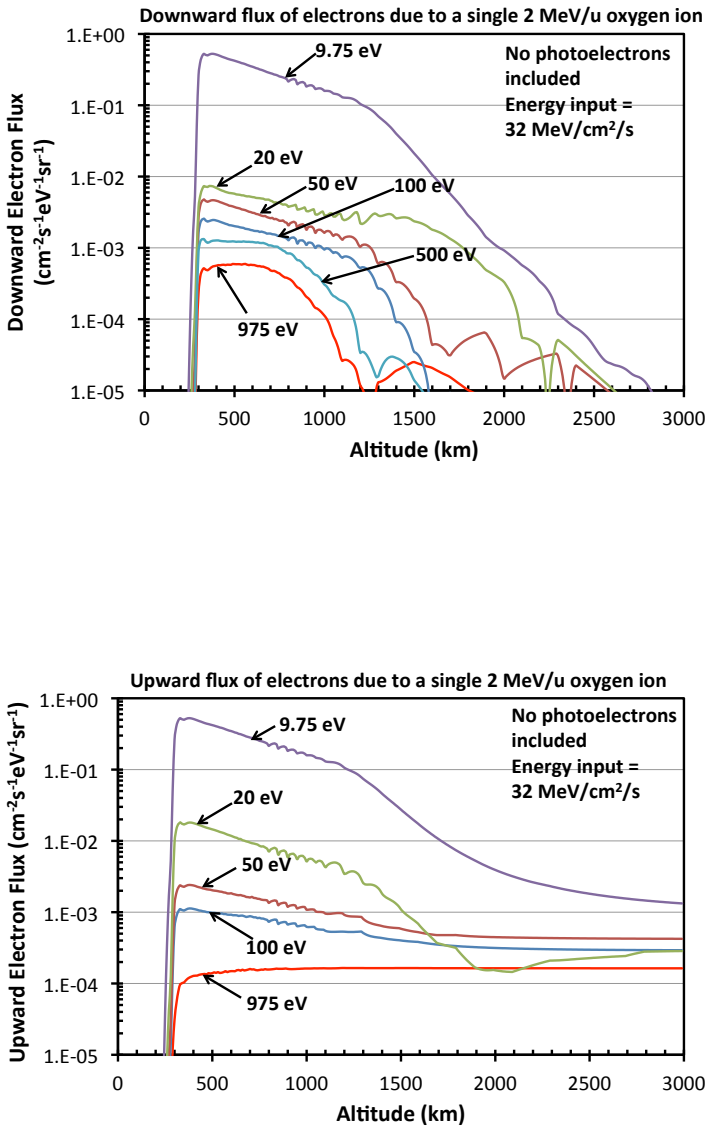

Figure 6.26: Downward (top) and upward (bottom) electron fluxes as a function of altitude calculated with the two-stream transport equations for specific electron energies as labeled in the figure. This figure shows the fluxes due to secondary electron fluxes from a single 2 MeV/u oxygen ion (energy flux = 32 MeV/cm^2/s). There is no other external input of electrons, i.e., no magnetospheric electron beams or photoelectrons are considered here.

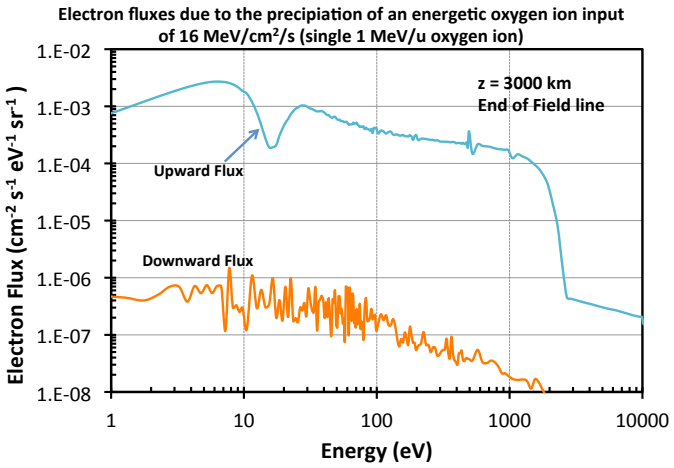

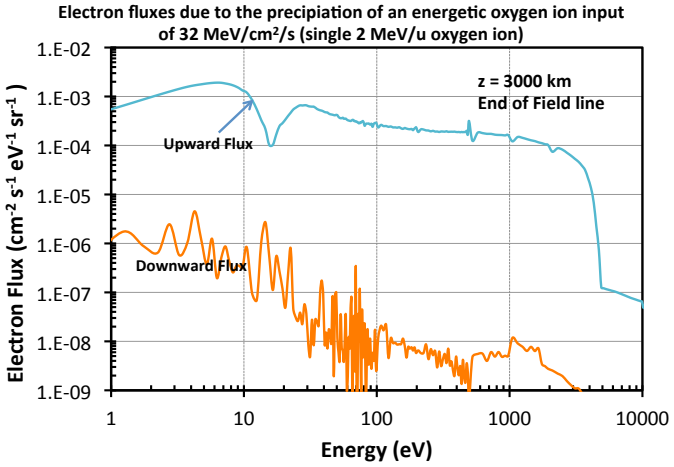

Figure 6.27: Upward and downward electron fluxes at the top of the atmosphere (z = 3000 km) due to a single oxygen ion precipitating in the atmosphere with an initial energy of 1 MeV/u (top) and 2 MeV/u (bottom).

Table 6.1: Secondary electron fluxes and their energy flux carried upward or downward at the top of the atmosphere. Each case shows our calculation due to the secondary electrons produced by a **single** oxygen ion precipitating in the atmosphere with an initial energy or 1, 1.5 or 2 MeV/u.

Ion Energy	(eV/cm^2/s)	(eV/cm^2/s)	(elect/cm^2/s)	(elect/cm^2/s)
MeV/u	upward	downward	upward	downward
1.0	1.71×10^3	1.71×10^{-1}	1.20	2.91×10^{-4}
1.5	2.82×10^3	1.38×10^{-1}	1.77	1.97×10^{-4}
2.0	2.24×10^3	1.19×10^{-1}	1.44	1.06×10^{-4}

Table 6.2: Airglow emissions due to secondary electrons produced by a **single** oxygen ion precipitating in the atmosphere with an initial energy or 1, 1.5 or 2 MeV/u. The table shows our results for the different emissions in a column of the atmosphere.

Process	1 MeV/u	1.5 MeV	2 MeV/u
Column rate	($cm^{-2}s^{-1}$)	($cm^{-2}s^{-1}$)	($cm^{-2}s^{-1}$)
Lyman bands (direct excit.)	3.91×10^4	5.59×10^4	7.17×10^4
Lyman bands (cascade)	4.44×10^3	6.40×10^3	8.23×10^3
Werner bands	3.5×10^4	5.0×10^4	6.38×10^4
Lyman alpha (from H_2 diss.)	8.64×10^3	1.24×10^4	1.58×10^4
Lyman alpha (from H)	7.69×10^1	5.90×10^1	4.77×10^1

6.3.2 Airglow Emission due Secondary Electrons

We have used equation 5.16 to calculate the airglow production rates due to the secondary electrons, just as it was done for the primary auroral electrons. Please see section 5.1.4 for a review of the processes that give rise to airglow emissions and Chapter 2 for the needed cross sections. The results are shown in Figures 6.28 to 6.30 and the column production rates are summarized in Table 6.2. We note that these production rates are due to a single ion precipitating in the atmosphere. In general, the Lyman bands have the largest production rate in a column of atmosphere. As we increase the ion energy at the top of the atmosphere the production of Lyman and Werner bands increases. As the ion energy increases, it is able to penetrate deeper in the atmosphere where the H_2 density is larger. Since this molecule is the source of such emission, we expect to see higher emissions with larger density. On the other hand, the Ly-α emissions decrease as we increase the ion energy. We observed the same behavior when we calculated their production rate due to the auroral electrons. We can explain this observation also by noticing that as the ion reaches lower altitudes in the atmosphere, the H density decreases deeper in the atmosphere below the homopause. Therefore, as the ions reach such low regions, there is less H to produce the Ly-α emissions.

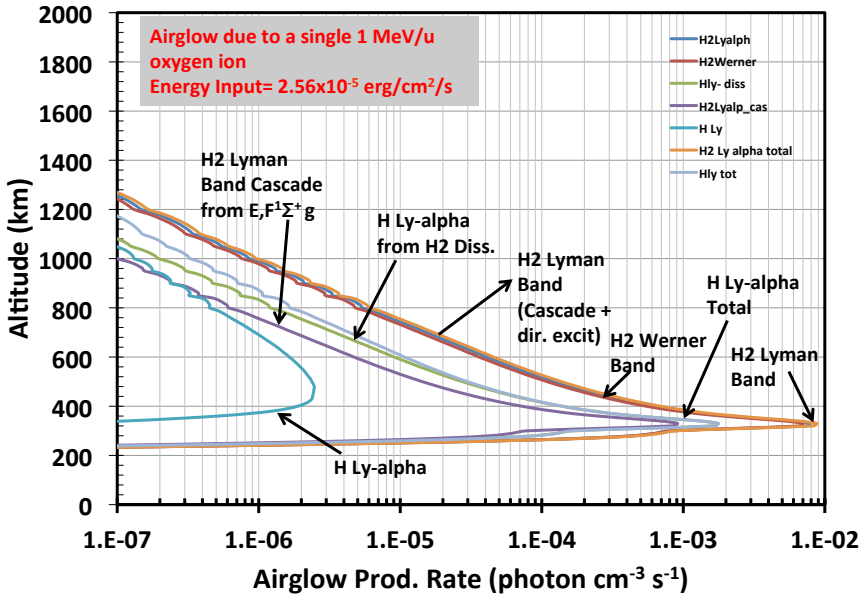

Figure 6.28: Production rate of airglow emissions due secondary electrons from a single 1 MeV/u ion precipitation in the jovian atmosphere (energy flux = 16 MeV/cm^2/s). No photoelectrons are considered in the calculations. The emissions are solely produced by the secondary electron collisions as they penetrate the atmosphere.

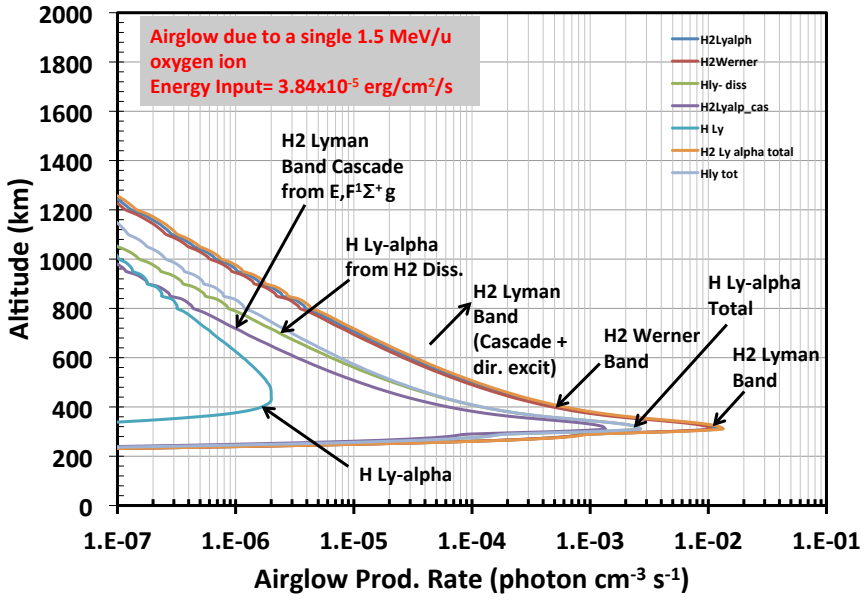

Figure 6.29: Production rate of airglow emissions due secondary electrons from a single 1.5 MeV/u ion precipitation in the jovian atmosphere (energy flux = 24 MeV/cm^2/s). No photoelectrons are considered in the calculations. The emissions are solely produced by the secondary electron collisions as they penetrate the atmosphere.

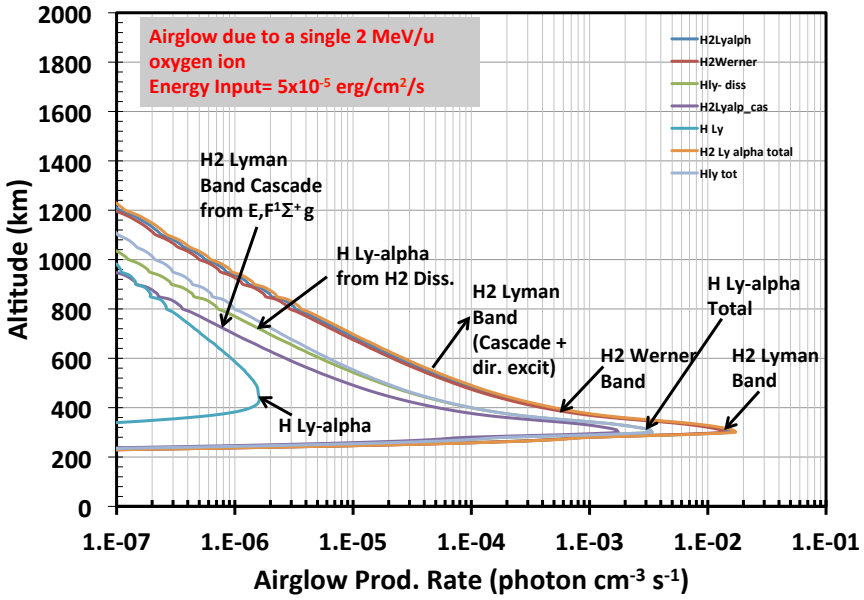

Figure 6.30: Production rate of airglow emissions due secondary electrons from a single 2 MeV/u ion precipitation in the jovian atmosphere (energy flux = 32 MeV/cm^2/s). No photoelectrons are considered in the calculations. The emissions are solely produced by the secondary electron collisions as they penetrate the atmosphere.

Table 6.3: H^+ and H_2^+ production rate in a column due to the precipitation of a **single** oxygen ion precipitating in the atmosphere with an initial energy or 1, 1.5 or 2 MeV/u.

Ion Energy	H_2^+	H^+
MeV/u	cm^2/s	cm^2/s
1.0	3.17×10^4	2.00×10^4
1.5	5.27×10^4	3.30×10^4
2.0	7.68×10^4	6.00×10^4

6.3.3 Ion Production Rates

The ion precipitation in the atmosphere creates new H^+ and H_2^+ ions due to ionization and charge transfer collisions as can be seen in Figure 6.1. In the Monte Carlo precipitation model we collect the number of H^+ and H_2^+ that are produced at each altitude bin as a product of the collision, which allows us to calculate an ion production rate due to the primary ion precipitation. This was done for each ion energy case (1, 1.5 and 2 MeV/u) and the results are shown in Figure 6.31. As we have seen in other results, the ion production rates due to higher energy ions occur deeper in the atmosphere. Also, the ion production rate increases as the initial oxygen ion energy increases. Table 6.3 summarizes the column production rates due to each ion energy for a flux of 1 ion/cm^2/s. For all three cases the H_2^+ production rate is higher than the H^+ production rate.

As we saw in the previous section, the energetic ion precipitation in the auroral region generates a large population of secondary electrons that also affects the ionospheric densities as the electrons are transported along the magnetic field lines. We use the secondary electron production and the fluxes calculated by the two-stream equations to calculate the ion production rate using equation 5.11. As a reminder, these production rates are calculated for a flux of 1 ion/cm^2/s. We expect the ion flux in the polar region to be significantly larger and therefore, the effects in the ionospheric

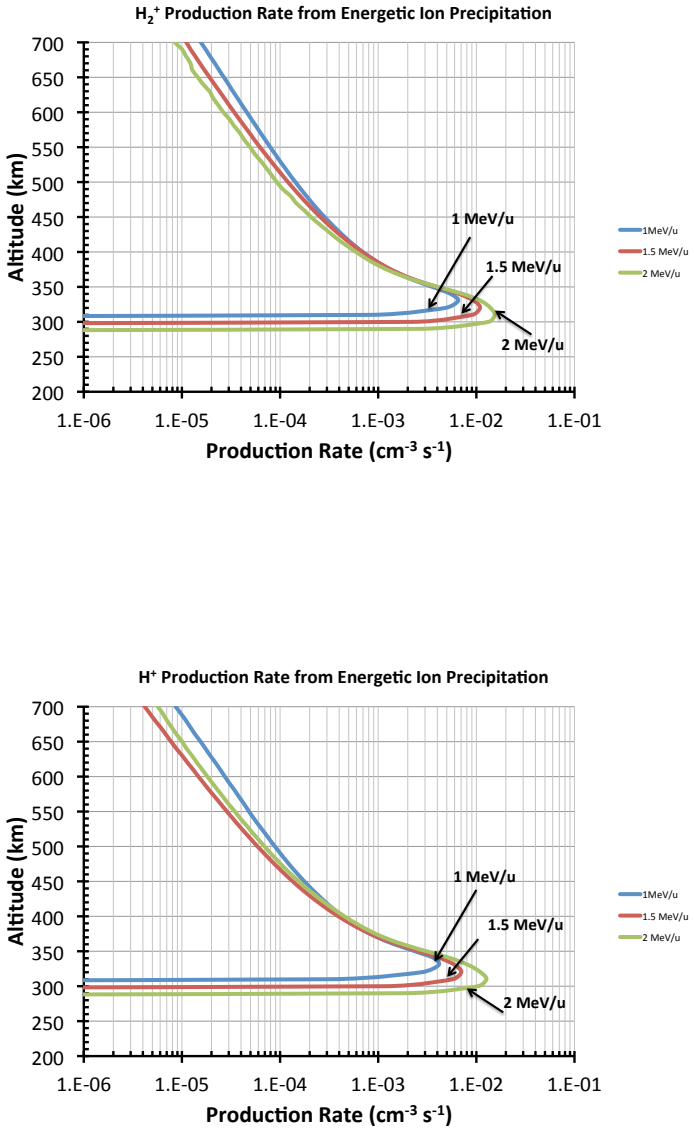

Figure 6.31: H_2^+ (top) and H^+ (bottom) ion production rates due to a single ion precipitating at the top of the atmosphere with an initial energy of 1, 1.5 or 2 MeV/u.

Table 6.4: Ion production rates due **secondary electrons** from oxygen ion precipitation. There are three initial ion energies considered at the top of the atmosphere: 1, 1.5 and 2 MeV/u. The table shows our results for the main ions produced in a column of the atmosphere for a flux of 1 ion/cm^2/s .

Ion Produced	1 MeV/u	1.5 MeV/u	2 MeV/u
Column production rate	($cm^{-2}s^{-1}$)	($cm^{-2}s^{-1}$)	($cm^{-2}s^{-1}$)
H_2^+	1.07×10^5	1.51×10^5	1.93×10^5
H^+	6.63×10^3	9.31×10^3	1.18×10^4
He^+	6.46×10^3	9.29×10^3	1.20×10^4
CH_4^+	4.53×10^2	6.91×10^2	9.13×10^2
CH_3^+	4.43×10^2	6.74×10^2	8.90×10^2

densities due to the secondary electrons should be important. Our results are shown in Figures 6.32 to 6.34 and the column production rates due to a single oxygen ion are summarized in Table 6.4. From the figures we can see that H_2^+ has the highest production rate, which increases with increasing ion energy. It is interesting to notice that the ion production rates for He^+ and H^+ become almost equal at low altitudes close to the peak production rate. The same behavior was observed for the photoelectrons in the secondary ion production peak as well as in the ion production rate for the same ions due to electron auroral beams. In all cases the peak production rate as well as the column production rate of CH_4^+ and CH_3^+ are almost identical.

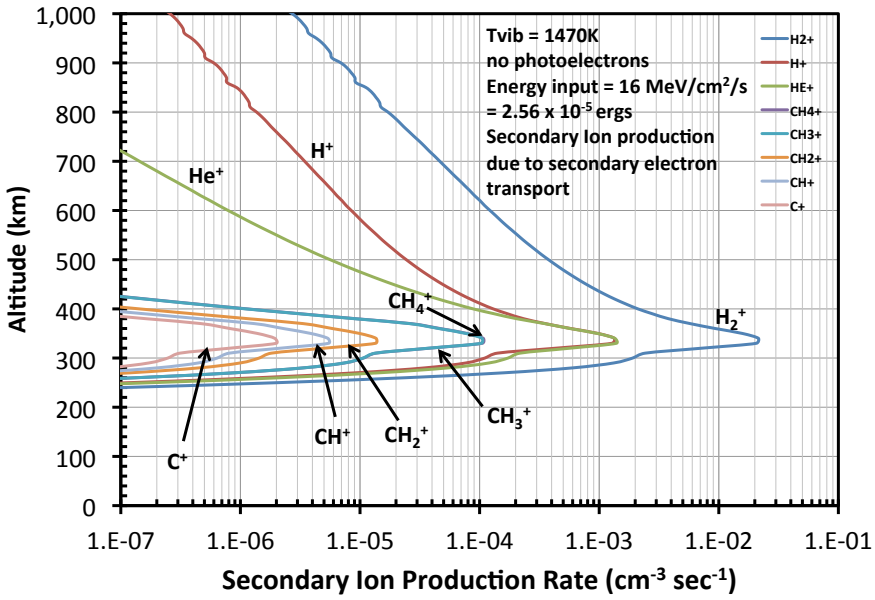

Figure 6.32: Ion production rates due to secondary electrons from a 1 MeV/u oxygen ion precipitating at the top of the atmosphere. No photoelectrons or magnetospheric electrons are included.

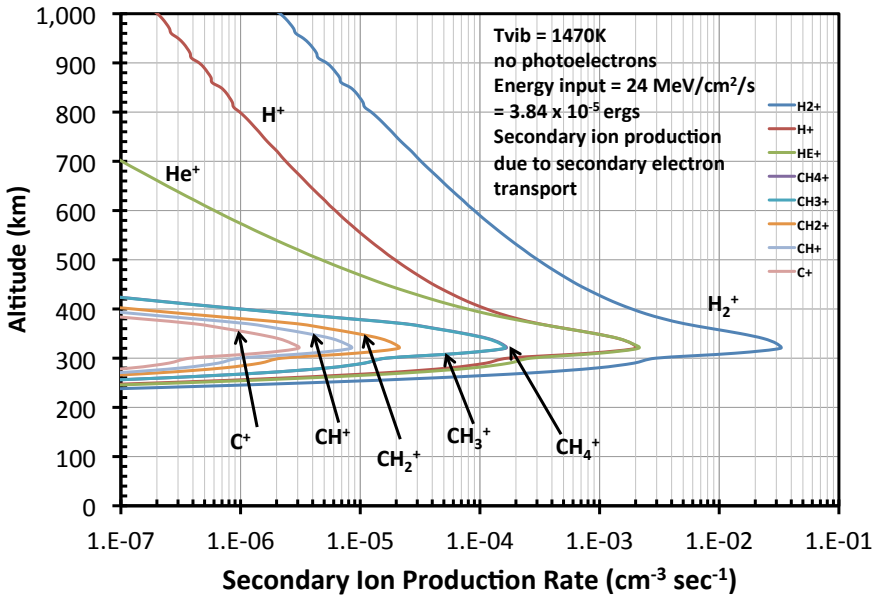

Figure 6.33: Ion production rates due to secondary electrons from a 1.5 MeV/u oxygen ion precipitating at the top of the atmosphere. No photoelectrons or magnetospheric electrons are included.

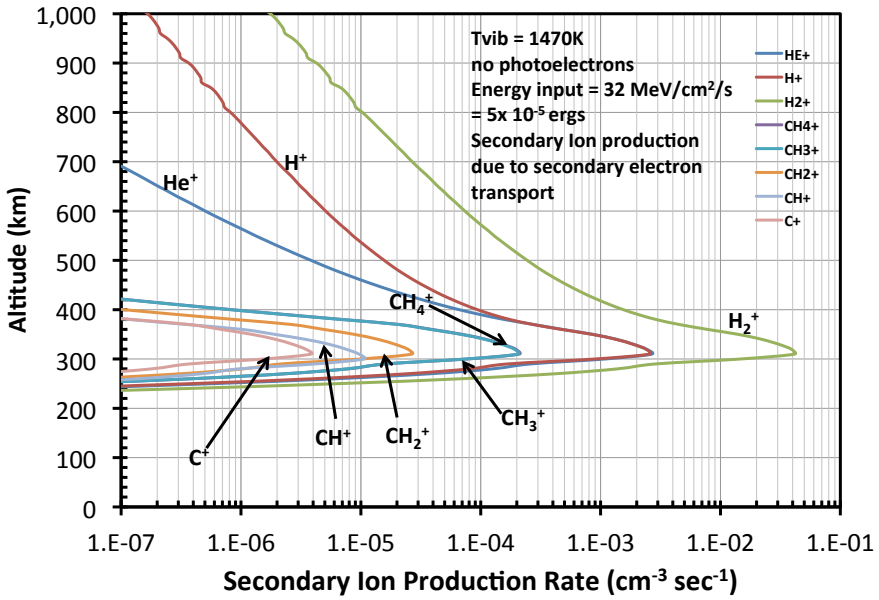

Figure 6.34: Ion production rates due to secondary electrons from a 2 MeV/u oxygen ion precipitating at the top of the atmosphere. No photoelectrons or magnetospheric electrons are included.

6.4 Implications of Auroral Ion Precipitation

In order to see the global effect that the auroral ion precipitation will have in the polar region we need to first estimate the total ion flux that is input in the ionosphere. Observations of the north and south x-ray aurora show a difference in the emission patterns. While the north x-ray aurora emissions appear to be concentrated in a so-called "hot spot", the south aurora is more diffused over a larger region. We estimate the emission are from observations done by CXO in 2003 reported by [54]. We use Figure 7 in their paper, which we show in Figure 6.35 for illustration purposes. In their figure the oval shows the north aurora emissions, which we have estimated to come from an area of $\sim 2 \times 10^{18}$ cm^2. Similarly in the south the rectangle encloses the south auroral emissions, which we have estimated to have an area of $\sim 1 \times 10^{19}$ cm^2. [54] derive an x-ray power emitted from the northern hot spot of 0.68 GW. We approximate the total emitted power at each polar region (north and south) to be $\sim$ 1 GW. For a 2 MeV/u oxygen ion [19] estimated an x-ray efficiency of 7×10^{-5} (see Chapter 4 for details). However, this efficiency might be a little low, so we prefer to use a value of 10^{-4} for the following estimates.

Given an efficiency of 10^{-4} we require an ion input power of 10^{13} W to get the required GW of x-ray power observed. For 2 MeV/u oxygen ions (the highest of our test initial ion energies and one of the most efficient x-ray producing energies) we would require an input flux of 2×10^{24} ion/s to match the observations. This means that for the north auroral region the ion flux is about 10^6 ions/cm^2/s and for the south it is about 2×10^5 ions/cm^2/s. As a reminder, all of our results given in the previous section were calculated for an ion flux of 1 ion/cm^2/s. We use this estimated total flux for the north and south aurora to calculate ion densities, airglow emissions, and energy outputs and compare them to the electron aurora cases as well as the photoelectron

results in order to put into perspective the effect of the ion aurora precipitation in the ionosphere. Our results are summarized in Tables 6.5 and 6.7. This results are very interesting, as they indicate that the integrated ion production for the main ion species in the atmosphere due to the ion aurora precipitation is very comparable to that of a 20 keV auroral electron beam with a 10 erg/cm^2/s input flux. This electron flux makes the bulk of the electrons that are responsible for the UV diffuse aurora in the polar cap [101]. The ion production due to the ion aurora is also much greater (by two orders of magnitude) than the ion production due to photoelectrons.

When we compare the airglow emissions, we see that the north aurora emissions are very comparable to those emissions due to the electron aurora! This means that just as the electron aurora is observable in the UV in the polar cap regions, there should be also observable UV emissions due to the ion aurora. It might be possible to compare x-ray and UV observations to look for such correlations, as the ion precipitation gives rise to the x-ray aurora as well. There is some concern regarding opacity effects of these airglow emissions due to the secondary electrons in the ion aurora as they originate very deep in the atmosphere below the homopause, which absorbs a lot of the emissions due to the hydrocarbons present. However, if we compare the peak emission for the 20 keV electron beam as calculated in the previous chapter we can see that this occurs at an altitude around 400 km. For a 2 MeV/u ion the peak airglow emission occurs at a lower altitude of about 340 km. Although we expect a higher absorption of the UV photons emitted, some of the emission should still be observed. Careful calculations must be done in the future to estimate this opacity effect.

Another important effect that is caused by the ion precipitation is the electrical current carried by the upward or escaping secondary electrons. For a flux of 1 MeV/u ion/cm^2/s precipitating in the atmosphere we calculate with the two-stream equations that only one electron/cm^2/s escapes the atmosphere. As we increase the initial ion

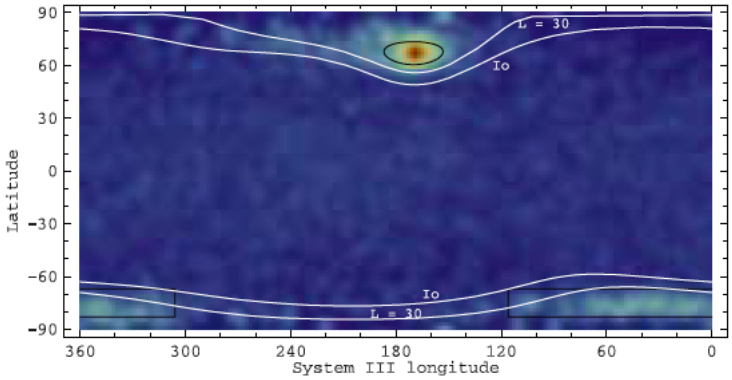

Figure 6.35: Soft x-ray emission (250 – 2000 eV) data map taken by CXO during 24 – 26 February 2003. The map shows System III coordinates. In the north, the oval represents a circle centered at 67°N latitude and 170°longitude with a radius of 6.5 °, which contains the x-ray aurora emissions. In the south, a rectangle between -67°S and -83°S latitude and 306°– 360° and 0°– 116° System III longitude.

Table 6.5: Comparison of integrated ion production rates due secondary electrons from auroral oxygen ion precipitation, a 20 keV electron auroral beam and photoionization and photoelectrons (solar case). We show the results for our north and south ion flux inputs separately for a 2 MeV/u oxygen ion. The solar case column shows our results for a solar zenith angle of 0°and the photoionization shows the primary ion production due to only solar photons. The integrated ion production rate due to the primary ions is shown in Table 6.6

Ion Produced	2 MeV/u (North)	2 MeV/u (South)	20 keV electron	solar case	Photoionization 0°
Production rate	($cm^{-2}s^{-1}$)	($cm^{-2}s^{-1}$)	($cm^{-2}s^{-1}$)	($cm^{-2}s^{-1}$)	($cm^{-2}s^{-1}$)
H_2^+	3×10^{11}	5×10^{10}	2×10^{11}	1×10^{9}	8×10^{8}
H^+	7×10^{10}	1×10^{10}	1×10^{10}	2×10^{8}	1×10^{8}
He^+	1×10^{10}	2×10^{9}	1×10^{10}	4×10^{7}	3×10^{7}
CH_4^+	9×10^{8}	2×10^{8}	7×10^{8}	1×10^{8}	1×10^{8}

Table 6.6: Comparison of integrated ion production rates auroral oxygen ion precipitation with an initial energy of 1, 1.5 and 2 MeV/u. We have used a flux of 10^6 ions/cm^2/s for the north aurora and 2×10^5 ions/cm^2/s for the south aurora. The integrated ion production rate due to the secondary electrons from the ion precipitation is shown in Table 6.5

Ion Produced	H_2^+ (North)	H_2^+ (South)	H^+ (North)	H^+ (South)
Production rate	($cm^{-2}s^{-1}$)	($cm^{-2}s^{-1}$)	($cm^{-2}s^{-1}$)	($cm^{-2}s^{-1}$)
1.0 MeV/u	3×10^{10}	6×10^9	2×10^{10}	4×10^9
1.5 MeV/u	5×10^{10}	1×10^{10}	3×10^{10}	7×10^9
2.0 MeV/u	8×10^{10}	2×10^{10}	6×10^{10}	1×10^9

energy at the top of the atmosphere to 2 MeV/u, we only increase the number of escaping electrons to 1.5 electrons/cm^2/s. For a 2 MeV/u oxygen ion the total number of secondary electrons produced is $\sim$5000 electrons/cm^2/s. However, only about 1.5 electrons/cm^2/s manage to escape. This means that most of the secondary electrons are lost in the atmosphere through collisions (probably thermalizing) and are unable to escape. Nevertheless, if we consider an input ion flux of 10^6 ions/cm^2/s, we would have $\sim 1.5 \times 10^6$ electrons/cm^2/s escaping the top of the atmosphere creating a current density of $\sim 3 \times 10^{-13}$A/cm^2. Using the estimated areas for the x-ray aurora emission, this would imply an electron carried downward current 0.6 MA for the north and 0.5 MA for the south. Considering our estimates for the ion flux (2×10^{24} ions/s) we estimate a downward current of about 0.7 MA. Together we have an downward field aligned current carried by downward moving ions and upward moving electrons of about 1 MA. This lies within the order of magnitude of the current estimated by [49], 8 MA.

Table 6.7: Comparison of airglow emission rates due secondary electrons from auroral oxygen ion precipitation, a 20 keV electron auroral beam and photoelectrons. We show the results for our north and south ion flux inputs separately for a 2 MeV/u oxygen ion. The solar case column shows our results for a solar zenith angle of 0°. The table shows our results for the different emissions in a column of the atmosphere.

Process	2 MeV/u (North)	2 MeV/u (South)	20 keV electron	solar case
Column rate	($cm^{-2}s^{-1}$)	($cm^{-2}s^{-1}$)	($cm^{-2}s^{-1}$)	($cm^{-2}s^{-1}$)
Lyman bands (direct excit.)	7×10^{10}	1×10^{10}	7×10^{10}	2×10^{8}
Lyman bands (cascade)	8×10^{9}	2×10^{9}	6×10^{9}	2×10^{7}
Werner bands	6×10^{10}	1×10^{10}	6×10^{10}	1×10^{8}
Lyman alpha (from H_2 diss.)	2×10^{10}	2×10^{9}	1×10^{10}	3×10^{7}
Lyman alpha (from H)	5×10^{7}	1×10^{7}	1×10^{8}	1×10^{7}

Chapter 7

Summary and Conclusions

7.1 Conclusions

We have learned the following main results from this work:

- X-ray aurora emissions at Jupiter's polar caps are produced by 1 – 2 MeV/u oxygen and sulfur ions. Higher energy ions can contribute to the x-ray emissions but with lower efficiency.

- Opacity effects to the emitted x-ray photons are important and need to be taken into account when modeling x-ray aurora observations. In particular, the opacity effect becomes more significant for initial ion energies above 1 MeV/u and for exit angles with respect to the zenith greater than about 80° , which is in general the viewing angle of the aurora from earth. It is important to note that the specifics of the absorption effects are highly dependent on the atmospheric model used.

- We found that quenching of the metastable n = 2 states of O^{6+} is significant for the inter combination and forbidden transitions. For initial ion energies greater than 1 MeV/u, i. e., those most efficient in x-ray production, the forbidden line is almost completely quenched in the observed spectrum.

- Energetic ion precipitation in the polar cap produces a large population of secondary electrons due to ionization and stripping collisions. We find that most secondary electrons are produced in ionization collisions between the neutral constituents (in our case H_2) and the ion. Therefore, the bulk of the electrons produced has energies bellow 100 eV.

- We model the secondary electron transport in the ionosphere and determine that their effect in the ionosphere is comparable to that of primary auroral electrons for a diffuse aurora case. Lyman and Werner band emissions in a column due to the secondary electrons have an intensity of 60 – 80 kR in the north and 10 – 20 kR in the south. These emissions are significant and in fact comparable to observed UV emissions from primary electron precipitation estimated to be 25 – 130 kR for faint regions and 250 kR for bright regions [115]. Auroral oval emissions are much brighter, ranging from 50 – 500 kR and reaching 1 MR at its brightest [116]. However, the airglow emissions due to the secondary electrons occur deep in the atmosphere and some percentage might be absorbed. Nonetheless, we expect that some of these emissions would escape and be observable by the UV observatories. In the future opacity effects should be calculated to estimate the brightness of the Lyman and Werner emissions due to the secondary electrons from the ion aurora.

- We have derived electron density profiles for the ion precipitation region due to the effect of the secondary electrons. We find the that the peak electron density is on the order of 10^5 cm^{-3} for the south aurora ion fluxes and about 5×10^5 cm^{-3} for the north. These electron profiles are very comparable to the effect caused by the energetic electron aurora and should be useful for comparison in radio occultation experiments.

- Another useful quantity derived in our model is the H_3^+ column density. Our calculated values are $\sim 5 \times 10^{11}$ cm^{-2} for the north aurora and $\sim 2 \times 10^{11}$ cm^{-2} for the south.

- The escaping electrons from each hemisphere contribute to downward currents that are part of the current system that gives rise to the ionosphere-magnetosphere coupling. We estimate that about a current of about 1 MA or slightly larger is carried by downward moving ions and upward moving electrons. As a comparison, the total upward Birkeland current that is related to the main auroral oval carried by electrons is estimated to be 100 MA [117].

7.2 Final Discussion

The plasma environment in a magnetosphere is a complex very complex. The aurora is an important tool for the understanding of the magnetosphere, the ionosphere and the electromagnetic coupling between the two. By understanding the underlaying mechanism that generates the auroral emissions we observe, we hope to understand the complex system that drives the magnetospheric dynamics, its structure, the ionospheric effects it may bring and to diagnose the complex electrical current system that exists within it.

In the past couple of decades we have learned a lot about the jovian magnetospheric system. For intense, we know that auroral emissions at Jupiter are caused by two different sources: the UV aurora is due to high energy electrons that precipitate in the atmosphere, while the x-ray aurora emission is due to energetic ion precipitation in the polar cap. The mechanism for the UV appears to be well understood and it is attributed to the break or lag in corotation by the plasma in the middle magnetosphere ($\sim$20 –

60 R_J) due to mass loading by iogenic plasma . The outward transfer of angular momentum translates to a radially outward magnetospheric current and an equatorward ionospheric current, which try to balance the centrifugal force of the rotating iogenic plasma with a $\vec{j} \times \vec{B}$ force. Birkeland currents are then required to close the current system. A downward current from the magnetosphere to the ionosphere and an upward current from the ionosphere to the magnetosphere complete the current loop (see Figure 1.5. In analogy to earth, the upward Birkeland current is carried by accelerated electrons that give rise to the UV aural oval in Jupiter. The downward current may be carried by upward low energy electrons and by downward moving ions, which we believe to produce the polar emissions.

The mechanism that produces the x-ray emissions is not yet completely understood. In this work, we have shown that oxygen and sulfur ions give rise to the line emissions observed at high latitudes by x-ray observatories. We have also found that if the ions are of magnetospheric origin, i.e., of low charge state, they need to be accelerated to high energies in order to produce the observed x-rays. However, no such mechanism is known to exist at this time. We have also modeled the secondary electrons produced by the ion precipitation at high latitudes and have found that indeed these secondary electrons are able to escape the ionosphere contributing to the downward Birkeland current mentioned above. We estimate that an electrical current of $\sim$ 1.5 MA may be carried by these ions and electrons in the polar cap. However, it is still not entirely clear where the ions come from and how the would be accelerated.

Recently, HST UV images showed a polar spot of aurora, which appears to be collocated with the jovian x-ray aurora and has a characteristic pulsation period of $\sim$ 45 min. Current models suggest that these emissions correspond to the cusp region and are associated with pulsed reconnection at the dayside magnetopause [59]. According to this latter model reconnection occurs between the planetary and magnetosheath field lines

at the magnetopause, resulting in the transfer of field lines across the open-closed field line boundary. When the magnetosheath plasma crosses to the magnetosphere on the open field lines, it is then expected to precipitate into the ionosphere forming a region of cusp plasma precipitation similar to that seen on earth. However, the models emphasize that this precipitation cannot be directly responsible for the observed polar emissions as the particle fluxes found in the magnetosheath cannot produce the observed emissions.

Heavy ions (oxygen and sulfur) are present in the outer magnetosphere, but only in low charge states (O^+ or O^{2+}). We have shown that highly charge states are required for x-ray production, implying highly energetic ions. Therefore, if the observed polar aurora is indeed related with the cusp, the magnetospheric and/or magnetosheath plasma must be somehow accelerated. In their model, [59] estimate accelerating voltages of 10 – 100 kV above regions of upward current and 0.5 – 5 MV above regions of downward current on the magnetospheric side of the open/close field line boundary. Their estimated voltage would be in agreement with the accelerating potential required to produce the x-ray emissions observed at the polar cap, as calculated by our model. See Figure 7.1 for a rough schematic of our understanding of the magnetospheric dynamics involved in the polar aurora.

There has been a vast improvement in the jovian auroral observations in the past few decades thanks to the state of the art observatories like HST, CXO and XMM-Newton. Although these observatories allowed the better understanding of the magnetospheric dynamics, there are still many unknowns. Last summer NASA launched the JUNO spacecraft hoping to answer some of these questions. Of special interest for this work are the planned polar orbits of the probe with the intension of mapping the magnetic field and exploring the three dimensional structure of the magnetosphere in the polar regions and the auroral emissions. The spacecraft is equipped with a so-called "Polar Magnetic Suite" instrument set that has the objective of measuring electric cur-

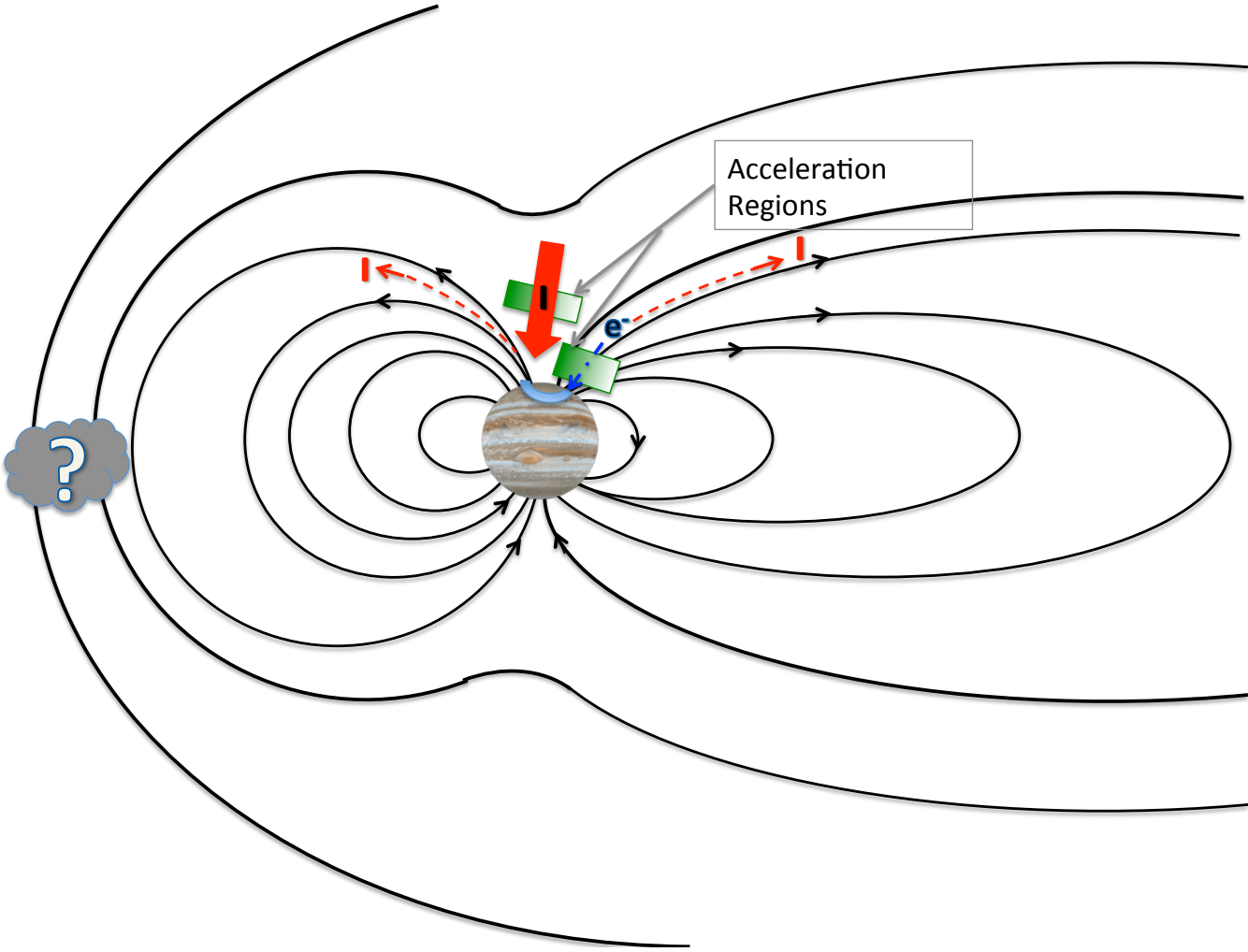

Figure 7.1: Rough schematic of magnetospheric dynamics that may lead to the polar auroral emissions. Periodic reconnection at the dayside magnetopause may be responsible for observed polar emissions. Above the pole, possible acceleration regions are expected at a distance of about 5 R_J. Downward moving electrons along the field line are accelerated to high energies and are responsible for the observed auroral oval emissions. Magnetosheath and/or magnetospheric ions follow downward Birkeland currents and are also accelerated to high energies, producing x-ray emissions in the polar cap.

rents along the polar magnetic field lines, emissions associated with aurora and electrostatic waves, the distribution of energetic particles and of auroral and magnetospheric plasma as well as measuring UV auroral emissions. The instruments for this purpose include plasma and energetic particle detectors (Jovian Auroral Distribution Experiment (JADE) and Jovian Energetic Particle Detector Instrument (JEDI)) which will measure the angular and energy distributions of polar particles and ions in the polar magnetosphere. A radio/plasma wave sensor (WAVES) will measure radio and plasma waves in the auroral region the regions of auroral emission and acceleration. And last, the Ultraviolet Imaging Spectrograph (UVS) will provide wavelength, position and time of UV auroral emissions at the poles.

We hope that the findings of Juno will help identify the origin of the acceleration regions that would bring the magnetospheric ions to high energies responsible for the x-ray aurora. If the orbit of the spacecraft is below this acceleration region, it should measure the accelerated ions that precipitate into the ionosphere and the upward moving electrons that escape with low energies. On the other hand, if the spacecraft is above the acceleration region, the ion energies observed would be lower than needed for the x-ray emission, but the upward moving electrons would have high energies after being accelerated by the MV potential. The energy distribution of the electrons and ions will be measured with the JADE and JEDI detectors. Considering the location of the spacecraft and the energy distributions of electrons and ions measured, we should be able to locate the acceleration region.

Our estimates on the upward electron fluxes escaping from the ionosphere as well as the downward ion flux estimates performed by our calculations should provide some clues on the observations. From our work, useful results like electron and ion densities, as well as electron fluxes and electrical currents will be of interest to other scientists and can used to find possible explanations to the observations. We hope that the UVS

on Juno will have optimal conditions to observe the UV emissions that will arise from the ion precipitation. We have calculated airglow emissions due to secondary electrons with an intensity of 10 – 20 kR. However, opacity effects will have to be taken into account as they were not included in our calculations. There may also be UV line emissions from the lower charge states of oxygen and sulfur as they become excited in the ionosphere. Observations from the UVS might give a better mapping on these emissions and provide a better understanding on where the ion precipitation occurs. The mapping will be complemented by the magnetometer on board Jupiter, which will concentrate on the polar regions, which have been difficult to map in the past. The Jovian Infrared Auroral Mapper (JIRAM) will study the auroral region as well. We have modeled the changes in the ionosphere due to ion precipitation and have calculated corresponding H_3^+ densities. We hope that the JIRAM instrument will be able to identify the regions in the ionosphere whose H_3^+ density matches our model. In that case, we should be able to compare to UVS measurements and see if the regions of emission identified as caused by ion precipitation by both instruments overlap.

Our results may also be used to calculate thermal profiles in the ionosphere of Jupiter and see the thermal effect or heating that the ion precipitation may cause. These heating profiles may be used in wind models, important for the ionosphere-thermosphere dynamics of the planet. The electron fluxes and electrical current estimates should be used to calculate the electrical conductivity changes that the ion aurora may present to the ionosphere. Our ion precipitation model may also be used to explore the possibility of x-ray emission due to solar wind ions, by starting the model with already high charge state ions and comparing the results to those obtained with magnetospheric ions.

Last, the set of codes developed in this work may be used to model ion precipitation in Saturn. Although no x-ray emission is observed in Saturn's auroral emissions,

there are observable UV emissions in the polar cap which may be produced by precipitating magnetospheric oxygen ions. The model that we developed for Jupiter can be implemented to model Saturn's ion precipitation. The precipitating ions would still be oxygen, as the largest magnetospheric ion population comes from the water group. Because the same atmospheric neutrals present at Jupiter are present at Saturn, the calculated and compiled set of cross sections may still be used. Our Monte Carlo code can model the ion precipitation in Saturn's ionosphere by adapting a Saturnian atmospheric model. However in Saturn the emissions produced due to ion precipitation are expected to originate from lower charge states, e.g., O^{5+}, O^{4+} and produce UV emissions. One may also calculate x-ray emissions from the oxygen ions, if any, and establish an upper limit in order to compare it with the observational limits that exist at the time.

Appendices

Table A.1: Excitation Cross Sections for H_2

STATE	THRESHOLD E (eV)	SOURCE	DETAILS
B ($^1\Sigma_u^+$)	13.01	[5]	Experimental data, recommended by [10]
C ($^1\Pi_u$)	12.46	[5]	Experimental data, recommended by [10]
E,F($^1\Sigma_g^+$)	12.40	[6]	Experimental data, recommended by [10]
B' ($^1\Sigma_u^+$)	14.4 (guess)	[7]	Adapted from Figure 4c in [7]
D ($^1\Pi_u$)	15.5 (guess)	[7]	Adapted from Figure 4c in [7]
D' ($^1\Pi_u$)B" ($^1\Sigma_u^+$)	20.0 (guess)	[7]	Adapted from Figure 4c in [7]
a($^3\Sigma_u^+$)	11.89	[8]	Experimental data, recommended by [10]
h($^3\Sigma_g^+$)	13.98	[73, 75]	Analytical expression
$(4s\sigma)(^3\Sigma_g^+)$	14.50	[73, 75]	Analytical expression
b($^3\Sigma_u^+$)	10.0	[118, 119]	Experimental data, recommended by [10]
e ($^3\Sigma_u^+$)	13.36	[8]	Experimental data, recommended by [10]
f ($^3\Sigma_u^+$)	14.47	[73, 75]	Analytical expression
c ($^3\Pi_u$)	11.87	[8]	Experimental data, recommended by [10]
d ($^3\Pi_u$)	13.97	[73, 75]	Analytical expression

Table A.1: Excitation Cross Sections for H_2 (continued)

STATE	THRESHOLD E (eV)	SOURCE	DETAILS
k ($^3\Pi_u$)	14.68	[73, 75]	Analytical expression
g ($^3\Sigma_u^+$)	13.98	[73, 75]	Analytical expression
p ($^3\Sigma_g^+$)	14.69	[73, 75]	Analytical expression
i ($^3\Pi_g$)	14.01	[73, 75]	Analytical expression
r ($^3\Pi_g$)	14.70	[73, 75]	Analytical expression
j ($^3\Delta_g$)	14.03	[73, 75]	Analytical expression
s ($^3\Delta_g$)	14.69	[73, 75]	Analytical expression
v ($^3\Pi_g$)	14.67	[73, 75]	Analytical expression

Table A.2: Parameters for Excitation Cross Sections of H_2

STATE	ν	Ω	W	f_0C_0	β	P_{auto}
B ($^1\Sigma_u^+$)	2.000	0.750	11.370	3.50×10^{-1}	1.000	0.000
C ($^1\Pi_u$)	2.000	0.750	12.460	3.50×10^{-1}	1.000	0.000
E,F($^1\Sigma_g^+$)	1.000	0.850	12.400	5.50×10^{-2}	0.600	0.000
B' ($^1\Sigma_u^+$)	11.900	0.600	14.400	5.55×10^{-2}	3.700	0.000
D ($^1\Pi_u$)	4.800	0.600	15.500	5.55×10^{-2}	2.400	0.000

Table A.2: Parameters for Excitation Cross Sections of H_2

(continued)

STATE	ν	Ω	W	f_0C_0	β	P_{auto}
D' ($^1\Pi_u$)B" ($^1\Sigma_u^+$)	2.200	0.800	20.000	5.55×10^{-2}	1.300	0.000
a($^3\Sigma_u^+$)	13.300	7.100	11.890	3.50	4.400	0.000
h($^3\Sigma_g^+$)	1.000	3.000	13.980	5.00×10^{-4}	3.000	0.000
$(4s\sigma)(^3\Sigma_g^+)$	1.000	3.000	14.500	3.00×10^{-4}	3.000	0.000
b($^3\Sigma_u^+$)	15.400	5.000	10.000	6.00	5.400	0.000
e ($^3\Sigma_u^+$	8.700	3.300	13.360	5.20×10^{-2}	6.100	0.000
f ($^3\Sigma_u^+$)	1.000	5.000	14.470	2.60×10^{-3}	3.000	0.000
c ($^3\Pi_u$)	18.700	5.500	11.870	3.50	5.100	0.000
d ($^3\Pi_u$)	1.000	3.000	13.970	6.50×10^{-3}	3.000	0.000
k ($^3\Pi_u$)	1.000	3.000	14.680	5.00×10^{-4}	3.000	0.000
g ($^3\Sigma_u^+$)	1.000	3.000	13.980	7.00×10^{-4}	3.000	0.000
p ($^3\Sigma_g^+$)	1.000	3.000	14.690	3.00×10^{-4}	3.000	0.000
i ($^3\Pi_g$)	1.000	3.000	14.010	5.00×10^{-4}	3.000	0.000

Table A.2: Parameters for Excitation Cross Sections of H_2

(continued)

STATE	v	Ω	W	f_0C_0	β	P_{auto}
r ($^3\Pi_g$)	1.000	3.000	14.700	1.30×10^{-3}	3.000	0.000
j ($^3\Delta_g$)	1.000	3.000	14.030	3.90×10^{-3}	3.000	0.000
s ($^3\Delta_g$)	1.000	3.000	14.690	2.00×10^{-4}	3.000	0.000
v ($^3\Pi_g$)	1.000	3.000	14.670	4.70×10^{-3}	3.000	0.000

Table A.3: Vibrational and Rotational Cross Sections of H_2

STATE	THRESHOLD E (eV)	SOURCE	DETAILS
v = 0 $\rightarrow$ v = 1	0.516	[10]	Experimental data combined from [120] and [121]
v = 0 $\rightarrow$ v = 2	1.800	[73]	Analytical expression
J = 0 $\rightarrow$ J = 2	0.044	[10]	Experimental data combined from [122], [123] and [120]
J = 1 $\rightarrow$ J = 3	0.073	[120]	Experimental data recommended by [10]
J = 2 $\rightarrow$ J = 4	0.101	[120]	Experimental data
J = 3 $\rightarrow$ J = 5	0.128	[120]	Experimental data

Table A.4: Parameters for Vibrational and Rotational Cross Sections for H_2

STATE	v	Ω	W	f_0C_0	β	P_{auto}
v = 0 → v = 1	-1.000	1.000	0.516	0.00	0.000	100.000
v = 0 → v = 2	3.000	2.000	1.800	0.013	1.000	0.000
J = 0 → J = 2	-1.000	2.000	0.044	0.00	0.000	16.000
J = 1 → J = 3	-1.000	13.000	0.073	0.00	0.000	16.000
J = 2 → J = 4	-1.000	14.000	0.101	0.00	0.000	11.000
J = 3 → J = 5	-1.000	15.000	0.128	0.00	0.000	11.000

Table A.5: Collision strength coefficients for electron impact dissociation cross sections of H_2 leading to the fast component of H Ly-α emission. Parameters obtained from Table 1 in [9].

STATE	PERCENT	E_{ij}	C_0	C_1	C_2	C_3	C_4	C_5	C_6	C_7	C_8
Q_1	40	23.0	-0.67184	0.034857	-0.099768	0.50682	-0.92647	0.20852	-0.20852	0.0	0.25704
Q_2	60	30.2	-0.67184	0.034857	-0.099768	0.50682	-0.92647	0.20852	-0.20852	0.0	0.25704

Table A.6: Cross section for the slow component of H Ly-α emission. Data obtained from [9].

ENERGY	CROSS SECTION (cm^2)
14.00	0.100E-18
15.00	0.500E-18
17.50	4.000E-18
20.00	5.000E-18
22.50	6.000E-18
25.00	6.100E-18
37.50	6.350E-18
50.00	6.500E-18
62.50	6.350E-18
75.00	6.000E-18
87.50	5.670E-18
100.00	5.300E-18
112.50	5.100E-18
125.00	4.900E-18
137.50	4.650E-18
150.00	4.400E-18
162.50	4.200E-18
175.00	4.050E-18
187.50	3.900E-18
200.00	3.800E-18

Table A.7: Parameters for Excitation Cross Sections of He. These parameters are taken from [11].

STATE	v	Ω	W	f_0C_0	β	P_{auto}
$2 \rightarrow^1 P$	2.100	0.750	21.220	4.05×10^{-1}	1.000	0.000
$3 \rightarrow^1 P$	2.000	0.750	23.090	1.15×10^{-1}	1.000	0.000
$4 \rightarrow^1 P$	1.850	0.750	23.740	4.58×10^{-2}	1.000	0.000
$n > 4 \rightarrow^1 P$	1.850	0.750	23.900	7.20×10^{-2}	1.000	0.000
$2 \rightarrow^1 S$	3.000	1.000	9.500	3.24×10^{-2}	1.000	0.000
$3 \rightarrow^1 S$	3.000	1.000	9.500	7.32×10^{-3}	1.000	0.000
$4 \rightarrow^1 S$	3.000	1.000	9.510	2.83×10^{-3}	1.000	0.000
$5 \rightarrow^1 S$	3.000	1.000	9.630	1.45×10^{-3}	1.000	0.000
$n > 5 \rightarrow^1 S$	3.000	1.000	9.630	3.10×10^{-3}	1.000	0.000
$3 \rightarrow^1 D$	1.000	1.000	21.000	3.77×10^{-3}	2.000	0.000
$4 \rightarrow^1 D$	1.000	1.000	21.590	1.63×10^{-3}	2.000	0.000
$5 \rightarrow^1 D$	1.000	1.000	22.200	8.62×10^{-4}	2.000	0.000
$n > 5 \rightarrow^1 D$	1.000	1.000	24.130	1.78×10^{-3}	2.000	0.000
$2 \rightarrow^3 S$	1.000	3.000	19.820	1.37×10^{-1}	0.785	0.000
$3 \rightarrow^3 S$	1.000	3.000	20.100	3.87×10^{-2}	1.060	0.000
$4 \rightarrow^3 S$	1.000	3.000	20.460	1.63×10^{-2}	1.280	0.000
$n > 4 \rightarrow^3 S$	1.000	3.000	23.910	2.58×10^{-2}	1.280	0.000
$2 \rightarrow^3 P$	1.000	3.000	20.960	1.20	0.124	0.000
$3 \rightarrow^3 P$	1.000	3.000	23.010	3.17×10^{-1}	0.133	0.000
$4 \rightarrow^3 P$	1.000	3.000	23.710	1.34×10^{-1}	0.133	0.000
$n > 4 \rightarrow 3P$	1.000	3.000	23.910	2.12×10^{-1}	0.133	0.000

Table A.8: Parameters for Excitation Cross Sections of H. The first set is for electron impact energies less than 3 keV. The parameters for the analytical function are taken from [12]. The second set of parameters is for energies greater than 3 keV. These parameters were obtained by fitting the data reported by [13].

For $E < 3$ keV	ν	Ω	W	$f_0 C_0$	β	P_{auto}
1s $\rightarrow$ 2p	1.300	0.750	10.204	6.60×10^{-1}	0.600	0.000
1s $\rightarrow$ 3p	1.200	0.750	12.094	1.29×10^{-1}	0.700	0.000
1s $\rightarrow$ 4p	1.100	0.750	12.755	5.30×10^{-2}	0.600	0.000
1s $\rightarrow$ 5p	1.000	0.750	13.061	2.43×10^{-2}	0.600	0.000
1s $\rightarrow$ 6p	1.100	0.750	13.228	1.43×10^{-2}	0.600	0.000
For $E > 3$ keV	B	a	E	f	b	c
1s $\rightarrow$ 2P	13.598	0.556	10.204	4.16×10^{-1}	0.272	0.000
1s $\rightarrow$ 3p	13.598	0.089	12.094	7.91×10^{-2}	0.060	-0.019
1s $\rightarrow$ 4p	13.598	0.031	12.755	2.90×10^{-2}	0.023	-0.009
1s $\rightarrow$ 5p	13.598	0.014	13.061	1.39×10^{-2}	0.011	-0.005
1s $\rightarrow$ 6p	13.598	0.008	13.228	0.78×10^{-2}	0.006	-0.003

Table A.9: Parameters for Excitation Cross Sections of CH_4, modeled after [15]

STATE	ν	Ω	W	f_0C_0	β	P_{auto}
Channel 1	0.641	1.129	8.200	5.87×10^{-3}	1.000	0.000
Ch2	1.549	0.838	9.700	1.79×10^{-1}	1.000	0.000
Ch3	0.880	0.807	11.200	2.80×10^{-1}	1.000	0.000
Ch4	0.835	0.620	12.700	4.32×10^{-1}	1.000	0.000
Ch5	0.835	0.620	12.700	4.32×10^{-1}	1.000	0.000
Diss. Excit. Ly-α	2.426	1.123	21.900	7.61×10^{-1}	1.000	0.000
Diss. Excit. Balmer α	2.721	1.176	21.900	2.34×10^{-1}	1.000	0.000
H(2s)-H(1s)	4.083	1.169	15.560	4.99×10^{-2}	1.000	0.000
CI(1657A)	1.568	1.364	41.200	1.35×10^{-2}	1.000	0.000
v=1 $\rightarrow$ v=3	-1.000	1.000	0.367	0.000	0.367	99.000
v=2 $\rightarrow$ v=4	-1.000	2.000	0.175	0.000	0.175	99.000

Table A.10: Ionization Cross Sections

STATE	THRESHOLD E (eV)	SOURCE	DETAILS
H_2^+	15.426	[77]	Experimental data recommended by [10] and analytical function by [74]
$H_2 \rightarrow H^+$	18.1	[77]	Experimental data recommended by [10]
He^+	24.58	[11]	Analytical function
H^+	13.303	[13, 14]	Analytical function
CH_4^+	12.60	[15]	Analytical function
CH_3^+	14.000	[15]	Analytical function
CH_2^+	15.100	[15]	Analytical function
$CH_4 \rightarrow H^+$	20.000	[15]	Analytical function
CH^+	20.000	[15]	Analytical function
C^+	19.600	[15]	Analytical function

Table A.11: Parameters for Ionization Cross Sections

STATE	I	K	K_b	J	J_b	T_s	T_a	T_b	Γ_s	Γ_b
H_2^+	15.400	1.760	0.000	0.059	0.000	1.8700	1000.0	30.80	7.70	-7.70
H^+	28.000	0.050	0.000	0.300	0.000	17.500	1500.0	56.00	12.80	-48.00
He^+	24.580	1.190	0.000	10.200	0.000	2.0500	1310.00	101.000	15.00	0.000
H^+	13.606	5.000	0.000	7.600	0.000	-6.0000	0.0	0.00	6.00	0.000
CH_4^+	12.600	8.260	0.000	25.000	0.626	3.450	0.000	0.000	7.06	-12.500
CH_3^+	14.000	8.260	0.000	25.000	0.644	3.450	0.000	0.000	7.06	-12.500
CH_2^+	15.100	1.150	0.000	24.000	0.395	3.450	0.000	0.000	7.06	-12.500
$CH_4 \rightarrow H^+$	20.000	0.105	0.000	1.000	0.000	19.000	0.000	0.000	11.300	0.000
CH^+	20.000	0.565	0.000	28.000	0.209	3.450	0.000	0.000	7.06	-12.500
C^+	19.600	0.231	0.000	32.200	0.150	3.450	0.000	0.000	7.06	-12.500

Table A.12: Total Eleastic Cross Sections and Backscatter Probability for H_2

ENERGY	CROSS SECTION [cm^2]	BACK SCATT. PROB
2.000	1.43E-15	0.65
3.000	1.53E-15	0.58
5.000	1.61E-15	0.42
7.000	1.37E-15	0.33
10.000	1.14E-15	0.24
15.000	7.57E-16	0.14
20.000	5.65E-16	0.11
30.000	3.28E-16	8.36E-02
40.000	2.40E-16	6.47E-02
60.000	1.34E-16	5.23E-02
100.000	8.08E-17	4.44E-02
150.000	5.67E-17	3.19E-02
200.000	4.10E-17	2.81E-02

Table A.13: Total Elastic Cross Sections for He and H

ENERGY	CROSS SECTION [cm^2]	BACK SCATT. PROB
2.000	5.800E-16	0.570
4.000	5.300E-16	0.570
5.000	5.100E-16	0.570
6.000	5.000E-16	0.565
7.000	4.800E-16	0.555
9.000	4.400E-16	0.540
10.000	4.200E-16	0.530
12.000	3.800E-16	0.500
20.000	3.000E-16	0.420
30.000	2.300E-16	0.340
40.000	1.700E-16	0.300
50.000	1.400E-16	0.270
60.000	1.200E-16	0.250
70.000	1.050E-16	0.230
80.000	9.000E-17	0.215
90.000	7.600E-17	0.205
100.000	6.600E-17	0.195
120.000	5.000E-17	0.180
150.000	4.000E-17	0.155
200.000	2.900E-17	0.130
270.000	2.000E-17	0.125
300.000	1.700E-17	0.120
350.000	1.400E-17	0.100
400.000	1.200E-17	0.086

Table A.14: Total Eleastic Cross Sections for CH_4

ENERGY	CROSS SECTION [cm^2]	BACK SCATT. PROB
0.100	4.48E-16	0.282
0.300	1.25E-16	0.095
0.400	1.03E-16	0.184
0.500	1.04E-16	0.314
0.700	1.32E-16	0.470
1.000	1.72E-16	0.511
2.500	5.55E-16	0.354
5.000	1.87E-15	0.464
7.500	2.52E-15	0.432
10.000	2.55E-15	0.383
12.500	2.39E-15	0.337
15.000	2.21E-15	0.300
20.000	1.89E-15	0.244
30.000	1.47E-15	0.185
50.000	1.02E-15	0.139
60.000	8.85E-16	0.126
80.000	7.12E-16	0.105
100.000	6.03E-16	0.090
200.000	3.55E-16	0.056
300.000	2.62E-16	0.041
400.000	2.11E-16	0.031

Table A.15: Emission line from synthetic spectra calculated by [21] for O^{6+} emissions due to initial ion energies of 1.2 MeV/u and 2.0 MeV/u

Photon Energy (eV)	# of photons per incident ion 1.2 MeV/u	# of photons per incident ion 2.0 MeV/u
560.984	10.3676	12.7024
568.474	3.11866	3.75367
574.001	4.37678	5.26414
663.94	0.0032977	0.0040136
665.616	1.36027	1.65589
697.01	0.0010145	0.0012361
697.834	0.588438	0.716518
712.266	4.86×10^{-4}	5.90×10^{-4}
712.758	0.320427	0.388738
720.503	3.01×10^{-4}	3.64×10^{-4}
720.88	0.18583	0.224806
725.743	0.110591	0.132973
728.925	0.0825089	0.100825
731.107	0.0562837	0.0677169
732.668	0.0434614	0.0522632

Table A.16: Emission line from synthetic spectra calculated by [21] for O^{7+} emissions due to an initial energy of 1.2 MeV/u and 2.0 MeV/u

Photon Energy (eV)	# of photons per incident ion 1.2 MeV/u	# of photons per incident ion 2.0 MeV/u
203.976	0.0358204	0.100531
203.976	0.0035684	0.011333
203.976	0.0051192	0.0162146
206.83	0.0036384	0.0115613
206.83	0.002217	0.0069782
206.83	0.0266678	0.0759532
208.871	0.0018637	0.0062368
208.871	0.0027763	0.0088512
208.871	0.0204592	0.059518
652.723	2.47014	7.92792
773.598	0.656434	2.20839
815.904	0.274857	0.917642
835.486	0.138007	0.443276
846.123	0.0829386	0.265669
852.536	0.0530491	0.171742
856.699	0.0351408	0.111305
859.553	0.024943	0.0792583
861.595	0.0190154	0.0606236

Table A.17: Emission line from synthetic spectra calculated by [21] for sulfur emissions due to an initial energy of 1.86 MeV/u.

Photon Energy (eV)	# of photons per incident ion S^{8+}	Photon Energy (eV)	# of photons per incident ion S^{9+}	Photon Energy (eV)	# of photons per incident ion S^{10+}
220.311	8.22076	246.595	0.295774	206.284	2.50×10^{-5}
220.903	2.36815	251.858	0.273361	213.362	1.44×10^{-6}
223.218	38.7029	252.334	0.518138	213.383	7.37×10^{-7}
228.225	22.5902	257.477	0.540562	214.913	1.92×10^{-9}
228.888	2.54195	259.47	0.815039	216.224	2.88×10^{-5}
233.701	4.47381	268.138	7.30791	229.134	4.63×10^{-4}
246.254	0.301857	273.793	7.89574	238.179	0.003198
251.808	0.625468	279.077	0.206255	238.858	0.0034643
254.243	1.57694	279.173	3.08585	254.858	0.0444703
255.301	1.87596	280.528	0.788587	269.49	1.18083
256.34	1.13859	284.703	0.188159	274.269	0.389764
257.442	1.88076	286.583	1.18174	277.17	0.991403
260.652	0.626934	288.657	4.67121	281.795	0.158532
260.92	0.626925	291.675	3.1161	282.425	1.27989
261.41	0.627567	295.166	0.518532	287.352	1.68568
261.926	0.997895	299.79	0.536216	288.678	0.675499
262.75	0.598629	361.365	0.519416	289.51	0.205472
264.325	0.0594112			289.629	0.370922
265.237	0.389894			292.816	0.368404
266.725	1.19647			294.464	1.19×10^{-4}
308.641	0.356673			295.376	1.24161
318.186	5.45433			296.407	2.08994
318.377	4.28204			298.802	1.38714
				300.153	2.20×10^{-6}
				303.092	0.144182
				304.577	0.384646
				305.635	0.258796
				312.169	1.5879
				312.712	0.150051
				312.733	0.0152226
				313.313	0.299204
				315.18	0.106191
				316.723	0.376007
				317.511	2.23049
				326.803	0.055428
				328.235	0.372398
				334.481	8.81×10^{-4}
				337.528	0.328526
				338.209	0.327127
				393.813	0.330117
				399.254	0.165686

Table A.18: Emission line from synthetic spectra calculated by [21] for sulfur emissions due to an initial energy of 1.86 MeV/u.

Photon Energy (eV)	# of photons per incident ion S^{11+}	Photon Energy (eV)	# of photons per incident ion S^{12+}	Photon Energy (eV)	# of photons per incident ion S^{13+}
244.551	7.69×10^{-7}	295.046	6.28×10^{-4}	200.184	0.0321752
255.105	1.36×10^{-5}	311.463	0.015345	222.061	0.0012027
256.577	2.97×10^{-4}	319.372	0.373094	222.5	0.255998
263.28	0.0018992	322.724	0.0460874	223.92	0.0055067
267.173	0.0110515	329.763	0.224885	225.59	0.0565334
267.243	0.0382319	339.144	0.110535	233.141	0.0193254
273.999	0.0026607	340.158	0.188107	241.905	6.84×10^{-4}
283.438	0.0011392	340.201	0.295919	242.157	0.141975
293.941	9.50×10^{-4}	346.799	0.476242	244.232	0.0036782
308.119	0.361693	347.616	0.744483	245.255	0.0356368
315.579	0.0444124	347.926	1.45465	253.003	0.0118441
319.115	0.529739	355.622	0.929482	254.762	4.20×10^{-4}
323.566	0.635739	356.574	0.009996	254.902	0.0836737
329.055	0.585714	357.025	0.601897	257.362	0.0019764
330.537	0.010287	358.622	0.197139	258.014	0.0208211
330.951	0.831513	363.398	0.144894	263.572	2.87×10^{-4}
339.576	0.208669	365.744	1.11453	263.684	0.0485284
341.132	0.194686	372.773	0.260019	265.861	0.0076159
342.846	0.194686	377.989	0.0750178	266.347	0.0015447
343.237	0.0022216	384.543	0.350208	266.767	0.0155269
344.841	0.874591	388.13	1.34662	269.883	1.91×10^{-4}
346.392	0.0430786	390.638	0.45668	269.942	0.0337844
351.84	1.71402	392.024	0.467971	272.763	8.72×10^{-4}
353.74	2.04×10^{-4}	412.223	0.0240554	273.033	0.0117322
358.306	0.347832	414.594	0.0023791	274.666	0.005363
362.433	0.239582	429.65	0.0080786	280.984	0.0036564
366.492	0.0057401	430.995	2.30×10^{-4}	370.492	0.203748
377.138	7.56×10^{-6}	435.475	0.0039397	381.257	3.83862
378.701	0.292695	437.867	6.03×10^{-4}	407.173	0.849298
388.787	1.86×10^{-4}	459.558	0.431326	506.784	0.0462375
399.305	8.26×10^{-5}	461.749	0.0728278	511.136	0.878195
413.143	4.36×10^{-4}	465.441	0.131617	538.71	0.240211
423.733	2.17×10^{-4}	470.231	0.0987866	569.128	0.0198671
424.207	0.648198	470.976	0.0248151	571.182	0.336535
427.974	2.16×10^{-4}	473.573	0.0230333	599.392	0.101959
438.503	0.585375	480.699	0.0565729	602.305	0.0087638
438.649	4.32×10^{-6}	486.957	0.0094427	603.821	0.160055
444.627	0.0697376	487.053	0.0922002	622.725	0.0059491
461.079	0.133449	489.921	0.0013576	623.351	0.100123
484.031	0.567642	504.083	0.0605028	632.411	0.0602013
507.716	0.0939527	506.886	0.215006	635.818	0.0032298
522.479	0.0945666	508.383	0.0197733	636.144	0.0582453
		511.359	0.394492	644.745	0.0025405
		511.718	1.58×10^{-5}	644.968	0.0433285
		523.14	0.0746538	651.179	0.03268
		532.99	0.408162	651.179	0.0014419
		2591.2	2.13×10^{-5}	652.205	0.0366686
				665.151	0.0234927
				673.827	0.0165263
				680.111	0.0112497

Table A.19: Emission line from synthetic spectra calculated by [21] for sulfur emissions due to an initial energy of 1.86 MeV/u.

Photon Energy (eV)	# of photons per incident ion S^{14+}	Photon Energy (eV)	# of photons per incident ion S^{14+}
216.624	2.90×10^{-5}	700.388	1.60×10^{-5}
217.343	2.15×10^{-4}	707.971	1.10×10^{-4}
217.381	2.86×10^{-6}	713.127	1.32×10^{-5}
217.817	7.33×10^{-7}	713.176	9.88×10^{-6}
218.016	9.19×10^{-4}	715.125	1.64×10^{-5}
219.26	2.87×10^{-5}	725.221	8.04×10^{-6}
220.78	1.98×10^{-4}	727.818	7.29×10^{-6}
221.054	8.22×10^{-6}	727.977	1.27×10^{-5}
225.012	6.79×10^{-5}	730.687	7.39×10^{-5}
254.364	1.44×10^{-5}	732.439	7.24×10^{-6}
254.78	1.21×10^{-4}	737.856	4.49×10^{-6}
255.093	1.33×10^{-6}	738.141	6.15×10^{-6}
255.221	3.69×10^{-7}	745.037	4.15×10^{-6}
255.445	3.70×10^{-4}	745.402	5.30×10^{-6}
257.403	1.32×10^{-5}	745.418	5.37×10^{-5}
258.24	8.77×10^{-5}	755.51	3.28×10^{-5}
258.458	4.59×10^{-6}	762.725	2.99×10^{-5}
262.733	3.53×10^{-5}	2445.94	0.0107874
277.09	1.05×10^{-5}	2459.72	0.0079796
277.778	2.45×10^{-7}	2878.97	2.16×10^{-4}
277.805	8.43×10^{-7}	2882.78	0.0014778
280.333	8.82×10^{-6}	3032.51	7.11×10^{-4}
281.015	3.25×10^{-6}	3101.34	3.87×10^{-4}
285.449	2.39×10^{-5}	3138.75	2.12×10^{-4}
291.827	1.07×10^{-5}	3161.3	1.49×10^{-4}
292.42	1.73×10^{-7}	3175.94	1.10×10^{-4}
292.533	5.89×10^{-7}	3185.98	6.77×10^{-5}
295.183	8.42×10^{-6}	3193.16	6.26×10^{-5}
295.657	2.41×10^{-6}		
300.18	1.73×10^{-5}		
301.923	5.23×10^{-6}		
302.458	1.04×10^{-7}		
302.623	3.50×10^{-7}		
305.347	4.05×10^{-6}		
305.695	1.48×10^{-6}		
309.141	4.71×10^{-6}		
309.639	9.49×10^{-8}		
309.837	3.13×10^{-7}		
310.272	1.06×10^{-5}		
312.608	3.50×10^{-6}		
312.876	1.38×10^{-6}		
317.487	9.69×10^{-6}		
414.675	4.07×10^{-6}		
419.328	2.19×10^{-4}		
422.185	3.53×10^{-5}		
422.511	0.0029547		
428.053	4.37×10^{-4}		
431.967	1.29×10^{-5}		
433.11	1.55×10^{-6}		
434.689	1.72×10^{-4}		
435.283	0.0059438		
435.763	8.22×10^{-5}		
436.294	3.20×10^{-4}		
449.827	0.0012801		
453.519	6.86×10^{-7}		
570.346	8.30×10^{-5}		
571.727	0.0010674		
581.523	1.01×10^{-4}		
584.383	4.58×10^{-5}		
584.393	0.0016603		
600.691	4.54×10^{-4}		
639.922	4.26×10^{-5}		
640.642	5.83×10^{-4}		
652.054	4.18×10^{-5}		
653.215	2.53×10^{-5}		
653.361	5.72×10^{-4}		
670.25	2.13×10^{-4}		
677.662	2.16×10^{-5}		
678.079	3.24×10^{-4}		
690.197	1.96×10^{-5}		
690.619	1.40×10^{-5}		
690.821	2.48×10^{-4}		

Table A.20: Electron Recombination for the Selected Reactions

Reaction	Rate Coefficient cm^3s^{-1}	Reference
$H^+ + e^- \rightarrow H + h\nu$	$4.00 \times 10^{-12}(300/T_e)^{0.64}$	[98]
$He^+ + e^- \rightarrow He + h\nu$	$4.60 \times 10^{-12}(300/T_e)^{0.64}$	[98]
$H_2^+ + e^- \rightarrow H + H$	$2.30 \times 10^{-7}(300/T_e)^{0.4}$	[98]
$H_3^+ + e^- \rightarrow H_2 + H$	$4.4 \times 10^{-8}(300/T_e)^{0.5}$	[124]
$H_3^+ + e^- \rightarrow H + H + H$	$5.6 \times 10^{-8}(300/T_e)^{0.5}$	[114]
$HeH^+ + e^- \rightarrow He + H$	$1.00 \times 10^{-8}(300/T_e)^{0.6}$	[98]
$CH^+ + e^- \rightarrow C + H$	$1.50 \times 10^{-7}(300/T_e)^{0.42}$	[124]
$CH_2^+ + e^- \rightarrow C + H_2$	$7.68 \times 10^{-8}(300/T_e)^{0.6}$	[124]
$CH_2^+ + e^- \rightarrow C + H + H$	$4.03 \times 10^{-7}(300/T_e)^{0.6}$	[124]
$CH_2^+ + e^- \rightarrow CH + H$	$1.60 \times 10^{-7}(300/T_e)^{0.6}$	[124]
$CH_3^+ + e^- \rightarrow CH + H_2$	$8.00 \times 10^{-7}(300/T_e)^{0.5}$	[111]
$CH_4^+ + e^- \rightarrow CH_3 + H$	$1.75 \times 10^{-7}(300/T_e)^{0.5}$	[124]
$CH_4^+ + e^- \rightarrow CH_2 + H + H$	$1.75 \times 10^{-7}(300/T_e)^{0.5}$	[124]
$CH_5^+ + e^- \rightarrow CH_3 + H + H$	$1.96 \times 10^{-7}(300/T_e)^{0.52}$	[124]
$CH_5^+ + e^- \rightarrow CH + H_2 + H_2$	$8.40 \times 10^{-9}(300/T_e)^{0.52}$	[124]
$CH_5^+ + e^- \rightarrow CH_4 + H$	$1.40 \times 10^{-8}(300/T_e)^{0.52}$	[124]
$CH_5^+ + e^- \rightarrow CH_2 + H_2 + H$	$4.76 \times 10^{-8}(300/T_e)^{0.52}$	[124]
$CH_5^+ + e^- \rightarrow CH_3 + H_2$	$1.40 \times 10^{-8}(300/T_e)^{0.52}$	[124]
$C_2H^+ + e^- \rightarrow C_2 + H$	$1.16 \times 10^{-7}(300/T_e)^{0.76}$	[124]
$C_2H^+ + e^- \rightarrow CH + C$	$1.53 \times 10^{-7}(300/T_e)^{0.76}$	[124]
$C_2H_3^+ + e^- \rightarrow C_2H_2 + H$	$5.00 \times 10^{-7}(300/T_e)^{0.84}$	[125]

Table A.20: Electron Dissociative Recombination (continued)

Reaction	Rate Coefficient cm^3s^{-1}	Reference
$C_2H_4^+ + e^- \rightarrow C_2H_3 + H$	$5.60 \times 10^{-7}(300/T_e)^{0.78}$	[125]
$C_2H_5^+ + e^- \rightarrow C_2H_4 + H$	$1.20 \times 10^{-6}(300/T_e)^{0.8}$	[125]
$C_2H_6^+ + e^- \rightarrow C_3H_3 + H_2 + H$	$1.00 \times 10^{-6}(300/T_e)^{0.7}$	[125]
$C_2H_7^+ + e^- \rightarrow C_3H_3 + H_2 + H_2$	$3.00 \times 10^{-7}(300/T_e)^{0.5}$	[124]
$C_3H^+ + e^- \rightarrow C_3 + H$	$2.00 \times 10^{-7}(300/T_e)^{0.7}$	[125]
$C_3H^+ + e^- \rightarrow C_2H + C$	$2.00 \times 10^{-7}(300/T_e)^{0.7}$	[125]
$C_3H_2^+ + e^- \rightarrow C_3H + H$	$4.00 \times 10^{-7}(300/T_e)^{0.7}$	[125]
$C_3H_3^+ + e^- \rightarrow C_3H_2 + H$	$7.00 \times 10^{-7}(300/T_e)^{0.5}$	[124]
$C_3H_4^+ + e^- \rightarrow C_3H_3 + H$	$2.95 \times 10^{-6}(300/T_e)^{0.67}$	[125]
$C_3H_5^+ + e^- \rightarrow C_3H_3 + H_2$	$2.00 \times 10^{-6}(300/T_e)^{0.7}$	[125]
$C_3H_6^+ + e^- \rightarrow C_3H_3 + H_2 + H$	$1.00 \times 10^{-6}(300/T_e)^{0.7}$	[125]
$C_3H_7^+ + e^- \rightarrow C_3H_3 + H_2 + H_2$	$1.90 \times 10^{-6}(300/T_e)^{0.67}$	[125]
$C_nH_m^+ + e^- \rightarrow C_nH_m$	$3.50 \times 10^{-7}(300/T_e)^{0.5}$	[125]
$H_2C_3H^+ + e^- \rightarrow C_2H_2 + CH$	$8.00 \times 10^{-7}(300/T_e)^{1.0}$	[125]

Table A.21: Selected Ion-Molecule Reactions in the Jovian Ionosphere

Reaction	Rate Coefficient [$cm^3 s^{-1}$]	Reference	React. Number
$H_2 + He^+ \rightarrow H^+ + HeH$	1.00×10^{-10}	[114]	R1
$H_2 + He^+ \rightarrow H_2^+ + He$	9.35×10^{-15}	[114]	R2
$H_2 + He^+ \rightarrow HeH^+ + H$	4.21×10^{-13}	[111]	R3
$H_2 + H_2^+ \rightarrow H_3^+ + H$	2.08×10^{-9}	[98, 111]	R4
$H_2 + HeH^+ \rightarrow H_3^+ + He$	1.05×10^{-9}	[98]	R5
$H_2 + CH_4^+ \rightarrow CH_5^+ + H$	3.30×10^{-11}	[124]	R6
$H_2 + CH_3^+ \rightarrow CH_4^+ + H$	1.30×10^{-14}	[124]	R7
$H_2 + CH_2^+ \rightarrow CH_3^+ + H$	1.60×10^{-9}	[124]	R8
$H_2 + CH^+ \rightarrow CH_2^+ + H$	1.20×10^{-9}	[124]	R9
$H_2 + C^+ \rightarrow CH^+ + H$	1.00×10^{-10}	[124]	R10
$H_2 + C_2H_2^+ \rightarrow C_2H_3^+ + H$	1.00×10^{-11}	[124]	R12
$H_2 + C_2H^+ \rightarrow C_2H_2^+ + H$	1.70×10^{-9}	[124]	R13
$He + H_2^+ \rightarrow HeH^+ + H$	1.40×10^{-10}	[114]	R14
$H + H_2^+ \rightarrow H^+ + H_2$	6.40×10^{10}	[98, 111]	R15
$H + H_3^+ \rightarrow H_2^+ + H_2$	1.00×10^{-20}	estimate	R16
$H + HeH^+ \rightarrow H_2^+ + He$	9.10×10^{-10}	[98, 111]	R17
$H + CH_5^+ \rightarrow CH_4^+ + H_2$	1.50×10^{-10}	[124]	R18
$H + CH^+ \rightarrow C^+ + H_2$	7.50×10^{-10}	[124]	R19
$H + C_2H_6^+ \rightarrow C_2H_5^+ + H_2$	1.00×10^{-10}	[114]	R20
$H + C_2H_5^+ \rightarrow C_2H_4^+ + H_2$	1.00×10^{-11}	[124]	R21
$H + C_2H_4^+ \rightarrow C_2H_3^+ + H_2$	3.00×10^{-10}	[124]	R22

Table A.21: Ion-Molecule Reactions (continued)

Reaction	Rate Coefficient [cm^3s^{-1}]	Reference	React. Number
$H + C_2H_3^+ \rightarrow C_2H_2^+ + H_2$	6.80×10^{-11}	[124]	R23
$H + C_3H_5^+ \rightarrow C_2H_3^+ + CH_3$	9.50×10^{-12}	[125]	R24
$H + C_3H_5^+ \rightarrow C_2H_2^+ + CH_4$	5.00×10^{-13}	[125]	R25
$H + C_3H_2^+ \rightarrow C_3H^+ + H_2$	6.00×10^{-11}	[125]	R26
$H + C_2H_6^+ \rightarrow C_2H_5^+ + H_2$	1.00×10^{-10}	[114]	R27
$CH_4 + H^+ \rightarrow CH_4^+ + H$	2.30×10^{-9}	[124]	R28
$CH_4 + H^+ \rightarrow CH_3^+ + H_2$	1.50×10^{-9}	[124]	R29
$CH_4 + He^+ \rightarrow H^+ + CH_3 + He$	4.80×10^{-10}	[124]	R30
$CH_4 + He^+ \rightarrow CH_4^+ + He$	5.10×10^{-11}	[124]	R31
$CH_4 + He^+ \rightarrow CH_3^+ + He + H$	8.50×10^{-11}	[124]	R32
$CH_4 + He^+ \rightarrow CH_2^+ + He + H_2$	9.50×10^{-10}	[124]	R33
$CH_4 + He^+ \rightarrow CH^+ + He + H_2 + H$	2.40×10^{-10}	[124]	R34
$CH_4 + H_2^+ \rightarrow CH_5^+ + H$	1.14×10^{-10}	[124]	R35
$CH_4 + H_2^+ \rightarrow CH_4^+ + H_2$	1.40×10^{-9}	[124]	R36
$CH_4 + H_2^+ \rightarrow CH_3^+ + H_2 + H$	2.30×10^{-9}	[124]	R37
$CH_4 + H_3^+ \rightarrow CH_5^+ + H_2$	2.40×10^{-9}	[125]	R38
$CH_4 + CH_4^+ \rightarrow CH_5^+ + CH_3$	1.50×10^{-9}	[124]	R39
$CH_4 + CH_3^+ \rightarrow C_2H_5^+ + H_2$	1.20×10^{-9}	[124]	R40
$CH_4 + CH_2^+ \rightarrow C_2H_5^+ + H$	3.60×10^{-10}	[124]	R41
$CH_4 + CH_2^+ \rightarrow C_2H_4^+ + H_2$	8.40×10^{-10}	[124]	R42
$CH_4 + CH^+ \rightarrow C_2H_4^+ + H$	6.50×10^{-11}	[124]	R43
$CH_4 + CH^+ \rightarrow C_2H_3^+ + H_2$	1.09×10^{-9}	[124]	R44

Table A.21: Ion-Molecule Reactions (continued)

Reaction	Rate Coefficient [cm^3s^{-1}]	Reference	React. Number
$CH_4 + CH^+ \rightarrow C_2H_2^+ + H_2 + H$	1.43×10^{-10}	[124]	R45
$CH_4 + C^+ \rightarrow C_2H_3^+ + H$	1.10×10^{-9}	[124]	R46
$CH_4 + C^+ \rightarrow C_2H_2^+ + H_2$	4.00×10^{-10}	[124]	R47
$CH_4 + C_2H_5^+ \rightarrow C_3H_7^+ + H_2$	9.00×10^{-14}	[124]	R48
$CH_4 + C_2H_3^+ \rightarrow C_3H_5^+ + H_2$	2.00×10^{-10}	[124]	R49
$CH_4 + C_2H_2^+ \rightarrow C_3H_5^+ + H$	6.64×10^{-10}	[124]	R50
$CH_4 + C_2H_2^+ \rightarrow C_3H_4^+ + H_2$	1.76×10^{-10}	[124]	R51
$CH_4 + C_2H^+ \rightarrow C_2H_2^+ + CH_3$	3.74×10^{-10}	[124]	R52
$CH_4 + C_2H^+ \rightarrow C_3H_4^+ + H$	1.32×10^{-10}	[124]	R53
$CH_4 + C_2H^+ \rightarrow H_2C_3H^+ + H_2$	3.74×10^{-10}	[124]	R54
$C_2H_2 + He^+ \rightarrow CH^+ + CH + He$	7.70×10^{-10}	[124]	R55
$C_2H_2 + He^+ \rightarrow C_2H^+ + H + He$	8.75×10^{-10}	[114]	R56
$C_2H_2 + He^+ \rightarrow C_2H_2^+ + He$	2.54×10^{-10}	[124]	R57
$C_2H_2 + H_2^+ \rightarrow C_2H_3^+ + H$	4.80×10^{-10}	[124]	R58
$C_2H_2 + H_2^+ \rightarrow C_2H_2^+ + H_2$	4.82×10^{-9}	[124]	R59
$C_2H_2 + H_3^+ \rightarrow C_2H_3^+ + H_2$	3.50×10^{-9}	[124]	R60
$C_2H_2 + CH_5^+ \rightarrow C_2H_3^+ + CH_4$	1.60×10^{-9}	[124]	R61
$C_2H_2 + CH_4^+ \rightarrow C_2H_3^+ + CH_3$	1.23×10^{-9}	[124]	R62
$C_2H_2 + CH_4^+ \rightarrow C_2H_2^+ + CH_4$	1.13×10^{-9}	[124]	R63
$C_2H_2 + CH_4^+ \rightarrow H_2C_3H^+ + H_2 + H$	1.51×10^{-10}	[124]	R64
$C_2H_2 + CH_3^+ \rightarrow H_2C_3H^+ + H_2$	1.20×10^{-9}	[124]	R65
$C_2H_2 + CH_2^+ \rightarrow H_2C_3H^+ + H$	2.50×10^{-9}	[124]	R66

Table A.21: Ion-Molecule Reactions (continued)

Reaction	Rate Coefficient [cm^3s^{-1}]	Reference	React. Number
$C_2H_2 + CH^+ \rightarrow C_3H_2^+ + H$	2.40×10^{-9}	[124]	R67
$C_2H_2 + C^+ \rightarrow C_3H^+ + H$	2.80×10^{-9}	[124]	R68
$C_2H_2 + C_2H_5^+ \rightarrow C_3H_3^+ + CH_4$	6.84×10^{-11}	[124]	R69
$C_2H_2 + C_2H_4^+ \rightarrow C_3H_3^+ + CH_3$	6.45×10^{-10}	[124]	R70
$C_2H_2 + C_2H_4^+ \rightarrow C_4H_5^+ + H$	1.93×10^{-10}	[124]	R71
$C_2H_2 + C_2H_3^+ \rightarrow C_4H_3^+ + H_2$	7.20×10^{-10}	[124]	R72
$C_2H_2 + C_2H_2^+ \rightarrow C_4H_3^+ + H$	9.10×10^{-10}	[124]	R73
$C_2H_2 + C_3H_5^+ \rightarrow C_5H_5^+ + H_2$	3.80×10^{-10}	[124]	R74
$C_2H_2 + C_3H_3^+ \rightarrow C_5H_3^+ + H_2$	1.10×10^{-9}	[124]	R75
$C_2H_2 + C_2H_6^+ \rightarrow C_2H_5^+ + C_3H_3$	2.20×10^{-10}	[114]	R76
$C_2H_2 + C_2H_6^+ \rightarrow C_3H_5^+ + CH_3$	8.19×10^{-10}	[114]	R77
$C_2H_2 + C_2H_6^+ \rightarrow C_4H_7^+ + H_3$	1.29×10^{-10}	[114]	R78
$C_2H_2 + C_2H_7^+ \rightarrow C_2H_3^+ + C_2H_6$	1.00×10^{-9}	[114]	R79
$C_2H_2 + H_2C_3H^+ \rightarrow C_3H_3^+ + C_2H_2$	2.50×10^{-10}	[114]	R80
$C_2H_2 + C_2H^+ \rightarrow C_4H_2^+ + H$	1.20×10^{-9}	[114]	R81
$C_2H_4 + He^+ \rightarrow CH_2^+ + CH_2 + He$	4.80×10^{-10}	[124]	R82
$C_2H_4 + He^+ \rightarrow CH_2H_4^+ + He$	2.40×10^{-10}	[124]	R83
$C_2H_4 + He^+ \rightarrow C_2H_3^+ + He + H$	1.70×10^{-10}	[124]	R84
$C_2H_4 + He^+ \rightarrow C_2H_2^+ + He + H_2$	2.20×10^{-9}	[124]	R85
$C_2H_4 + He^+ \rightarrow C_2H^+ + He + H_2 + H$	4.42×10^{-10}	[114]	R86
$C_2H_4 + H_2^+ \rightarrow C_2H_4^+ + H_2$	2.21×10^{-9}	[124]	R87
$C_2H_4 + H_2^+ \rightarrow C_2H_3^+ + H_2 + H$	1.81×10^{-9}	[124]	R88

Table A.21: Ion-Molecule Reactions (continued)

Reaction	Rate Coefficient [cm^3s^{-1}]	Reference	React. Number
$C_2H_4 + H_2^+ \rightarrow C_2H_2^+ + H_2 + H_2$	8.82×10^{-10}	[124]	R89
$C_2H_4 + H_3^+ \rightarrow C_2H_5^+ + H_2$	6.90×10^{-10}	[114]	R90
$C_2H_4 + H_3^+ \rightarrow C_2H_3^+ + H_2 + H_2$	1.15×10^{-9}	[124]	R91
$C_2H_4 + HeH^+ \rightarrow C_2H_4^+ + H + He$	7.00×10^{-10}	[114]	R92
$C_2H_4 + HeH^+ \rightarrow C_2H_3^+ + H_2 + He$	2.10×10^{-9}	[114]	R93
$C_2H_4 + CH_5^+ \rightarrow C_2H_5^+ + CH_4$	1.50×10^{-9}	[124]	R94
$C_2H_4 + CH_4^+ \rightarrow C_2H_5^+ + CH_3$	4.23×10^{-10}	[124]	R95
$C_2H_4 + CH_4^+ \rightarrow C_2H_4^+ + CH_4$	1.38×10^{-9}	[124]	R96
$C_2H_4 + CH_3^+ \rightarrow C_2H_3^+ + CH_4$	3.50×10^{-10}	[124]	R97
$C_2H_4 + CH_3^+ \rightarrow C_3H_5^+ + H_2$	5.24×10^{-10}	[124]	R98
$C_2H_4 + CH_3^+ \rightarrow H_2C_3H^+ + H_2 + H_2$	4.60×10^{-11}	[124]	R99
$C_2H_4 + C^+ \rightarrow C_2H_4^+ + C$	1.70×10^{-10}	[124]	R100
$C_2H_4 + C^+ \rightarrow C_2H_3^+ + CH$	8.50×10^{-11}	[124]	R101
$C_2H_4 + C^+ \rightarrow C_3H_2^+ + H_2$	3.40×10^{-10}	[124]	R102
$C_2H_4 + C^+ \rightarrow C_3H^+ + H + H_2$	8.50×10^{-11}	[124]	R103
$C_2H_4 + C^+ \rightarrow H_2C_3H^+ + H$	1.02×10^{-9}	[124]	R104
$C_2H_4 + C_2H_5^+ \rightarrow C_3H_5^+ + CH_4$	3.90×10^{-10}	[124]	R105
$C_2H_4 + C_2H_4^+ \rightarrow C_3H_5^+ + CH_3$	7.11×10^{-10}	[124]	R106
$C_2H_4 + C_2H_4^+ \rightarrow C_4H_7^+ + H$	7.90×10^{-11}	[124]	R107
$C_2H_4 + C_2H_3^+ \rightarrow C_2H_5^+ + C_2H_2$	8.90×10^{-10}	[124]	R108
$C_2H_4 + C_2H_2^+ \rightarrow C_2H_4^+ + C_2H_2$	4.14×10^{-10}	[124]	R109
$C_2H_4 + C_2H_2^+ \rightarrow C_4H_5^+ + H$	3.17×10^{-10}	[124]	R110

Table A.21: Ion-Molecule Reactions (continued)

Reaction	Rate Coefficient [cm^3s^{-1}]	Reference	React. Number
$C_2H_4 + C_2H_2^+ \rightarrow H_2C_3H^+ + CH_3$	6.62×10^{-10}	[124]	R111
$C_2H_4 + C_2H_6^+ \rightarrow C_2H_4^+ + C_2H_6$	1.15×10^{-9}	[124]	R112
$C_2H_4 + C_2H_7^+ \rightarrow C_2H_5^+ + C_2H_6$	1.00×10^{-9}	[114]	R113
$C_2H_4 + C_2H^+ \rightarrow C_nH_m^+$ products	1.71×10^{-9}	[114]	R114
$C_2H_6 + H^+ \rightarrow C_2H_5^+ + H_2$	1.30×10^{-9}	[124]	R115
$C_2H_6 + H^+ \rightarrow C_2H_4^+ + H_2 + H$	1.40×10^{-9}	[124]	R116
$C_2H_6 + H^+ \rightarrow C_2H_3^+ + H_2 + H_2$	2.80×10^{-9}	[124]	R117
$C_2H_6 + He^+ \rightarrow C_2H_4^+ + He + H_2$	4.20×10^{-10}	[124]	R118
$C_2H_6 + He^+ \rightarrow C_2H_3^+ + He + H_2 + H$	1.80×10^{-9}	[124]	R119
$C_2H_6 + He^+ \rightarrow C_2H_2^+ + He + H_2 + H_2$	8.40×10^{-10}	[124]	R120
$C_2H_6 + H_2^+ \rightarrow C_2H_6^+ + H_2$	2.94×10^{-10}	[124]	R121
$C_2H_6 + H_2^+ \rightarrow C_2H_5^+ + H_2 + H$	1.37×10^{-9}	[124]	R122
$C_2H_6 + H_2^+ \rightarrow C_2H_4^+ + H_2 + H_2$	2.35×10^{-9}	[124]	R123
$C_2H_6 + H_2^+ \rightarrow C_2H_3^+ + H_2 + H_2 + H$	6.86×10^{-10}	[114]	R124
$C_2H_6 + H_2^+ \rightarrow C_2H_2^+ + H_2 + H_2 + H_2$	1.96×10^{-10}	[114]	R125
$C_2H_6 + H_3^+ \rightarrow C_2H_7^+ + H_2$	2.90×10^{-11}	[111]	R126
$C_2H_6 + H_3^+ \rightarrow C_2H_5^+ + H_2 + H_2$	2.40×10^{-9}	[124]	R127
$C_2H_6 + HeH^+ \rightarrow C_2H_5^+ + He + H_2$	1.05×10^{-9}	[114]	R128
$C_2H_6 + HeH^+ \rightarrow C_2H_3^+ + He + H_2 + H_2$	1.05×10^{-9}	[114]	R129
$C_2H_6 + CH_5^+ \rightarrow C_2H_7^+ + CH_4$	1.15×10^{-9}	[111]	R130
$C_2H_6 + CH_5^+ \rightarrow C_2H_5^+ + CH_4 + H_2$	2.03×10^{-10}	[111]	R131
$C_2H_6 + CH_4^+ \rightarrow C_2H_4^+ + CH_4 + H_2$	1.91×10^{-9}	[114]	R132

Table A.21: Ion-Molecule Reactions (continued)

Reaction	Rate Coefficient [cm^3s^{-1}]	Reference	React. Number
$C_2H_6 + CH_3^+ \rightarrow C_2H_5^+ + CH_4$	1.48×10^{-9}	[124]	R133
$C_2H_6 + CH_3^+ \rightarrow C_3H_7^+ + H_2$	1.00×10^{-10}	[114]	R134
$C_2H_6 + CH_3^+ \rightarrow C_3H_5^+ + H_2 + H_2$	1.57×10^{-10}	[124]	R135
$C_2H_6 + C^+ \rightarrow C_2H_5^+ + CH$	2.31×10^{-10}	[124]	R136
$C_2H_6 + C^+ \rightarrow C_2H_4^+ + CH_2$	1.16×10^{-10}	[124]	R137
$C_2H_6 + C^+ \rightarrow C_2H_3^+ + CH_3$	4.95×10^{-10}	[124]	R138
$C_2H_6 + C^+ \rightarrow C_2H_2^+ + CH_4$	8.25×10^{-11}	[124]	R139
$C_2H_6 + C^+ \rightarrow C_3H_2^+ + H_2 + H_2$	1.65×10^{-11}	[124]	R140
$C_2H_6 + C^+ \rightarrow C_3H_3^+ + H_2 + H$	7.10×10^{-10}	[124]	R141
$C_2H_6 + C_2H_6^+ \rightarrow C_3H_8^+ + CH_4$	7.98×10^{-12}	[114]	R142a
$C_2H_6 + C_2H_6^+ \rightarrow C_3H_9^+ + CH_3$	1.10×10^{-11}	[114]	R142b
$C_2H_6 + C_2H_5^+ \rightarrow C_3H_7^+ + CH_4$	5.46×10^{-12}	[125]	R143
$C_2H_6 + C_2H_5^+ \rightarrow C_4H_9^+ + H_2$	4.00×10^{-11}	[114]	R144
$C_2H_6 + C_2H_4^+ \rightarrow C_3H_7^+ + CH_3$	4.62×10^{-12}	[124]	R145
$C_2H_6 + C_2H_4^+ \rightarrow C_3H_6^+ + CH_4$	5.15×10^{-13}	[124]	R146
$C_2H_6 + C_2H_3^+ \rightarrow C_2H_5^+ + C_2H_4$	2.91×10^{-10}	[124]	R147
$C_2H_6 + C_2H_3^+ \rightarrow C_3H_5^+ + CH_4$	2.48×10^{-10}	[124]	R148
$C_2H_6 + C_2H_3^+ \rightarrow C_4H_7^+ + H_2$	8.06×10^{-11}	[114]	R149
$C_2H_6 + C_2H_2^+ \rightarrow C_2H_5^+ + C_2H_3$	1.31×10^{-10}	[114]	R150
$C_2H_6 + C_2H_2^+ \rightarrow C_2H_4^+ + C_2H_4$	2.48×10^{-10}	[124]	R151
$C_2H_6 + C_2H_2^+ \rightarrow C_3H_5^+ + CH_3$	7.45×10^{-10}	[124]	R152
$C_4H_2 + H^+ \rightarrow C_4H_2^+ + H$	2.00×10^{-9}	[124]	R153

Table A.21: Ion-Molecule Reactions (continued)

Reaction	Rate Coefficient [cm^3s^{-1}]	Reference	React. Number
$C_4H_2 + H_3^+ \rightarrow C_4H_3^+ + H_2$	2.60×10^{-9}	[124]	R154
$C_4H_2 + CH_3^+ \rightarrow C_5H_3^+ + H_2$	1.30×10^{-10}	[124]	R155
$C_4H_2 + CH_3^+ \rightarrow H_2C_3H^+ + C_2H_2$	1.27×10^{-9}	[124]	R156
$C_4H_2 + C^+ \rightarrow C_3H^+ + C_2H$	1.45×10^{-10}	[124]	R157
$C_4H_2 + C^+ \rightarrow C_5H^+ + H$	1.45×10^{-9}	[124]	R158a
$C_4H_2 + C^+ \rightarrow C_4H_2^+ + C$	1.31×10^{-9}	[124]	R158b
$C_4H_2 + C_2H_5^+ \rightarrow C_4H_3^+ + C_2H_4$	3.00×10^{-10}	[125]	R159
$C_4H_2 + C_2H_2^+ \rightarrow C_4H_2^+ + C_2H_2$	1.26×10^{-9}	[124]	R160
$C_4H_2 + C_2H_2^+ \rightarrow C_6H_3^+ + H$	1.40×10^{-10}	[124]	R161
$C_4H_2 + C_3H_2^+ \rightarrow C_7H_3^+ + H$	3.00×10^{-10}	[124]	R162a
$C_4H_2 + C_3H_2^+ \rightarrow C_7H_2^+ + H_2$	3.00×10^{-10}	[124]	R162b
$H_{2vib} + H^+ \rightarrow H_2^+ + H$	1.00×10^{-9}	[98] est.	R163

A.1 Glossary

- *Birkeland current*: current aligned with the magnetic field.

- *bow shock*: When the supersonic solar wind encounters an obstacle (magnetosphere or planet), it must first become subsonic to be able to flow around it forming a shock.

- *Chapman function*: is a consequence of approximating planet surfaces as flat surfaces. It is defined as:

$$Ch(\chi) = \frac{\int_s^\infty n(s)ds}{\int_h^\infty n(h)dh}$$

  where n is the atmospheric density, s is the line of sight to the Sun and h is the vertical distance. χ is the solar zenith angle.

- *Collision mean free path*: $\lambda = (\sigma n)^{-1}$

- *Coronal Mass Ejection (CME)*: massive explosion at the sun's atmosphere that ejects material from the solar corona into the interplanetary medium.

- *EPIC*: European photon imaging camera.

- *flux tube*: a flux tube can be represented by a bundle of magnetic field lines. When several flux tubes become twisted they form what is called a flux rope.

- *homopause*: the altitude level in the atmosphere, above which diffusion rather than turbulent mixing becomes the controlling process.

- *Interplanetary Magnetic Field (IMF)*: Magnetic field originating in the sun and carried by the solar wind along the interplanetary medium.

- *iogenic*: generated in Jupiter's moon Io.

- *loss cone*: missing portion of a distribution of particles that arises as particles manage to escape the magnetic field that is "trapping" them. The shaped of the missing particles takes the shape of a cone in velocity distribution.

- *magnetopause*: Boundary surface that separates the magnetosphere from the solar wind. At the magnetopause the magnetic field is discontinued, since it changes directions.

- *plasmasphere*: region in the inner magnetosphere when cold plasma and energetic particle populations coexist.

- *plasma mantle*: when the magnetosphere is open, plasma from the solar wind can flow along the open magnetic field lines directly into the magnetotail, forming the plasma mantle

- *pitch angle*: angle between the velocity vector of a charged particle and the magnetic field line around which it gyrates.

- *reconnection*: in general, magnetic reconnection occurs at an X-point, where two pairs of separatrices meet. During this process, pairs of magnetic field lines are disconnected and reconnected [27].

- *solar wind*: outward plasma flow that originates in the solar corona and extends throughout the solar system. It carries the coronal field lines with it.

Bibliography

[1] J. T. Clarke, D. Grodent, S. T. H. Cowley, Bunce, P. E. J., Zarka, J. E. P. Connerney, and T. Satoh. *Jupiter's aurora*, chapter 26, pages 639 – 670. Cambridge, 2004.

[2] G. Branduardi-Raymont, A. Bhardwaj, R. Elsner, R. Gladstone, G. Ramsay, P. Rodriguez, R. Soria, H. Waite, and T. Cravens. XMM-Newton Observations of X-Ray Emission from Jupiter. In W.-H. Ip & A. Bhardwaj, editor, *Advances in Geosciences, Volume 3: Planetary Science (PS)*, volume 3, pages 203–+, 2006.

[3] S. W. H. Cowley and E. J. Bunce. Origin of the main auroral oval in Jupiter's coupled magnetosphere-ionosphere system. *Planet. Space. Sci.*, 49:1067–1088, August 2001.

[4] S. W. H. Cowley, E. J. Bunce, T. S. Stallard, and S. Miller. Jupiter's polar ionospheric flows: Theoretical interpretation. *GRL*, 30(5):050000–1, March 2003.

[5] X. Liu, D. E. Shemansky, S. M. Ahmed, G. K. James, and J. M. Ajello. Electron-impact excitation and emission cross sections of the H_2 Lyman and Werner systems. *J. Geophys. Res.*, 103:26739–26758, November 1998.

[6] X. Liu, D. E. Shemansky, H. Abgrall, E. Roueff, S. M. Ahmed, and J. M. Ajello. Electron impact excitation of H_2: resonance excitation of and effective excita-

tion function of . *Journal of Physics B Atomic Molecular Physics*, 36:173–196, January 2003.

[7] A. Dalgarno, M. Yan, and W. Liu. Electron Energy Deposition in a Gas Mixture of Atomic and Molecular Hydrogen and Helium. *Astrophys. J. Suppl. Ser.*, 125:237–256, November 1999.

[8] J. Wrkich, D. Mathews, I. Kanik, S. Trajmar, and M. A. Khakoo. Differential cross-sections for the electron impact excitation of the states of molecular hydrogen. *Journal of Physics B Atomic Molecular Physics*, 35:4695–4709, November 2002.

[9] J. M. Ajello, I. Kanik, S. M. Ahmed, and J. T. Clarke. Line profile of H Lyman α from dissociative excitation of H_2 with application to Jupiter. *J. Geophys. Res.*, 1002:26411–26420, 1995.

[10] J. S. Yoon, M. Y. Song, J. M. Han, S. H. Hwang, W. S Chang, and B. J. Lee. Cross sections for electron collisions with hydrogen molecules. *J. Phys. Chem. Ref. Data*, 37(2):913 – 931, 2009.

[11] C. H. Jackman, R. H. Garvey, and A. E. S. Green. Electron impact on atmospheric gases. I - Updated cross sections. *J. Geophys. Res.*, 82:5081–5090, November 1977.

[12] J. J. Olivero, J. N. Bass, and A. E. S. Green. Photoelectron excitation of the Jupiter dayglow. *J. Geophys. Res.*, 78:2812–2826, 1973.

[13] P. M. Stone and Y.-K Kim. Electron-Impact Cross Sections for Dipole- and Spin-Allowed Excitations of Hydrogen, Helium, and Lithium. *J. Res. of Natl. Inst. Stand. Technol.*, 107(4):327 – 337, July-August 2002.

[14] M. B. Shah, D. S. Elliott, and H. B. Gilbody. Pulsed crossed-beam study of the ionisation of atomic hydrogen by electron impact. *J. of Phys. B: At. Mol. Phys.*, 20:3501–3514, July 1987.

[15] L. Gan and T. E. Cravens. Electron impact cross-sections and cooling rates for methane. *Planet. Space Sci.*, 40:1535–1544, November 1992.

[16] T. W. Shyn and W. E. Sharp. Angular distributions of electrons elastically scattered from H_2. *Phys. Rev. A*, 24:1734–1740, October 1981.

[17] A. N. Maurellis and T. E. Cravens. Ionospheric Effects of Comet Shoemaker-Levy 9 Impacts with Jupiter. *Icarus*, 154:350–371, December 2001.

[18] D. R. Schultz, Y.-W. Hui, M. Rakovic, P. C. Stancil, V. Kharchenko, and A. Dalgarno. Atomic data and nuclear data tables. In preparation, 2011.

[19] N. Ozak, D. R. Schultz, T. E. Cravens, V. Kharchenko, and Y.-W. Hui. Auroral x-ray emission at jupiter: Depth effects. *J. Geophys. Res.*, 115:A11306, November 2010.

[20] H. Paul and A. Schinner. An empirical approach to the stopping power of solids and gases for ions from li to ar. *Nucl. Instrum. Methods Phys. Res., Sect. B*, 179:299, 2001.

[21] Y. Hui, D. R. Schultz, V. A. Kharchenko, A. Bhardwaj, G. Branduardi-Raymont, P. C. Stancil, T. E. Cravens, C. M. Lisse, and A. Dalgarno. Comparative analysis and variability of the Jovian X-ray spectra detected by the Chandra and XMM-Newton observatories. *J. Geophys. Res.*, 115:7102, July 2010.

[22] J. H. Waite, T. E. Cravens, J. Kozyra, A. F. Nagy, S. K. Atreya, and R. H. Chen. Electron precipitation and related aeronomy of the Jovian thermosphere and ionosphere. *J. Geophys. Res.*, 88:6143–6163, August 1983.

[23] H. Menager, M. Barthélemy, and J. Lilensten. H Lyman α line in Jovian aurorae: electron transport and radiative transfer coupled modelling. *Astron. Astrophys.*, 509:A56, January 2010.

[24] A. Bhardwaj. X-Ray Emission from Jupiter, Saturn and Earth: A Short Review. In W.-H. Ip & A. Bhardwaj, editor, *Advances in Geosciences, Volume 3: Planetary Science (PS)*, volume 3, pages 215–+, 2006.

[25] T. Gold. Motions in the magnetosphere of the Earth. *J. Geophys. Res.*, 64(9), 1959.

[26] Thomas E. Cravens. *Physics of Solar System Plasmas*. Atmospheric and Space Science. Cambridge, 1997.

[27] C. J. Schrijver and G. L. Siscoe. *Heliophysics: Plasma Physics of the Local Cosmos*. Cambridge, 2009.

[28] T. W. Hill. Inertial limit on corotation. *J. Geophys. Res.*, 84:6554–6558, November 1979.

[29] A. J. Dessler. *Physics of the Jovian Magnetosphere*. Cambridge University Press, 1983.

[30] T. W. Hill. The Jovian auroral oval. *J. Geophys. Res.*, 106:8101–8108, May 2001.

[31] F. J. Crary, J. T. Clarke, M. K. Dougherty, P. G. Hanlon, K. C. Hansen, J. T. Steinberg, B. L. Barraclough, A. J. Coates, J.-C. Gérard, D. Grodent, W. S.

Kurth, D. G. Mitchell, A. M. Rymer, and D. T. Young. Solar wind dynamic pressure and electric field as the main factors controlling Saturn's aurorae. *Nature*, 433:720–722, February 2005.

[32] J. T. Clarke, J.-C. Gérard, D. Grodent, S. Wannawichian, J. Gustin, J. Connerney, F. Crary, M. Dougherty, W. Kurth, S. W. H. Cowley, E. J. Bunce, T. Hill, and J. Kim. Morphological differences between Saturn's ultraviolet aurorae and those of Earth and Jupiter. *Nature*, 433:717–719, February 2005.

[33] A. Bhardwaj and G. R. Gladstone. Auroral emissions of the giant planets. *Reviews of Geophysics*, 38:295–354, 2000.

[34] J. Clarke, S. Durrance, W. Moos, J. Murthy, S. Atreya, A. Barnes, J. Mihalov, J. Belcher, M. Festou, and C. Imhoff. Continued observations of the H LY alpha emission from Uranus. *J. Geophys. Res.*, 91:8771–8781, August 1986.

[35] Michele Dougherty, Larry Esposito, and Tom Krimigis. *Saturn from Cassini-Huygens*. Springer, first edition, 2009.

[36] T. W. Hill. Auroral structures at Jupiter and Earth. *Advances in Space Research*, 33:2021–2029, 2004.

[37] E. J. Bunce, C. S. Arridge, J. T. Clarke, A. J. Coates, S. W. H. Cowley, M. K. Dougherty, J.-C. Gérard, D. Grodent, K. C. Hansen, J. D. Nichols, D. J. Southwood, and D. L. Talboys. Origin of Saturn's aurora: Simultaneous observations by Cassini and the Hubble Space Telescope. *J. Geophys. Res.*, 113:9209–+, September 2008.

[38] J.-C. Gérard, E. J. Bunce, D. Grodent, S. W. H. Cowley, J. T. Clarke, and S. V. Badman. Signature of Saturn's auroral cusp: Simultaneous Hubble Space Tele-

scope FUV observations and upstream solar wind monitoring. *J. Geophys. Res.*, 110:11201–+, November 2005.

[39] G. Paschmann, S. Haaland, and R. Treumann. Auroral Plasma Physics. *Space Science Reviews*, 103, April 2002.

[40] A. E. Metzger, D. A. Gilman, J. L. Luthey, K. C. Hurley, H. W. Schnopper, F. D. Seward, and J. D. Sullivan. The detection of X rays from Jupiter. *J. Geophys. Res.*, 88:7731–7741, October 1983.

[41] J. E. P. Connerney, M. H. Acuña, N. F. Ness, and T. Satoh. New models of Jupiter's magnetic field constrained by the Io flux tube footprint. *J. of Geophys. Res.*, 103:11929–11940, June 1998.

[42] J. H. Waite, Jr., F. Bagenal, F. Seward, C. Na, G. R. Gladstone, T. E. Cravens, K. C. Hurley, J. T. Clarke, R. Elsner, and S. A. Stern. ROSAT observations of the Jupiter aurora. *J. Geophys. Res.*, 99:14799–+, August 1994.

[43] J. H. Waite, Jr. Comment on 'Bremsstrahlung X rays from Jovian auroral electrons' by D.D. Barbosa. *J. Geophys. Res.*, 96:19529–+, November 1991.

[44] D. D. Barbosa. Heavy ion dynamics and auroral arc formation in the Jovian magnetosphere. *Advances in Space Research*, 12:7–13, August 1992.

[45] M. Horanyi, T. E. Cravens, and J. H. Waite, Jr. The precipitation of energetic heavy ions into the upper atmosphere of Jupiter. *J. Geophys. Res.*, 93:7251–7271, July 1988.

[46] T. E. Cravens, E. Howell, J. H. Waite, and G. R. Gladstone. Auroral oxygen precipitation at Jupiter. *J. Geophys. Res.*, 100:17153–17162, September 1995.

[47] V. Kharchenko, W. Liu, and A. Dalgarno. X ray and EUV emission spectra of oxygen ions precipitating into the Jovian atmosphere. *J. Geophys. Res.*, 103:26687–26698, November 1998.

[48] W. Liu and D. R. Schultz. Jovian X-Ray Aurora and Energetic Oxygen Ion Precipitation. *Astrophys. J.*, 526:538–543, November 1999.

[49] T. E. Cravens, J. H. Waite, T. I. Gombosi, N. Lugaz, G. R. Gladstone, B. H. Mauk, and R. J. MacDowall. Implications of Jovian X-ray emission for magnetosphere-ionosphere coupling. *J. Geophys. Res.*, 108:1465–+, December 2003.

[50] V. Kharchenko, A. Dalgarno, D. R. Schultz, and P. C. Stancil. Ion emission spectra in the Jovian X-ray aurora. *Geophys. Res. Lett.*, 33:11105–+, June 2006.

[51] V. Kharchenko, A. Bhardwaj, A. Dalgarno, D. R. Schultz, and P. C. Stancil. Modeling spectra of the north and south Jovian X-ray auroras. *J. Geophys. Res.*, 113:8229–+, August 2008.

[52] Y. Hui, D. R. Schultz, V. A. Kharchenko, P. C. Stancil, T. E. Cravens, C. M. Lisse, and A. Dalgarno. The Ion-induced Charge-exchange X-ray Emission of the Jovian Auroras: Magnetospheric or Solar Wind Origin? *Astrophys. J.*, 702:L158–L162, September 2009.

[53] G. R. Gladstone, J. H. Waite, D. Grodent, W. S. Lewis, F. J. Crary, R. F. Elsner, M. C. Weisskopf, T. Majeed, J. M. Jahn, A. Bhardwaj, et al. A pulsating auroral X-ray hot spot on Jupiter. *Nature*, 415(6875):1000–1003, 2002.

[54] R. F. Elsner, N. Lugaz, J. H. Waite, T. E. Cravens, G. R. Gladstone, P. Ford, D. Grodent, A. Bhardwaj, R. J. MacDowall, M. D. Desch, and T. Majeed. Si-

multaneous Chandra X ray, Hubble Space Telescope ultraviolet, and Ulysses radio observations of Jupiter's aurora. *J. Geophys. Res.*, 110:1207–+, January 2005.

[55] G. Branduardi-Raymont, R. F. Elsner, G. R. Gladstone, G. Ramsay, P. Rodriguez, R. Soria, and J. H. Waite, Jr. First observation of Jupiter by XMM-Newton. *Astron. Astrophys.*, 424:331–337, September 2004.

[56] G. Branduardi-Raymont, A. Bhardwaj, R. F. Elsner, G. R. Gladstone, G. Ramsay, P. Rodriguez, R. Soria, J. H. Waite, Jr., and T. E. Cravens. A study of Jupiter's aurorae with XMM-Newton. *Astron. Astrophys.*, 463:761–774, February 2007.

[57] G. Branduardi-Raymont, R. F. Elsner, M. Galand, D. Grodent, T. E. Cravens, P. Ford, G. R. Gladstone, and J. H. Waite. Spectral morphology of the X-ray emission from Jupiter's aurorae. *J. Geophys. Res.*, 113:2202–+, February 2008.

[58] N. Gehrels and E. C. Stone. Energetic oxygen and sulfur ions in the Jovian magnetosphere and their contribution to the auroral excitation. *J. Geophys. Res.*, 88:5537–5550, July 1983.

[59] E. J. Bunce, S. W. H. Cowley, and T. K. Yeoman. Jovian cusp processes: Implications for the polar aurora. *J. Geophys. Res.*, 109:9–+, July 2004.

[60] T. Stallard, S. Miller, H. Melin, M. Lystrup, S. W. H. Cowley, E. J. Bunce, N. Achilleos, and M. Dougherty. Jovian-like aurorae on Saturn. *Nature*, 453:1083–1085, June 2008.

[61] D. Grodent, J.-C. Gérard, S. W. H. Cowley, E. J. Bunce, and J. T. Clarke. Variable morphology of Saturn's southern ultraviolet aurora. *J. Geophys. Res.)*, 110:7215–+, July 2005.

[62] W. R. Pryor, A. M. Rymer, D. G. Mitchell, T. W. Hill, D. T. Young, J. Saur, G. H. Jones, S. Jacobsen, S. W. H. Cowley, B. H. Mauk, A. J. Coates, J. Gustin, D. Grodent, J.-C. Gérard, L. Lamy, J. D. Nichols, S. M. Krimigis, L. W. Esposito, M. K. Dougherty, A. J. Jouchoux, A. I. F. Stewart, W. E. McClintock, G. M. Holsclaw, J. M. Ajello, J. E. Colwell, A. R. Hendrix, F. J. Crary, J. T. Clarke, and X. Zhou. The auroral footprint of Enceladus on Saturn. *Nature*, 472:331–333, April 2011.

[63] S. Wannawichian, J. T. Clarke, and D. H. Pontius. Interaction evidence between Enceladus' atmosphere and Saturn's magnetosphere. *J. Geophys. Res.*, 113:7217–+, July 2008.

[64] G. Branduardi-Raymont, A. Bhardwaj, R. F. Elsner, G. R. Gladstone, P. Rodriguez, J. H. Waite, Jr., and T. E. Cravens. X-rays from Saturn: A study with XMM-Newton and Chandra over the years 2002-05. *Astron. Astrophys.*, June 2009. Manuscript no 200609.

[65] A. Bhardwaj, R. F. Elsner, J. H. Waite, Jr., G. R. Gladstone, T. E. Cravens, and P. G. Ford. Chandra Observation of an X-Ray Flare at Saturn: Evidence of Direct Solar Control on Saturn's Disk X-Ray Emissions. *Ap.J.*, 624:L121–L124, May 2005.

[66] A. Bhardwaj, R. F. Elsner, J. H. Waite, Jr., G. R. Gladstone, T. E. Cravens, and P. G. Ford. The Discovery of Oxygen Kα X-Ray Emission from the Rings of Saturn. *Ap. J.*, 627:L73–L76, July 2005.

[67] G. R. Gladstone, J. H. Waite, and W. S. Lewis. Secular and local time dependence of Jovian X ray emissions. *J. Geophys. Res.*, 103:20083–20088, September 1998.

[68] G. Branduardi-Raymont, A. Bhardwaj, R. F. Elsner, and P. Rodriguez. X-rays from Saturn: a study with XMM-Newton and Chandra over the years 2002-05. *A&A*, 510:A73, February 2010.

[69] Y. Hui, T. E. Cravens, N. Ozak, and D. R. Schultz. What can be learned from the absence of auroral X-ray emission from Saturn? *Journal of Geophysical Research (Space Physics)*, 115:A10239, October 2010.

[70] V. M. Vasyliunas. *Plasma distribution and flow*, pages 395–453. Planetary Science. Cambridge, 1983.

[71] R.W. Schunk and A.F. Nagy. *Ionospheres: Physics, Plasma Physics, and Chemistry*. Atmospheric and Space Science. Cambridge, 2000.

[72] A. E. S. Green and S. K. Dutta. Semi-Empirical Cross Sections for Electron Impacts. *J. Geophys. Res.*, 72:3933–+, August 1967.

[73] W. T. Miles, R. Thompson, and A. E. S. Green. Electron-Impact Cross Sections and Energy Deposition in Molecular Hydrogen. *Journal of Applied Physics*, 43(2):678–686, February 1972.

[74] A. E. S. Green and T. Sawada. Ionization cross sections and secondary electron distributions. *J. Atmos. Terr. Phys.*, 34(10):1719 – 1728, October 1972.

[75] R. H. Garvey, H. S. Porter, and A. E. S. Green. Relativistic yield spectra for H2. *Journal of Applied Physics*, 48:4353–4359, October 1977.

[76] D. E. Shemansky, D. T. Hall, and J. M. Ajello. Electron impact excitation of H2 - Rydberg band systems and the benchmark dissociative cross section for H Lyman-alpha. *Astrophys. J.*, 296:765–773, September 1985.

[77] H. C. Straub, P. Renault, B. G. Lindsay, K. A. Smith, and R. F. Stebbings. Absolute partial cross sections for electron-impact ionization of h_2, n_2, and o_2 from threshold to 1000 ev. *Phys. Rev. A*, 54(3):2146–2153, Sep 1996.

[78] L. Gan, C. N. Keller, and T. E. Cravens. Electrons in the ionosphere of Titan. *J. Geophys. Res.*, 97:12137, August 1992.

[79] T. E. Cravens, J. Clark, A. Bhardwaj, R. Elsner, J. H. Waite, A. N. Maurellis, G. R. Gladstone, and G. Branduardi-Raymont. X-ray emission from the outer planets: Albedo for scattering and fluorescence of solar X rays. *Journal of Geophysical Research (Space Physics)*, 111:A07308, July 2006.

[80] J. W. Gallagher, C. E. Brion, J. A. R. Samson, and P. W. Langhoff. Absolute Cross Sections for Molecular Photoabsorption, Partial Photoionization, and Ionic Photofragmentation Processes. *J. Phys. Chem. Ref. Data*, 17:9–153, January 1988.

[81] G. R. Cook and P. H. Metzger. Photoionization and Absorption Cross Sections of H2 and D2 in the Vacuum Ultraviolet Region. *J. Opt. Soc. Am.*, 54:968–+, August 1964.

[82] W. F. Huebner, J. J. Keady, and S. P. Lyon. Solar photo rates for planetary atmospheres and atmospheric pollutants. *Astrophys. Sp. Scie*, 195:1–289, September 1992.

[83] R. Abrines and I. C. Percival. Classical theory of charge transfer and ionization of hydrogen atoms by protons. *Proceedings of the Physical Society*, 88:861–872, August 1966.

[84] R. E. Olson and A. Salop. Charge-transfer and impact-ionization cross sections for fully and partially stripped positive ions colliding with atomic hydrogen. *Phys. Rev. A*, 16:531–541, August 1977.

[85] L. Meng, C. O. Reinhold, and R. E. Olson. Electron removal from molecular hydrogen by fully stripped ions at intermediate energies. *Phys. Rev. A*, 40:3637–3645, October 1989.

[86] L. Meng, C. O. Reinhold, and R. E. Olson. Subshell electron capture in collisions of fully stripped ions with He and H_2 at intermediate energies. *Phys. Rev. A*, 42:5286–5291, November 1990.

[87] J. H. McGuire and L. Weaver. Independent electron approximation for atomic scattering by heavy particles. *Phys. Rev. A*, 16:41–47, July 1977.

[88] P. C. Stancil, D. R. Schultz, M. Kimura, J.-P. Gu, G. Hirsch, and R. J. Buenker. Charge transfer in collisions of O^+ with H and H^+ with O. *Astron. Astrophys. Suppl. Ser.*, 140:225–234, December 1999.

[89] P. C. Stancil, A. R. Turner, D. L. Cooper, D. R. Schultz, M. J. Rakovic, W. Fritsch, and B. Zygelman. Electron capture in collisions of S^{4+} with atomic hydrogen. *J. Phys. B At. Mol. Opt. Phys.*, 34:2481–2504, June 2001.

[90] J. G. Wang, A. R. Turner, D. L. Cooper, D. R. Schultz, M. J. Rakovic, W. Fritsch, P. C. Stancil, and B. Zygelman. Electron capture in collisions of S^{4+} with helium. *J. Phys. B At. Mol. Opt. Phys.*, 35:3137–3156, July 2002.

[91] S. J. Bauer and H. Lammer. *Planetary Aeronomy*. Springer, 2004.

[92] A. Seiff, D. B. Kirk, T. C. D. Knight, J. D. Mihalov, R. C. Blanchard, R. E. Young, G. Schubert, U. von Zahn, G. Lehmacher, F. S. Milos, and J. Wang.

Structure of the atmosphere of jupiter: Galileo probe measurements. *Science*, 272:844–845, May 1996.

[93] A. Seiff, D. B. Kirk, T. C. D. Knight, L. A. Young, F. S. Milos, E. Venkatapathy, J. D. Mihalov, R. C. Blanchard, R. E. Young, and G. Schubert. Thermal structure of jupiter's upper atmosphere derived from the galileo probe. *Science*, 276:102–104, April 1997.

[94] P. V. Sada, G. L. Bjoraker, D. E. Jennings, G. H. McCabe, and P. N. Romani. Observations of CH_4, C_2H_6, and C_2H_2 in the Stratosphere of Jupiter. *Icarus*, 136:192–201, December 1998.

[95] C. T. Chantler. Theoretical Form Factor, Attenuation, and Scattering Tabulation for Z=1-92 from E=1-10 eV to E=0.4-1.0 MeV. *Journal of Physical and Chemical Reference Data*, 24:71–643, January 1995.

[96] J. I. Gersten. Theory of collisional quenching of fast metastable ions. *Phys. Rev. A*, 15:940–942, March 1977.

[97] W. L. Wiese, J. R. Fuhr, and T. M. Deters. *Atomic transition probabilities of carbon, nitrogen, and oxygen : a critical data compilation*. AIP Press, 1996.

[98] R. V Yelle and S. Miller. *Jupiter's Thermosphere and Ionosphere*, chapter 9. Planetary Science. Cambridge, 2004.

[99] S. K. Atreya, T. M. Donahue, and M. Festou. Jupiter - Structure and composition of the upper atmosphere. *Astrophys. J.*, 247:L43–L47, July 1981.

[100] A. L. Broadfoot, M. J. Belton, P. Z. Takacs, B. R. Sandel, D. E. Shemansky, J. B. Holberg, J. M. Ajello, H. W. Moos, S. K. Atreya, T. M. Donahue, J. L. Bertaux, J. E. Blamont, D. F. Strobel, J. C. McConnell, R. Goody, A. Dalgarno,

and M. B. McElroy. Extreme ultraviolet observations from Voyager 1 encounter with Jupiter. *Science*, 204:979–982, June 1979.

[101] D. Grodent and J.-C. Gérard. A self-consistent model of the Jovian auroral thermal structure. *J. Geophys. Res.*, 106:12933–12952, July 2001.

[102] L. Gan and T. E. Cravens. Electron energetics in the inner coma of Comet Halley. *J. Geophys. Res.*, 95:6285–6303, May 1990.

[103] P. M. Banks and A. F. Nagy. Concerning the Influence of Elastic Scattering Upon Photoelectron Transport and Escape. *J. Geophys. Res.*, 75:1902–1910, 1970.

[104] A. F. Nagy and P. M. Banks. Photoelectron Fluxes in the Ionosphere. *J. Geophys. Res.*, 75:6260–6270, 1970.

[105] M. H. Rees. *Physics and chemistry of the upper atmosphere*. Cambridge Univ Pr, 1989.

[106] X. Liu, D. E. Shemansky, H. Abgrall, E. Roueff, D. Dziczek, D. L. Hansen, and J. M. Ajello. Time-resolved Electron Impact Study of Excitation of H_2 Singlet-Gerade States from Cascade Emission in the Vacuum Ultraviolet Region. *Astrophys. J. Suppl. Series*, 138:229–245, January 2002.

[107] J. M. Ajello, S. K. Srivastava, and Y. L. Yung. Laboratory studies of UV emissions of H2 by electron impact - The Werner- and Lyman-band systems. *Phys. Rev. A*, 25:2485–2498, May 1982.

[108] W. K. Tobiska and F. G. Eparvier. EUV97: Improvements to EUV Irradiance Modeling in the Soft X-Rays and FUV. *Solar Phys.*, 177:147–159, 1998.

[109] A. N. Maurellis. *Non-Auroral Models of the Jovian Ionosphere*. PhD thesis, University of Kansas, 1998.

[110] M. Galand, L. Moore, B. Charnay, I. Mueller-Wodarg, and M. Mendillo. Solar primary and secondary ionization at Saturn. *J. Geophys. Res.*, 114(A13):A06313, June 2009.

[111] J. J. Perry, Y. H. Kim, J. L. Fox, and H. S. Porter. Chemistry of the Jovian auroral ionosphere. *J. of Geophys. Res.*, 1041:16541–16566, July 1999.

[112] G. R. Gladstone, M. Allen, and Y. L. Yung. Hydrocarbon Photochemistry in the Upper Atmosphere of Jupiter. *Icarus*, 119:1–52, January 1996.

[113] T. E. Cravens. Vibrationally excited molecular hydrogen in the upper atmosphere of Jupiter. *J. Geophys. Res.*, 92:11083–11100, October 1987.

[114] Y. H. Kim and J. L. Fox. The chemistry of hydrocarbon ions in the Jovian ionosphere. *Icarus*, 112:310–325, December 1994.

[115] Y. H. Kim, J. J. Caldwell, and J. L. Fox. High-Resolution Ultraviolet Spectroscopy of Jupiter's Aurora with the Hubble Space Telescope. *Astrophysical Journal*, 447:906, July 1995.

[116] D. Grodent, J. T. Clarke, J. Kim, J. H. Waite, and S. W. H. Cowley. Jupiter's main auroral oval observed with HST-STIS. *J. Geophys. Res.*, 108:1389, November 2003.

[117] S. W. H. Cowley, E. J. Bunce, and J. D. Nichols. Origins of Jupiter's main oval auroral emissions. *J. Geophys. Res.*, 108:8002, January 2003.

[118] M. A. Khakoo and J. Segura. Differential cross sections for the electron impact excitation of the $b^3 Sigma_u^+$ continuum of molecular hydrogen. *Journal of Physics B Atomic Molecular Physics*, 27:2355–2368, June 1994.

[119] M. A. Khakoo, S. Trajmar, R. McAdams, and T. W. Shyn. Electron-impact excitation cross sections for the b $3\Sigma_u^+$ state of H_2. *Phys. Rev. A*, 35:2832–2837, April 1987.

[120] H. Ehrhardt, L. Langhans, F. Linder, and H. S. Taylor. Resonance scattering of slow electrons from h_2 and co angular distributions. *Phys. Rev.*, 173(1):222–230, Sep 1968.

[121] M. J Brunger, S. J Buckman, D. S Newman, and D. T Alle. Elastic scattering and rovibrational excitation of h 2 by low-energy electrons. *Journal of Physics B: Atomic, Molecular and Optical Physics*, 24(6):1435, 1991.

[122] R. W. Crompton, D. K. Gibson, and A. I. McIntosh. The cross section for the J = $0 \rightarrow 2$ rotational excitation of hydrogen by slow electrons. *Australian Journal of Physics*, 22:715–730, December 1969.

[123] M. A. Morrison, B. C. Saha, R. W. Crompton, and Z. L. Petrovic. Near-threshold rotational and vibrational excitation of H2 by electron impact - Theory and experiment. *Australian Journal of Physics*, 40:239–281, 1987.

[124] J. Woodall, M. Agundez, A. J. Markwick-Kemper, and T. J. Millar. The UMIST Database for Astrochemistry 2006. *A&A*, pages 1197 – 1204, January 2007.

[125] I. P. Robertson, T. E. Cravens, J. H. Waite, R. V. Yelle, V. Vuitton, A. J. Coates, J. E. Wahlund, K. Ågren, K. Mandt, B. Magee, M. S. Richard, and E. Fattig. Structure of Titan's ionosphere: Model comparisons with Cassini data. *Planet. Space Sci.*, 57:1834–1846, December 2009.